Modelling fluvial responses to episodic sediment supply regimes in mountain streams

by

Josef Tobias Müller (Mueller)

Diplom-Geograph, Geographisches Institut, Rheinische Friedrich-Wilhelms-Universität Bonn, 2011

A THESIS SUBMITTED IN PARTIAL FULFILLMENT OF THE REQUIREMENTS FOR THE DEGREE OF

Doctor of Philosophy

in

THE FACULTY OF GRADUATE AND POSTDOCTORAL STUDIES

(Geography)

The University of British Columbia
(Vancouver)

March 2019

The following individuals certify that they have read, and recommend to the Faculty of Graduate and Postdoctoral Studies for acceptance, the dissertation entitled:

Modelling fluvial responses to episodic sediment supply regimes in mountain streams

---

submitted by Josef Tobias Müller (Mueller) in partial fulfillment of the requirements for the degree of Doctor of Philosophy in Geography

Examining Committee:

Marwan A. Hassan
Supervisor

Erkan Istanbulluoglu
Supervisory Committee Member

Ian McKendry
Supervisory Committee Member

Brett Eaton
University Examiner

Roger Beckie
University Examiner

Abstract

Large, episodically occurring sediment supply events may temporarily dominate channel morphology and sediment transport in mountain streams. Field studies of channel response to these events are challenging to undertake, as a long data record is needed to reasonably assess a system's state of response in the context of episodic supply. Greater confidence in the observed state of response of a system can be achieved with flume experiments where fluvial response can be observed in detail after episodic events are introduced in a controlled fashion. Yet, the amount of work necessary to carry out these experiments is large, which limits the number of experimental conditions that can be studied, and thus their utility for addressing applied problems of channel adjustment.

To overcome this limitation, I developed the 1-D morphometric sediment transport model BESMo, which allows large numbers of simulations to be run in batches, generating ensemble results. This model was used to recreate results from flume experiments, after which the experimental conditions were extended to include a broader range of simulated pulse frequencies, magnitudes, and grain size compositions. It was shown that the sequencing of pulse events of different magnitudes has only a short term effect on the slope and grain size response of the channel. Furthermore, thresholds were identified that allow for the categorization of fluvial response to episodic sediment supply regimes into one of (a) constant-feed-like, or (b) pulse-dominated.

The practical utility of BESMo for studying fluvial response to large sediment supply events was demonstrated through the study of potential geomorphic effects following the removal of a dam in the Carmel River, California, USA. This showed the advantage of BESMo for simulating many different future scenarios, as stochasticity could be explicitly included through varied hydrographs. This allowed results to be interpreted in light of the uncertainty in future flood occurrence. Finally, to overcome data limitations on surface grain size distributions, I developed machine-learning based methods to detect grain size distributions from images. Collectively, this work has advanced our understanding and ability to characterise downstream channel response to episodic supply events, and to better obtain data needed for this characterisation.

Lay Summary

The objective of this thesis is to understand how mountain streams adjust to sediment from episodic events, such as landslides. This is difficult to study in the field or lab, where long observation times are needed to capture a river's response to multiple events. To overcome this limitation, I developed BESMo, a versatile model for studying channel adjustment to sediment additions. I found that in the long term, the ordering of events is not important for the adjustment of the river. Furthermore, rivers adjusts to episodic events in different modes, based on whether events occur more (or less) frequently than the river can rework them. I then used BESMo to simulate how the Carmel River adjusts to the removal of a dam, helping to determine the best options for river management in the future. Finally, I developed a machine-learning based method to detect grain size distributions from images.

Preface

This thesis is original work completed by J. Tobias Müller. Guidance was given by the supervisory committee. This thesis includes one manuscript, and two complementary chapters that are planned to be submitted for publication as individual manuscripts. Chapter 2 is published in *Earth Surface Dynamics* (Müller and Hassan, 2018) with co-author Marwan A. Hassan, who supervised the work. Chapter 3 and Chapter 4 are complementary Chapters.

The work in Chapter 3 is based on a project done for the Monterey Peninsula Water Management District (MPWMD) and the California American Water Company (CalAM) in cooperation with Balance Hydrologics and AECOM, resulting in a separate report that was submitted for review in November 2018 and is being prepared for publication. Shawn Chartrand and Kealie Pretzlav helped with gathering the data, and Leonora King helped editing the text.

Müller, T. and M. A. Hassan (2018), Fluvial response to changes in the magnitude and frequency of sediment supply in a 1-D model. *Earth Surface Dynamics*, 6(4), 10411057.

Contents

List of Tables

List of Figures

List of Symbols

Symbol	Definition
AR_{elp}	Armouring ratio at end of last pulse
AR_{const}	Armouring ratio at end of constant feed run
D_{sg}	Surface geometric mean grain size [m]
D_{subg}	Subsurface geometric mean grain size [m]
D_{s50}	Surface 50th percentile grain size [m]
D_{s84}	Surface 84th percentile grain size [m]
D_{s90}	Surface 90th percentile grain size [m]
D_{fg}	Feed geometric mean grain size [m]
D_{f90}	Feed 90th percentile grain size [m]
D_{ag}	Armoured geometric mean grain size [m]
D_{a90}	Armoured 90th percentile grain size [m]
f_{Ii}	Proportion of ith grain size class exchanged between the surface and the subsurface
F_i	Surface frequency of ith grain size class
Fr	Froude number
F_{pulse}	Pulse frequency [$1/s$]
g	Gravity [m/s^2]
GSD_{fluv}	Channel surface grain size distribution
GSD_{pulse}	Pulsed sediment feed grain size distribution
h	Water depth [m]
k_s	Roughness height [m]
l_r	Channel length [m]
L_a	Active layer thickness [m]
M_{pulse}	Pulse magnitude [m^3]
n_k	Roughness height coefficient
n_a	Scale of bed height fluctuation
p_{bi}	Bedload transport rate fraction of ith grain size class
q_b	Bedload transport rate [m^2/s]
q_{bi}	Fractional bedload transport rate [m^2/s]
Q_w	Water discharge [m^3/s]
S_f	Friction slope [m/m]
S_0	Bed slope [m/m]
S_{mlp}	Mean channel slope at end of last pulse [m/m]

S_{const}	Slope at the end of constant feed run [m/m
t	Time [s]
T_{pp}	Pulse period [s]
T_{fe}	Fluvial evacuation time [s]
T_{ar}	Fluvial armouring time [s]
T_{sim}	Duration of simulation [s]
u^*	Dimensionless shear velocity
U_{fluv}	Fluvial export velocity [m/s]
U_{pulse}	Virtual pulse velocity [m/s]
w_r	Channel width [m]
x	Downstream distance [m]
α_r	Manning-Strickler coefficient
α	Active layer exchange ratio
η_b	Bed surface elevation [m]
λ	Bed porosity
ρ	Water density [kg/m^3]
σ	Wideness of generated grain size distribution
τ_b	Boundary shear stress [Pa]
τ_{rm}	Reference shear stress [Pa]

List of Acronyms

Acronym	Description
AM	Dataset of flume images collected by Alex Mitchell
AECOM	Architecture, Engineering, Consulting, Operations, and Maintenance (engineering company)
BESMo	Bedload Scenario Model (modelling software developed for this thesis)
BOMC	Bed Of Many Colours
CNN	Convolutional Neural Network (type of machine learning architecture)
CSUMB	California State University, Monterey Bay (educational institution)
CRRDR	Carmel River Reroute and Dam Removal (project)
DistID	Distribution Identification (Method developed in Chapter 4)
GIS	Geographic Information System (software for spatial analysis)
GSD	Grain size distribution
HEC-RAS	Hydraulic Engineering Center - River Analysis System, US Army Corps (modelling software)
HEC-SSP	Hydraulic Engineering Center - (modelling software)
HSV	Hue, Saturation, Value (digital colour representation)
LPD	Los Padres Dam (structure)
MPWMD	Monterey Peninsula Water Management District (public agency)
MEI	Mussetter Engineering Inc. (engineering company)
PRMS	Precipitation-Runoff Modeling System (modelling software)
ResNet50	Residuals Network, size 50 (type of CNN)
RGB	Red, Green, Blue (digital colour representation)
SRH-1D	Sedimentation and River Hydraulics - One Dimension, US Bureau of Reclamation (modelling software)
StoneID	Stone Identification (Method developed in Chapter 4)
UAV	Unmanned Aerial Vehicle (remote controlled aircraft, commonly known as a drone)
URS	United Research Services (engineering company, now part of AECOM)
USGS	United States Geological Survey (public agency)
VGG19	Visual Geometry Group, size 19 (type of CNN)
YW	Dataset of flume images and GSDs collected by Yinlue Wang

Acknowledgements

I first want to thank my family for their love and moral support. Even though I moved far away to write this thesis, my parents, sisters, and brothers-in-law could always cheered me up with calls and videos of my nieces and nephews. I want to thank all my friends back in Germany, who showed in visits that 6 years abroad never caused our friendships to change. This is especially true for my lifelong friends Felix M., Martin H., and Matthias. Urs, Felix S., Steph, and crew kept me on my heels, thank you for that. Christoph Disch, along with all my other friends from Bonn, provided moral support over the blackest of coffees. Thank you Thomas Hoffmann for getting the first stones rolling.

The journey through the PhD program would have been immensely harder without my friends and colleagues in Vancouver. Thank you Leah and Bodhi for cheering me up many times. Leonora King and David Reid are the best housemates to have (especially while finishing a thesis) and helped greatly with proof-reading. The labgroup was an amazing support in discussing all things from raw ideas to the tiniest details of plots. Thank you Shawn for offering me the chance to work on a great project.

Thank you Marwan for being an amazing supervisor, whose door was always open to provide advice, encouragement, and support. Thank you for being patient even though I overshot all deadlines, thank you for catching my worst mistakes, and thank you for trusting in my abilities. Thank you Erkan and Ian for supporting me in this endeavour.

Regarding the second chapter, I thank Maria Elgueta and Claudia von Flotow for their collaboration in conducting the flume experiments, Conor McDowell for comments on an early draft of this work, and Eric Leinberger for improving the figures for publication. I am grateful

for suggestions by Gary Parker and Chenge An that improved this chapter, editing by Kimberly Hill, and reviews by three anonymous referees. Carles Ferrer-Boix helped greatly in the development of an early version of BESMo. Regarding the third chapter, I thank Shawn Chartrand and Kealie Pretzlav for sourcing some of the input data for the model and providing support for writing the text. Final editing support from Leonora King improved this chapter greatly. I thank Alex Michell and Yinlue Wang for providing data of their flume experiments that was used to develop the methods in the fourth chapter, and Matteo Saletti for providing valuable insights on the stone identification approach.

Computational resources for both the numerical simulations and the machine learning training were provided by WestGrid[1] and Compute Canada[2].

I thank the University of British Columbia for supporting me with a Four Year Fellowship and the Stiftung für Kanadastudien for providing a travel grant that helped me to conduct the flume experiments.

[1] www.westgrid.ca, last access: Jan 1st, 2019
[2] www.computecanada.ca, last access: Jan 1st, 2019

Dedication

Für meine Eltern Ellen und Karl-Josef. Danke für die unendliche Unterstützung.

Chapter 1

Introduction

Figure 1.1: Landslide providing episodic sediment supply into a stream in Hinton, Alberta. Credit: Marwan A. Hassan.

Rivers are commonly affected by large and episodic sediment inputs, a result of both naturally occurring landslides (*Korup*, 2013), and human activity, such as mining (*Nelson and Church*, 2012) or dam removals (*Grant and Lewis*, 2015). These large sediment supply events might temporarily dominate sediment transport and storage regimes within river channels (*Hassan*

et al., 2005, 2008a). *Hassan et al.* (2018) found that especially in formerly glaciated mountain environments the coupling of fluvial channels to hillslopes is widespread, leading to a high potential for colluvial input into the channel. Consequently, these episodic supply events lead to downstream impacts that can impact fish habitat (*May and Lisle*, 2012) and human infrastructure (*Kondolf and Piégay*, 2011).

The range and magnitude of natural and anthropogenic supply events, in combination with the complexity of geomorphic mountain channel processes (*Wohl*, 2013), make mountain river form and behaviour particularly challenging to manage and predict. This complexity necessitates a better understanding of how large sediment supply events affect the morphology and sediment transport dynamics of mountain streams. Despite over a century of research into sediment transport, we continue to lack understanding of many aspects of channel response to changing sediment supply (*Hassan and Zimmermann*, 2012).

Sediment supply plays an important role in shaping the morphology and the sediment texture of gravel bed rivers from the reach to the catchment scale (*Hassan et al.*, 2008a; *Pfeiffer et al.*, 2017). In the context of sediment transport, rivers are often conceptualized to be in one of two states: (1) supply limited, or (2) transport limited (*Montgomery and Buffington*, 1997). When the sediment supply rate exceeds the transport capacity of a stream, storage of material increases and the system is considered transport limited. If the transport capacity of the stream is higher than the sediment supply rate, stored sediment is depleted and the channel is considered supply limited. However, this simple conceptualization is rendered more complex when storage dynamics are considered, which temper a channel's response to external sediment supply (*Lisle and Church*, 2002). Finally, sediment supply plays an important role in changes in the bed surface grain sizes and the development of bed surface structures, which can reduce the sediment transport capacity by stabilizing the bed surface (*Dietrich et al.*, 1989; *Church et al.*, 1998).

To better understand the impact of changes in frequency, magnitude, and grain size of sediment supply events on a fluvial channel, simplified process interactions can be studied in both flume experiments (e.g. *Cui et al.*, 2003; *Elgueta-Astaburuaga and Hassan*, 2017; *Johnson et al.*, 2015; *Sklar et al.*, 2009) and numerical models (e.g. *Cui and Parker*, 2005; *An et al.*, 2017a).

While both approaches have provided significant insight into the complex process interactions in the fluvial reworking of supply events, these studies simulated channel response to a relatively limited range of event frequencies and magnitudes. For this thesis the 1-D morphometric model BESMo ('Bedload scenario model') was developed, which allows for many different configurations of sediment supply and hydrology conditions to be evaluated concurrently. BESMo has the advantage of incorporating computational methods that allow for the consideration of uncertainty and stochasticity in a channel's response to episodic sediment supply.

Using the developed model, this thesis investigates the following general questions:

1. How do changes in the frequency and magnitude of sediment pulses impact gravel bed rivers at the reach scale?

2. How do different sediment supply regimes in combination with different hydrologic conditions impact the river downstream?

Associated to these questions and motivated by a lack of data in answering the earlier questions, a methodological problem was identified:

3. What method can improve the identification of grain size distributions in flume experiments?

After a general introduction to the research approach and the significance of numerical models, Chapter 2 describes the development of BESMo and how it is used to expand upon supply conditions examined in flume experiments, which provides insight into research question 1 (above). The second research question is explored in Chapter 3 using a dam removal case study on the Carmel River in California. For this chapter, different sediment supply conditions were simulated in BESMo with hundreds of different simulated hydrographs, which were generated using a stochastic approach based on historical flood records. Due to the important role that armouring and channel bed features play in the bed surface response to episodic sediment supply, a need for better grain size characterisation in flume experiments was identified. To address this issue (stated in the third research question), an automated sta-

tistical approach for identifying both grain size distributions and individual grains in images taken of flume surfaces was developed, described in Chapter 4.

The following section provides an overview of the role episodic events play in geomorphic systems. This leads into a section on the advantages of numerical models to explore this role in greater detail, providing grounds for the use of numerical models to answer the research questions of this thesis.

1.1 Systems approach to episodic events

Chorley and Kennedy (1971) suggest a system hierarchy to structure the understanding of natural processes. One of the theoretical frameworks suggested is to order processes and forms into 'cascading systems'. Within these systems, components are characterized by chained energy or mass throughputs, and therefore the output of one subsystem is the input of the next. This concept is used for studies of sediment dynamics in mountain catchments in the form of sediment budgets, in which stored and transported sediment volumes are quantified for all relevant processes (*Slaymaker*, 2003). This puts the spatial hierarchy of a sediment cascade in the temporal context of time spent in storage or transport and allows a picture of catchment scale sediment dynamics to be derived. The spatial components of the system are homogeneous areas, distinguishable by material, morphometry or type of active processes. These can be derived from field mapping or GIS analysis, as for example done by *Schrott et al.* (2003) and *Hoffmann et al.* (2013).

Morphometric indices such as curvature, slope, or catchment area can be used to delineate system components in the landscape. *Montgomery and Foufoula-Georgiou* (1993) describe a distinctive relation between the morphometric indices 'local slope' and 'contributing area', which, when applied to their study catchments, depict an inflection point that indicates a change from debris-flow-dominated channels to alluvial channels. *Montgomery* (1999) further investigate the spatial and temporal aspects of form-process relationships to develop a 'process domain' concept. He argues that spatial variability in process activity must be considered to understand temporal patterns of system change and forcing of system reactions to disturbance. An application of this concept to a formerly glaciated catchment in British Columbia is

given by *Brardinoni and Hassan* (2006). In their study area, the topographic signatures do not match currently active processes. The authors ascribe this disequilibrium to the relict glacial forms, whose legacy is more dominant than the morphologic activity of contemporary processes. Hence, the application of the process domain concept must be viewed in the context of the individual history and configuration of the system studied.

After characterising the spatial extent of the sediment cascade, knowledge of the temporal patterns of linkage functionality between the components of the geomorphic system is needed to understand sediment transport dynamics. If the action of a process is episodic, the easiest way to assess volumes of transported sediment is by building a relationship between the frequency and magnitude of events. In debris flow dominated catchments in particular, information about event frequency is of high importance in the study of sediment transport (*Dietrich and Dunne*, 1978).

Both fluvial and hillslope domains are subject to the action of highly episodic processes. *Wolman and Miller* (1960) introduced the term geomorphic effectiveness, which is calculated as the product of frequency and magnitude of events. They found that most work is done by moderately sized events, as the events highest in magnitude are low in frequency (see Figure 1.2). River channels are shaped by the sequenced action of floods with varying magnitudes and frequencies, but fluvial sediment transport is in most cases simulated as an linear function of discharge. Even though the frequency-magnitude concept could allow for the calculation of a long-term average impact, the relationship between flood magnitudes and sediment transport is more complex. For example, flows of similar peak magnitude show different geomorphic effectiveness in shaping morphology or transporting sediment due to hydrograph characteristics (*Hassan et al.*, 2006a, 2014). *Guthrie and Evans* (2007) analyse geomorphic effectiveness of landslides in terms of work (material transported), persistence (residence time) and formation (morphological impact) and find moderately sized events to be most efficient. They also find the persistence time of the impact to be the most meaningful measure of the effectiveness of events.

The effect of episodic supply events on the fluvial system can be viewed under a disturbance concept. *Bull* (1991) describes a hypothetical temporal succession of disturbance events

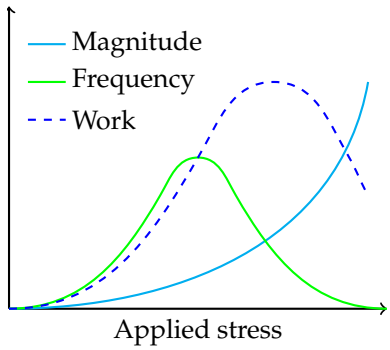

Figure 1.2: Event effectiveness as a function of frequency and magnitude. After: *Wolman and Miller* (1960).

with the example of sediment storage in a stream-bed (see Figure 1.3). Episodic disturbance events of sediment contribution and sediment export result in an increase or decrease of the stream-bed elevation, respectively. This reaction is not instantaneous, but delayed by a reaction time (Ra) in which no adjustment takes place. The system processes the disturbance over the relaxation time (Rx), which together with the reaction time constitutes the total response time (Rt). If there is no further disturbance, the system status remains unchanged over a time of persistence (Ps). Sequenced disturbance events might lead to overlap of reaction times and relaxation times and thus create a complex pattern of system changes. Due to the complexity of geomorphic systems, it might be impossible to discern these temporal phases of system reaction in field studies.

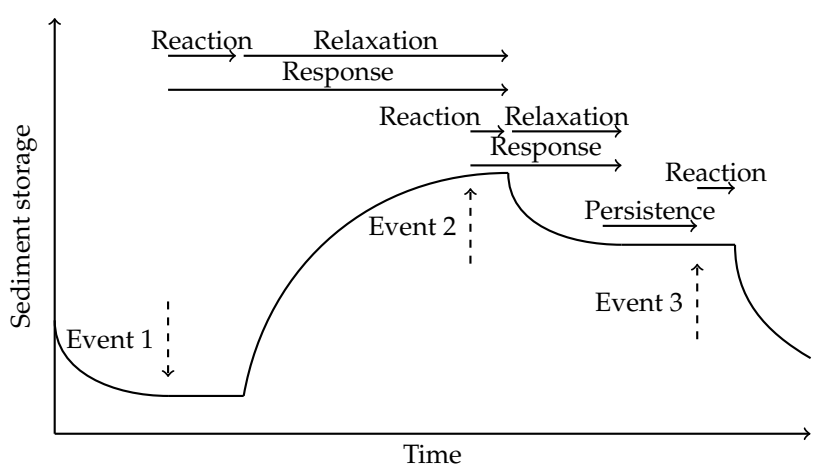

Figure 1.3: Temporal features of disturbance reaction with the example of sediment storage in a streambed. After: *Bull* (1991).

1.2 System understanding from numerical models

Numerical models are used to combine the understanding of multiple processes in a framework that enables us to study process interactions that represent complex real world systems (*Phillips*, 2003). Use of these models can serve to meet practical objectives linking cause and consequence, but can also allow for exploration of new research questions and experimental designs (*Escauriaza et al.*, 2017). *Wilcock and Iverson* (2003) state that while prediction without a model is just speculation, using models without making predictions can be helpful for reviewing our understanding how processes interact and expose knowledge gaps.

Numerical process modelling has a long tradition in fluvial geomorphology (*Coulthard and Van De Wiel*, 2013) and is based on the development of process understanding through measuring process rates. *Dietrich et al.* (2003) give an overview of mechanistic mathematical models of separate morphological processes, which if combined in a framework and solved together builds a landscape evolution model. These models open up the opportunity to predict behaviour of rivers from the reach to the landscape scale, for instance by linking hillslopes with fluvial domains (*Tucker and Bras*, 1998). Recently, modelling has focussed on the effects of environmental change (*Van De Wiel et al.*, 2011), necessitating the inclusion of processes that were not traditionally a focus in geomorphology, such as the effect of vegetation on landscape evolution (*Istanbulluoglu*, 2005).

The development of combined process models is rooted in the previously described 'systems approach'. Numerical models in geomorphology must be based on an understanding of the process interactions at play, which can be illustrated in the form of a sediment cascade. If a process that affects the studied phenomena is not represented numerically, the prediction of the model will be (within the accuracy that can be expected from a simplified model) false and potentially misleading. In general, more complex problems require more complex models, as the effect of more processes and/or conditions must be considered (*Van De Wiel et al.*, 2011).

Model predictions must be critically evaluated as a matter of course. Real geomorphic systems are thermodynamically open systems, where we cannot know all energetic exchanges and processes at play within the boundary of a particular study. Furthermore, the history of

the modelled system might be more important for the result than the mechanics of the process interactions, which is typical for chaotic systems (*Phillips*, 2003). This makes finding realistic approximations of complex open systems difficult, which would still be true even if we had perfect formal descriptions of the individual contemporary processes (*Beven*, 2002).

A way to approximate uncertainty is to link the range of model results to the uncertainty in input conditions by running many simulations 'Monte-Carlo style', where the separate simulations begin with varied initial conditions (*Willgoose et al.*, 2003). This approach is used here and is a main advantage of BESMo over previous models, due to its capability of running many simulations at once on a computing cluster and easily compiling batch results. The model was calibrated with results from flume experiments and then used to explore the effect of varied event frequency, magnitude and grain size composition (see Chapter 2). In this way, the model was used to expand our theoretical understanding of the impact of hillslope processes on the fluvial system. The capability of the model to explore different management options in a river is demonstrated in Chapter 3 for a dam removal case. This case study brought challenges of low data availability and unknown future hydrology: while these difficulties might appear to present a problematic situation in which to apply a model, a modelling effort here is the best way to assess the sensitivity of the system to future conditions (*Oreskes et al.*, 1994).

Chapter 2

Fluvial response to changes in the magnitude and frequency of sediment supply in a 1-D model

2.1 Summary

In steep headwater reaches, episodic mass movements can deliver large volumes of sediment to fluvial channels. If these inputs of sediment occur with a high frequency and magnitude, the capacity of the stream to rework the supplied material can be exceeded for a significant amount of time. To study the equilibrium conditions in a channel following different episodic sediment supply regimes (defined by grain size distribution, frequency, and magnitude of events), we simulate sediment transport through an idealized reach with our numerical 1-D model "BESMo" (Bedload Scenario Model). The model performs well in replicating flume experiments of a similar scope (where sediment was fed constantly, in one, two, or four pulses) and allowed the exploration of alternative event sequences. We show that in these experiments, the order of events is not important in the long term, as the channel quickly recovers even from high magnitude events. In longer equilibrium simulations, we imposed different supply regimes on a channel, which after some time leads to an adjustment of slope, grain

size, and sediment transport that is in equilibrium with the respective forcing conditions. We observe two modes of channel adjustment to episodic sediment supply. (1) High-frequency supply regimes lead to equilibrium slopes and armouring ratios that are like conditions in constant-feed simulations. In these cases, the period between pulses is shorter than a "fluvial evacuation time", which we approximate as the time it takes to export a pulse of sediment under average transport conditions. (2) In low-frequency regimes the pulse period (i.e., recurrence interval) exceeds the "fluvial evacuation time", leading to higher armouring ratios due to the longer exposure of the bed surface to flow. If the grain size distribution of the bed is fine and armouring weak, the model predicts a decrease in the average channel slope. The ratio between the "fluvial evacuation time" and the pulse period constitutes a threshold that can help to quantify how a system responds to episodic disturbances.

2.2 Introduction

Mass movements in mountainous regions often deliver sediment directly to the stream network, resulting in coupled conditions that can trigger immediate channel responses during relatively large delivery events. Notably, delivery events can reset the local channel profile and govern construction and maintenance of channel bed architecture downstream of delivery points. The local response rate and trajectory following a delivery event is a function of the prevailing watershed flow regime, the magnitude of the delivery event, gradients in channel width (*Ferrer-Boix et al.*, 2016), and in some instances the concentrated activity of aquatic species such as salmon (*Hassan et al.*, 2008b). While lowland river systems have been the focus of a substantial body of research, less work has been carried out within steep mountain streams, particularly concerning mountain channel responses to changes in flow or sediment supply regimes.

In mountain streams, large, episodic inputs may temporarily dominate channel processes and morphology, significantly altering sediment transport and storage within the stream channel (*Hassan et al.*, 2005, 2008a). *Lisle et al.* (1997) conducted flume experiments and numerical modelling that showed that sediment pulses are mainly reworked in situ, in contrast to a downstream translation in the form of a sediment wave. This finding is supported by *Lisle*

et al. (2001), where little evidence of sediment waves was found in the field. *Lisle and Church* (2002) suggested that a stream channel responds to changes in the sediment supply by altering both storage and sediment transport rates. They describe that after a sediment pulse occurs, a first phase with low armouring rates allows for high transport rates in reworking the introduced material, corresponding to supply limited conditions. This is followed by a second phase in which armouring develops and transport rates decrease, corresponding to transport limited conditions. If the fluvial capacity is too low to evacuate the mass or grain size of material in the current hydrological regime, lag sediment can remain in the channel and dominate the local morphology for a long time (e.g., *Benda et al.*, 2005; *Brummer and Montgomery*, 2006). Patterns of cyclic behaviour, associated with the rapid input of sediment from external sources, have been described in a number of field observations (e.g., *Roberts and Church*, 1986; *Madej and Ozaki*, 1996; *Madej*, 1999, 2001; *Miller and Benda*, 2000; *Hoffman and Gabet*, 2007; *Hassan et al.*, 2008a) and some experimental studies (e.g., *Cui et al.*, 2003; *Sklar et al.*, 2009; *Venditti et al.*, 2010; *von Flotow*, 2013; *Elgueta*, 2014; *Ferrer-Boix and Hassan*, 2014, 2015; *Johnson et al.*, 2015; *Elgueta-Astaburuaga and Hassan*, 2017; *An et al.*, 2017a). These studies observed fining of the bed surface, higher mobility and thus increased transport rates following such episodic sediment supply events. A reverse trend for coarsening and stabilizing of the bed was also noted as the supply was exhausted and a decrease in sediment transport rates followed (e.g., *Dietrich et al.*, 1989; *Church et al.*, 1998; *Hassan and Church*, 2000; *Nelson et al.*, 2009). *Cui and Parker* (2005) support these findings using numerical modelling and further point out that abrasion can play an important role in the reworking of sediment pulses. Field observations (e.g., *Benda*, 1990; *Pryor et al.*, 2011), and flume experiments (e.g., *Pryor et al.*, 2011; *Luzi*, 2014) also document cycles of aggradation and degradation due to changes in the sediment supply. The observations discussed above suggest that changes in the sediment supply rate may lead to significant changes in bed elevation, bed surface texture, channel stability, and bed morphology. An analytical model developed by *Blom et al.* (2017) showed that the local channel geometry and surface grain size composition is mainly governed by long-term mean sediment supply rates and not by short-term changes in supply conditions. In contrast to cyclic sediment supply, cyclic hydrographs were found to mainly affect sediment transport rates and

have a lesser impact on bed surface texture and channel morphology (*Parker et al.*, 2007). *Wong and Parker* (2006) reported that cyclic hydrographs cause a part of the channel bed to undergo cyclic aggradation and degradation forming a hydrograph boundary layer. Cyclic sediment supply causes a similar effect which is termed the sedimentograph boundary layer (*An et al.*, 2017b).

These findings imply that the morphological impact of the sediment pulse is most prevalent at the point of entrance, while the downstream portion mostly conveys the subsequently eroded material. The time needed for channel adjustments to occur after a large sediment input event depends on the amount and the texture of the delivered material. *Brummer and Montgomery* (2006) reported that 2 years after the supply event, the most mobile fractions (e.g., the fine fractions) were evacuated by a series of moderate floods while the largest grain sizes remained in the channel as lag deposits because flows were below their flow competence. Further, they showed that selective transport of sediment led to the development of an armour layer after only a few flow events. This armour layer protects the supplied material in the bed subsurface, increases bed stability, and causes lateral erosion and channel widening.

We expect the sediment transport rate in a channel to reach a long-term balance between erosional and depositional forces, even though there can be periodic changes in the short term. This state is defined as a "dynamic equilibrium" following *Ahnert* (1994). If the external forcing on the system changes, the channel will be in a transient state of adjustment towards a new dynamic equilibrium. Little attention has been directed to the question of what effect a change in the frequency of sediment supply events may have on the response of alluvial streams. *Brunsden and Thornes* (1979) proposed that if the frequency (i.e., recurrence interval) of disturbing events is shorter than the time necessary for a system to adjust to new boundary conditions ("relaxation time"), then transience will dominate the system and it may never achieve equilibrium (*Brunsden*, 1980). *Wolman and Miller* (1960) suggest that mountain channels experiencing direct inputs of sediment are good examples of such systems, where form is defined by extreme events rather than events of intermediate magnitude and frequency. The concept of this so-called "temporal sensitivity" was later elaborated on by *Thomas* (2001) and *Brunsden* (2001), although since their studies little attempt has been made in fluvial geomor-

phology to address this issue in practice. *Bull* (1991) applies the theory of *Brunsden and Thornes* (1979) to the impact of a hypothetical temporal succession of disturbance events on sediment storage, which can either increase or decrease the stream-bed elevation. The system processes the disturbance over the relaxation time, which together with a potential reaction time constitutes the total response time. If there is no further disturbance, the system status remains unchanged over a time of persistence. The concept from Bull (1991) is based on a system's trend towards a dynamic equilibrium between the forcing by, and the reworking of, disturbances. *Howard* (1982) concluded that if episodic inputs occur with a frequency that matches the inverse of the relaxation time, the output of the system will remain in a constant equilibrium with the average value of the forcing. Flume based insights about equilibrium conditions and timescales of adjustment to changes in sediment supply rates are discussed in some studies (e.g., *Elgueta-Astaburuaga and Hassan*, 2017; *Pryor et al.*, 2011), but response times are only quantified in few cases (e.g., *Podolak and Wilcock*, 2013).

The paragraphs above illustrate how the frequency at which events occur may be fundamental in defining the response of a fluvial system to a change in boundary conditions. Therefore, it appears that event frequency should be a central aspect in investigations regarding the effect of episodic sediment supply on streams. Consequently, our understanding of involved processes remains incomplete. For example, it is uncertain whether the freshly delivered sediment that buries and is transferred over the bed surface is simply removed by the subsequent floods or whether there is some exchange between armoured and structured bed and the fine and mobile deposits. Furthermore, *Hassan and Zimmermann* (2012) asserted that it is important to study how quickly internal changes in grain size, channel morphology, and sediment storage occur when the stream shifts between cycles of aggradation and degradation.

Our main research objective is to describe the impact of episodic sediment supply on channel bed evolution in simulations using a 1-D morphodynamic numerical model for a bed of multiple grain sizes. We use the model to recreate conditions from experiments conducted at the Mountain Channel Hydraulic Experimental Laboratory, University of British Columbia, where a set of experiments were carried out to examine the impacts of episodic sediment supply on bed surface evolution and channel adjustment of a gravel bed stream (*von Flotow*, 2013;

Elgueta, 2014; *Elgueta-Astaburuaga and Hassan*, 2017; *Elgueta-Astaburuaga*, 2018). Although these experiments provide detailed information on channel adjustment to changes in the sediment supply regime, they are limited in terms of the number of experiments and the range of scenarios that could be conducted. The performance of the model is tested against the experimental results obtained in the laboratory and then used to further explore controls and responses of the fluvial system to changes in flow and sediment supply regimes. The specific research questions addressed in this study are as follows:

1. Can the numerical model recreate the channel response that was observed in flume experiments of similar scope?

2. Does the sequencing of supply events play a role in the reaction of a gravel-bed stream, when several events of specified magnitudes occur in a different order?

3. How will different combinations of episodic sediment supply, obtained by varying their magnitude and frequency, impact channel evolution of a gravel-bed stream?

2.3 Methods

We applied the 1-D morphodynamic model BESMo (Bedload Scenario Model) to calculate capacity based sediment transport under different sediment supply regimes. We chose values for model parameters to match the flume experiments as closely as possible and used measurements of sediment transport rate, surface grain size distribution, and slope to calibrate the model. Matching our research questions, we then conducted two types of simulations:

1. In "event sequencing simulations", we simulated different permutations of events to understand the role event succession plays in long-term channel response.

2. In "equilibrium simulations", we used the same model setup and imposed different, but within each run regular, supply event frequencies. These simulations were run until we achieved a recurrent pattern in slope and grain size adjustment, allowing us to identify how the channel adjusts to the supply regime in the long term.

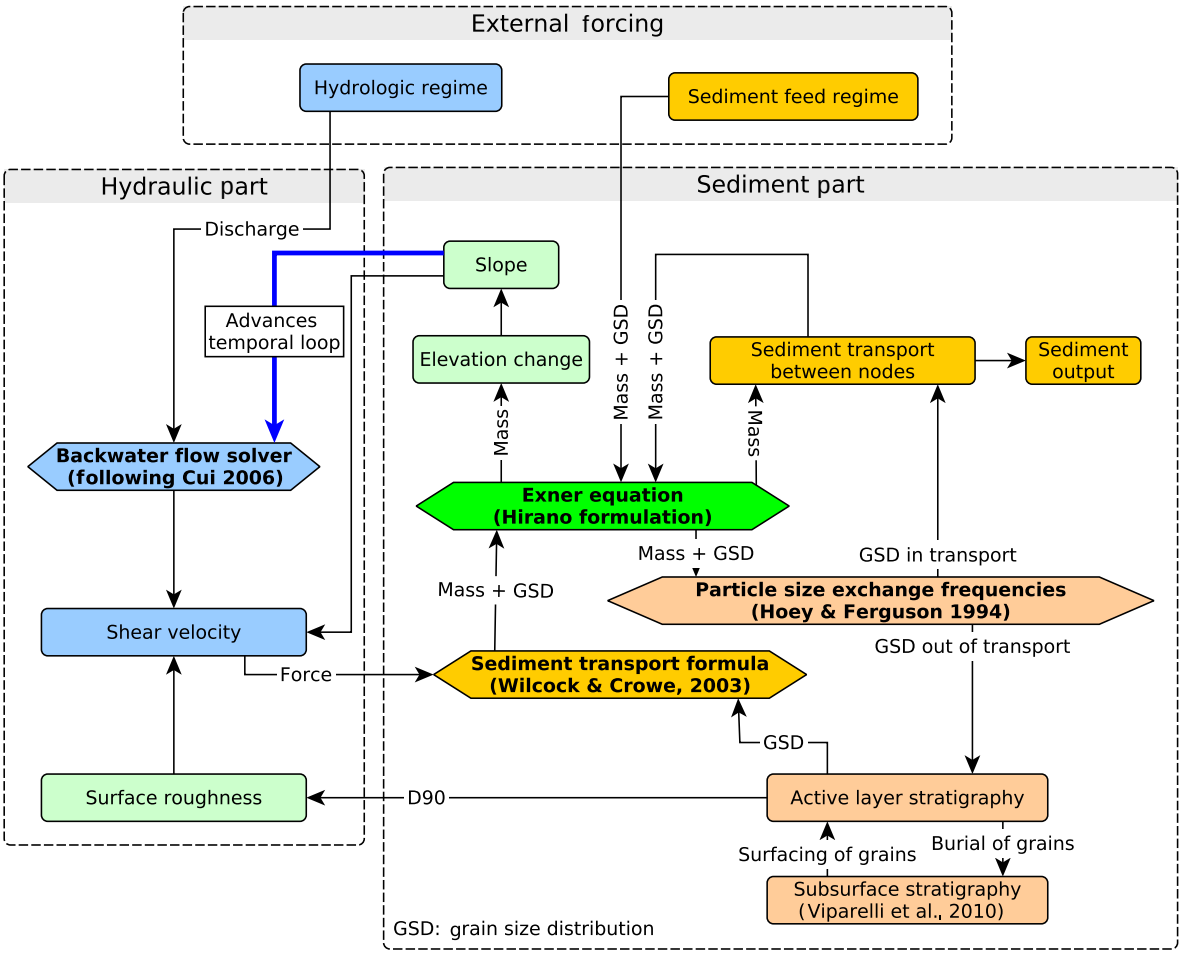

Figure 2.1: Flowchart stating the main components of the model and the flow of information between them. The temporal loop is advanced as the new elevation affects the slope in the flow model. The components are coloured as follows: blue – flow related, dark yellow – sediment volume related, peach – particle size related, and green – geometry related.

2.3.1 Model setup

The structure of the model is similar to other models designed to reproduce and interpret data from flume experiments (e.g., *Cui and Parker*, 2005; *Wong and Parker*, 2006; *Ferrer-Boix and Hassan*, 2014; *An et al.*, 2017a). Figure 2.1 gives an overview of the implemented model components and their basic interaction. The model can be subdivided into a "hydraulic part" and a "sediment part", both of which are subject to "external forcing" that varies in according to the modelling scenarios.

We set up the modelling environment to run on a Compute Canada research cluster, which

allows us to simulate many different input conditions in parallel and compare results quickly. We use a backwater flow model as suggested by *Cui et al.* (2006), implementing a threshold Froude number (Fr) to switch conditions between supercritical and subcritical flow:

$$Fr = \sqrt{\frac{Q_\mathrm{w}^2}{g w_\mathrm{r}^2 h^3}}. \tag{2.1}$$

The Froude number (Fr) is calculated as a function of discharge (Q_w), gravity (g), channel width (w_r) and water depth (h) (Eq. 2.1). The threshold $Fr = 0.9$ simplifies the calculation of flow conditions, allowing us to spatially iterate through the nodes only once from downstream to upstream. In the case of subcritical flow, the water depth is solved locally as a function of downstream friction slope (S_f) and bed slope (S_0) (Eq. 2.2a):

$$\frac{\mathrm{d}h}{\mathrm{d}x} = \frac{S_0 - S_\mathrm{f}}{1 - Fr^2} \quad \text{for subcritical: } Fr < 0.9 \tag{2.2a}$$

$$h = \left(\frac{n^2 Q_\mathrm{w}^2}{S_\mathrm{f}}\right)^{3/10} \quad \text{for supercritical: } Fr \geq 0.9. \tag{2.2b}$$

Water depth under supercritical flow conditions is calculated locally assuming steady uniform flow using the Manning–Strickler formulation (Eqs. 2.2b and 2.3), where α_r is a coefficient of 8.1 (*Parker*, 1991) and roughness height (k_s):

$$n = \frac{k_s^{1/6}}{\alpha_\mathrm{r} g^{1/2}}. \tag{2.3}$$

k_s is calculated using the constants n_k and D_s90, the surface grain size for which 90 % of the surface is finer:

$$k_s = n_k D_\mathrm{s90}. \tag{2.4}$$

In the case of steady and uniform flow the bed slope S_0 is equal to the friction slope (S_f) with bed elevation (η_b) at downstream position x:

$$S_\mathrm{f} = \frac{-d\eta_\mathrm{b}}{\mathrm{d}x} = S_0. \tag{2.5}$$

If the solution of the water depth with Eq. (2.2a) is numerically unstable on the current node distribution, the model subdivides the channel into more nodes and reiterates the subdivision until a stable backwater curve is found. This approach does not properly represent the location of hydraulic jumps (*Cui et al.*, 2006), which should not be a problem as we average conditions over a node spacing of at least one channel width. Boundary shear stress (τ_b) is then calculated with the depth-slope product:

$$\tau_\mathrm{b} = \rho g h S_\mathrm{f}, \tag{2.6}$$

where ρ is the water density. τ_b is then converted to the shear velocity u^*, which is used in the sediment routing component:

$$u^* = \sqrt{\tau_\mathrm{b}/\rho}. \tag{2.7}$$

The volumetric unit bedload transport rate per size class $q_{\mathrm{b}i}$ is calculated using the sediment transport function provided by *Wilcock and Crowe* (2003). The change in bed elevation $\partial\eta_\mathrm{b}$ for each node x per time step t follows from the Exner equation of mass conservation:

$$(1-\lambda)\frac{\partial \eta_\mathrm{b}}{\partial t} = -\frac{\partial q_\mathrm{b}}{\partial x}, \tag{2.8}$$

where λ is bed porosity. The volumetric bedload transport rate per unit width is given as q_b and is calculated per grain size class i in the sediment mixture of n size classes:

$$q_\mathrm{b} = \sum_{i=1}^{n} q_{\mathrm{b}i}. \tag{2.9}$$

The model incorporates subsurface stratigraphy using the active layer concept (*Parker*, 2008), which gives the Hirano equation:

$$(1-\lambda)\left[\frac{\partial}{\partial t}(L_\mathrm{a}F_i) - f_{Ii}\frac{\partial L_\mathrm{a}}{\partial t}\right] = -\left(\frac{\partial q_{\mathrm{b}i}}{\partial x} - f_{Ii}\frac{\partial q_\mathrm{b}}{\partial x}\right), \tag{2.10}$$

where L_a is the active layer thickness, F_i is the surface frequency of the ith grain size class, f_{Ii} is the ith grain size class proportion exchanged between the surface and the subsurface, and $q_{\mathrm{b}i} = p_{\mathrm{b}i}q_\mathrm{b}$ is the volumetric unit bedload transport rate of the ith grain size class where $p_{\mathrm{b}i}$

represents the ith fraction of the bedload transport rate. The active layer thickness is calculated as $L_\mathrm{a} = n_\mathrm{a} D_{\mathrm{s}90}$, with the parameter n_a, representing the scale of bed fluctuations.

The grain size distribution of the sediment flux between the active layer and the substrate is either calculated from the subsurface texture when the bed degrades, or from a linear combination of surface and bedload grain size distributions when the bed aggrades (*Hoey and Ferguson*, 1994):

$$f_{Ii} = \begin{cases} f_i & \text{for } \frac{\partial \eta_\mathrm{b}}{\partial t} < 0 \\ \alpha F_i + (1-\alpha) p_{\mathrm{b}i} & \text{for } \frac{\partial \eta_\mathrm{b}}{\partial t} > 0, \end{cases} \tag{2.11}$$

where f_i is the fraction of the ith grain size class in the subsurface, and α is a constant. The vertical stratigraphy is stored in 10 cm high layers following *Viparelli et al.* (2010). By keeping track of grain size distributions within the surface and subsurface layers, the model can preserve the history of phases of erosion or aggradation. This allows emergent properties such as armouring layers to occur. To study the combined effect that the active layer thickness factor n_a and the active layer exchange ratio α have on the model results, we executed sensitivity runs shown in the Supplement to this paper (Supplement Figs. S1–S4).

The Exner equation (Eq. 2.8) in combination with the expression for the friction slope in Eq. (2.2) and the sediment transport function by *Wilcock and Crowe* (2003) form an non-linear advection–diffusion system that allows the calculation of bed elevation as a function of space and time (*An et al.*, 2017a). An upwind scheme was used for the numerical discretization. The model needs an initial bed profile and an initial value of the surface grain size to be solvable. Sediment boundary conditions are given by the sediment feed rate and grain size distributions on the inlet, and a fixed bed elevation at the outlet of the simulated reach. The flow boundary condition is a water surface height of 0.1 m over normal flow at the outlet. The bedload transport function is used to calculate transport rates for each channel cross section. During the model run, changes of the sediment transport rate are dependent on changes in the sediment supply, channel slope, and surface grain size distribution.

2.3.2 Model calibration

We used data from flume experiments to calibrate the model. The objective of the flume experiments was to measure the adjustment of an alluvial steep channel to different frequencies of sediment supply. The experiments were carried out in a water recirculating flume which is 18 m long, 1 m wide, and 1 m deep in the Mountain Channel Hydraulic Experimental Laboratory at the University of British Columbia. Here we will provide a brief summary of the flume setup and experimental design, for more details see *von Flotow* (2013), *Elgueta* (2014), *Ferrer-Boix and Hassan* (2015), and *Elgueta-Astaburuaga and Hassan* (2017).

The experiment consisted of seven 40 h long runs with different sediment supply frequencies, while keeping the total sediment input the same at 300 kg per run. The experiments were run continuously, i.e., the bed surface at the end of run 1 was the starting condition for run 2 and so on. For all runs, flow was held constant so that the sediment feed regime could be studied with no changes in flow regime (Table 2.1). The difference between the runs was the spreading of the supply over a changing input frequency, which was either constant, in one pulse, in two pulses, or in four pulses. The bed was fixed in the first 1 m downstream section of the flume head box with stones equivalent to about D_{s84} of the experimental bed material. In the remainder of the flume the bed initially consisted of 0.1 m of loose material with particle sizes ranging from 0.5 to 64 mm with a D_{s50} of 5.64 mm, matching downscaled (by a factor of 3) conditions of a study reach in East Creek, British Columbia, Canada. The flume slope was set to 0.022 m m^{-1}. Measurements include water depth, water surface slope, water velocity, bed surface slope, bed surface particle size distribution, bed elevation, sediment transport rate, and bedload texture. Measurements of the water surface elevation were conducted throughout the experiment using a mechanical point gauge with 0.001 m precision. Photos were used to manually sample bed surface grain size distributions and the bed elevation was recorded with a green laser scanner at a 2 mm resolution. The bed surface scans were used to measure the bed surface slope along the thalweg, i.e., the line of lowest elevation along the flume. Flow velocity measurements were conducted using an ADV profiler. The grain size and count of particles exiting the flume were recorded with a camera and a light table at the outlet of flume (*Zimmermann et al.*, 2008). The transport rate measurements were done at 30 Hz and validated

after the experiments by total exported weight.

Using the model described, we simulated a 12 m long and 1 m wide channel in 13 downstream nodes each spaced 1 m apart. The model was set to calculate sediment transport for all nodes in time steps of 10 s. All simulations used a constant water discharge of $0.065\,\mathrm{m^3\,s^{-1}}$ and a geometric mean grain size of 5.64 mm for both initial bed and sediment feed (full distribution shown in Fig. 2.2a). We chose to use a normally distributed approximation of the flume grain size with a width of $\sigma = 1.6$ to be consistent with distributions used for the equilibrium simulations. This distribution and the original flume GSD are statistically the same. The initial channel slope was $0.022\,\mathrm{m\,m^{-1}}$, also matching the parameters from the flume experiments.

We calibrated the model by visually reducing the difference between measured and simulated values of bed slope (S), surface grain size parameters (D_{sg}, D_{s90}), and transport rate (q_{b}). In the calibration runs more importance was given to recreating S, D_{sg}, and q_{b} than to a good match in D_{s90}. We first increased the reference Shields stress (τ^*_{rm}) in the Wilcock and Crowe formula to roughly match simulated and measured q_{b}. Afterwards, we varied the grain exchange ratio (α) (Eq. 2.11) and the coefficient of the active layer thickness (n_{a}). As we achieved a good visual match between simulation and flume measurements, we did not see the need to calibrate more parameters.

Table 2.1: Overview of runs in the flume experiments. All runs were 40 h long. The texture of the initial bed mixture and the sediment feed were identical. Plots of resulting slope, D_{sg}, D_{s90}, and sediment transport are shown in Fig. 2.3. The symbols in column two signify the feed regime where 0 represents no feed, C represents constant feed, and 1, 2, and 4 represent the number of pulses in 40 h.

Flume run	Symbol	Feed regime	Mean water depth after 40 h (m)	Bed slope after 40 h ($m\,m^{-1}$)	Water surface slope at 40 h ($m\,m^{-1}$)	Feed rate ($g\,ms^{-1}$)	Feed duration (min)	Pulse magnitude (kg)	Pulse period (h)
R1	0	None	NA	0.017	NA	0	–	–	–
R2	C	Constant	0.073	0.016	0.017	2.0833	–	–	Const.
R3	1	One pulse	0.080	0.018	0.019	83.3	60	300	40 h
R4	4	Four pulses	0.083	0.020	0.020	83.3	30	75	10 h
R5	2	Two pulses	0.072	0.022	0.020	83.3	15	150	20 h
R6	C	Constant	0.075	0.022	0.020	2.0833	–	–	Const.
R7	0	None	0.073	0.022	0.020	0	–	–	–

Initial slope 2.2 %; mixture $D_{s50} = 5.64$ mm; mixture $D_{s90} = 11.2$ mm, $Q_w = 65\,L\,s^{-1}$; duration of each run = 40 h; total feed = 300 kg per run. NA represents not available.

Table 2.2: Sequencing of events in runs that were simulated as permutations of the original flume experiment. Each of the seven periods was 40 h long and each run lasted 280 h in total. There was no sediment input during the no feed runs (0). Within all other period types, 300 kg of sediment was fed over 40 h, either constantly (C) or in pulses (one, two, or four events). Besides recreating the original flume sequence (OF), we simulated two runs where the pulsed events occur either in order from many pulses to few (MtF) or from few to many (FtM). To explore if the system could rebound from the impact of a certain pulse phase during a constant-feed phase, we created two additional runs where this was the case (cMtF and cFtM), which led to a 600 kg higher total sediment feed.

Simulation run		Event sequence symbol							Mass fed total (kg)
OF	Original flume	0	C	1	4	2	C	0	1500
MtF	Many to few	0	C	4	2	1	C	0	1500
FtM	Few to many	0	C	1	2	4	C	0	1500
cMtF	C-buffered: many to few	C	4	C	2	C	1	C	2100
cFtM	C-buffered: few to many	C	1	C	2	C	4	C	2100

2.3.3 Event sequencing simulations

We explored the role that the sequencing of the pulse events could have on the flume study by simulating the "original flume" event sequence and comparing the result to alternative sequencing of events (see Table 2.2). The alternative event sequences are using the same pulse distributions (four pulses, two pulses, or one pulse over 40 h), but the pulse order is either from "few to many" (FtM) (i.e., one pulse, then two pulses, then four pulses) or from "many to few" (MtF) (i.e., four pulses, then two pulses, then one pulse) per 40 h phase. To allow the system more time to recover from pulse events, we simulated two more cases where each pulsed phase is buffered from the next one by a 40 h constant-feed phase. These runs are called "c-buffered: many to few" (cMtF) and "c-buffered: few to many" (cFtM).

2.3.4 Equilibrium simulations

In our final set of experiments, we kept the frequency and magnitude of pulse events constant to achieve equilibrium slope and grain size conditions. The use of numerical modelling allows for the comparison of many simulations with differing grain size distributions, pulse frequencies, and pulse magnitudes. We expect a channel under episodic sediment supply to adjust

synchronously to the frequency of external forcing events. The added sediment volume from a supply event will increase the channel slope at first. After the supply of sediment ends and material is removed from the channel, the slope will decrease, and the surface grain size will begin to reflect the sediment starved conditions. As the long-term sediment input equals the long-term sediment output, the channel will eventually achieve a condition where the capacity to erode material (through increased slope in conjunction with changes in the surface grain size) equals the depositional forcing (i.e., long-term sediment input) of the supply regime. In this state the adjustment of channel slope and grain size to each sediment input event will return to the same values after every pulse. All runs achieved this equilibrium condition within 20 000 simulation hours.

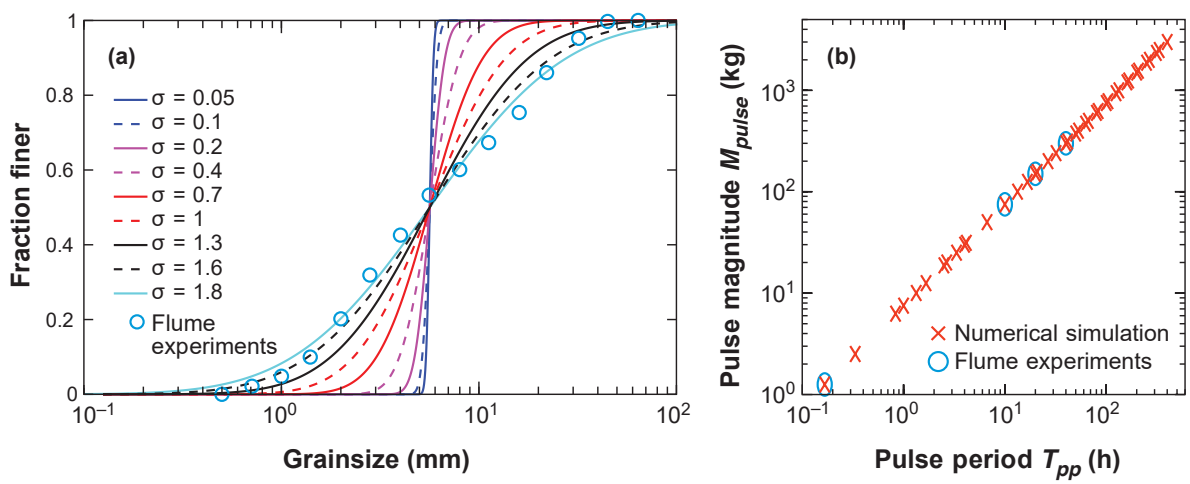

Figure 2.2: (a) Variation of the grain size distribution between model runs (lines) and values from the flume experiments (circles). All distributions have a geometric mean grain size (D_{sg}) of 5.64 mm. The different σ values represent the width of the distribution, calculated for normal distributions in phi-scaled sediment sizes. The data for the flume experiments are roughly matched with $\sigma = 1.6$. **(b)** Combinations of pulse magnitude and pulse period (or recurrence interval) used in the equilibrium model runs. As the total mass of supplied material is the same for all simulations, runs with high pulse frequencies (i.e., low pulse periods T_{pp}) are smaller in magnitude. Four of the combinations match the flume runs (circles).

To find the equilibrium slope resulting from different sediment supply regimes, we simulated different combinations of sediment supply frequency (F_{pulse}) and magnitude (M_{pulse}) for nine different grain size distributions (Fig. 2.2a). All distributions have the same mean grain

size of 5.64 mm, but differ in the width of the distribution by the standard deviation (σ), which was chosen for a phi-scaled, normally distributed sample. While $\sigma = 0.05$ represents a nearly uniform sediment mixture, $\sigma = 1.6$ roughly matches the grain size distribution of the flume experiments. We used 11 grain size classes in the simulations and set the initial GSD to the feed GSD. Under the hydraulic conditions applied all grain sizes are initially mobile, which might change during the simulations due to the effect of armouring and changes in bed slope. Figure 2.2b shows the combinations of frequency and magnitude used in this study. Each model run delivered the same input mass over the simulation time (150 000 kg over 20 000 h). We then distributed this total mass over different pulse frequencies, with four of the combinations matching the flume experiments. Each pulse was 10 min in length. The lowest frequency was chosen to be one pulse every 400 h (pulse period time: $T_{\mathrm{pp}} = 400$ h), and the highest frequency was constant feed (one 10 min long pulse every 10 min). We selected a range of 40 pulse frequencies for which the whole number of cycles summed to 20 000 h. In total we executed 360 simulations, 9 different σ with 40 frequencies each.

2.4 Results

2.4.1 Model calibration

Elgueta-Astaburuaga and Hassan (2017) describe the flume results we used for model calibration in detail. We will give a short summary of the findings here. An initial run without sediment feed over an unstructured bed showed a high sediment output while the bed armoured. This run was similar in output grain sizes and grain mobility to the run with one sediment pulse over a structured bed. This shows that active restructuring of the bed occurred in both of these runs. On the other end of the spectrum, the constant feed and four pulse runs were similar in their low sediment output and showed different grain mobility. This implies that the system reacts differently at a threshold frequency somewhere between two pulses per 40 h and four pulses per 40 h, which *Elgueta-Astaburuaga and Hassan* (2017) interpret as the relaxation time of the bed to a pulse event.

We used these experiments to test the ability of the numerical model to recreate the flume

results in discharge, pulse frequency, pulse magnitude, slope, and grain sizes. In the experiment, mean grain size (D_{sg}) and slope (S) were measured over a central 2 m long section to avoid a bias of bed surface measurements due to inflow and outflow conditions. The measurement intervals varied between every 1 and every 20 h (depending on the pulse interval). The values for the numerical simulation are averaged over the whole reach and were recorded every 10 min during the simulation time. We achieved a best match in slope S, D_{sg}, D_{s90}, and the transport rate q_b by increasing the reference Shields stress τ^*_{rm} in the Wilcock and Crowe formula by a factor of 2. *Wilcock* (2001) suggests taking the same approach of increasing the threshold shear stress to match a sediment transport calculation to field data. Other researchers use this method to calibrate models to field and flume data (Gary Parker, personal communication, 2018; *Chartrand et al.*, 2015).

Figure 2.3 shows the comparison between flume measurements and the calibrated model results with the grain exchange ratio $\alpha = 0.45$ (Eq. 2.11) and the active layer thickness factor $n_a = 2$. The sensitivity of the model to changes in α and n_a is shown in Supplement Figs. S1–S4. Due to the long interval between measurements in the flume experiments, some short-term slope responses to individual sediment pulses might be hidden (e.g., after hours 80 and 180 in Fig. 2.3a). The model underpredicts both the slope and the mean surface grain size (D_{sg}) (see Fig. 2.3b) in the first 60 h, while the coarse grain size fractions (D_{s90}) and average transport rate are over predicted for the first 30 h (see Fig. 2.3c and d). This might be due to imperfect initial conditions or boundary effects in the flume experiments. For the rest of the simulation both slope and D_{sg} show good agreement with the flume results. D_{90} is overpredicted in the model, but this is seen as a minor issue because the simulated transport rates mainly depend on D_{sg} and the slope. The transport rate in the simulation lags behind the light table data, which might be due to our numerical implementation of diffusion. As the model matches the average transport rates well, we did not see the need to improve the temporal agreement.

2.4.2 Event sequencing simulations

After obtaining a good match between the model and the flume data, we simulated alternative event sequences as described in Table 2.2. Figure 2.4a shows the adjustment of slope in runs

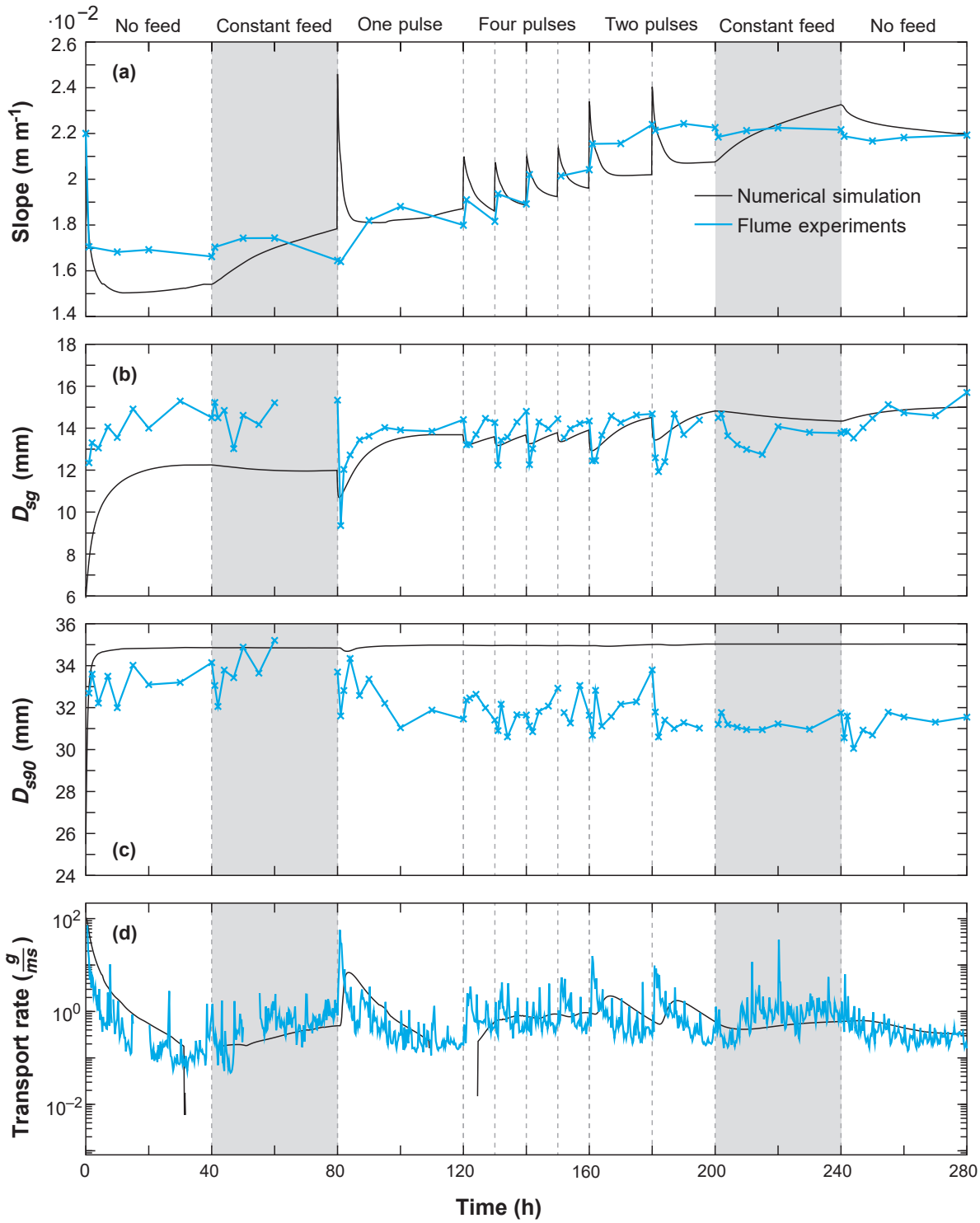

Figure 2.3: Comparison of **(a)** slope, **(b)** mean surface D_{sg}, **(c)** surface D_{s90}, and **(d)** sediment transport rate between the numerical simulation and the flume experiments.

that preserved the same sediment feed volume and had the same duration as the flume experiments (OF, MtF, and FtM), but the frequency of events is ordered differently. At the end of the simulations, all runs approach the same slope value of $0.022\,\mathrm{m\,m^{-1}}$, which shows that the main factor determining the long-term slope is the total volume of sediment fed. The sequencing of events seems to play a role in the slope adjustment over the short term, here about 80 h after the events. On this short timescale, large pulses increase the slope quickly, while the smaller, more frequent pulses lead to a more gradual adjustment of slope. Figure 2.4b shows the runs where pulse phases were buffered by constant-feed phases (cMtF and cFtM), increasing the total sediment feed by 600 kg. This did not change the pattern of adjustment significantly compared to the earlier runs, as the constant-feed phases only prolonged the effect of the previous pulse phase.

The effect of event sequencing on the channel response in D_{sg} is shown in Fig. 2.4c for all runs in Table 2.2. The order of events only has a weak impact on patterns of adjustment in D_{sg}, as maximum grain size conditions are reached within 20–30 h. Afterwards no further adjustment occurs until the introduction of fine material with the next pulse lowers the surface grain size again. This means that armouring of the channel surface happens quickly in relation to the time between pulse events. The subsurface is made of the same grain size distribution as the sediment feed, so its mean size is 5.56 mm. Therefore, we can infer that an armouring ratio ($D_{\mathrm{sg}}/D_{\mathrm{subg}}$) of about 2.2 was reached within 20 h and then increased towards 2.7 over the following 260 h. A finer, less armoured surface at the time of each supply event is followed by a coarsening of the surface as the finer grain sizes are more mobile, and thus more easily evacuated in the time without feed between pulses.

2.4.3 Equilibrium simulations

Our second set of simulations explored the equilibrium conditions that are reached under different supply regimes. As we will explain in the discussion, the effect of the supply regime can be constrained to changes in slope (S) and the surface grain size distribution ($\mathrm{GSD_{fluv}}$), which in the following will be characterized by the armouring ratio between surface and subsurface mean grain size ($D_{\mathrm{sg}}/D_{\mathrm{subg}}$). After different times in the simulations, these parameters reach

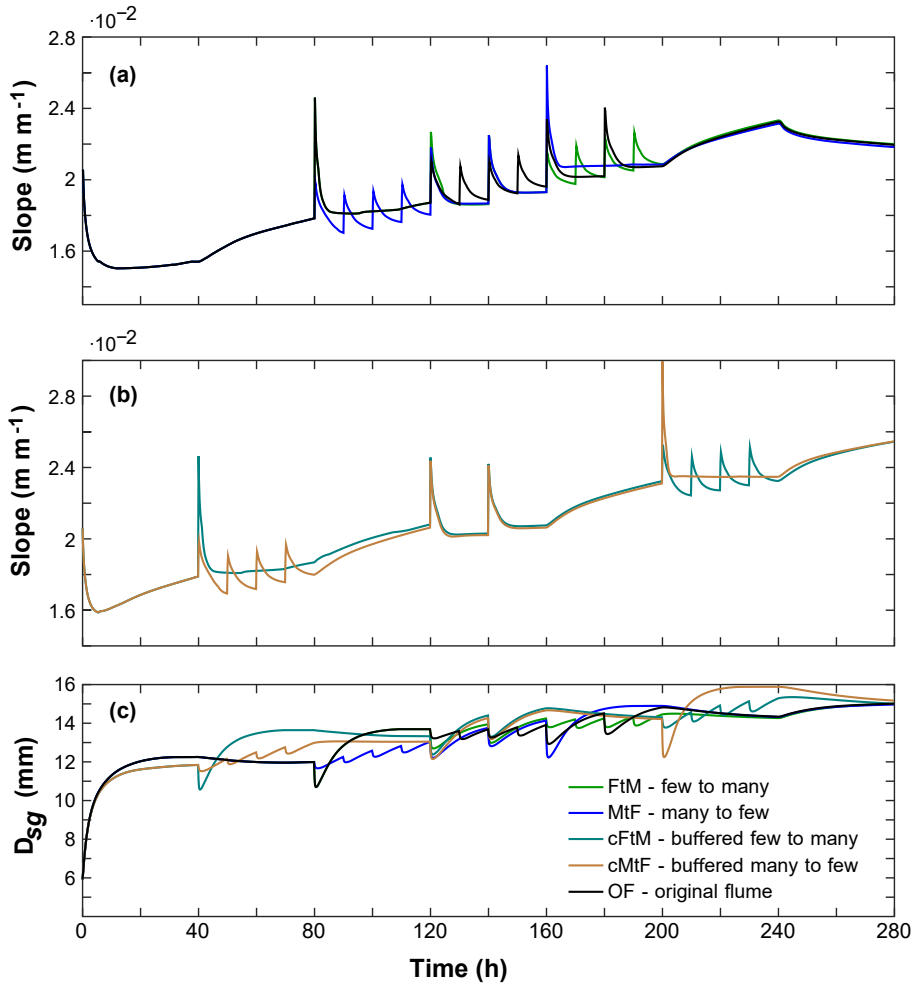

Figure 2.4: Comparison of slope and mean surface grain size D_{sg} from runs with different event sequencing (see Table 2.2) ($\sigma = 1.6$, factor of 2 increase of τ^*_{rm}). Event sequences are **(a)** rearranged pulse phases to the flume experiments and **(b)** a setup where the pulsed phases are buffered with constant-feed phases. Panel **(c)** shows D_{sg} for the runs in both **(a)** and **(b)**.

a time-independent periodic adjustment that is illustrated in Fig. 2.5 for the last 400 h of two simulations. Figure 2.6a shows box plots of the distribution of slope values during the last pulse of all 40 runs with $\sigma = 1.6$. The presented normalized slopes (S/S_{const}) indicate how the slope for each pulse frequency compares to the constant-feed slope of runs with the same grain size distribution. Figure 2.6b shows the change in normalized mean slope (S_{mlp}/S_{const}) with pulse frequency, which corresponds to the red lines in Fig. 2.6a and is our main indicator for the equilibrium state of the channel slope. Each line represents a different width σ of the GSD over 40 runs with increasing T_{pp}.

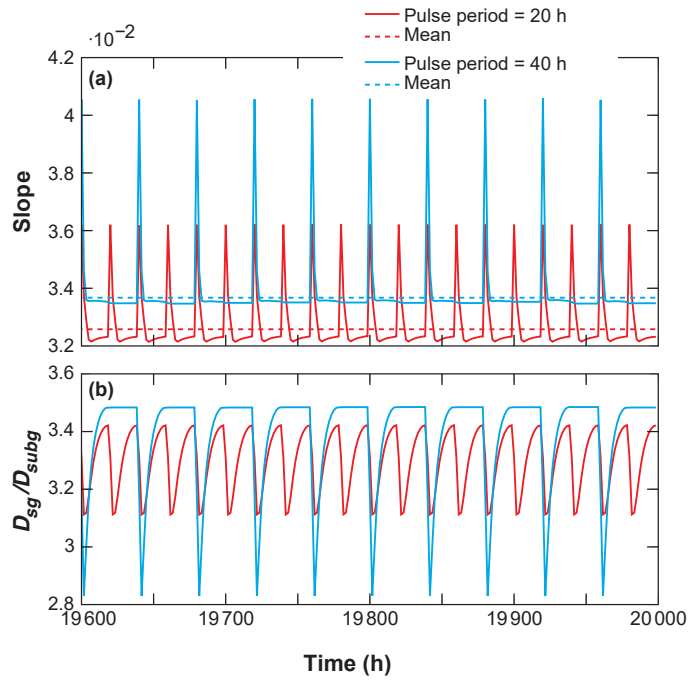

Figure 2.5: (a) Slope and **(b)** armouring ratio for the last 400 h of 2 out of 40 experiments using $\sigma = 1.6$. A run with a low event frequency is shown in blue, and a run with a high event frequency is shown in red. In these example runs the mean slope in equilibrium is higher for the run with longer pulse periods.

2.5 Discussion

2.5.1 Extension of flume results with the numerical model

The numerical model shows good agreement with the temporal response of mean surface grain size and slope from the flume experiments. As the initial bed grain size distributions were well mixed, the good match in mean surface grain size also implies a good match in the armouring ratios. A series of runs with an alternative sequencing of events showed that, while the adjustment of mean surface grain size was not sensitive to the order of the pulsed phases, the evolution of slope differed considerably. In the cases where the first pulsed phase consisted of one large magnitude event (FtM and cFtM), the slope increased quickly and the following higher-frequency, lower magnitude pulse phases did not modify the system considerably. In contrast, cases where multiple smaller event phases occurred first (MtF and cMtF), the slope increased more gradually. All runs ended at about the same slope after the 280 h simulation

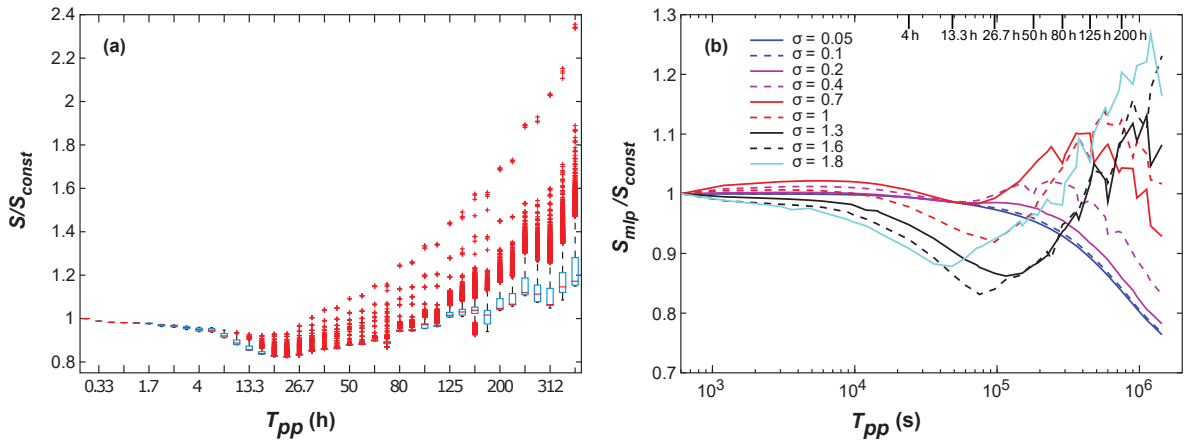

Figure 2.6: (a) Distribution of the ratios of slope during the last pulse to the constant-feed slope for all 40 runs with $\sigma = 1.6$. We normalized the values of the slope in the last pulse with the slope of the constant-feed run of the same grain size distribution width (σ), allowing for the comparison of the equilibrium slopes between runs with different σ. The red lines represent the normalized mean slopes ($S_{\mathrm{mlp}}/S_{\mathrm{const}}$), which we chose as the main indicator for the equilibrium state of the channel slope. Note that data from longer pulse periods T_{pp} will contain more data points for the box plots, as there are more slope values recorded during the longer time between pulses (sampling every 10 min). The red crosses are outliers in the distribution of slope values, illustrating the extreme slope values during the time right after the pulse was introduced into the channel. **(b)** Mean slope ratios for all runs grouped by width of GSD (σ).

time, which implies that while the low frequency, large magnitude events strongly alter the channel in the short term, the sequencing of events does not play an important role in the long run. The constant-feed-buffered runs (cFtM and cMtF) show similar behaviour to their unbuffered counterparts, as the constant-feed phases preserve the bed state of the previous pulse phase. The main driver of the slope adjustment is the total sediment feed, which is consistent with findings by *Blom et al.* (2017).

2.5.2 Development of timescales from the equilibrium simulations

The definition of a sediment supply regime can be based on different aspects of sediment input into a stream, either from outside or within the channel. For simplicity, we restrict the definition of a sediment supply regime to the input of material into the fluvial system from outside the active channel. Sediment supply from storage close to the channel can be viewed as exter-

nal supply if it only occurs episodically (e.g., less than yearly) in large flooding events. This view allows us to describe the sediment supply regime by a combination of frequency, magnitude, and grain size distribution of sediment supply events over a multi-event time frame (as in *Benda and Dunne*, 1997a). The time frame must be long enough to contain enough sediment supply events to allow the stream bed to adjust to the external forcing by changing its internal configuration of sediment storage and bed structuring. Even though a natural channel might never reach an equilibrium to a certain sediment supply regime, it might produce regular patterns of transient adjustment to the supply events.

In our case, the forcing on the system is a combination of pulse frequency (F_{pulse}), pulse magnitude (M_{pulse}), pulse grain size distribution ($\mathrm{GSD}_{\mathrm{pulse}}$), and water discharge ($Q_{\mathrm{w}}$). Due to the simple geometry and the lack of bedforms in a 1-D numerical model, the fluvial reaction to the forcing is restricted to the bedload transport rate (q_{b}), channel slope (S), and channel grain size distribution ($\mathrm{GSD}_{\mathrm{fluv}}$) (see Table 2.3). Pulse frequency and magnitude can be combined in the virtual pulse velocity (U_{pulse}), with the magnitude normalized by reach width (w_{r}) and length (l_{r}):

$$U_{\mathrm{pulse}} = F_{\mathrm{pulse}} \cdot M_{\mathrm{pulse}} / (w_{\mathrm{r}} \cdot l_{\mathrm{r}}). \tag{2.12}$$

A characteristic pulse period time (T_{pp}) for a sediment supply regime is the inverse of the pulse frequency:

$$T_{\mathrm{pp}} = 1 / F_{\mathrm{pulse}}. \tag{2.13}$$

We define a reach averaged fluvial export velocity $U_{\mathrm{fluv}} = q_{\mathrm{b}} / l_{\mathrm{r}}$ in order to compare the sediment export of material to the pulsed sediment input. Considering a multi-event time frame $T_{\mathrm{sim}} (\gg T_{\mathrm{pp}})$ for each simulation, we can assume that the fluvial system will adjust to the external forcing over time, leading to an adjustment of the reach averaged fluvial sediment transport to match the external forcing of the virtual pulse velocity:

$$T_{\mathrm{sim}} \gg T_{\mathrm{pp}} : \quad U_{\mathrm{fluv}} \approx U_{\mathrm{pulse}}. \tag{2.14}$$

The time it takes to achieve an equilibrium state is highly dependent on the initial condi-

tions of the simulations. Instead of using a process rate threshold to find an equilibrium time, we can infer a simulation-time independent relation between the supply regime (i.e., T_{pp}) and the state of the system in equilibrium (i.e., U_{fluv}, S, and $\mathrm{GSD}_{\mathrm{fluv}}$). This way we only have to run simulations for long enough to verify equilibrium with the respective supply regime (in our case 20 000 h), and then observe properties of the channel at the very end of the simulation, even though equilibrium might have been achieved earlier.

When comparing the system state in equilibrium between many different supply regimes, while keeping the initial fluvial reworking capacity constant (mainly geometry and Q_{w}), we can identify how the equilibrium conditions change under different supply regimes. Due to the fixed channel geometry in the 1-D model, only the bed slope (S) and the grain size distribution ($\mathrm{GSD}_{\mathrm{fluv}}$) can adjust to the change in the supply regime.

To better compare the temporal adjustment to sediment pulses of different magnitudes and frequencies, we non-dimensionalized the pulse period T_{pp} with a fluvial evacuation time T_{fe}:

$$T_{\mathrm{fe}} = \frac{l_{\mathrm{r}} w_{\mathrm{r}} D_{\mathrm{fg}}}{U_{\mathrm{fluv}}} \left(\frac{D_{\mathrm{fg}}}{D_{\mathrm{ag}}} \right)^2 . \tag{2.15}$$

This timescale is a representation of how long it would take to remove a layer of sediment as long and as wide as the flume (l_{r} and w_{r}) with the thickness of the median feed grain size D_{fg}, under the average transport rate U_{fluv}, multiplied by an estimate of the ratio of feed grain size to armoured grain size $(D_{\mathrm{fg}}/D_{\mathrm{ag}})^2$, which can be interpreted as an inverse of the degree of potential bed armouring similar to $D_{\mathrm{s90}}/D_{\mathrm{s50}}$ (*Recking*, 2012). We developed Eq. (2.15) visually by matching the inflection of lines in Fig. 2.7a to $T_{\mathrm{pp}}/T_{\mathrm{fe}} = 1$.

Figure 2.7a shows the same data as Fig. 2.6b, but in non-dimensionalized time $T_{\mathrm{pp}}/T_{\mathrm{fe}}$. A ratio of $T_{\mathrm{pp}}/T_{\mathrm{fe}} < 1$ can be interpreted as a condition in which the pulsed input of material occurs faster than the fluvial removal of a D_{fg} thick theoretical layer of material under average transport conditions modified by armouring. At a ratio of $T_{\mathrm{pp}}/T_{\mathrm{fe}} > 1$, the sediment is fed in time steps longer than the time that the fluvial system needs to remove said theoretical layer.

Figure 2.7b shows the normalized armouring ratio ($\mathrm{AR}_{\mathrm{elp}}/\mathrm{AR}_{\mathrm{const}}$), which was obtained by dividing the armouring ratio $\mathrm{AR}_{\mathrm{elp}} = D_{\mathrm{sg}}/D_{\mathrm{subg}}$ at the end of the last pulse for each simu-

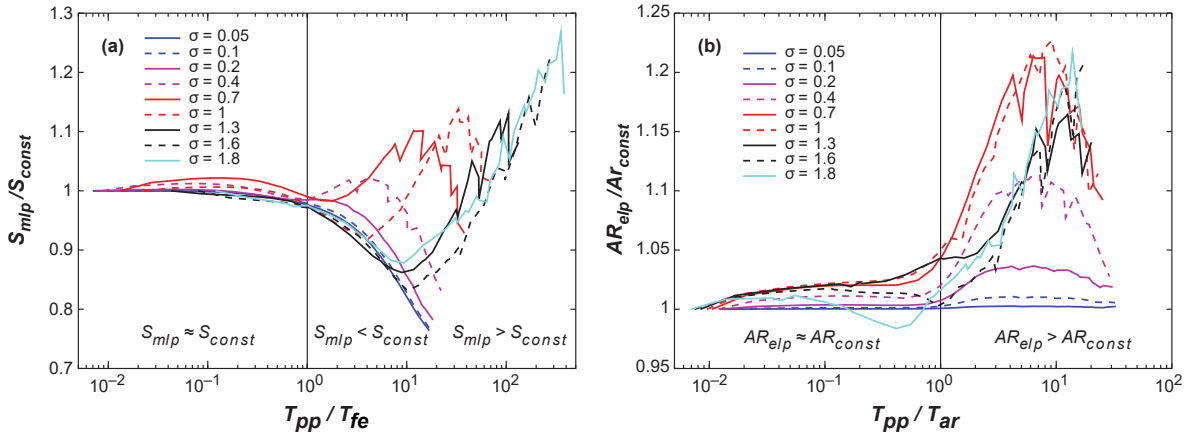

Figure 2.7: (a) Mean slope ratios in non-dimensional timescale. $T_{\mathrm{pp}}/T_{\mathrm{fe}} < 1$: model runs with a high-frequency sediment supply show similar equilibrium slopes and armouring ratios as conditions of constant sediment feed ($S_{\mathrm{mlp}} \approx S_{\mathrm{const}}$). $T_{\mathrm{pp}}/T_{\mathrm{fe}} > 1$: if the GSD is narrow ($\sigma < 0.4$) or the pulse period is not much longer than the fluvial evacuation time, we observe lower equilibrium slopes than in constant-feed runs ($S_{\mathrm{mlp}} < S_{\mathrm{const}}$). Runs with either very low frequency of supply events or wide GSD ($\sigma \geq 0.4$) show equilibrium slopes that are higher than the respective constant-feed runs ($S_{\mathrm{mlp}} > S_{\mathrm{const}}$). **(b)** Relative armouring ratio in non-dimensional timescale. $T_{\mathrm{pp}}/T_{\mathrm{ar}} > 1$: low frequency of supply events leads to an increase in armouring ratio compared to constant-feed runs ($\mathrm{AR}_{\mathrm{elp}} > \mathrm{AR}_{\mathrm{const}}$), especially for wide GSDs ($\sigma \geq 0.4$).

lation with the armouring ratio at the end of the corresponding constant-feed run. Similarly to the fluvial evacuation time that we used to non-dimensionalize the slope adjustment, we used an armouring time T_{ar} to non-dimensionalize the grain size adjustment:

$$T_{\mathrm{ar}} = \frac{l_{\mathrm{r}} w_{\mathrm{r}} D_{f90}}{U_{\mathrm{fluv}}} 0.5 \left(\frac{D_{f90}}{D_{\mathrm{a}90}} \right)^2. \tag{2.16}$$

This timescale represents how long it would take to remove a layer of sediment as long and as wide as the flume (l_{r} and w_{r}) with the thickness of the supplied D_{f90}, under the reach averaged transport rate $U_{\mathrm{fluv}} = q_{\mathrm{b}}/l_{\mathrm{r}}$, multiplied by an estimate of the ratio of the sediment supply $D_{\mathrm{f}90}$ to the $D_{\mathrm{a}90}$ of an armoured bed. We developed Eq. (2.16) visually by matching the inflection of lines in Fig. (2.7b) to $T_{\mathrm{pp}}/T_{\mathrm{ar}} = 1$.

2.5.3 Interpretation of the equilibrium simulations

The condition of $T_{\mathrm{pp}}/T_{\mathrm{fe}} = 1$ constitutes a threshold in the slope adjustment to pulsed sediment supply. Pulse periods shorter than the fluvial evacuation time ($T_{\mathrm{pp}}/T_{\mathrm{fe}} < 1$) lead to equilibrium slopes similar to the constant-feed equilibrium slopes ($S_{\mathrm{mlp}} \approx S_{\mathrm{const}}$). In the case of narrow GSDs ($\sigma < 0.4$), simulations with pulse periods longer than the fluvial evacuation time ($T_{\mathrm{pp}}/T_{\mathrm{fe}} > 1$) show an up to 20 % lower slope than in the constant-feed equivalent run ($S_{\mathrm{mlp}} < S_{\mathrm{const}}$). In contrast, runs with either very low frequency of supply events or wide GSD ($\sigma \geq 0.4$) show equilibrium slopes that are up to 30 % higher than the respective constant-feed runs ($S_{\mathrm{mlp}} > S_{\mathrm{const}}$). Simulations with a wider range of material ($\sigma > 1$) show a drop in $S_{\mathrm{mlp}}/S_{\mathrm{const}}$ right at $T_{\mathrm{pp}}/T_{\mathrm{fe}} = 1$, but then an increase in $S_{\mathrm{mlp}}/S_{\mathrm{const}}$ at longer pulse distances. We interpret conditions of lower S_{mlp} to be less armoured, as they coincide with lower values of $\mathrm{AR}_{\mathrm{elp}}/\mathrm{AR}_{\mathrm{const}}$ as shown in Fig. 2.7b. The simulations showing an intermittent decrease of S_{mlp} seem to be in a state in which material can be efficiently exported from the system without having intense armouring limiting the slope adjustment. These large pulses increase the slope rapidly, leading to high shear velocities which causes high transport rates.

We interpret the cause for increasing slope and armouring ratios for long pulse periods in the following way. A longer time between pulses ($T_{\mathrm{pp}} > T_{\mathrm{ar}}$) causes more intense armouring, which shows that the channel bed is starved of sediment between pulses, as finer grain fractions are removed from the surface. This leads to the development of an armouring layer, which restricts the incision into lower deposits, initially limiting the sediment output of the system ($U_{\mathrm{fluv}} < U_{\mathrm{pulse}}$). This imbalance between input and output of material leads to an increased sediment storage over time, which due to the fixed geometry of the channel leads to an increase in slope. This can increase the shear velocity and in return leads to higher sediment output rates. This response loop between armouring and slope adjustment will continue until the sediment output matches the long-term sediment supply ($U_{\mathrm{fluv}} \approx U_{\mathrm{pulse}}$). Note that due to the restricted geometry of our model, slope and grain size are the main parameters in the channel that can change in response to the sediment supply regime. It is possible that other morphological adjustments (e.g., channel width) could compensate for the transport rate disequilibrium in a similar fashion.

The non-dimensionalized presentation of the simulation results shows two distinct modes of adjustment of the fluvial system to episodic sediment supply regimes: (1) "constant-feed-like" behaviour in runs where supply events are of high frequency and low magnitude. Under this kind of forcing the equilibrium slopes and armouring ratios are similar to equilibrium conditions of runs with constant sediment feed. (2) "Pulse-dominated" behaviour occurred in runs where sediment was fed in low frequency and high magnitude events.

An interesting finding is that when $T_{\mathrm{pp}} > T_{\mathrm{fe}}$, an increase in slope only occurs in simulations that have grain size distributions wide enough to allow armouring to occur. In these cases, we could use the timescale of T_{ar} to determine if the armouring would be significant enough to prevent a decrease of the equilibrium slope. Even though armouring develops very quickly in both our simulations and the flume experiments, its long-term persistence in the time between sediment pulses is what governs the channel response. Hence, the grain size distribution in a series of supply events can be more important for the channel response in the long term than the frequencies and magnitudes of the individual events themselves.

It is notable that the channel response at $T_{\mathrm{pp}} = T_{\mathrm{fe}}$ does not change abruptly, but the system response slowly tilts to either pulse-dominated on the one end, or constant-feed-like on the other end of the spectrum. While all constant-feed-like channels (for each σ) have very similar equilibrium properties, all pulse-dominated channels are different in both slope and armouring ratios.

2.5.4 Implications of the equilibrium simulations

Applying the threshold of $T_{\mathrm{pp}}/T_{\mathrm{fe}} = 1$ between constant-feed-like and pulse-dominated supply regimes to the flume experiments is inconclusive. The unity of $T_{\mathrm{pp}} = T_{\mathrm{fe}} \approx 6\,\mathrm{h}$ lies between the constant-feed runs and the highest frequency runs (four pulses with $T_{\mathrm{pp}} = 10\,\mathrm{h}$), which means that we have no experimental constant-feed-like pulsed regime where $T_{\mathrm{pp}} < T_{\mathrm{fe}}$. *Elgueta-Astaburuaga and Hassan* (2017) found that the four-pulse phase caused a sediment transport response that was similar to the constant-feed runs, implying that T_{fe} would lie between 10 h and 20 h. The flume experiments were not executed long enough to reach equilibrium, which complicates the attribution of a specific channel response to a specific forcing.

Besides recreating the 280 h flume experiment in the model, the 360 equilibrium simulations include four configurations that repeat the constant-feed and three pulse periods for 20 000 h. These four configurations only reached the equilibrium after about 12 000 h of simulated time, which is very long in comparison to the conditions of the flume experiments where each supply regime only lasted 40 h.

Table 2.3: List of forcing and reacting parameters, and timescales in our simulations with abbreviations and their dimension (T represents time and L represents length).

Forcing parameters		Reacting parameters		Timescales	
Pulse frequency	F_{pulse} ($1\,\mathrm{T}^{-1}$)	Fluvial export velocity	U_{fluv} ($\mathrm{L\,T}^{-1}$)	Simulation time	T_{sim} (T)
Pulse magnitude	M_{pulse} (L^3)	Channel slope	S ($\mathrm{L\,L}^{-1}$)	Pulse period	T_{pp} (T)
Pulse grain size distr.	$\mathrm{GSD}_{\mathrm{pulse}}$ (L)	Surface grain size distr.	$\mathrm{GSD}_{\mathrm{fluv}}$ (L)		
Water discharge	Q_{w} ($\mathrm{L}^3\,\mathrm{T}^{-1}$)			Derived from simulations:	
Derived parameters:				Fluvial evacuation time	T_{fe} (T)
Virtual pulse velocity	U_{pulse} ($\mathrm{L\,T}^{-1}$)			Armouring time	T_{ar} (T)

Table 2.4: Application of the fluvial evacuation time to the rapids reach in East Creek. The system is assumed to be in equilibrium with a matching fluvial transport rate and long-term sediment supply rate. The time of active fluvial transport is estimated to be 100 h yr^{-1}. We approximated the long-term fluvial transport rate U_{fluv} with three years of data from a sediment trap below the reach. We assumed that the subsurface grain size measurements reflect the average supply GSD and the surface grain size measurements represent the long-term average state of armouring in the reach. Besides the original "East Creek" data and the two "threshold" pulse frequency fits, we assumed four more scenarios with doubled armoured grain sizes or doubled fluvial transport rates to give a rough estimate of error bounds.

	Fluvial parameters			Supply regime		Timescales			
	$U_{\mathrm{fluv}}(=U_{\mathrm{pulse}})$ (m^3 yr^{-1})	D_{a50} (mm)	D_{a90} (mm)	M_{pulse} (m^3)	F_{pulse} (1 yr^{-1})	T_{fe} (yrs)	T_{ar} (yrs)	$T_{\mathrm{pp}}/T_{\mathrm{fe}}$	$T_{\mathrm{pp}}/T_{\mathrm{ar}}$
East Creek	0.75	57	150	0.75	1	2.23	3.58	0.45	0.28
Threshold T_{fe}	0.75	57	150	1.67	0.45[a]	2.23	3.58	1	0.62
– with $2 \times U_{\mathrm{fluv}}$	1.5	57	150	1.67	0.90[a]	1.11	1.79	1	0.62
– with $2 \times D_{\mathrm{a50}}$ and D_{a90}	0.75	114	300	0.42	1.80[a]	0.56	0.89	1	0.62
Threshold T_{ar}	0.75	57	150	2.68	0.28[b]	2.23	3.58	1.61	1
– with $2 \times U_{\mathrm{fluv}}$	1.5	57	150	2.68	0.56[b]	1.11	1.79	1.61	1
– with $2 \times D_{\mathrm{a50}}$ and D_{a90}	0.75	114	300	0.67	1.12[b]	0.56	0.89	1.61	1

For all calculations: supply $D_{\mathrm{f90}} = 90$ mm, supply $D_{\mathrm{f50}} = 32$ mm, channel width $= 2.5$ m, channel length $= 72$ m. Some frequencies calculated to match. [a] $T_{\mathrm{pp}} = T_{\mathrm{fe}}$ and [b] $T_{\mathrm{pp}} = T_{\mathrm{ar}}$

The numerical model was calibrated with only one set of flume experiments. As our study mainly focusses on comparing different simulation results from the same model, the applicability of our results to other flume studies or field cases is uncertain. However, we are confident that the numerical model is an adequate tool to gain insight on the effect of episodic sediment supply on fluvial channels in a general sense. For example if there was an inaccuracy in the calculation of the shear velocity, it would affect all model runs and thus be counterbalanced by relating the changed resulting slope to the constant-feed slope ($S_{\mathrm{mlp}}/S_{\mathrm{const}}$), and the changed armouring ratio to the constant-feed armour ratio ($\mathrm{AR}_{\mathrm{elp}}/\mathrm{AR}_{\mathrm{const}}$).

We tested this by executing two additional batches of simulations with a 25 % decrease and a 25 % increase in the total mass fed respectively. If the experimental design would strongly affect the threshold between constant-feed-like and pulse-dominated conditions, we would expect these simulations to plot differently than the data in Fig. 2.7b. But as shown in Supplement Fig. S5 for the case of $\sigma = 1.6$, the change in the slope ratio $S_{\mathrm{mlp}}/S_{\mathrm{const}}$ is relatively insensitive to the total feed volume. We also expect this to be the case when changing the grain size distributions to include large particles that are initially immobile with the applied discharge. In such simulations, the slope would increase to a point where these initially immobile grain sizes become mobile at a very high equilibrium slope. As we compare all results to the corresponding constant-feed equilibrium slope of the same grain size distribution, these conditions might collapse on the existing data as well. However, it is possible that the channel parameters would become extreme in a way that the empirically derived transport function by Wilcock and Crowe would no longer be realistically applicable.

As we developed the fluvial evacuation time T_{fe} and the armouring timescale T_{ar} purely from observations in numerical simulations, their usefulness remains to be proven in the field. If such a threshold behaviour between episodic sediment supply event frequency and the fluvial adjustment of a channel exists, it should be possible to find signatures in channel morphology, sediment storage volume, or channel slope when comparing streams subject to different pulse periods and with different fluvial transport capacities. It is possible to use Eq. (2.15) with information about the long-term sediment supply volume, grain size supply, and average channel dimensions to calculate T_{fe} and thus infer the matching threshold pulse period

where $T_{\mathrm{pp}} = T_{\mathrm{fe}}$. If the long-term sediment supply occurs in more frequent events than this threshold, the system can be assumed to experience constant-feed-like sediment supply. If the supply frequency is lower, we would expect to find a morphological signature of a pulse-dominated supply regime.

To provide an example application of the developed timescales, we applied Eqs. (2.15) and (2.16) to data from East Creek, which is a small creek in the Fraser watershed close to Vancouver in BC, Canada. The "rapids" channel section of this creek was used to design the flume experiments as a 1 to 6 Froude scaled model. Table 2.4 shows the resulting timescales in seven different scenarios that use the reported values for sediment supply, grain size distribution, and channel dimensions from *Cienciala and Hassan* (2013) and *Papangelakis and Hassan* (2016). In East Creek, we assume that of all the supplied sediment is contributed by annual events with a magnitude that matches the annual fluvial transport. As the calculated fluvial evacuation time T_{fe} is 2.23 years, this scenario implies that the system would behave in a constant-feed-like manner, which would only change if the supply events were more than 2.23 years apart on average (i.e., $T_{\mathrm{pp}} = 2.23$ years), as shown in the "threshold T_{fe}" calculation. Due to the high uncertainty in our assumption that the measured values represent equilibrium conditions, we calculated two more scenarios with double transport rates ($2 \times U_{\mathrm{fluv}}$) and double armoured grain size ($2 \times D_{\mathrm{a50}}$ and D_{a90}). The last three calculations in Table 2.4 show which pulse frequency is needed to match the armouring timescale (T_{ar}). While we do not know if East Creek is in equilibrium with the sediment supply regime and the measurements used do not reflect long-term conditions, these calculations can still give a rough idea of whether a system is constant-feed-like in our classification of channel response to episodic supply regimes.

2.6 Summary and conclusions

We characterized an episodic sediment supply regime in terms of event frequency, magnitude, and supplied grain size distribution. To test the effect that different episodic sediment supply regimes can have on the morphology of a mountain stream, we developed a numerical model to recreate and extend simulations from flume experiments. The model performs well in recreating the flume experiments in both slope and grain size distributions (GSD), which

are the two variables that represent morphological adjustment in our model. Channel width is fixed and bedforms are assumed to be absent, even though bedforms did occur in the flume experiments.

To understand the extent to which event succession plays a role in the flume experiments, we simulated alternative pulse successions of large-to-small events (i.e., infrequent-to-frequent) and small-to-large events (i.e., frequent-to-infrequent), while keeping the total sediment volume feed the same. These simulations show that different pulse frequency sequences have no strong effect on the long-term slope and GSD of the bed surface. In the short term large pulse events can dominate the channel response causing an abrupt increase in slope, while the effect of subsequent smaller events is subdued as the channel is still adjusted to the large pulse. If smaller events dominate at first, the channel adjusts more gradually.

In our second set of simulations, we imposed different episodic sediment supply regimes with the same total sediment supply volume on the same initial channel geometries with constant discharge. While being kept constant within a run, the episodic supply regimes differed in event frequencies, magnitudes, and GSD. We simulated 40 different event frequencies for which the sum of event magnitudes matched an overall equal total sediment supply. All 40 pulse configurations were calculated for 9 GSD that differed in the width of the distribution σ around the same geometric mean grain size. The channels adjusted to the episodic sediment supply until they reached an equilibrium state in which each successive pulse led to the same slope and grain size adjustment. We compared this state between runs and found a distinctive regime change when the time between pulses (T_{pp}) became lower than a fluvial evacuation time (T_{fe}), which we developed as a measure of the time it takes to remove a D_{s50} thick layer from the channel surface under average transport conditions, modified by a measure of potential armouring (see Eq. 2.15).

The condition of $T_{\mathrm{pp}} < T_{\mathrm{fe}}$ causes a constant-feed-like sediment supply regime, as the model runs show similar slopes and surface grain size distributions as constant-feed runs of the same GSD. When $T_{\mathrm{pp}} > T_{\mathrm{fe}}$ the sediment supply regime becomes pulse-dominated. Under these conditions, we observed a lower relative slope in cases where the GSD is narrow ($\sigma < 0.4$), as the long time between pulses in combination with a low armouring potential

allows more erosion in the reach, ultimately lowering the equilibrium slope. If the GSD is wide enough to allow armouring ($\sigma \geq 0.4$), a stronger armouring layer can develop during the periods of selective transport of smaller grain sizes and bedload starvation. This limits the minimum slope and increases sediment storage (and thus slope) in the long term.

The application of the episodic supply regime classification to data from East Creek shows that the threshold to a pulse-dominated regime lies at the fluvial evacuation time of roughly 2.2 years. This creek probably receives sediment at a lower interval, which indicates a pulse-dominated regime. The armouring timescale lies around 3.5 years, indicating that if the long-term sediment supply was introduced over event frequencies between 2.2 and 3.5 years, it would be removed most efficiently and result in a lower slope.

Steeper channels than East Creek could show both a lower fluvial evacuation time (due to higher slope, smaller channel area) and a lower pulse frequency (more landslide dominated), which could make these channels more likely to be pulse-dominated. Further study of field cases is needed to strengthen the case for our classification of channel response types to episodic supply regimes. In natural rivers, there are further modes of adjustment that the system can undergo after receiving sediment pulses, for example changes in bed forms or the storage of excess material in sediment bodies along the channel. Still, the condition when a channel is receiving more material per pulse than what can be exported in the same time frame (i.e., the ratio of $T_{\mathrm{pp}}/T_{\mathrm{fe}}$ is above 1), should be observable in natural rivers as irregularities in channel long profiles due to increased sediment storage. In our model, we only supplied grain sizes that were transportable by the imposed flow conditions. In field streams it can be that the biggest clasts (e.g., boulders) are only transportable by extreme flow events, which would further increase the slope of reaches with high sediment supply.

Chapter 3

Simulation of sediment pulse effects on Carmel River after the Los Padres Dam removal, Monterey County, California, USA

3.1 Summary

We used a one-dimensional bedload transport model (BESMo) model to study the effect of the proposed removal of the Los Padres Dam (LPD) on the Carmel River in Monterey Bay, California, USA. Based on multiple sediment management options currently being considered, we developed general sediment supply scenarios that represent conditions of continued sediment retention, the re-establishment of background sediment supply, or the exposure of the reservoir sediment to erosion. To explicitly include the stochastic nature of floods in their effect on sediment transport, we developed a method to generate synthetic hydrographs that are based on the frequency, magnitude, shape, and timing of flood events in the historical record. All scenarios that restore sediment feed below LPD cause large parts of the channel to aggrade. We found that establishing a long-time sediment feed (e.g. in the 'Pulse supply'

scenario through managing how material is sluiced out of the reservoir) is most effective in establishing a channel bed that has finer bed material than current conditions. In contrast, the 'Uncontrolled supply' scenario with rapid erosion of the reservoir fines the bed for about 10 years, after which the bed surface becomes significantly coarser through armouring. Over the 60 year timeframe, the style of dam removal might be not be geomorphically significant. The establishment of connectivity between the upstream reaches and the main stem is what governs the system response between 10-60 years after the Los Padres dam is removed. This echoes the previously recognized importance of the upstream areas for the supply of fine sediment on the channel morphology of the Carmel River.

3.2 Introduction

In the United States, a large number of dams were constructed between the late 1950s and the late 1970s (*Graf*, 1999), trapping sediment and decreasing sediment yield from the mountains to the coast by 20% (*Kondolf and Piégay*, 2011). Older dams pose a contemporary safety risk due to surpassing the design age, particularly in areas like California that are at risk of earthquakes. Further, dams can have negative ecological impacts as they change the flow and sediment regimes and can hinder fish passage (*Grant*, 2001; *Grant and Lewis*, 2015; *Major et al.*, 2017).

While there exist a range of sediment management options to restore downstream river functions, (*Kondolf et al.*, 2014), the removal of dams is shown to be particularly effective in efforts to restore biotic diversity due to unregulated flow regimes and the re-establishment of diverse channel features (*Bednarek*, 2001). Additionally, the removal of dams that block fish passage opens up upstream habitat (*Grant and Lewis*, 2015). Recent removals of large dams ($>$ 30 m) on the US west coast were undertaken at the Elwha river with both the Elwha dam (2012) and the Glines Canyon dam (2014) (*East et al.*, 2015), and the Condit dam on the White Salmon River in 2011 (*Wilcox et al.*, 2014). The geomorphological downstream effects of dam removal vary due to the different reservoir characteristics and removal approaches, yet the sediment release from the reservoir is commonly coupled with an increase in downstream sediment transport and increased deposition (*Major et al.*, 2017). Giving a recent overview of dam removal studies, *Foley et al.* (2017) state that the geomorphic response to removals is

typically fast, and that both geomorphic and ecological connectivity are restored quickly.

This study focuses on the Carmel River where the San Clemente Dam (SCD) was removed in 2015 (*Harrison et al.*, 2018), and where further upstream the Los Padres Dam (LPD) is being considered for removal (*MPWMD*, 2016), motivating this study. The geomorphology of the Carmel River is still adjusting to the removal of SCD and to a partial rerouting of the main river channel that was done to prevent erosion of former reservoir sediments.

The dam removal project of LPD is highly complex. The potential geomorphic response of the river to the upcoming LPD removal will be superimposed onto the ongoing river adjustment to the SCD removal. Additionally, the river is impacted by a wide range of natural disturbance events such as wildfire and landslide activity which have historically contributed significant sediment to the river and are known to impact sediment transport dynamics. Finally, the climatic regime of the area leads to highly variable precipitation patterns which are likely to change in unpredictable ways due to climate change over the coming decades. Collectively, the co-occurrence of complexity across so many variables and scales requires novel approaches to integrating uncertainty and stochasticity into predictions of river morphology adjustment.

Numerical modelling has been shown to be useful in assessing potential downstream impacts of dam removal (*Cui and Wilcox*, 2008; *De Rego*, 2018), providing information for managers to understand long-term effects of dam removal (*Foley et al.*, 2017). To simulate the effects of possible management scenarios on the Carmel River, we used the numerical 1-D model BESMo (Bedload Scenario Model; Chapter 2 of this thesis), which was developed to study the sediment transport and geomorphological effect of large sediment pulses in fluvial systems, making it highly suitable for this task of simulating a dam removal. The model integrates approaches from other studies in calculating both hydraulic and sediment dynamics based on input discharge and sediment supply conditions (e.g., *Cui and Parker*, 2005; *Wong and Parker*, 2006; *Ferrer-Boix and Hassan*, 2014; *An et al.*, 2017a), and is similar to other models used to simulate the effects of dam removal (e.g. *Viparelli et al.*, 2011; *Cui et al.*, 2006).

However, past modeling efforts have been computationally limited and cannot adequately integrate the range of complex process at work in the Carmel River. Integrating stochasticity

and uncertainty is particularly important in forecasting dam removal impacts due to interrelations between multiple poorly constrained fluvial, climatic, and hydrological processes. The BESMo model employed in this study is a novel modelling approach that overcomes the limitations of prior models by facilitating computation of multiple stochastic sedimentological and hydrological scenarios to be run in parallel to investigate uncertainty in river response. Unlike methods of traditional platforms such as the US Army Corps Hydraulic Engineering Center River Analysis System (HEC-RAS) or the US Bureau of Reclamations Sedimentation and River Hydraulics - One Dimension (SRH-1D), this allows us to simulate hundreds of different hydrographs per scenario and thus to explore the effects of uncertainty in future hydrology.

In this context, the objectives of this chapter are twofold. First, we want to provide a practical assessment of the response of the Carmel River to four different management options to inform managers and decision makers in charge of the dam removal. The second objective is to situate BESMo within the broader context of modelling dam removals. We assess the utility of BESMo for capturing the complexity and uncertainty of hydrological and sedimentological variables that impact river response to dam removal, and we consider the insight that can be gained from this computational approach.

3.3 Study area

The Carmel River Watershed is approximately 660 km^2, originating in the Santa Lucia Mountains and terminating at the Carmel Lagoon into Carmel Bay, just south of the town of Carmel-by-the-Sea (see Figure 3.1). Following decades of decoupling of the channel from upstream sediment supply, the elevation of the river bed has lowered and the bed surface has coarsened (*Kondolf*, 1982; *GMA*, 2008). Furthermore, along the lowermost 24.5 km of the mainstream Carmel River the banks were altered by installation of a variety of materials to decrease the probability of bank erosion during flood events (*Hampson*, 2018).

The 32 m high San Clemente Dam was build 1921 for water storage and removed in 2015 in the Carmel River Reroute and Dam Removal (CRRDR) project, as the dam was deemed seismically unsafe, threatening 1,500 homes and other buildings on the floodplains of the lower

Carmel River (*Harrison et al.*, 2018). Furthermore, Carmel River provides a crucial anchor habitat for the threatened steelhead trout species *Oncorhynchus mykiss*, of which the juveniles had limited access upstream until the dam was removed (*Harrison et al.*, 2018). During the CRRDR project, the Carmel River was rerouted into the lower end of its tributary, San Clemente Creek, to prevent the erosion of former reservoir deposits, which were additionally protected with a diversion dike. The re-route channel itself was constructed as a step-pool reach fixed with large boulders and excess sediment was added on the banks to be redistributed in floods.

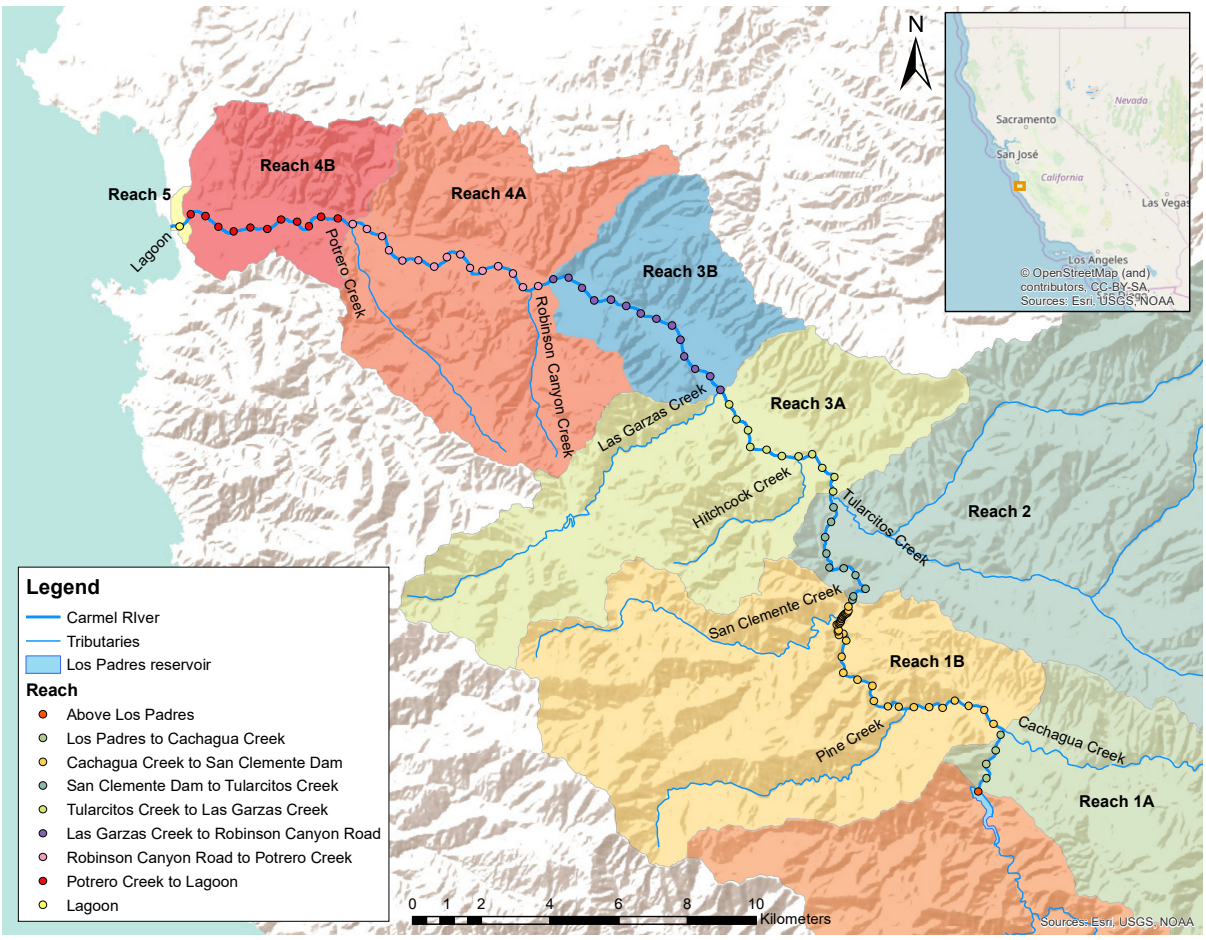

Figure 3.1: Map of simulation reaches. The exact location of each node can be found in Appendix Table B.2

Los Padres Dam is located approximately 40 river km upstream from the river mouth and was constructed in 1948 and 1949 as an earth fill barrier 45 m high. The contributing watershed above Los Padres Dam is approximately 114 km^2, with a mean annual precipitation of 993 mm (*AECOM*, 2017). Much of the upper Carmel River watershed has been burned in previous

wildfires that introduced episodic sediment supply in the years 1977, 1999, 2008 and 2016. The Marble Cone fire in 1977 was the most significant supply event, transporting 727,800 m^3 of sediment into the reservoir. The initial water storage capacity was 3.9 Mio m^3, which over time has been reduced through sediment accumulation to about 48% of usable storage. The future sediment accumulation is estimated to be between 12,300-24,600 m^3 per year (*MPWMD*, 2016). The reservoir sediment storage was estimated to be 1,550,000 m^3 (*AECOM*, 2017), of which roughly 75% is transportable as bedload. We estimate the background sediment feed from upstream of the reservoir to follow the same size distribution as the material stored in the reservoir, giving a mean estimate of sand and gravel transport rate of about 13,400 m^3yr^{-1}.

3.4 Methods

We simulated the response of Carmel River to different sediment supply scenarios using BESMo. We calculated bedload sediment transport in a 1-D channel with a node spacing of 500 m with the transport function developed by *Wilcock and Crowe* (2003). We introduced an unerodible boundary condition at the former SCD site to prevent unrealistic erosion (see Section 3.4.1) and reduced the node spacing in the re-route channel to between 30 m and 150 m to test the model by comparing the simulated profile adjustment with surveys done over a three-year period (see Appendix B.1).

We used the best available data to initialize elevation and grain size values at each node (see Section 3.4.2). For the full 60-year simulations, we generated synthetic hydrographs (see Section 3.4.3) and explored the effects of sediment supply defined in four different management scenarios that are presented in Section 3.4.4. We present a summary of model input parameters in Table 3.1, which for many parameters are the same across all four sediment supply simulations.

Table 3.1: Complete list of model parameters for No Action simulation and changes applied to Historical, Pulse, and Uncontrolled Supply simulations.

Parameter	No Action	Historical Supply	Pulse Supply	Uncontrolled Supply
Simulation Spatial Boundaries	Los Padres Dam to Carmel Lagoon	Same as No Action	Same as No Action	Same as No Action
Simulation Time Period	60 years (2017-2077)	Same as No Action	Same as No Action	Same as No Action
Node Distribution	500 m	500 m, ∼100 m in the San Clemente reach	Same as Historical Supply	Same as Historical Supply
Riverbed Sediment Layers	100 Layers: 1 active layer and 99 subsurface layers; surface layer depth ranges from 0.5 to 1 m	Same as No Action	Same as No Action	Same as No Action
Sediment Transport Mechanics	*Wilcock and Crowe* (2003)	Same as No Action	Same as No Action	Same as No Action
Model Time Step	Variable, between 5 s and 1 min	Same as No Action	Same as No Action	Same as No Action
Hydrology	Random annual hydrographs and number of floods based on MPWMD[1] discharge data of entire basin, internal boundary conditions at tributary confluences	Same as No Action	Same as No Action	Same as No Action
Sediment Transport Peaking Factor	Hydrograph peaking factor applied to days of flood peak ranging from 3 to 1.6	Same as No Action	Same as No Action	Same as No Action
Upstream Flow Boundary Condition	Hydrographs interpolated from Robles del Rio gauge to Los Padres Reservoir assuming no flood peak attenuation	Same as No Action	Same as No Action	Same as No Action

[1]Monterey Peninsula Water Management District

Downstream Lagoon Boundary Condition	0.85 m water surface elevation (*URS*, 2013)	Same as No Action	Same as No Action	Same as No Action
Sediment Supply Boundary Conditions	Main stem and major tributary sediment supply rating curves for chronic conditions with boundary conditions at tributaries	Same as No Action, with added sediment supply equal to 13,400 m^3yr^{-1} inferred from long-term sedimentation rate including Marble-Cone fire	Sediment supply at Los Padres dam based on RC 1-6 through a culvert. Tributaries same as in No Action.	Sediment supply at Los Padres dam based on Exp 1-3. Tributaries same as in No Action.
River Bed Surface Sediment Sizes	Data sourced from *MEI* (2002), 2015 CSUMB data courtesy of Doug Smith	Same as No Action, added *Tetra Tech* (2015) data to represent boulder steps in San Clemente Reach	Same as Historical Supply	Same as Historical Supply
River Bed Subsurface Sediment Sizes	Subsurface grain sizes set to distribution reported as MEI80K, *MEI* (2002), subsurface maximum grain size set to between 512 and 2048 mm to control bed erosion based on trial runs completed Oct-Nov 2017	Same as No Action	Same as No Action	Same as No Action
Reservoir evacuation curve	N/A	N/A	N/A	Modelled after Marmot Dam removal, See Table 3-6
Number of 60-year hydrographs	300 60-year hydrographs	Same as No Action	Same as No Action	Same as No Action
River Bed Longitudinal Profile	Profile constructed using *Whitson Engineers* (2017), *URS* (2013), and NED19 datasets; resulting profile used in simulation	Same as No Action	Same as No Action	Same as No Action

River Cross Sectional Geometry	Sourced from *Normandeau* (2016) and supplemented with *URS* (2013) data when not available	Same as No Action	Same as No Action	Same as No Action

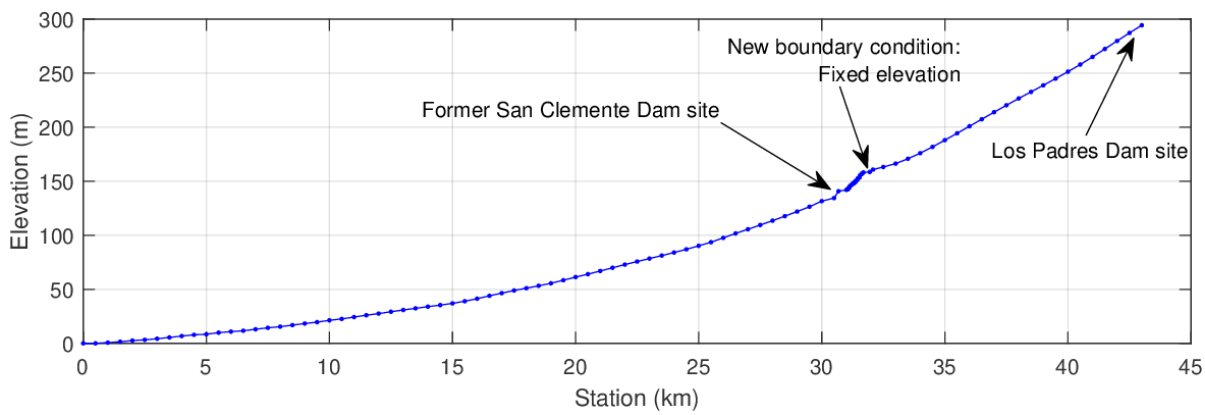

Figure 3.2: Long profile of the full run simulation domain with annotation showing the position of the fixed-elevation boundary condition.

3.4.1 Model boundary conditions

The simulations required specification of several boundary conditions: (a) the riverbed elevation at the downstream-most node at the Pacific Ocean (which we assume is fixed), (b) the bedload sediment supply rate at the upstream-most node at Los Padres Dam and from each of the major tributaries, and (c) the water flow rate at the upstream-most node at Los Padres Dam and from each of the major tributaries. Additionally, test simulations revealed that the model calculates unrealistic riverbed erosion within the re-route reach at the San Clemente Dam Removal project site. Construction conditions at the upstream end of the re-route reach introduced a relatively fixed river profile condition at the transition from the former reservoir deposit to the reroute section. This was accomplished by capping shallowly occurring bedrock at this location (depth below bed surface is approximately 1.5 m) with steel rebar and concrete. We emulate this constructed condition in the model with an internal fixed elevation boundary condition by splitting the model domain into two parts: (1) the upper part from Los Padres Dam to the beginning of the reroute upstream of the former San Clemente Dam and (2) the lower part from the reroute to the mouth of Carmel River (see Figure 3.2). This adjustment prevented both erosion and aggradation at this point in the channel and sediment was fully conveyed through this node. However, the local grain size distribution could adjust according to the composition of the upstream bedload supply.

3.4.2 Node initialization

To begin each simulation, the 87 model nodes along the river long profile (see Figures 3.1 and 3.2) were initialized with values of elevation and grain size distribution. A detailed list of the data used for each node is provided in Appendix Table B.2.

Elevation profile

The initial elevation profile was based on two different channel surveys and DEM data, as the surveys are available only for the lower parts of the river (see Appendix B.2). We calculated the elevation for nodes in the upper Carmel River from a 3m-resolution digital elevation model.

Grain size distributions

For each model node, we specified three different initial Grain Size Distributions (GSDs): (1) initial active layer GSD, (2) initial subsurface GSD, and (3) maximum subsurface GSD. The grain sizes used for this purpose were collected from several different sources: *MEI* (2002), *URS* (2013) and *Chow et al.* (2016) [2]. Through initial model runs we determined that model results are sensitive to the initial configuration of the surface and subsurface grain size distributions. This is unsurprising for two reasons. First, the bed surface GSD is used to estimate channel roughness through the 90th-percentile grain size (D_{90}), which affects the calculated cross-sectional average velocity. This in turn can impact the calculation of water depth and the associated cross-sectional average shear stress. Second, mass balance calculations for adjustment of the grain size fractions present on the channel bed surface are dependent on the thickness of the active layer. The active layer concept simplifies bedload transport as a two-layer system: grains in transport within the active layer and immobile subsurface grains. The interface between the active layer and the subsurface is an exchange surface for grain size fractions.

The active layer thickness is typically parametrized as the local D_{90} grain size multiplied by a constant which ranges from 1 to 2 (we use a value of 2 following *Parker*, 2008). As a result, the D_{90} affects both the bed surface roughness and the depth of the bed which participates

[2] from here forward referred to as the CSUMB data, provided to us by Douglas Smith

in bedload transport. Relatively small D_{90} grain sizes led to unrealistically large depths of bed erosion along the mainstem Carmel River reach downstream of the Narrows within trial simulations. As a result, we have carefully identified a defensible, but not demonstrable (due to a lack of field data), initialization of grain sizes for the No Action Simulation. Our choices generally reflect field observations of bed surface grain sizes where data is not available, most notably within the vicinity of the so-called Steinbeck pool, and construction specifications of the bed surface for the San Clemente Dam Removal step-pool reach. In general, all channel evolution models are sensitive to the initialization of bed surface and subsurface grain size distributions. Unfortunately, almost all studies like the present one lack actual information to minimize uncertainty with respect to this model input because it is impractical to sample the bed to minimize this uncertainty (i.e. *Church et al.*, 1987; *Rice and Church*, 1996; *Bunte and Abt*, 2001), or data is collected for reasons that go beyond channel evolution modelling and therefore concessions are made in order to collect a diversity of data rather than data for one particular purpose, and subsurface data is rarely collected, as in the present case. Grain size specifications for each model node are provided in Appendix Table B.2 and the distributions are presented in Figure B.19.

Initial active layer GSD The active layer GSD is important mainly at the beginning of the simulations, as it describes the transportable size classes directly exposed at the channel surface. For the initialization of this layer, we used the active-layer data specified within the URS simulations, except for the lowest reaches where the coarser CSUMB data is a better representation of current condition. The CSUMB data also mitigated unrealistically large simulated channel bed erosion depths in the spin-up runs.

Initial subsurface GSD The subsurface GSD lies directly beneath the active layer and the size classes get incorporated into the active layer if the channel erodes. We deemed the URS subsurface data too fine for the initial subsurface GSD, as the channel eroded significantly in the spin-up runs. The MEI subsurface GSD data mitigated simulated erosion and was deemed a better representation of subsurface conditions. Note, however, that both datasets are derived

from surface population estimates because we lack measured subsurface GSDs.

Maximum subsurface GSD Whereas the URS model (*URS*, 2013) assumed the subsurface GSD to be present for the whole depth of the subsurface (virtual depths of multiple meters), we found that to prevent unrealistic erosion directly at the dam site and in the lower reaches, we had to introduce layers of coarser maximum grain sizes below the first few subsurface layers. We generated these by removing all smaller size classes in these layers and only specified the presence of a uniform, large grain size (either 512 mm or 256 mm). We do not have field data to support the presence of these more erosion resistant layers, but the approach yields model results which are on average consistent with previous model results of the spatial patterns of erosion and deposition (*URS*, 2013), and more importantly with observed conditions at the San Clemente Dam removal project site (see Appendix B.1). We specify the depth at which this layer begins and which size we use in Appendix Table B.2.

3.4.3 Hydrology submodel

To generate synthetic hydrographs, we relied on statistical data derived from both historical flow records and simulated tributary discharge provided by MPWMD, who generated the data from watershed scale hydrologic modelling with PRMS (*Markstrom et al.*, 2015). Below, we specify the methods used to randomly select an annual peak flow magnitude from historical distributions, as well as the number of peak flows for each year of the 60-year simulation period. An overview of the different components of this calculation is given in Figure 3.3. It is important to note that BESMo simulation uses the same randomly constructed hydrologic time series for each sediment supply scenario.

Reach and tributary discharge We segmented the Carmel River into 5 main reaches following *AECOM* (2017). We then further subdivided reaches 1, 3, and 4 to better represent the effect of tributaries as we recalculated the hydrology for each sub reach. A map of the reach locations, catchment areas, tributaries, and the position of model nodes is shown in Figure 3.1. For each simulation, we generated a random hydrograph of mean daily flow for the reference reach that

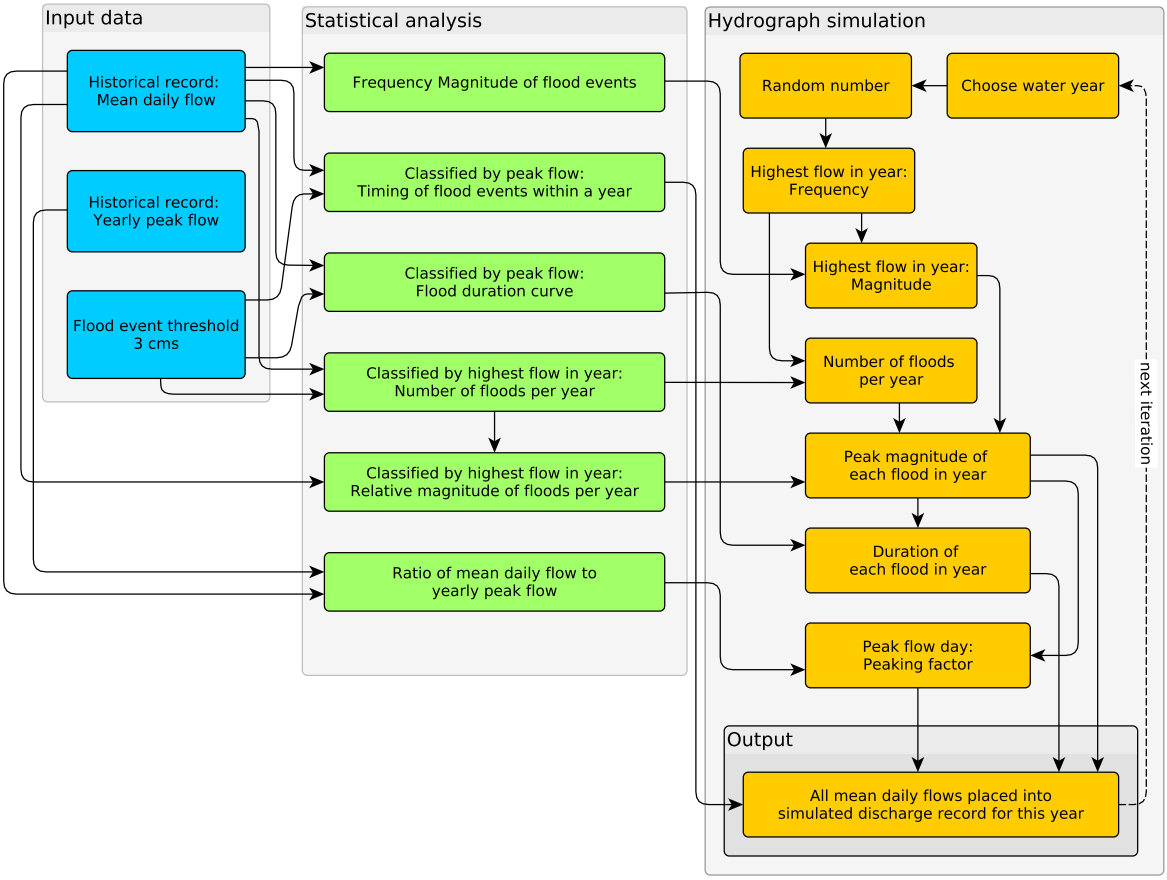

Figure 3.3: Components of the calculation of the flood time series with the hydrology submodel. Blue: Input data from historical records and watershed modelling. Green: statistical data per flood class. Orange: steps to generate flood time series

included the Robles del Rio (RR) USGS gauge (Reach 3A). We then calculated the discharge for all other reaches by multiplying the D3A reach discharge by the historical discharge ratio of each of the other simulation reaches. The discharge ratios for both the main stem (used for modelled sediment transport) and the tributaries (used for tributary sediment feed from rating curves) are listed in Table 3.2 and were calculated as averages from 4748 days of overlapping records provided by the MPWMD as part of ongoing watershed scale hydrologic modelling with PRMS (*Markstrom et al.*, 2015). The overlapping period of records extends from October 1st, 2001 to September 30th, 2014. For each simulation reach, the estimated hydraulics for each sequential daily discharge was simulated in a backwater flow calculation.

Table 3.2: Carmel River main stem discharge ratio from 4748 days of overlapping mean daily flow data (Oct 1st, 2001-Sept 30th,2014). The flow data is from historical record where available, and otherwise modeled.

Main Stem	ID	Reach	Discharge Ratio to RR	Standard deviation
Below Los Padres	'BL'	D1A	0.66	0.11
Below Los Padres + Cachagua Creek	'BL+CA'	D1B	0.70	0.11
Sleepy Hollow Weir	'SHW'	D2	0.93	0.08
Robles del Rio Gauge	'RR'	D3A	1.00	0.00
Don Juan	'DJ'	D3B	1.05	0.11
Near Carmel Gauge	'NC'	D4A	1.06	0.18
Highway 1	'HWY1'	D4B	1.02	0.21
Tributaries				
Cachagua Creek	'CA_trib'	D1B	0.04	0.02
San Clemente Creek	'CL_trib'	D2	0.12	0.03
Tularcitos Creek	'TU_trib'	D2	0.01	0.01
Las Garcas Creek	'GA_trib'	D3B	0.07	0.03
Robinson Canyon Creek	'RC_trib'	D4A	0.01	0.01
Potrero Creek	'PO_trib'	D4A	0.01	0.01
Hitchcock Creek	'HI_trib'	D3A	0.01	0.00

Random hydrographs with flood events We generated random hydrographs for the 60-year analysis period to simulate plausible future hydrologic conditions. We did so by assuming that future conditions will be statistically similar to the historical record of flood magnitude and frequency, flood duration, and number of floods per year. As a result, we extracted the following information from the historical records to develop the hydrographs: (1) annual peak flows, (2) number of floods per year, (3) flood duration, and (4) timing of flood events within a year. With this information, we first defined a flood event as any flow above a threshold of 3 m^3s^{-1} mean daily flow for at least two consecutive days (flood duration) in the historical record. We then group all flood events into 5 classes by the maximum mean daily flow, with roughly a minimum of 10-20 events in each of the higher flood classes for the 60-year simulation period (Table 3.4). After this step, we used this catalogue of historical flood events to develop random 60-year daily simulation hydrographs.

Table 3.3: Flood frequency table for the Robles del Rio USGS gauge using mean daily discharge on the day of yearly peak flow.

Expected discharge (m^3s^{-1})	Exceedance chance (%)	Lower confidence interval (5%) (m^3s^{-1})	Higher confidence interval (95%) (m^3s^{-1})
1282.76	0.2	2156.36	710.75
986.28	0.5	1631.56	573.05
787.14	1	1279.66	474.49
608.41	2	968.32	381.48
405.14	5	620.98	268.27
275.71	10	407.83	190.97
168.11	20	237.79	121.77
59.07	50	78.76	44.53
17.83	80	24.67	12.76
8.88	90	13.16	5.99
4.79	95	7.69	3.06
1.33	99	2.66	0.78

Annual peak flow, number of floods per year and flood magnitudes For each full simulation, we randomly generated a 60-year record of daily flows by simultaneously carrying out three modelling steps: (1) randomly choosing an annual mean daily peak flow magnitude, (2) determining peaking factors (see below) to apply to the annual mean daily peaks, and (3) determining the number of floods for each simulation year. For each year in a simulation, we randomly selected from among the flood frequency classes previously calculated with HEC-SSP and described in *AECOM* (2017, Section 2.6.3 Flood Frequency Analysis). However, instead of using the instantaneous annual peak flows to prepare the flood frequency statistics, we calculated the frequency and magnitudes of the mean daily flows for each specific day corresponding to an instantaneous flood peak within the historical record (Table 3.3). This is consistent with the modelling approach of past local studies (*MEI*, 2002; *URS*, 2013, e.g.). However, unlike previous studies, we applied peaking factors: the ratio between mean daily flow and the instantaneous peak flow at the day of highest flood discharge (Table 3.4). This captures the non-linear relationship between instantaneous discharge and the rate of bedload transport, which would be lost by only using mean daily flow values.

Table 3.4: Peaking factor for flood classes from the historical peak flows.

Flood Class:	1	2	3	4	5
Mean daily flow	3-7 m^3s^{-1}	7-21 m^3s^{-1}	21-42.5 m^3s^{-1}	42.5-85 m^3s^{-1}	>85 m^3s^{-1}
# in historical record	63	43	22	25	11
Peaking factor	1.6	1.6	2	3	3

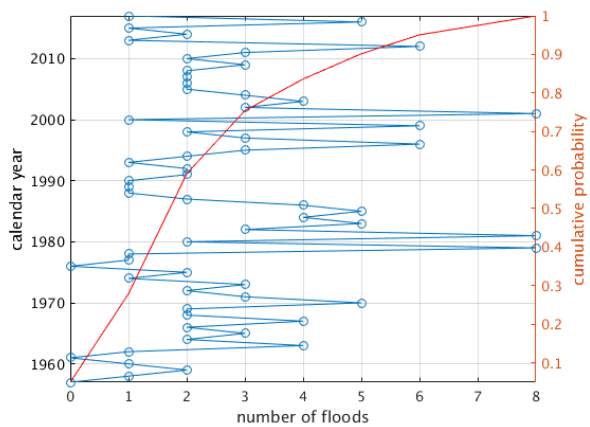

Figure 3.4: Number of floods per water year from the historical record at the Robles del Rio USGS gage.

We simultaneously decided how many floods occur in each simulation year by using associated probabilities for the historical period. With the historical RR gauge data, we calculated flood occurrence probabilities for between 0-8 floods per year based on a flood discharge threshold of 3 m^3s^{-1} (Table 3.5 and Figure 3.4). We then randomly sampled from this distribution to determine the number of floods for each simulation year. The choice of flood magnitude and the number of floods for each simulation year was carried out independent of each other so that the simulations are not strictly constrained by the hydrologic character of the historical record. This method of developing the hydrologic records for the simulation period means we are not overly restricting our analysis to assumptions of stationarity, despite reliance on the historical discharge records. Next, we determine how intra-annual flood peaks compare if more than 2 floods are randomly chosen for a simulation year.

We analysed the historical data to determine how intra-annual flood peaks varied from

Table 3.5: Probability of number of floods per year and ordered peak mean daily flow ratios between the floods within one year in relation to the highest mean daily flow at the Robles del Rio USGS gauge. The cumulative probability column indicates that most years in the historical record have two floods per year.

Number of floods per year	Occurrences in record	Cumulative probability	Average maximum daily mean flow ratios
0	3	0.05	0
1	14	0.23	1
2	19	0.31	1, 0.36
3	10	0.75	1, 0.42, 0.19
4	5	0.84	1, 0.42, 0.22, 0.12
5	4	0.90	1, 0.59, 0.30, 0.23, 0.14
6	3	0.95	1, 0.66, 0.24, 0.13, 0.09, 0.09
8	3	1.00	1, 0.52, 0.36, 0.29, 0.20, 0.10, 0.08, 0.07

event to event, depending on how many floods occurred in a given year. The results are shown in the far right-hand column of Table 3.5, presented as the ratio of the highest mean daily flow at the RR gage to the flood peak associated mean daily flow. This data is important for a few reasons. First, it is a critical link for construction of the random annual hydrographs for the 60-year simulation period because the statistical analysis of annual peak flows only recognizes the maximum flow event for each year and does not contain information on more than one flood within the same water year. Second, like the data in Table 3.3 and Table 3.4, information on average intra-annual flood variability permits us to remain consistent with the statistical nature of historical floods, while supporting a stochastic approach.

Flood duration and timing within each year We assumed the duration of each flood event to be mainly dependent on the peak flow magnitude. To attribute a flood duration to each flood in the randomly constructed records, we calculated average hydrographs within the historical record at the RR gauge for the five flood categories in Table 3.4. The average hydrographs are shown in Figure 3.5 (left panel) where floods have average durations of approximately 10 to 50 days or more, based on flow conditions prior to the peaks. We assign the timing of each flood event within a year based on the most likely flood day-of-year observed from the

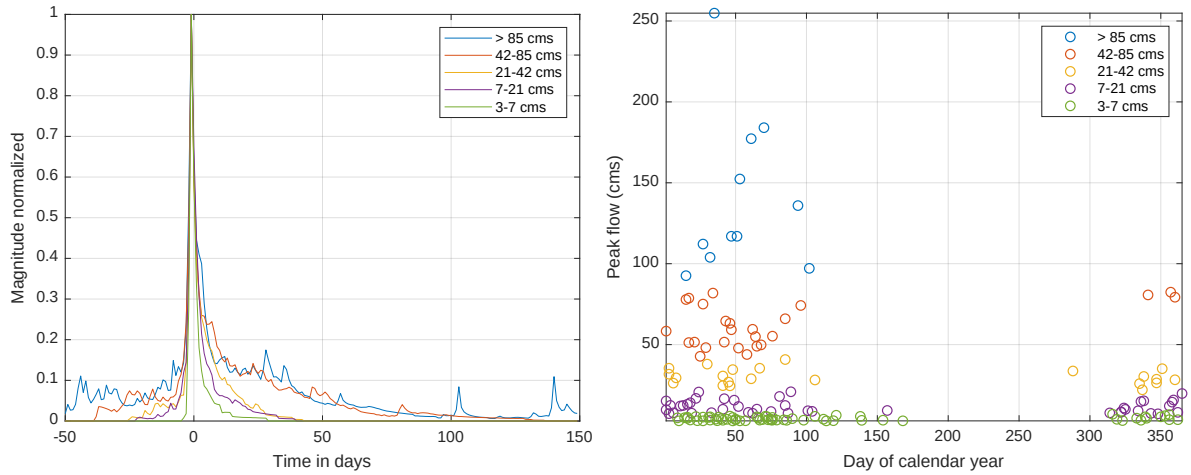

Figure 3.5: Left: Relative mean daily flow as time series in five flow classes from the averages of all events in the historical record. The flood classes in the legend are in mean daily flow at peak day. Right: Timing of floods in the calendar year in relation to mean daily peak flood magnitude.

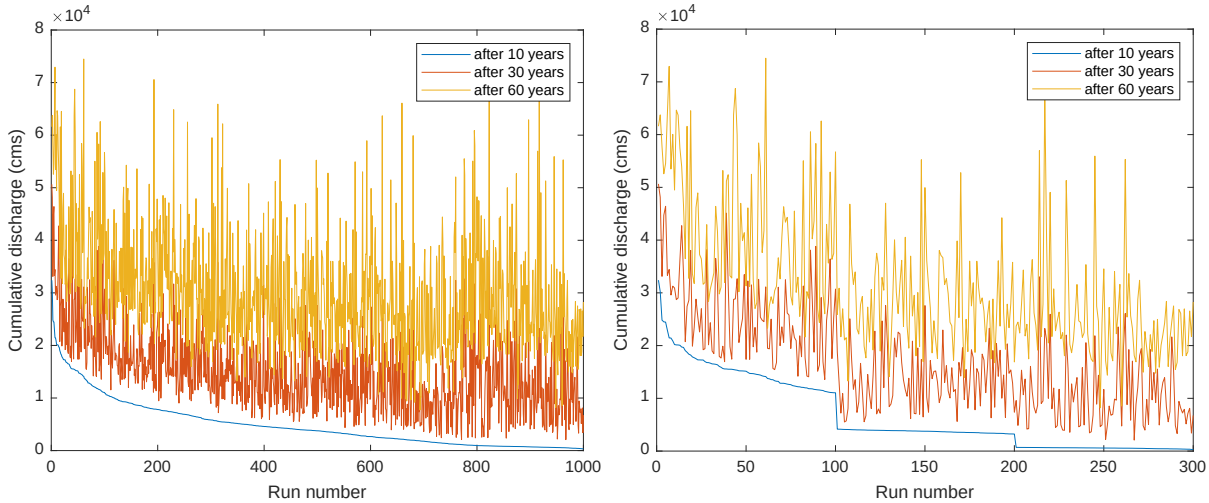

Figure 3.6: Left: Cumulative discharge for 1000 randomly generated hydrographs after 10, 30, and 60 years, sorted by 10-year cumulative discharge. Right: Subsection of 300 runs that were simulated for each project simulation with BESMo. Runs 1-100 represent the 100 wettest cases of first 10-year cumulative discharge (10th percentile and lower), runs 101-200 represent average conditions (45th-55th percentile), and runs 201-300 represent dry conditions in the first 10 years (90th percentile and higher).

historical record (Figure 3.5, right panel) for the associated hydrologic category. In the event of overlapping flood events in time, we move the overlapping event to center around another likely flood day.

Hydrograph use in BESMo We used the described approach to generate a population of 1,000 synthetic hydrographs that statistically match the historical record. It is important to note that we do not use climate projections to develop future records of possible daily discharge, but it is feasible to do so by changing the underlying flood frequency-magnitude relation. For this study we are interested in the effect that very dry or very wet conditions have on the Carmel River after the potential dam removal. To create a subset of hydrographs to simulate, we ranked the resulting discharge time series from driest to wettest based on cumulative discharge during the first 10 years, during which we expect the channel adjustment to be most responsive. We then chose the 100 wettest, the 100 driest, and 100 average[3] simulations from the 1,000 randomly constructed hydrographs (Figure 3.6). Because a given hydrograph is classified based only on the first 10 years of discharge, annual cumulative discharge is still highly variable after 30 and 60 simulation years.

An advantage of using the sorted collection of hydrographs is that our simulation results can be linked to statistical tendencies of the range of hydrologic conditions (*Wilcock*, 2001). Based on the flood statistics, the 100 wet-year hydrographs have discharges higher than what 90% of the historical record indicates. Similarly, the average hydrologic conditions are designed to represent hydrographs that produce discharges within 45% and 55% of what the historical record indicates. The dry hydrologic conditions have discharges lower than 90% of what the historical record shows.

Hydraulics BESMo simulates river flow with the normal flow approximation and the backwater solution to the momentum equation(*Cui et al.*, 2006). It does not directly incorporate the effect of a non-uniform cross-sectional channel shape on bed shear stress. However, we do account for such conditions in calculation of the water surface profile with the backwater solution. This permits us to better represent the effect of high flows on the average channel bed shear stresses at each model node. To accomplish this, we capture the non-uniformity of cross-sectional shape through data previously reported which relates water depth and flow area to discharge, averaged for each model reach (*URS*, 2013). With this information, we cal-

[3] 50 simulations on either side of the median.

culate an approximated water surface width based on water mass conservation (i.e. discharge = cross-sectional average velocity times flow area) and a relationship between discharge and flow velocity from *MEI* (2003) (see Appendix B.9).

3.4.4 Sediment supply

We describe available sediment transport data for both the Carmel River and its tributaries in Appendix B.3. Based on the general management options for the Los Padres dam and reservoir, we developed the following four sediment supply scenarios:

No Action simulation The No Action project alternative assumes no action is taken at Los Padres dam or within the reservoir. This means coarse material would continue to accumulate in the reservoir, and the only sediment to bypass the dam is that which is carried in suspension over the top of the dam during floods. As a result, the only bedload sediment supply to reaches downstream of the former San Clemente Dam in this scenario is that from tributaries downstream of Cachagua Creek. This simulation is the baseline simulation for comparative purposes.

Historical Supply simulation The historical sediment supply simulation assumes that some actions are taken to restore historical sediment supply in the Carmel River. This means that bedload-sized sediment supplied from the watershed contributing to the Los Padres reservoir would once again contribute to the sediment budget for the watershed downstream of the Dam. The simulation does not account for any of the bedload sediment presently stored within the reservoir deposit. This simulation can serve as a baseline end member for the Carmel River watershed under approximated unmodified sediment yields. However, the effects of resumed historical supply to the watershed downstream of Los Padres is a function of present-day river conditions downstream of the Dam, which are the result of a mixture of human-driven impacts related to dam construction and river/floodplain modification. This simulation can also serve as a representation of controlled dam removal alternatives, after the existing reservoir deposit has been stabilized, removed, or otherwise is no longer a factor.

AECOM (2017) report a total dry unit weight of 1,831,850 tons reservoir sediment[4], which includes 26% of silt- and clay-sized particles. Including the Marble-Cone fire in 1977, this deposit of sediment corresponds to a long-term average sedimentation rate of 18,100 m^3yr^{-1}. A bedload rating curve was calculated by scaling down the sedimentation rate of 18,100 m^3yr^{-1} by 74%, resulting in 13,400 m^3yr^{-1} of bedload sediment. This rating curve was applied to flood events with flows higher than 3 m^3s^{-1}. Simulation hydrology used for the Historical Supply is identical to that used for the No Action simulations.

Pulse Supply simulation The Pulse Supply simulation assumes that some actions are taken to manage the introduction of pulses of bedload from the Los Padres reservoir deposits into the Carmel River, which may include a sluicing tunnel, or dredging. A preferred means of sediment relocation has not been identified, but the Pulse Supply simulation is intended to mimic the behaviour of sediment introduced below Los Padres Dam in any of these scenarios.

The Pulse Supply simulation is designed to evaluate probable downstream responses under a range of conditions which emulate how passive sediment transfer may affect downstream reaches with the introduction of sediment pulses. The Reservoir Alternatives memo (*AECOM*, 2017) highlights four different sediment management alternatives for Los Padres Reservoir: (a) excavate, truck and dump, (b) sluice tunnel, (c) bypass tunnel, (d) some combination of these three approaches. Our implementation most closely reflects the sluice tunnel, as we use flow-weighted sediment rating curves for a flow range up to[5] 140 m^3s^{-1}. We further impose a minimum flow of 8.5 m^3s^{-1} for sediment transport to start, which represents the closing of the sluice gate to improve reservoir fill times.

Sediment delivered through the sluice structure to downstream reaches is sourced from the Los Padres reservoir deposits. Additionally, upstream sediment supply replenishes the reservoir deposit in the same way the sediment feed was calculated in the Historical scenario (flow weighted). The rating curves are of the form $Q_s = aQ_w^b$, with Q_s as sediment feed in

[4]This figure was updated and revised in 2018, but because estimated reservoir capacity changed by less than one percent, model simulations were not re-run as they would likely have a similarly negligible effect.

[5]The Report indicates an approximate maximum operational flow of just over 140 m^3s^{-1} for a horseshoe-shaped sluice tunnel of approximately 4.5 m in width.

tons per day and Q_w as discharge in ft^3s^{-1}. The relationship is based on empirical data from tributaries of the Carmel River, suggesting coefficient values for a ranging from 0.0002 - 0.6, and exponent values for b ranging from 1.2 - 3.6. We assume that sediment supply during the simulations to the structure is at or near the respective capacity of the daily simulated flow, mimicking open-channel conditions. The grain size distribution of the pulsed sediment supply is a mixture of the sand and coarser fractions presently within the reservoir.

We use the same 300 60-year hydrographs as previously outlined for simulations of wet, average and dry conditions. We present 6 different rating curves across the 3 different hydrologic conditions (18 different pulse-like sediment supply scenarios) in Table 3.6. One benefit of using flow-weighted rating curves is that sediment pulse size is scaled by flow, and therefore the hydrologic time series remains one of the primary control parameters of the simulations. Plots of sediment yield and reservoir evacuation over time for all hydrologic conditions are presented in Appendix B.10.

Table 3.6: Overview of sediment feed scenarios by rating curve type. We use the pre-calculated hydrographs to predict both the storage depletion time and the median sediment supply that would follow from each sediment feed scenario. RC 1 to 6: Take effect only at minimum discharge of 8.5 m^3s^{-1} and limit flow to a maximum of 144 m^3s^{-1}. Flow over the maximum is delayed to subsequent days until the flow volume of the simulated flood was conveyed through the structure.

Sediment feed type		Median time to depletion (years)			Median time to 50% of storage (years)			Median sediment supply in first 10 years (m^3yr^{-1})		
ID	Formula	wet	average	dry	wet	average	dry	wet	average	dry
RC 1	$Q_s = 0.35 * Q_{w,inst}^{1.5}$	34.91	never	never	7.42	never	never	73,300	10,100	500
RC 2	$Q_s = 0.50 * Q_{w,inst}^{1.5}$	6.87	never	never	4.82	37.88	54.89	84,100	14,400	800
RC 3	$Q_s = 0.05 * Q_{w,inst}^{1.75}$	58.84	never	never	8.29	never	never	72,600	8000	400
RC 4	$Q_s = 0.15 * Q_{w,inst}^{1.75}$	3.96	28.43	34.92	3.18	17.93	26.92	87,800	24,000	1100
RC 5	$Q_s = 0.025 * Q_{w,inst}^{2}$	3.36	21.90	29.90	2.92	11.43	23.98	87,800	32,300	1200
RC 6	$Q_s = 0.05 * Q_{w,inst}^{2}$	2.97	14.92	24.87	2.87	6.87	18.99	87,800	46,200	1800

Table 3.7: Exponential decay curves for the three simulated scenarios.

ID	Formula	description
Exp 1	$S = -6 * \log Q_{w,cum} + 150$	Low storage decay
Exp 2	$S = -9.3 * \log Q_{w,cum} + 178.59$	USGS best fit for Marmot dam
Exp 3	$S = -10 * \log Q_{w,cum} + 180$	High storage decay

Uncontrolled Supply simulation The Uncontrolled Supply simulation assumes that the Los Padres dam is removed without taking steps to manage the subsequent erosion of the reservoir deposits. Our approach of simulating this case is based on observations by *Major et al.* (2012), who describe that the sediment storage of the Marmot reservoir decreased in an exponential fashion after the removal of the dam. This indicates that the initial sediment supply is very high but decreases quickly. *Grant and Lewis* (2015) found this observation to be valid for multiple dam removal cases. As the Marmot reservoir is similar in both reservoir size and particle size, we assumed the Los Padres reservoir would deplete in a similar fashion. We designed three potential decay curves (Exp 1 to 3) which envelope the natural decay rates reported by *Major et al.* (2012). The curve Exp 2 matches the data from Marmot dam, while Exp 1 and Exp 3 represent higher and lower storage decay rates, respectively (see Table 3.7 and Figure 3.7). The rating curves are of the form:

$$S = -a * \log Q_{w,cum} + b$$

where S represents storage (expressed in percent remaining), $Q_{w,cum}$ is the cumulative discharge (in m^3) since the removal of the dam, and a and b are empirically determined.

We assumed that the material from all zones would leave the reservoir well mixed and excluded all grain sizes < 1 mm. A background sediment feed rate of 13,400 $m^3 yr^{-1}$ is added to the sediment export calculated from the decay curve (spread over the simulated hydrograph). This is different from the Pulse Supply scenario, in which the background feed replenished the reservoir sediment storage. In contrast to the Pulse Supply scenarios, we did not impose a minimum discharge to erode the reservoir deposits. We imposed the same 300 60-year hydrographs as in all other simulations. The remaining model specifications are the same as in the Pulse Supply scenarios and summarized in Table 3.1.

In general, the simulation of uncontrolled sediment release in form of exponential decay curves leads to:

1. Large volumes of the reservoir sediment are eroded early even during small floods, as the decay curve is not depending on flood magnitude.

2. Following this, the erosion of sediment in the reservoir will decrease substantially within

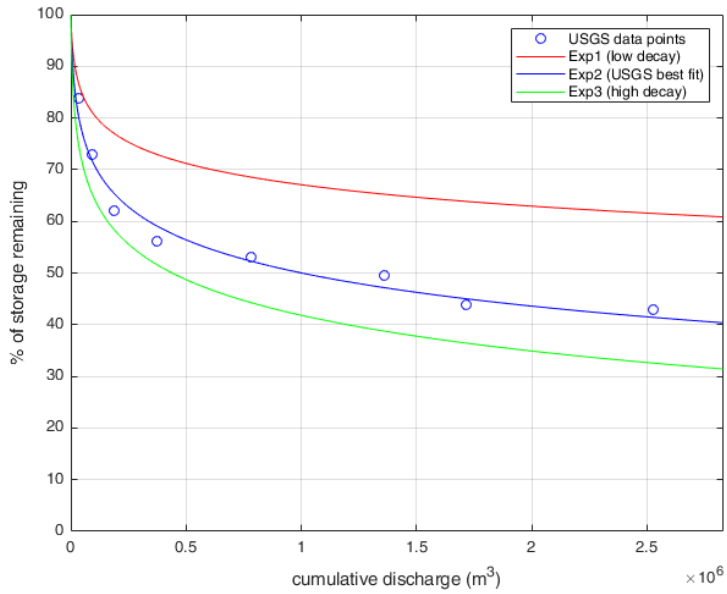

Figure 3.7: Exponential decay curves modelled after Marmot dam removal data. The 'USGS best fit' matches our 'Exp 2' scenario, while the 'Exp 1' matches a visually fit 'low scenario' and 'Exp 3' matches a visually determined 'high scenario'.

10-20 years.

3. A lot of material will never be eroded, as the decay curves approach a set minimum fill percentage asymptotically. The volume of material left, represents sediment out of reach of the stream, between 2% and 40% of the initial volume in this simulation).

Plots of sediment yield and reservoir evacuation over time for all hydrologic conditions are presented in Appendix B.10.

Tributary sediment input Sediment input from each of the tributaries is calculated using the bedload sediment rating curves given in Appendices B.4 and B.5, and is introduced at the node closest to the confluence. Because only relatively large flood events are simulated (flows greater than 3 m^3s^{-1} at the Robles del Rio gage), episodic bedload rating curves are used to calculate tributary sediment inputs.

3.5 Results

We focus our review and comparison on those results which occurred in the wet hydrograph simulations. These simulations represent more frequent and larger floods for the first 10 simulation years than estimated for 90% of the historical record (see Section 3.4.3). These wet conditions are most relevant to project planning, as they represent a worst-case in terms of sediment transport activity. The associated comparative plots for the dry and average hydrologic conditions are described in detail in Appendix B.11 and overview figures are presented in Appendix B.12. To further focus the discussion, we only present results of one sediment supply curve each for the 'Pulse supply' and the 'Exponential decay' scenarios (RC 4 and Exp 2, respectively), which were designed to represent the conservative assumptions for these management options.

We assess management scenario impacts on channel geomorphology through changes to bed elevation[6], mean surface grain size D_g and the 90th-percentile fractional grain size D_{90} from Los Padres Dam to the Pacific Ocean. In general, all four simulations lead to an increase of channel bed elevations through net bedload deposition from the former San Clemente Dam to the Pacific Ocean over the 60-year simulation time period (Figure 3.8). The most rapid rates of deposition occur from years 1 through 10, and diminish thereafter through year 60, indicating that the depositional rate is proportional to flood magnitude early in the simulation time period. Upstream of the former San Clemente Dam, the primary response to resumption of Los Padres (and upstream) sediment supply is net deposition. In contrast, the No Action simulation results in up to two meters of further bed erosion up until the profile approaches the former San Clemente reservoir site. Projected bed elevation responses over the entire model domain are associated with coarsening of the bed surface relative to initial conditions (Figure 3.9 and Figure 3.10). Coarsening is most pronounced under the No Action simulation and decreases with the additional sediment supplied from the Los Padres reservoir storage and upper contributing watershed. This outcome suggests that the gravel and coarser bedload

[6]Elevation change is calculated by projecting the deposited sediment volumes equally across the average reach-based cross-sectional shape (see Section 3.6.1 and Appendix B.8). For the case of bed erosion, we calculate elevation change based on a rectangular channel.

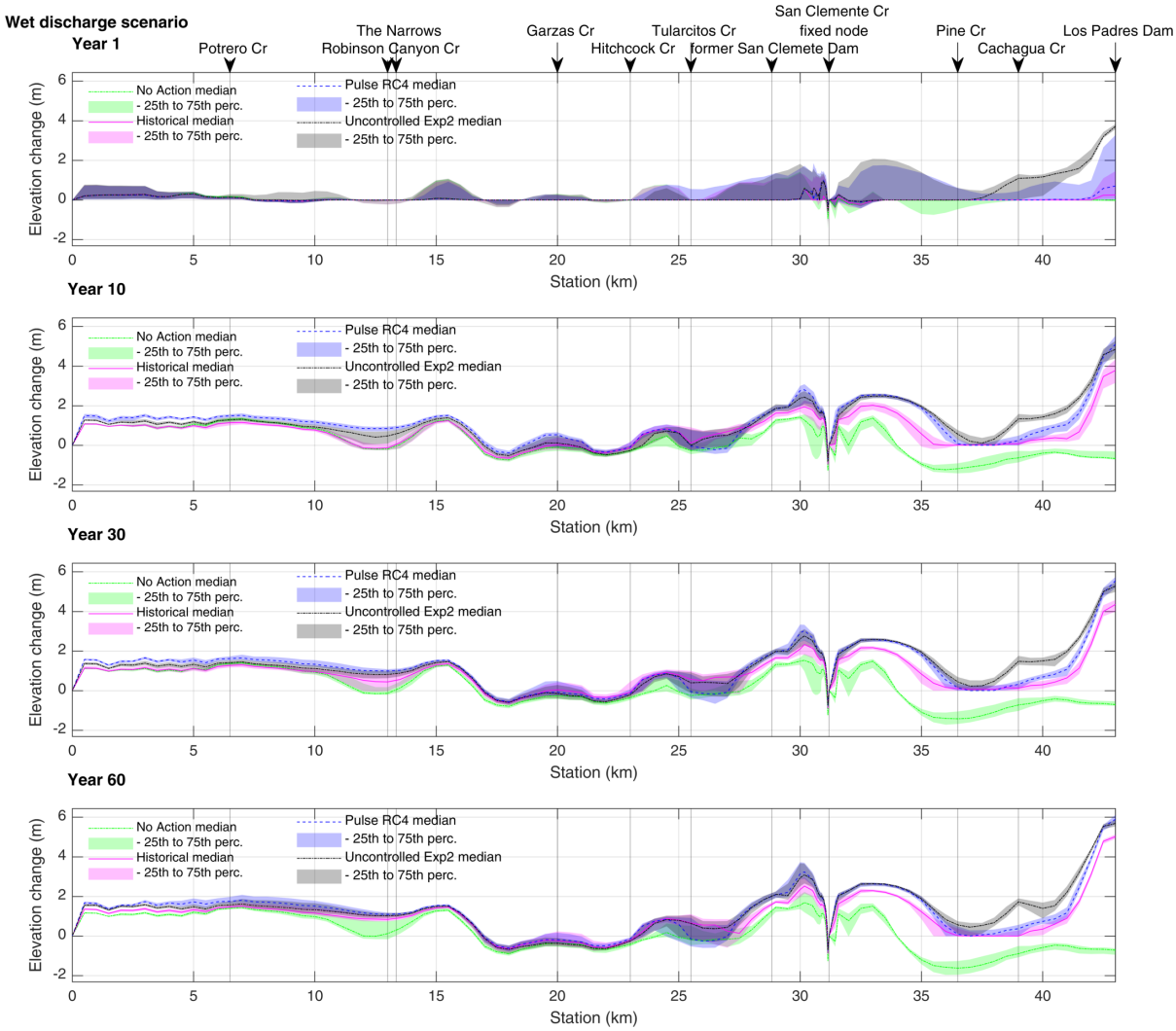

Figure 3.8: Comparison of projected bed elevation change from the 2017 initial profile for the wet hydrologic condition and the Historical, Pulse and Uncontrolled sediment supply simulations. Shaded regions capture the 25th-75th percentile responses across the 100 simulations for the wet condition. Results shown for simulation year 1, 10, 30 and 60.

content from the watershed area upstream of the former San Clemente Dam is large relative to the fractional content of bedload supplied along the lower mainstem and is therefore important in setting the ultimate texture of the riverbed surface. Furthermore, the bedload supply sourced from the Los Padres reservoir storage and the upstream contributing watershed is important in terms of moderating the overall coarsening response. This result has clear implications for expectations around future steelhead habitat conditions related to actions at Los Padres Dam.

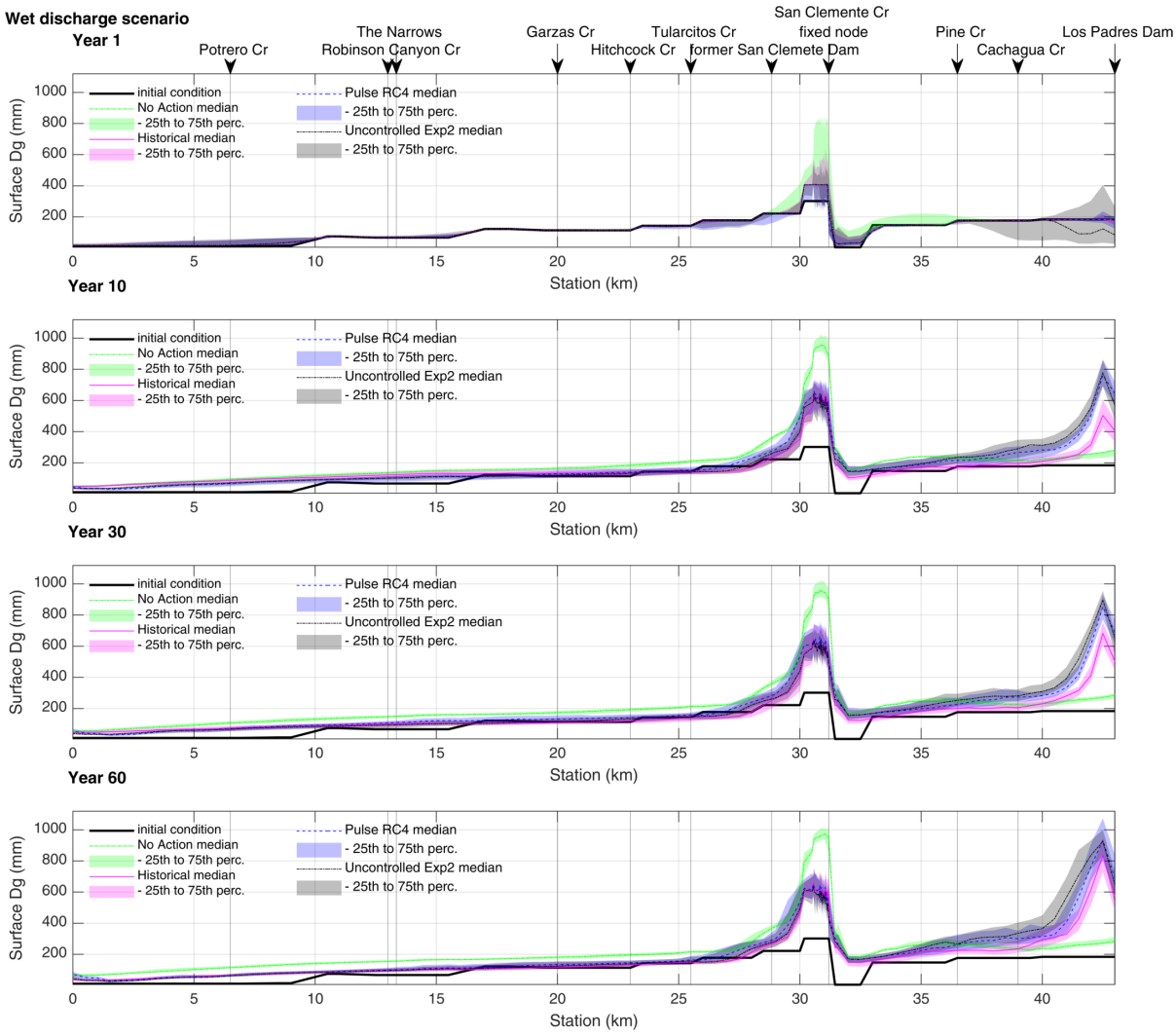

Figure 3.9: Comparison of projected change of the geometric mean grain size of the bed surface D_g for the wet hydrologic condition and the Historical, Pulse and Uncontrolled sediment supply simulations. Shaded regions capture the 25th-75th percentile responses across the 100 simulations for the wet condition. Results shown for simulation year 1, 10, 30 and 60.

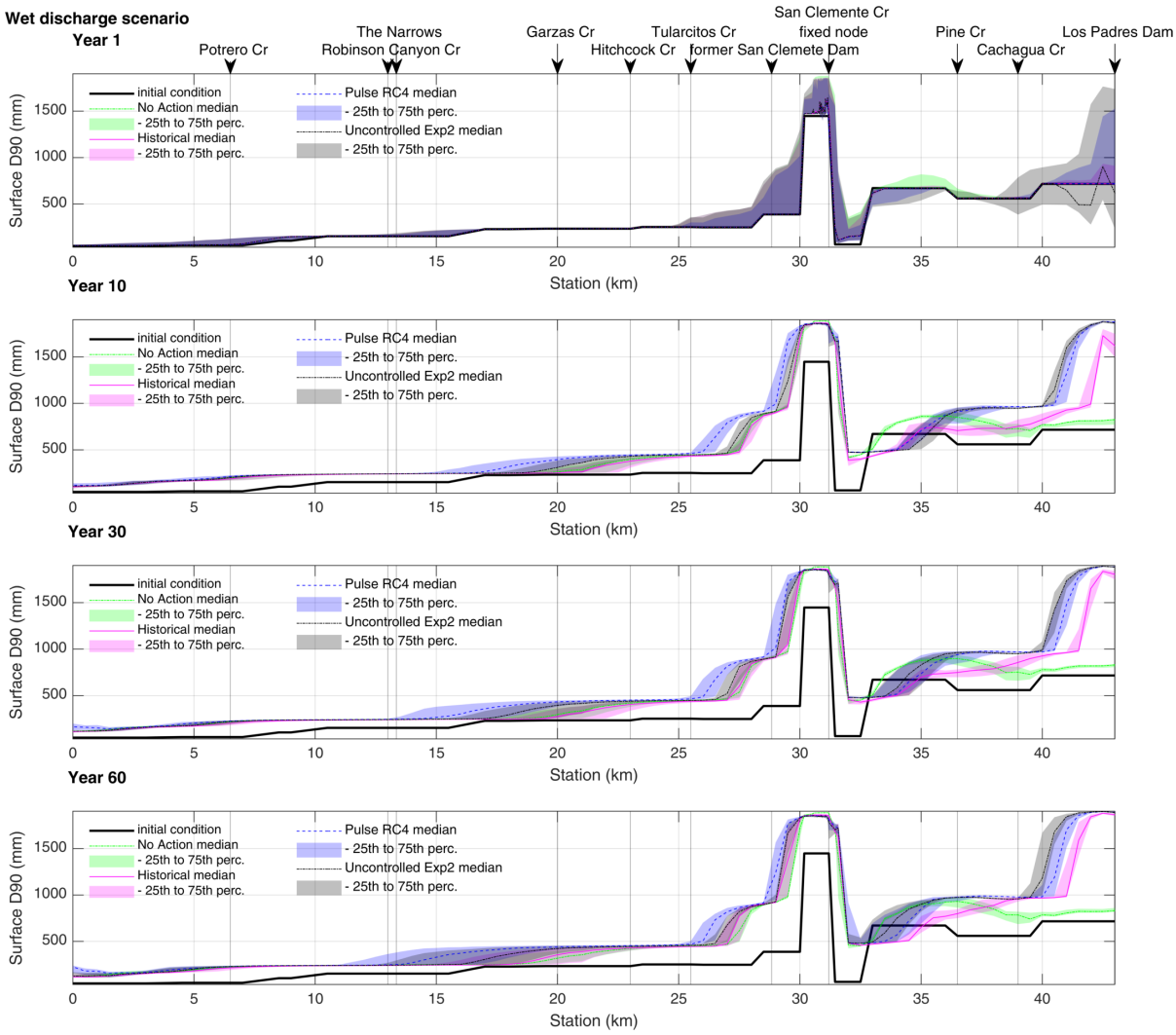

Figure 3.10: Comparison of projected change of the geometric mean grain size of the bed surface D_{90} for the wet hydrologic condition and the Historical, Pulse and Uncontrolled sediment supply simulations. Shaded regions capture the 25th-75th percentile responses across the 100 simulations for the wet condition. Results shown for simulation year 1, 10, 30 and 60.

The range of depositional depths between the 25th and 75th percentiles is characteristically large for year 1, decreases at most locations by year 10, and continues to decrease through years 30 and 60 from the Narrows to the Pacific Ocean (Figure 3.8). Reduction in the projected range of depositional depths through time from Los Padres Dam to the Pacific Ocean suggests that:

- The net effect of the 100 random wet hydrographs diminishes in time; and
- Projected bed elevations across the 100 random wet hydrographs evolve to a narrow set of response trajectories spatially, regardless of the supply simulation.

These two results imply a reasonable degree of confidence for the spatial and temporal trends of projected bed elevation change under the four different sediment supply simulations. However, the magnitudes of projected bed elevation change in particular are limited by (a) the basic method used to translate projected channel bed volume changes to bed elevations, (b) the 1-D BESMo model build, and (c) the available topographic data. We provide more discussion related to limitations (b) in Section 3.6.1.

There is one notable exception to the response generalizations made in the previous paragraphs. The evolution of projected bed elevations within the vicinity of the Tularcitos Creek confluence is indicated by ranges of elevation values between the 25th and 75th percentiles that are larger than the median values. This result suggests that projected average bed elevations along the mainstem Carmel River around Tularcitos Creek are sensitive to the sequence of future floods under the simulated wet conditions. Consideration of this result with projections for the evolution of the D_{90} grain size provides some insight for the coupled bed elevation-grain size response around the Tularcitos Creek confluence (Figure 3.8 and Figure 3.10). The magnitude of deposition at the former San Clemente Dam sets the average longitudinal bed slope along the mainstem Carmel River, which in turn leads into the Tularcitos Creek confluence reach. Larger magnitudes of deposition lead to larger average bed slopes, and hence higher bedload transport rates. Higher bedload transport rates drive the downstream advance of a relatively coarse D_{90} grain size response, which makes it as far as the Tularcitos Creek confluence (Figure 3.10). The downstream shape of the D_{90} grain size response indicates that the coarse fraction of the bed surface has a relatively large amount of

spatial variability in the vicinity of Tularcitos Creek, with projected spatial changes of several hundred millimetres over about 1.5 km of river length. However, variation in the downstream extent of the D_{90} grain size response for any given supply simulation upstream of Tularcitos Creek spans about 1 km or more of river length. The spatial domain of this D_{90} grain size variation correlates with the upstream zone of relatively large variations in the bed elevation projections. This implies that the range of bed elevation responses in the vicinity of Tularcitos Creek is conditioned by the magnitude of bedload deposition at the former San Clemente Dam during the first 10 projection years, coupled with the particular and associated downstream advance of coarse grain size fractions, which serves to limit future bed elevation adjustments as the simulations proceed beyond year 10. This highlights that field-based monitoring of bed elevation and bed surface texture response upstream of Tularcitos Creek may provide the data needed to make informed decisions regarding the likely trajectory of channel responses at this location.

3.5.1 Overview of bed elevation changes along the channel

Projected bedload sediment deposition magnitude differs by location and across the four sediment supply simulations. Deposition is greatest just downstream of Los Padres Dam of the three Los Padres supply simulations, ranging from 5-6 m with the Uncontrolled simulation projecting the most deposition and the Historical Supply simulation projecting the smallest amount (Figure 3.8). The projected magnitude of deposition just downstream of Los Padres Dam is plausible because topographic data local to the Dam suggests about 6 m of net bed elevation decline since the Dam was constructed in 1949 (Appendix B.11.2). By contrast, the No Action simulation projects 0.3-0.6 m of additional bed elevation decreases near the Dam over the 60-year model time period. It is thus expected that simulations which resume downstream bedload supply from areas upstream of Los Padres Dam (i.e. sediment stored in the reservoir or from the upstream contributing basin) would lead to recovery of local average channel bed elevations because steeper bed slopes are needed to facilitate transport of increased bedload supply.

The magnitude of deposition varies spatially, with an upper bound given by the Uncon-

trolled Supply simulation and a lower bound given with the No Action simulation, which even shows net bed erosion of up to 1.5 m. Projected deposition reaches between 1.5 and 2.4 m as the former San Clemente reservoir area is approached. This magnitude of deposition seems reasonable given that the former reservoir pool drove upstream sediment deposition, which led to significant average longitudinal bed slope reduction close to the former reservoir pool. The Carmel River Reroute and Dam Removal (CRRDR) project locked in the effect of the reservoir pool into the post-construction local channel profile (San Clemente Creek fixed node; Figure 3.2). As a result, steeper bed slopes leading into the former reservoir pool area are required in order to transport the increased upstream bedload supply, particularly for the three supply simulations which pass bedload sediment downstream of Los Padres Dam.

The CRRDR project also introduced segments of bed slope through the former San Clemente Creek arm of the San Clemente Dam reservoir pool which were considerably different from and larger than those bedslopes downstream of the former dam site. As a result, solutions of the BESMo model for the wet hydrologic conditions lead to deposition magnitudes between 2.1 and 3.7 m at the former San Clemente Dam site. This magnitude of projected deposition and the downstream advance of deposition beyond the former dam site acts to smooth out abrupt profile changes and facilitate bedload transport rates which converge to similar magnitudes across locations of profile change. As discussed above, this model result is relevant for the Tularcitos Creek confluence area because steepening of the bed profile downstream of the former San Clemente Dam leads to a range of possible average bed elevation responses in this area.

Downstream of Hitchcock Creek and as far downstream as beyond Garza Creek (station 18.3 km), all four supply simulations are projected to yield little bed elevation changes and fluctuate around the initial bed elevation. This suggests that this roughly 4.6 km of mainstem Carmel River is already adjusted to a bedload transport capacity (i.e. under 2017 profile and texture conditions) that can accommodate upstream supply increases across a majority of the grain size classes. This relatively high transport capacity lessens moving toward The Narrows at station 13.7 km. Approaching The Narrows, all four upstream supply simulations project roughly 1.5 m of deposition by year 10, and this magnitude of deposition continues through

year 60 of the simulations. The deposition response at The Narrows may be attributed to the lateral confinement of the channel, such that bed elevation is the primary mechanism to facilitate transport of increased bedload supply. Just downstream of The Narrows, the No Action simulation exhibits between 0 and 1 m of net deposition, whereas the three scenarios with higher sediment supply converge to an approximate net deposition magnitude of 1.2 m.

Moving farther downstream toward the mouth at the Pacific Ocean, the four supply simulations diverge slightly, but yield between 1.2 and 1.8 m of net deposition at year 60. Notably however, a majority of the projected deposition along the lowermost 11 km of the mainstem Carmel River occurs by year 10 of the simulations. Therefore, resuming bedload supply from contributing areas upstream of the former San Clemente Dam and Los Padres Dam coupled with relatively large floods early within the simulations drives rapid movement of bedload through the system to the lowermost mainstem reaches, resulting in deposition there. Under the average and dry hydrologic conditions, the downstream delivery of bedload supply to the lowermost mainstem Carmel River is significantly delayed compared to the wet conditions, with the overall depositional pattern present by simulation year 30 (as shown by figures in Appendix B.12).

3.5.2 Overview of surface grain size changes along the channel

Under the wet hydrologic conditions, all four sediment supply simulations project increases to the D_g and D_{90} grain sizes from Los Padres Dam to the Pacific Ocean by year 10 of the simulations (Figure 3.9 and Figure 3.10). Coarsening over time is due to high relative transport rates of the finer size classes within the supply and bed surface distributions. Within this overall coarsening trend, however, maintenance of fining of the bed surface is projected as a possibility. At the end of simulation year 1, some of the wet hydrographs for the Los Padres supply simulations result in no or little change in D_g and D_{90} conditions compared to the initial bed surface, except through the CRRDR project reach. Directly below the Los Padres dam, the Uncontrolled Supply scenario shows a potential fining of the bed reaching about 12 km downstream. This may be attributed to the relatively large supply of fine material from dam removal. By year 5 (not shown), bed surface texture conditions begin evolving to coarser

states. We observe a similar fining response for average and dry hydrologic conditions (figures provided in Appendix B.12). Persistence of the grain size fining responses ranges from 1 to 60 years, depending on location, and is modulated by the co-evolution of the longitudinal bed profile and bed surface texture. When the time scale of bed surface texture evolution occurs at rates comparable to bed profile adjustments, the bed texture can maintain a finer texture compared to conditions which drive the profile to adjust more rapidly. Under more rapid profile adjustment, texture change cannot keep pace and is subsequently reset by younger episodes of deposition and sediment sorting.

The lowermost 10.7 km of mainstem Carmel River follow the more rapid topographic profile evolution trajectory across all hydrologic conditions, and as a result end up generally more coarse than initial conditions. Moving upstream, texture conditions for the reach between Tularcitos and Las Garzas Creek typically trends to the initial texture states, with a tendency to smooth out spatial jumps in the initial bed texture configuration. At the former San Clemente Dam and downstream of Los Padres Dam, bed texture conditions evolve to significantly coarser conditions across all three hydrologic and sediment supply simulations. A coarser texture represents a coupled response with relatively large depths of sediment deposition at both locations. In other words, steeper bed slopes are generally maintained by coarser bed surfaces.

3.5.3 Comparison to MEI simulations

MEI (2002) conducted simulations to inform about effects of the San Clemente Dam removal and also reported early fining in response to the release of bedload sediment stored within the San Clemente reservoir pool, followed by recovery toward, and in some cases coarser than initial bed surface grain size conditions. In particular, MEI reported that early simulations periods characterized by relatively dry conditions show the strongest downstream fining response.

Figure 3.11 illustrates a comparison of longitudinal bed elevation profiles reported by: (a) *MEI* (2002) for the 1985-750C simulation, and (b) the present study for the No Action simulation at Los Padres Dam. The comparison is generally favourable for two specific reaches. First,

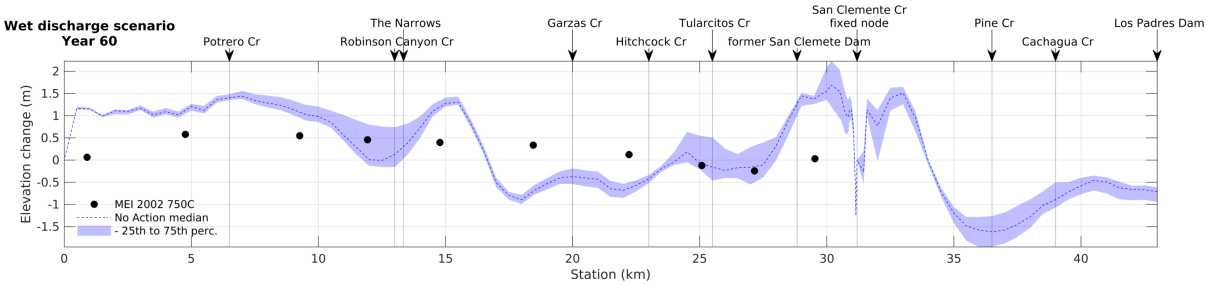

Figure 3.11: Comparison of projected bed elevation change simulated by BESMo and reported by *MEI* (2002) for the roughly equivalent condition of removing San Clemente Dam and no bedload bypass at Los Padres Dam. The *MEI* (2002) condition represents their 1985-750C simulation results (data from Table 7.8 therein), which are plotted at the mid-point within the study sub-reaches. The 1985-750C simulation represents a reasonable basis of comparison to the No Action simulation at Los Padres Dam under the wet hydrologic condition because both simulations have elevated rates of sediment supply to the mainstem Carmel River downstream of the former San Clemente Dam (see Appendix D.23 of *MEI*, 2002)

both studies suggest a tendency for little to no net bed elevation change within the vicinity of the Tularcitos Creek confluence. Second, both studies suggest a net depositional condition for the lowermost 15 km of the mainstem, extending roughly from the Narrows to the Highway 1 bridge. Compared to the HEC-6T results, BESMo generally projects more deposition along the lowermost 11 km of the mainstem. Depositional differences between the two projections along the lower mainstem range from 0.3 to 0.8 m, excluding conditions at the downstream boundary. Although there is general consistency between the models in the vicinity of the Tularcitos Creek confluence, the BESMo model projects up to a meter of bed elevation response variability between the 25th and 75th percentile values.

The projected profile consistency between the four different upstream supply simulations as well as that reported by *MEI* (2002) highlights that deposition should be anticipated and could range upwards of 2 m on average 60 years into the future. The timing of the depositional signal depends on the sequence and magnitude of floods (Figure 3.8). The variability projected by BESMo is due to model sensitivity related to the timing and sequencing of future floods, as well as the associated sorting of bed surface sediments which tends to reinforce the persistence of early bed slope responses. Flooding observed during the winter of 2017 along Paso Honda

Road (Monterey Herald, January 9, 2017) suggests a depositional trajectory may be evolving downstream of the Tularcitos Creek confluence given the relatively large magnitude of floods that occurred from January-February 2017 (*Harrison et al.*, 2018).

3.6 Discussion

In this section, we first discuss BESMo model limitations and how these might affect the simulation results. This is followed by an interpretation of the results in the Carmel River context. We then compare our results to other dam removal projects and a give a reflection on the use of BESMo for this task.

3.6.1 Limitations

Evaluation of BESMo results must be understood through model construction limitations regarding the fixed channel geometry, the bed elevation change calculation, and the accuracy of input data for the model.

Fixed channel geometry BESMo does not account for the partitioning of streamflows between the main channel and adjacent floodplain areas. This limitation was addressed by using field observations of discharge and average flow velocity to capture the effect that increasing cross-sectional flow area has on the structure of flow velocity within the main channel. This is important because flow velocity is a key parameter used to estimate the rate of bedload transport. BESMo also does not account for lateral channel migration, nor widening of the channel at any model node. Both limitations are moderated to some degree by the common occurrence of channel bank protection as well as bedrock along the mainstem Carmel River from Carmel Valley Village to the mouth at the Pacific Ocean. The primary challenge that this introduces related to projection of channel conditions is that a lack of channel migration or widening means that local sources of sediment are not represented in the model. This introduces unknown short-term effects into model projections roughly at a 5-year time scale. Since effects will be local in spatial scale, likely at the level of one to two model nodes, we do not expect local widening effects to change the larger-scale spatial trends of the results reported here.

Additionally, due to the 1-D construction of BESMo, model results do not provide reliable projections of how flooding conditions may change in association with any particular set of results. Flooding could be evaluated with model runs within HEC-RAS using projected bed elevation and surface texture conditions generated by BESMo.

The enhanced deposition projected by BESMo in comparison with the results presented by *MEI* (2002) (for the Narrows to Highway 1) might also be attributed to the 1-D model construction, specifically as the model does not directly represent overbank flows. The 1-D model build of BESMo means that cross-sectionally averaged downstream velocities at sediment transporting flows are larger compared to *MEI* (2002). A higher average velocity would lead to comparatively lower bed elevations due to increased bedload transport capacities. However, it appears the BESMo No Action simulation evolves to bed surface grain sizes which may be several factors larger than those for the MEI 1985-750C simulations. Larger grain sizes will lead to comparatively lower average velocities due to higher particle drag, which in general will promote deposition of the larger grain sizes in transport. As a result, the larger magnitude of projected deposition simulated by BESMo may be due to at least two contributing and coupled factors related to the 1-D model build, but other factors related to differences in model builds may also be important. Nevertheless, in the context of the lower mainstem Carmel River and the present study, we suggest that BESMo may over-project the magnitude of deposition by approximately 0.3 m.

With respect to the present discussion, it is pertinent to ask the following question: How does the BESMo model build introduce uncertainty with respect to drawing conclusions regarding the nature of future channel adjustments under the four different sediment supply simulations? This question is particularly relevant within the context of understanding the BESMo results with respect to considerations specific to the Carmel River watershed.

Elevation change calculations The fixed channel width in BESMo further means that any deposition (or erosion from the channel bed) of sediment leads to a linear increase (or decrease) in channel elevation at each modelling node. Because our focus is to project the most probable river profile response over the simulation period given the model configuration and set-up

and input data relative to a specific response for any particular year, this simplification has only a small impact on the simulated sediment budget. It does, however, lead to unrealistic increases or decreases in channel elevations if the stored sediment volume changes. Therefore, we focus on interpreting the projected absolute channel storage changes at each model node, and secondarily discuss how projected storage changes may translate to actual changes of channel bed elevation. We approximate how storage may translate to elevation changes at each model node by proportionally distributing storage change projections based on the average reach-based cross-sectional shape (see Appendix B.8) for the case of deposition. For the case of bed erosion, we attribute the volume change equally across the average reach-based cross-sectional shape.

Accuracy of input data Last, it is important to note that all results presented and discussed here are a reflection of the Carmel River BESMo build for this project, along with the model configuration, setup and input data. There are many uncertainties with regard to actual field conditions and how they are accounted for with the input data. First, channel profile data between the former San Clemente Dam and Los Padres Dam is based on the USGS National Elevation Dataset (1/9 arc-second) and, as a result, might not resolve the channel bottom elevation. Second, the present model has been developed with the best available grain size data. However, bed surface grain size census data is spatially limited with respect to the model domain, and subsurface data is largely lacking. Therefore, we recommend model results be interpreted with respect to general spatial trends across the simulations, as opposed to results at a particular location and point in time. Third, sediment transport rating curves were developed using data largely collected in the 1980s and do not reflect recent shifts in sediment supply.

With these limitations in mind, results from modelling of the four different sediment supply simulations show clear spatial trends. Temporal trends, on the other hand, are directly related to the timing and magnitude of larger floods within the 60-year simulation time period. Consistency of spatial trends between the four supply simulations suggests that results presented here can be used to plan for expected outcomes related to sediment management

actions at Los Padres Dam.

3.6.2 Placing simulation results within the Carmel River context

Prior to 2015 and the removal of the San Clemente Dam, channel bed elevation and bed surface grain size conditions along the mainstem Carmel River were governed by the combined effects of: (1) constructing the San Clemente Dam (1921) and Los Padres Dam (1949), which led to a significant reduction in the supply of bedload sediment from the upper watershed to the downstream mainstem Carmel River; (2) in-stream gravel mining along the middle mainstem in the 1950s and 60s, which amplified the effects from dam construction because bedload available for downstream transport was further reduced; and (3) channel bank armouring along many reaches of the mainstream Carmel River along the lowermost 24.5 km of river, which decreased bedload supply available from lateral channel migration (*Paola et al.*, 1999) or cross-section enlargement as a result of bank erosion.

The reduction to bedload supply since 1921 has led to widespread lowering of river bed elevations to varying magnitudes from Los Padres Dam to the Pacific Ocean as well as a general coarsening of the bed surface over the same reach (*Kondolf*, 1982; *GMA*, 2008). Given these past actions in the watershed, we expect that any resumption of bedload supply from the upper watershed will drive increasing average bed elevations over time, and possibly a reduction in the bed surface coarseness, depending on the grain size distribution of the supply and the riparian vegetation conditions (*Kondolf and Curry*, 1986). However, river flows have changed since river flows were first known to have been diverted to support local agriculture in 1771. This (*Gudde*, 2010) means that the response of the Carmel River mainstem to actions taken at Los Padres Dam today or in the near future will not necessarily occur in a way that drives river conditions to pre-existing states. The mainstem river is in some ways irrevocably changed, and therefore the present simulations can help to build understanding of how the mainstem Carmel River may respond to bedload-focused actions at Los Padres.

The three supply simulations which pass bedload to the mainstem Carmel River downstream of Los Padres Dam (Historical, Pulse, and Uncontrolled supply) show a consistent bed elevation response from Hitchcock Creek to the mouth at the Pacific Ocean. This find-

ing mostly holds across dry, average and wet hydrologic conditions and at year 60 there is clear trend of between 1.2 to 2 m of net sediment deposition along the lowermost 9 km of the mainstem, with a peak in net deposition of 1.5 m just upstream of The Narrows. While this finding fits with the expectation of bed aggradation following the long period of lower sediment supply, it represents an unquantified risk of increased flooding. We recommend that future studies should carefully evaluate this risk using results reported herein. Interestingly, a net depositional response in these locations also brings potential benefit to channel morphology and natural riverine function because rising bed elevations will more frequently activate side and alternate channels and will lead to natural construction of in-channel habitat elements and features. The potential benefits will be locally and randomly accentuated as rising bed elevations will also lead to a temporal spike in wood contributions from channel banks due to increased mortality with a rising riparian water table. Along developed river corridors it is common for potential negative impacts to be mirrored by potential positive impacts. Going forward this counterpoint should be carefully evaluated with respect to local and feasible mitigating actions that can minimize or otherwise remove the expected risk. Similar considerations should be given to the mainstem Carmel River downstream of the Tularcitos Creek confluence through Carmel Valley Village, where projected conditions are particularly sensitive to the timing and sequencing of future large floods.

All four sediment supply simulations suggest further evolution of conditions through the Carmel River Reroute and Dam Removal project reach. The primary projected response is a widespread increase in average bed elevations. Bed surface grain sizes are also projected to show a strong coarsening trend. The three sediment supply simulations which pass sediment downstream of Los Padres Dam are projected to drive significant local bed elevation gains, ranging from near to 6 m at the Dam to about a meter downstream of the Cachagua Creek confluence. Deposition of this magnitude will trigger a complete resetting of the river corridor. Corridor resetting at this level will also likely result in the delivery of significant quantities of large wood to the Carmel River Reroute and Dam Removal project reach, and possibly beyond. Wood delivery to the Dam removal project reach will likely benefit to physical habitat as wood can anchor development of diverse channel patterns and local morphologic conditions, as

well as instream and overbank habitat elements and features. Potential benefits are likely to be proportional to the magnitude of sediment supply at Los Padres Dam. Risks to further downstream reaches are anticipated to be moderated by an intact riparian corridor between the former San Clemente Dam site and the Tularcitos Creek confluence.

3.6.3 Comparison to other dam removal projects

To get a better idea about the relative geomorphic impact of the post-dam removal sediment supply, *Major et al.* (2017) suggest to use V^*, a ratio between the volume of stored sediment to the background sediment load. To gauge the impact of geomorphic change in the first year after the dam removal, *Grant and Lewis* (2015) suggest to use E^*, which represents a ratio between the volume eroded in the first year after removal and the background sediment flux. To use these parameters in context of our simulation results for the Carmel River, it is important to consider the relative impact of the Marbel Cone fire to a potential sediment release by dam removal, as it delivered nearly half of the stored sediment in the reservoir. If sediment pulses the size of the Marbel Cone fire are used as examples of naturally occurring events, then the removal of LPD would cause a sediment pulse at maximum just twice the size of natural events.

For the Los Padres reservoir, V^* is 79.1 if the the Marbel Cone fire event is included in the natural sediment transport conditions, and 167.7 if it is discounted. *Major et al.* (2017) describe dam removals where $V^* > 20$ as having a high geomorphic impact on downstream reaches, meaning that downstream channel adjustment to the event might take multiple years, potentially decades. Following this statement, a management option that restricts the sediment volume released by the dam removal to a maximum of 392,200 m^3 would cause moderate geomorphic response, meaning that the channel morphology would potentially recover within a few years. In light of the fact that the Marbel Cone fire event alone of 727,800 m^3 exceeds this magnitude, the release of at least 50% of the currently stored reservoir sediment might cause a high geomorphic impact on Carmel River, but it would be within the magnitude of a naturally occurring sediment supply events.

The value of E^* is shown to be correlated well with the transport distance of coarse sed-

Table 3.8: Values of E^*, the ratio between sediment volume eroded in the first year after the management action begins with the first flood event in each time series, calculated from median sediment supply values after 1 simulation year for bedload material.

Sediment supply scenario		E^* wet	average	dry
Pulse Supply	RC 1	2.71	0.28	0.14
	RC 2	3.87	0.4	0.2
	RC 3	2.17	0.2	0.09
	RC 4	6.52	0.6	0.28
	RC 5	8.78	0.7	0.32
	RC 6	12.54	1	0.46
Uncontrolled Supply	Exp 1	12.2	11.45	8.43
	Exp 2	18.85	17.66	13.06
	Exp 3	20.25	18.97	14.03

iment after the dam removal (*Major et al.*, 2017). We present this value for the Pulse Supply and Uncontrolled Supply scenarios in Table 3.8. Mechanically, the main difference between the Pulse Supply and the Uncontrolled Supply scenarios is the dependence of sediment feed rates on the flow record. In the Pulse Supply management option, sediment is only released in flow events larger than 3 m^3s^{-1}, which leads to low supply in the first year for the average and dry hydologic scenarios. On the other hand, the Uncontrolled Supply scenario shows higher values of E^* even in the average and dry hydrologic scenarios, as the sediment feed rate is dependent on the cumulative discharge through the reservoir. These calculations show that the sediment release from LPD would have the largest impact on downstream channel geomorphology in the Uncontrolled Supply scenarios, matching the spatial trends shown for year 1 in Figures 3.8 to 3.10. However, Figure 3.10 shows that the Pulse Supply scenario RC 4 has a farther-reaching impact on the surface grain size D_{90} than the Uncontrolled Supply scenario Exp 2, indicating that while E^* might be a good indicator for geomorphic effects of a dam removal in the short term, other effects than the magnitude of introduced sediment will dominate the geomorphic response on longer timescales.

The values of V^* and E^* help to place the potential LPD sediment release scenarios within

the context of estimates reported by other studies and summarized by *Major et al.* (2017). Both the initial sediment reservoir volume and the ratio V^* for LPD are comparable to Condit dam. The Uncontrolled Supply simulations all show at least 10 times lower values of E^* for the wet hydrographs than the data reported for Condit dam, attributable to its much finer and more easily erodible sediment *Wilcock* (2001). Values for both E^* and V^* are comparable to the Glines Canyon removal, which was about 10 times larger in initial sediment volume (16 Mio m^3) and was removed in several stages *East et al.* (2015).

An interesting observation from our simulations is that the re-establishment of historical supply conditions without additional release of reservoir sediments already causes an aggradational response and a significant change in surface grain sizes of the mainstem Carmel River. It seems that the magnitude of the short-term release of reservoir sediments has a comparably small effect in comparison to the general addition of fine sediments from the upper Carmel River and its tributaries. Over the 60 year timeframe, the style of dam removal might be not be geomorphically significant. The establishment of connectivity between the upstream reaches and the main stem is what governs the system response between 10-60 years after the Los Padres dam is removed. This echoes the previously recognized importance of the upstream areas for the supply of fine sediment on the channel morphology of the Carmel River (*Kondolf*, 1982).

3.6.4 Reflection on the use of BESMo

Despite the limitations discussed earlier, BESMo is an appropriate tool for the task of estimating the geomorphic adjustment to the presented management options on LPD, and offers significant advantages over prior modelling work. Previous modelling efforts generally underestimated the time it took for significant geomorphic change to occur after dam removals (*Foley et al.*, 2017). As BESMo is based on similar transport relations as these models, we might also expect to underestimate the fluvial response time until geomorphic change occurs. Yet, as our focus is the long term adjustment of Carmel River and the relative impact of the four management alternatives, we see this as a minor issue. Further, the employment of stochastically based hydrographs in BESMo is an important improvement over other models in regards of

predicting response times and magnitudes, as we explicitly include the effects of early large floods in the wet hydrograph scenarios.

In addition to methodological limitations, a significant factor of uncertainty is due to the limited availability of data with which to initialize the model. However, all models would include this limitation. BESMo was developed to explicitly cope with the variation of parameters, which in this study was the uncertainty of future hydrology and the sediment supply variations from the dam management options. In our view we could further improve the presented results by varying more input parameters. This would have provided better insight into the effect of data limitations, and offered a way to give specific advice to planners about which parameters should be collected in the future to improve the understanding of dam removal effects on the Carmel River.

3.7 Concluding remarks

This study was conducted to gain insight into potential effects of different management actions taken on the Los Padres Dam and reservoir. It is yet to be decided if the dam will be removed or if other actions on the dam and reservoir are more feasible. For our purposes, four scenarios of sediment management were specified as: (1) 'No Action' would be taken, which would lead to continued accumulation of sediment in the reservoir and no sediment supply immediately downstream of LPD; (2) 'Historical supply' would be re-established, routing all material entering the reservoir downstream of LPD, preventing further accumulation in the reservoir; (3) 'Pulse supply' represents a controlled removal of LPD, flushing reservoir sediment downstream through a sluice gate which would be opened under certain flow conditions; and (4) 'Uncontrolled supply' represents the full removal of LPD without any measures undertaken to prevent rapid erosion of the reservoir deposits.

The Carmel River watershed offers a complex setting for a dam removal in multiple aspects: The climate is dry, but floods constituting large sediment transport events occur regularly. Additionally, the river was altered significantly first by the construction of two dams in the 1920s and 1940s, and the removal of San Clemente Dam in 2015. The ensuing low sediment availability and related decrease in fine material was further pronounced by efforts to

stabilize the banks in the lower river. Furthermore, fires historically supplied large volumes of sediment into the channel, with the exceptional Marble Cone fire in 1977 constituting about 50% of all material stored behind LPD. This means that an uncontrolled release of all material out of the reservoir would only constitute twice the volume of that natural event.

In adapting BESMo to the Los Padres Dam and Reservoir Alternatives Study, considerable effort was undertaken to build defensible model inputs. There is little available elevation and grain size data for the watershed upstream of the former San Clemente Dam in particular. While the sediment supply conditions were developed based on the given management options, the uncertainty in the occurrence of significant floods shortly after a potential dam removal necessitated an approach of creating synthetic hydrographs based on historical discharge records. This allowed us to explicitly test wet conditions with early floods, which have shown to be associated with situations in which the sediment supply scenarios diverge most significantly. In the longer time frame of 60 years, the supply scenarios converge to the conditions of the Historical Supply scenario, which most closely resembles natural conditions. However, the response of channel geomorphology to actions taken at the dam site can have further complex effects that are hard to predict, especially on a long time-scale (*Foley et al.*, 2017).

Our findings show that the removal of the dam can move the Carmel River sediment dynamics closer to natural conditions, primarily due to the re-establishment of connectivity of the upper watershed to the main stem, causing a fining of the channel bed surface. In comparison to the use of BESMo to explore the effect of event frequency and magnitude on channel morphology in the previous chapter, we found that the frequent pulses in the Pulse Supply alternative are more effective in keeping the surface grain size distribution relatively fine for more than a decade. Given enough time for armouring to occur, for example after an uncontrolled dam removal was reworked, the channel surface coarsens within a few years. These findings are significant for the decision of which actions should be taken on LPD, as both patterns of channel aggradation/degradation and bed surface fining are important for both flood mitigation and the preservation of fish habitat.

Chapter 4

Identifying surface grain size distributions from images using computer vision and machine learning methods

During the previous chapters, the modelling efforts with BESMo demonstrated the need for improved input data of surface grain size distributions. Higher temporal resolution of surface grain size data would have allowed for a more detailed model calibration using flume experiments in Chapter 2. A better spatial coverage of initial surface grain size distributions for the Carmel River would have reduced the uncertainty in the modelling of the dam removal alternatives in Chapter 3. This chapter presents newly developed methods that can overcome these data limitations in future work. The chronologic nature of how this work was executed led to these methods being presented at the end of the thesis.

4.1 Summary

Insufficient temporal and spatial coverage of grain size distributions in field data limits studies of channel response to episodic events in estimating grain size distributions of sediment

supply, channel surface adjustment, and sediment mobility. This lack in data might be overcome by collecting images of channel surfaces and automatically classifying grain sizes with computer vision methods. Colour based semi-automatic methods to identify grain size distributions from images are currently employed in the flume lab at UBC, but have shown to be unreliable due to paint chipping off stones and irregular lighting conditions. Furthermore, changing conditions between experiments (such as used camera type) make it necessary to recalibrate colour thresholds for grain size class identification. This chapter presents three different methods to identify grain size distributions from images of coloured grains. Firstly, an algorithm to identify individual stones is developed (referred to as StoneID), which can be used to study spatial stone distributions in the bed and to calculate GSDs of images. Secondly, the outputs of this algorithm are used to train a neural network to determine GSD (referred to as DistID). Thirdly, individual stone locations from StoneID are used to explore the performance of the U-Net machine learning method to find stone locations (referred to as U-Net+StoneID).

These methods were developed on two datasets of images showing grains coloured by size class, with the objective of reducing the manual work needed for the analysis of both the locations of coarse grains and grain size distributions. Machine learning methods are less sensitive to variations in colouring of stones and lighting conditions when trained with datasets that reflect this range in conditions and that are manually validated. Even though the used datasets were not fully validated manually, the employed methods show good results in matching the available data. Especially the larger grain size classes such as D_{90} were estimated within 2 mm by the DistID and the StoneID methods. The U-Net model was successfully used to classify stone areas within the accuracy of the training data, which shows potential in automatically identifying individual stones if combined with the StoneID method. More manually validated training data is needed if these methods are to be applied to more datasets.

4.2 Introduction

The bed surface grain size distribution (GSD) in rivers is the most important factor used to estimate sediment mobility (*Church and Ferguson*, 2015). The distribution of grain sizes also

provides information about channel structuring (*Church et al.*, 1998; *Zimmermann et al.*, 2010) and sediment supply from upstream of the study reach, hillslopes, and tributaries (*Rice and Church*, 1998), and is therefore an important factor in assessing aquatic habitat and channel morphology (*Kondolf and Wolman*, 1993). Both numerical and analytical sediment transport models simplify GSDs with statistical parameters such as the median grain size (D_{50}), or the 90th percentile (D_{90}). These parameters have been shown to be useful tools for describing fluvial processes such as the onset of meandering (*MacKenzie and Eaton*, 2017) or the development of channel bed armouring which reduces particle entrainment and transport (*Hassan et al.*, 2006b).

A popular method to collect GSDs in the field was suggested by *Wolman* (1954), which includes a grid-based sampling of individual stones by hand. To obtain a statistically satisfactory sample, approximately 400 stones must be individually measured. Detailed information on fine grain sizes (< 8 mm) is not possible to obtain with this approach (*Rice and Church*, 1996, 1998). A similar method of grid-bound sampling can be employed using images of channel bed surfaces. However, if stone sizes are determined from visual measurements, only the visible surface axis can be estimated, which leads to error as stones may be partly obscured due to imbrication (*Church et al.*, 1987). *Sthly et al.* (2017) used the semi-automatic software BASEGrain (*Detert and Weitbrecht*, 2013) to measure the stone b-axis from images and compare them to manual measurements. They report a ratio between the manual b-axis length to the image-based b-axis length that is comparable to the ratio between the manual b-axis length and the sieve size. This means that both methods might yield similar results, but both have different systematic errors: the sieving-method measures a combination of b and c-axis, while the visual method does not capture the stone surface completely. It is likely that these systematic errors vary with particle shape.

Another way of estimating grain size parameters in the field is by using surface roughness derived from terrestrial laser scanning (*Heritage and Milan*, 2009). Recently, advances were made in deriving grain size parameters from images taken with UAVs (Unmanned Aerial Vehicles) (*Carrivick and Smith*, 2018; *Detert et al.*, 2018; *Woodget et al.*, 2018).

In a laboratory setting, stones can be coloured by their respective size fraction (termed 'Bed

Of Many Colours', BOMC), which permits the inference of a sieve-measured stone size with the visual occurrence of a stone. A BOMC allows for the visual identification of the flume bed surface composition, for example by converting images to a visual point count (*Wilcock and McArdell*, 1993).

While these field and flume methods to acquire grain size distributions are reliable, the effort required to collect statistically robust samples (or to colour all grains in an experiments) is great, especially when sediment is coarser than sand or fine gravel (*Church and Kellerhals*, 1978). The analysis of experimental flume results and numerical modelling in Chapter 2 shows that the response of a fluvial channel to sediment supply is highly dependent on the history of surface grain size, and therefore many successive measurements are needed. Furthermore, the case study presented in Chapter 3 demonstrates that a lack of grain size data is a major source of uncertainty for predicting the response of rivers to changes in sediment supply. It is therefore of great importance to develop methods which can be used to collect statistically robust samples in both field and lab settings to accurately characterise bed surface sediment texture. Furthermore, in a laboratory setting it is important that these methods are rapid and non-intrusive, so that grain sizes can be reliably measured during an experiment.

There are a number of studies with the objective to automate grain size detection from images, following two main approaches: (1) use image segmentation to find and measure individual stones; or (2) extract statistical image properties and find correlations to respective GSDs. *Graham et al.* (2005) developed an image segmentation based photo-sieving method for automated stone detection and grain size estimates based on greyscale images. The method then segments individual stones by enhancing stone interstices and extracts stone surfaces with a watershed-algorithm. The b-axis of stones are then measured by automatically fitting stone areas with ellipses. A similar approach is used in the free software BASEGrain, where grains are separated by two automatically determined thresholds in greyscale images and then measured geometrically (*Detert and Weitbrecht*, 2013). *Chung and Chang* (2013) followed the same approach, but use machine learning to find appropriate greyscale-thresholds. The bias of computer vision based image segmentation methods and a general discussion of limitations of automated grain size detection is given by *Graham et al.* (2010). An example for the second

class of methods based on statistical image properties is the software Cobblecam developed by *Warrick et al.* (2009). Their approach uses correlations between spatial scales of image contrast to known GSDs, and is stated to be less sensitive to lighting conditions than methods that segment and measure individual stones. *Buscombe* (2013) suggests that linking these kinds of image statistics to GSDs can overcome some limitations of photo-sieving methods. When applied to coloured sediments, all mentioned greyscale-based approaches are problematic, as the contrast between dark shaded areas in grain interstices, and bright areas on top of grains is weak.

Convolutional Neural Networks (CNNs) are a class of machine learning methods that can be a powerful tool for computer vision, especially for image classification (*Witten et al.*, 2016). While classical computer vision algorithms rely on pre-defined filters to extract features of images, CNNs 'learn' filters by matching input images to a classified output. The network of neurons is flexible enough to by itself learn the importance of image properties such as spatial scales of image contrast as used in the autocorrelation method mentioned earlier.

In this study, different machine learning algorithms are trained to detect grain size distributions from BOMC images that were collected during experiments at the Mountain Channel Hydraulic Experimental Laboratory at the University of British Columbia. Data from two experiments were used: (1) Yinlue Wang's experiment (referred to as YW) was designed to study the development of transverse ribs under different constant discharges; (2) Alex Mitchell's experiment (referred to as AM) studied sediment transport conditions and morphology changes under symmetrical hydrographs.

In this chapter three methods for image based detection of grain size data are presented and evaluated: Firstly, an algorithm to identify individual stones is developed (hereafter referred to as StoneID), which can be used to study spatial stone distributions in the bed and to calculate GSDs of images. Secondly, the outputs of this algorithm are used to train a neural network to determine GSD (hereafter referred to as DistID). Thirdly, individual stone locations from StoneID are used to explore the performance of the U-Net machine learning method to find stone locations (hereafter referred to as U-Net+StoneID). These methods were developed with a large collection of bed surface images from flume experiments in combination with

manually acquired grain size distributions. The three approaches complement each other: StoneID is used to define both GSDs and individual stone locations, which can then be used to generate data with which the machine learning methods can be trained reliably.

4.3 Methods

An overview of the methods used in this chapter is given in Table 4.1. While the fully manual grid-based stone count was used for validation, the other approaches require different degrees of manual adjustment when applied to new datasets.

4.3.1 Bed surface datasets

The StoneID method was developed on nine BOMC images, each covering a 5 m long and 0.5 m wide area of a flume. GSDs for the images were sampled manually from 100 points

Table 4.1: Overview of the grain detection methods used in this chapter.

Method	Description	Required manual work per dataset
Grid-based stone count	Stones are counted by colour along a spatial grid and an area-based grain size frequency is derived.	Manual sampling of at least 100 locations on a regular grid.
StoneID	Algorithm to identify individual stone locations and sizes from colour thresholded images.	Definition of colour thresholds, min. and max. expected diameters and stone areas.
DistID	Machine learning method to match GSDs to images.	None after training. Retraining needed if applied to images that are not similar to the training dataset.
U-Net	Machine learning method to extract coloured stone areas from images.	Same as DistID.
U-Net+StoneID	Use of StoneID on the stone areas detected with U-Net.	Same as DistID. Additionally min. and max. expected diameters and stone areas.

with a grid-based colour count. The dataset (referred to as YW) was collected by Yinlue Wang. To develop DistID, a dataset of 1522 images was used. These images were acquired during eight flume experiments conducted by Alex Mitchell (dataset referred to as AM). Each image shows a 320 mm by 320 mm section along the centre of a 1 m wide and 12 m long flume. The images were either 1 m apart covering 8 m of the flume length (448 images), or six images were taken adjacent to each other covering a 2 m central section of the flume length (1074 images). The grain size mixtures used for these experiments are coloured by sieved grain size class in half-phi intervals.

4.3.2 Identifying individual grains: StoneID

Due to the colouring of the stones, an estimate of the surface coverage of each grain size class can be based on the digital colour values in the images. As each stone does not display uniform colouring, this method requires the definition of pixel value ranges for each grain colour by which the image can be classified. Colour values are typically stored as RGB values, splitting the data into bands of red (R), green (G), and blue (B) colour information. While RGB represents different colours (e.g. yellow) as combinations of these three individual channels, testing showed that the HSV representation showed better results for all colours except black. This is due to the clearer segmentation of colours in HSV, where the colour is represented as hue (H), the intensity of the colour as saturation (S), and the light-dark shading as value (V). The colour, mean size, and HSV threshold values for each class is listed in Table 4.2

While the colour-based mapping of each pixel in the image to a grain size class might be sufficient to get area estimates for each size class, errors are introduced through both colour chipping and colour variations e.g. from reflections. Further, an area estimate based on pixel counts is not sufficient to identify stone locations. To overcome these limitations, additional parameters are used to extract individual stone locations in images. The method was implemented in MATLAB. The algorithm iterates through each size class, starting with the largest size class. The approach is similar to the one described by *Graham et al.* (2005), but seperates the stone identification by colour class. A flowchart of the method is given with Figure 4.1.

While finding locations of individual stones with StoneID works automatically for a set

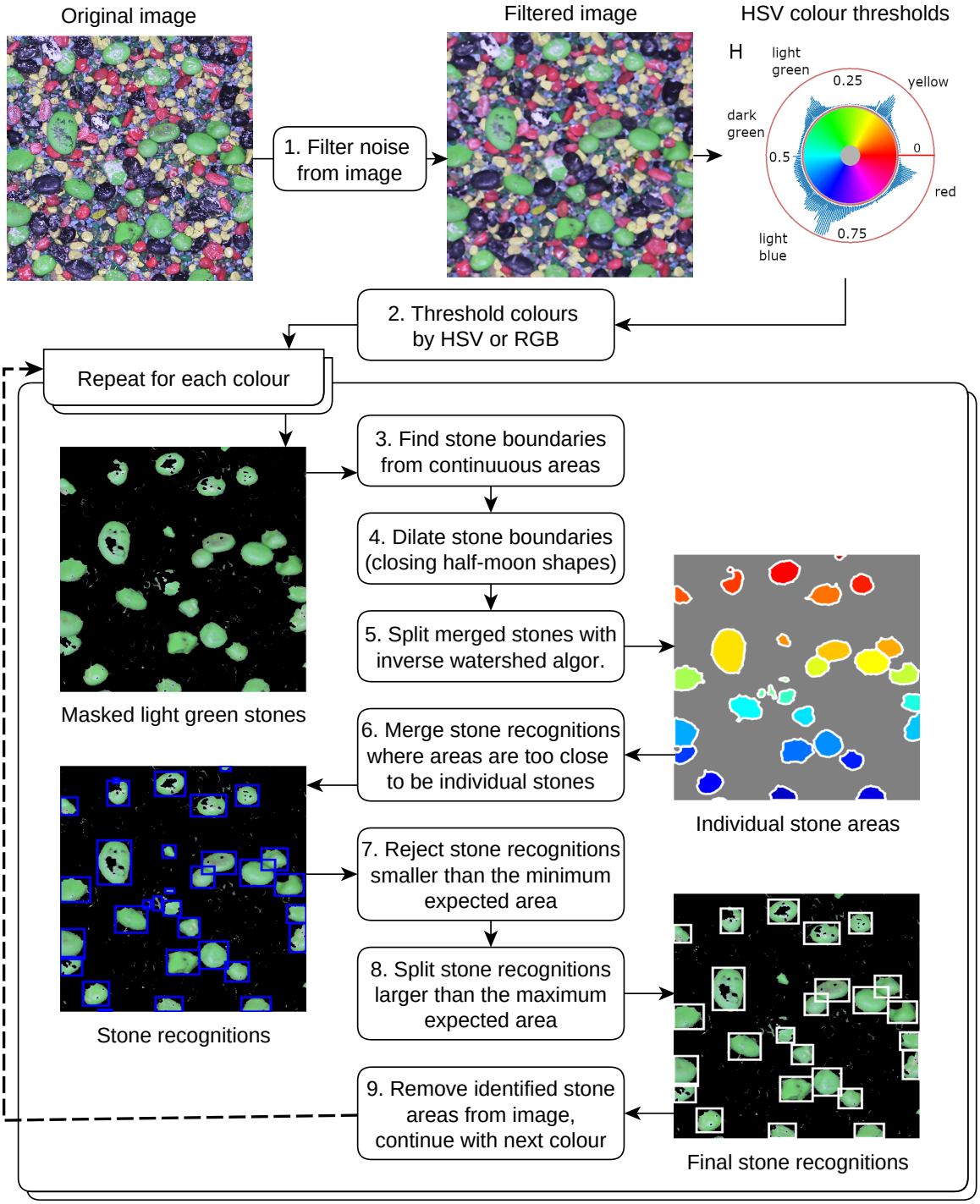

Figure 4.1: Identification of individual stones from colour thresholded images with StoneID. After the image data is prepared in steps 1 and 2, steps 3 to 9 are repeated for each colour class. The example image is from the AM dataset and the steps are illustrated with results for the light green size class.

Table 4.2: Overview of colour thresholds per size class in the experiments, some developed from HSV data, some from RGB data. Each colour threshold had to be reconfigured for each set of experiments due to changes in lighting and grain size classes. AM images do not contain white stones.

Colour	Mean size (mm)	HSV values Hue	Saturation	Value	Size thresholds min Area (mm^2)	max Area (mm^2)	min Diam. (mm)
light blue AM	4.8	0.59-0.65	0.27-1.00	0.00-1.00	8	100	1
light blue YW	4.8	0.60-0.74	0.00-1.00	0.00-1.00	8	100	1
dark green AM	6.75	0.47-0.57	0.25-1.00	0.00-0.65	15	200	2
dark green YW	6.75	0.31-0.47	0.00-1.00	0.00-1.00	15	200	2
yellow AM	9.6	0.11-0.19	0.00-1.00	0.00-1.00	22	350	3
yellow YW	9.6	0.09-0.16	0.32-1.00	0.58-1.00	22	350	3
red AM	13.6	0.90-1.00	0.16-1.00	0.00-1.00	100	1100	8
red YW	13.6	0.98-0.02	0.28-1.00	0.49-1.00	100	1100	8
light green AM	27	0.24-0.47	0.00-1.00	0.00-1.00	300	2100	15
light green YW	27	0.18-0.31	0.00-1.00	0.46-1.00	300	2100	15
white YW	38.5	0.00-1.00	0.00-0.30	0.77-1.00	600	4000	35
		RGB values Red	Green	Blue			
black (wet) YW	19	0-57	0-43	0-122	160	1600	10
black (dry) YW	19	0-115	0-104	72-164	160	1600	10
black (all) AM	19	0-72	0-73	0-156	160	1600	10

of images, the colour value parameters have to be reconfigured for new lighting conditions or changed camera properties, and new thresholds have to be found when new grain size classes are introduced. Besides the identification of individual stones, this method permits an

estimation of the GSD of an image based on the surface areas of each stone class.

4.3.3 Matching GSDs to colour images: DistID

A Convolutional Neural Network (CNN) is a machine learning type which uses convolutional filters, computational operations iterating over an image. The input image undergoes many convolutional filter layers with a successive reduction in the filter extent, while the number of filter layers increases. The output of the convolutional part of the network is fed into a 'fully connected' layer of neurons, which undergoes further reduction until the specified output shape is reached (e.g. six grain size classes). The layers are in sequence connected by neurons, which have an input, an output and a weight which can be 'trained'. This training adjusts the weights of millions of neurons iteratively until the network 'learns' to match the image input to the output (in this case the GSD).

The DistID model was developed in python with the machine learning library Keras. Both the ResNet50 (*He et al.*, 2016) and the VGG19 (*Simonyan and Zisserman*, 2014) architectures were used, as these are reported to perform well in image classification tasks, for example in the 'ImageNet' challenge, a benchmark dataset for visual recognition (*Witten et al.*, 2016). ResNet50 features more weights than VGG19, but is trained more quickly due to a 'shortcut' connection that skips individually training multiple layers. Both the ResNet50 and VGG19 were initialized with weights that were trained for the ImageNet challenge. Even though the pre-trained weights were developed for the task of identifying 1000 different objects in images, the weights are expected to represent generally usable filters such as edge detectors. Testing confirmed that using a pre-trained model yields a better training accuracy and a lower mean squared error than a random model initialization (see Table 4.3). While propagating from an image input to a classified output, the layers of the neural network represent a decreasing amount of image-locational information (by systematically sub-sampling the layer, e.g. with max-pooling) and an increasing amount of information that has proven to be helpful to determine the trained output. In the last 'fully-connected' layers of both the ResNet50 and the VGG19 models, each individual neuron is connected with all neurons of the previous and the next layer. This means that there is no image-locational dependence of the neurons any more. This 'fully-connected'

part of the network is easily fit to any output shape (e.g. the number of grain size classes) and is not initialized with pre-trained weights. The final 'full-connected' configuration chosen was found by experimenting with the number, sizes, and activation functions of layers. A detailed list of the model layers used for this study is given in Appendix C.

The AM dataset was used to develop DistID. As the pre-trained versions of both ResNet50 and VGG19 used input image shapes of 300 by 300 pixels in 3 channels, the images were median-filtered, rescaled to a resolution of 1 pixel per mm, and cropped to 300 by 300 pixels. The colour channels were converted to HSV values for most of the training runs (as specified in Table 4.3). The matching GSDs for each image in the AM dataset were generated with StoneID, while manual GSD were created for 9 images using a grid-based colour count with 150 samples per image.

The model was trained with 1,215 images and the performance tested with 307 images that were not used in the training steps. This assures that over-fitting the model with the training data can be detected, where the model learns aspects specific to the training data, but not the general task. The training data was augmented by flipping the images horizontally and vertically, artificially increasing the number of images for training by a factor of four.

4.3.4 CNN to map grain areas to colour images: U-Net+StoneID

Besides the mapping of images to a limited number of classes, some machine learning methods can be trained to achieve spatial predictions between input images and classified output images. One example is U-Net (*Ronneberger et al.*, 2015), where the input image is mapped to a fully connected layer (similarly to VGG19), which is then mapped back to the spatial scale of the input image. The training data for this method was generated with the StoneID method described earlier.

The U-Net model was trained on a subset of the AM dataset of 500 images, split into 450 training and 50 validation images. Due to the U-Net architecture requirements, the images were rescaled to 512 by 512 pixels. Details on the model configuration can be found in Appendix C. The output of the U-Net model can be used both as input to the individual stone identification (step 3, Figure 4.1) in the StoneID method and to directly estimate GSDs from

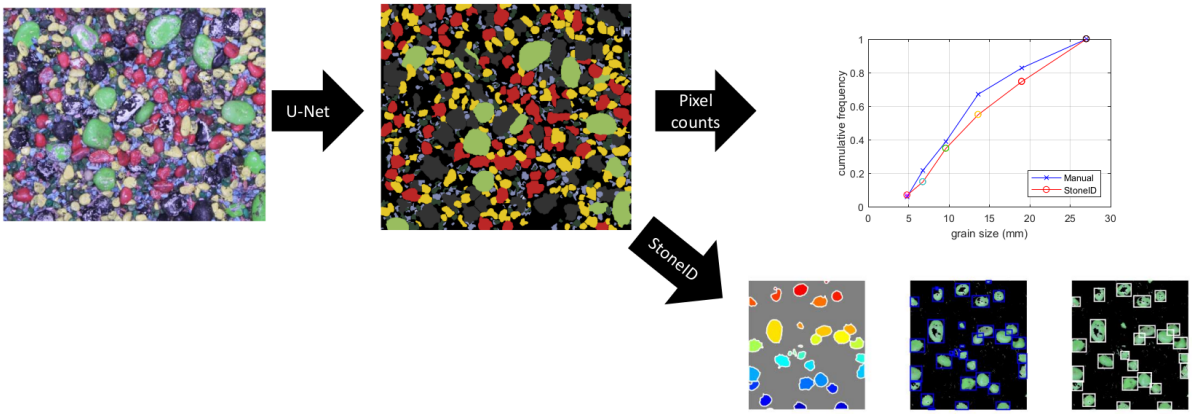

Figure 4.2: Using classified stone areas from U-Net with the StoneID method and direct pixel count GSD prediction. The surface images show StoneID-generated training data and not U-Net generated output.

pixel counts (see Figure 4.2). This combination of methods is in the following referred to as U-Net+StoneID.

4.4 Results

4.4.1 StoneID

An example of the image input for StoneID is given with Figure 4.3a, showing part of an image in the YW dataset. Figure 4.3b shows the 2,426 stones which were identified in their corresponding colour classes. The residual areas of the image where no stones were found is shown in Figure 4.3c. Over all nine images, a total of 72,209 stones were identified, on average covering 58.5% of the total image area. The undetected 41.5% in area are composed by a mix of (1) grain sizes that were too small to be included in the method, (2) grains that partly or fully lost colour, and (3) grains that were submerged in pools changing the apparent colour.

The StoneID method was used to derive GSDs from the surface coverage of identified stones. The resulting distributions for sizes $\geq$ 5 mm are shown in Figure 4.4 with the corresponding manually validated GSDs. The StoneID GSDs match the manual data well for the coarser fractions, which is illustrated by the mean of nine GSDs shown in Figure 4.5. The finer fractions are under represented, which is a limitation of this method.

Table 4.3: Difference in reported accuracy and loss from model configurations. All models were run in Keras on a Compute Canada cluster using a Tesla P100 with 12GB of memory. Training was done for 50 epochs, where one epoch is an iteration through all training images. The most reliable accuracy estimation is for the test data performance (bold), as good training data performance can be due to overfitting.

			Training data performance		Test data performance	
Model type	Initial weights	Colours	Accuracy	Mean squared error	Accuracy	Mean squared error
VGG19	ImageNet	HSV	0.87	0.0079	**0.80**	0.0115
VGG19	ImageNet	RGB	0.88	0.0076	**0.79**	0.0101
ResNet50	ImageNet	HSV	0.86	0.0085	**0.67**	0.0195
ResNet50	ImageNet	RGB	0.87	0.0080	**0.66**	0.0193
ResNet50	random	HSV	0.65	0.0220	**0.58**	0.0240

A sample for the performance of StoneID with the AM dataset is shown in Figure 4.6, where panel (a) shows the original image, (b) shows the cropped stone locations, (c) shows the residual area, and (d) shows the GSD derived from stone areas.

4.4.2 DistID

The AM dataset of 1,215 images was used to develop a neural network to learn the prediction of GSDs from images. The resulting performance reported by Keras is shown in Table 4.3 for the models used, with details provided in Appendix C. All models were trained for 50 epochs (full iterations through the dataset) to make performance comparable. The VGG19 was most accurate (80%) with HSV colour images when using pre-trained ImageNet weights. The ResNet50 models all showed lower accuracy, but the computational time was about 40% lower.

The accuracy describes the match of the model output GSD in relation to the input GSD, with discrepancies being measured with the mean squared error. Due to the large amount of images, the input GSDs were created with StoneID, which means that the model is not trained against perfect data from the beginning. Nonetheless, the good performance of 80% of the VGG model indicates that image patterns were found that correlate well with the input GSDs

during the training of the model.

To test the performance in more detail, 9 images were manually validated with 150 grid-based colour counts each. The comparison of resulting GSDs from manual counts, StoneID input data, and resulting DistID are shown in Figure 4.7. Surprisingly, on this dataset DistID performs better than StoneID, with both methods being within 1 and 2 mm of the manual data (see Figure 4.8).

4.4.3 U-Net+StoneID

A comparison of a StoneID classification with a prediction from U-Net is shown in Figure 4.9. Notably, this specific image was not part of the training dataset, meaning that the shown U-Net prediction (Figure 4.9d) was generated independently from the StoneID classification (Figure 4.9b). The U-Net model performs well in recreating the grain size class based area estimates from StoneID. Differences between the predictions occur mainly on the borders of the grains, as illustrated by an image of the difference of predictions in Figure 4.9c. The U-Net model was not trained to separate grains directly, which is why the StoneID methods (from step 5 on, Figure 4.1) have to be employed on the U-Net output classes to separate merged stones and extract individual stone locations, as outlined in Figure 4.2.

4.5 Discussion

The three developed methods (StoneID, DistID, and U-Net+StoneID) offer new ways of estimating GSDs from bed surface images of coloured stones. StoneID and U-Net+StoneID further can be used to locate individual stones and derive properties on the clustering of large stones, a descriptive parameter that is currently used in a study on the formation of transverse ribs in flume experiments.

StoneID works well for large grain sizes, matching the manually estimated D_{65}, D_{85}, and D_{90} in the YW dataset within 0.15 mm (see Figure 4.5), and in the AM dataset within 2 mm (see Figure 4.8). For these comparisons the GSDs were created from material $\geq$ 5 mm, as the individual identification of grains was unsuccessful for smaller material. These small grain sizes overlapped in colour space with the larger grains in red and black, preventing the lumping

of fines into one class. StoneID misses some of the larger stones that lost colour due to chipping or showed unexpected colour values due to changes in lighting conditions. Generally, the method shows more false negatives than false positives in the colour classification, which introduces a systematic error that is hard to quantify. Further, some stones are identified as being smaller than they actually are, sometimes splitting them in multiple identifications. This is a clear limitation of this method and some manual validation could be done.

The DistID method was trained with GSDs generated with StoneID, meaning that the accuracy of the trained model depends on the accuracy of StoneID, which likely underestimated the frequency of smaller grain size classes. Due to the large amount of images, manual data was not created for the full set of images. However, manual validation against nine samples shows that the method performs reasonably well (see Figure 4.8). The VGG19 architecture used for DistID has the potential to be improved by customizing the network architecture and creating model ensembles, which will improve the predictive performance of the method. While the training of the current DistID implementation required a large amount of data, the retraining on other datasets can be quicker and less data intensive as the model already learned the basic relation of BOMC image data to GSDs. DistID can be expected to be advantageous over the other methods in situations where the bed surface contains material which is too small for a grid-based stone count (i.e. < 8 mm). In these cases, several bulk samples of sediment can be sieved to obtain the GSDs to be used in combination with surface images of the sampled bed surface areas as training data for DistID.

The initial grain area estimates of StoneID can be done with a U-Net model instead, which might offer the advantage not to require the respecification of colour thresholds when the method is applied to a different experimental setup. This advantage has to be further tested, as in this study U-Net+StoneID was only trained and applied to one dataset. The performance of the U-Net based grain area classification can be improved greatly if a dataset of about 100 images would be manually validated. This would allow to train the model without missing stone predictions in the training dataset.

While all discussed methods were developed on coloured beds, they can be extended to uncoloured beds. While the loss of colour information will reduce the accuracy of the meth-

ods, the use of elevation data might offset this loss. Elevation data could not be utilized in this study, as the available laser-scanner DEMs are of low resolution (2 mm) and contain many artefacts. For all current and future experiments a newer method of generating DEMs is employed, which uses overlapping high resolution images. These new DEMs can improve the machine learning methods by switching the third channel in the HSV colour space to contain the DEM values. This approach also can be used for real-time UAV-based grain size detection.

4.6 Conclusions

Machine learning methods offer a great potential to automate data collection from bed surface images. All methods perform reasonably well, particularly with respect to larger grain sizes. For some studies the inability to identify small grain sizes might be of less importance, as these sizes are also missed during stone counts in the field (*Rice and Church*, 1996). In settings where the bed surface contains significant amounts of sand and fine gravel, DistID could be trained using GSDs derived from sieving, avoiding the problem of image based segmentation of small grains. The addition of training data is expected to enhance the performance of DistID and U-Net+StoneID. This lack of data limited the results in the presented study.

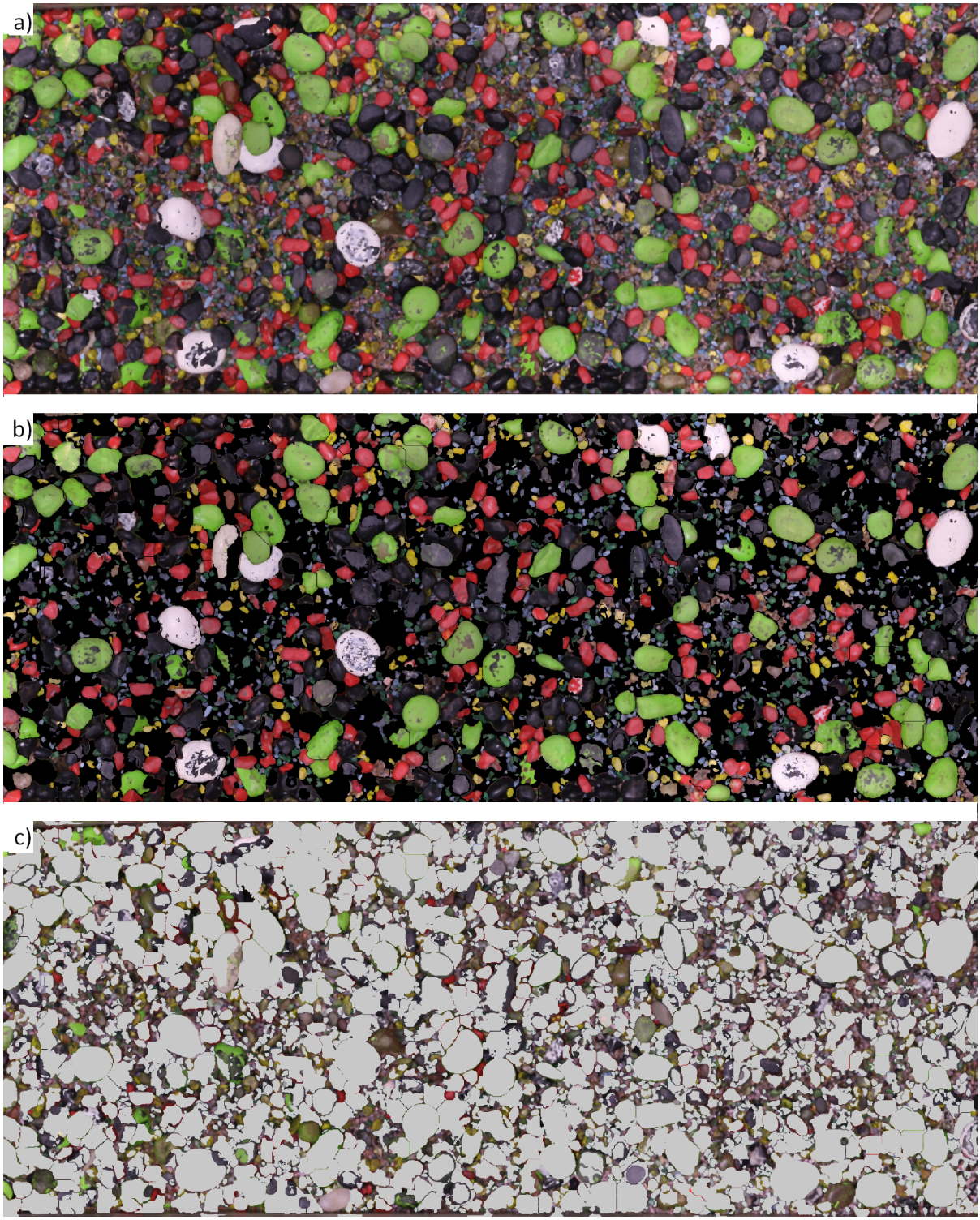

Figure 4.3: (a) Median-filtered input image for the stone recognition with StoneID. (b) Resulting image cropped by areas where 2426 stones were identified. (c) Residual area where no stones were identified shown in colour with grey background.

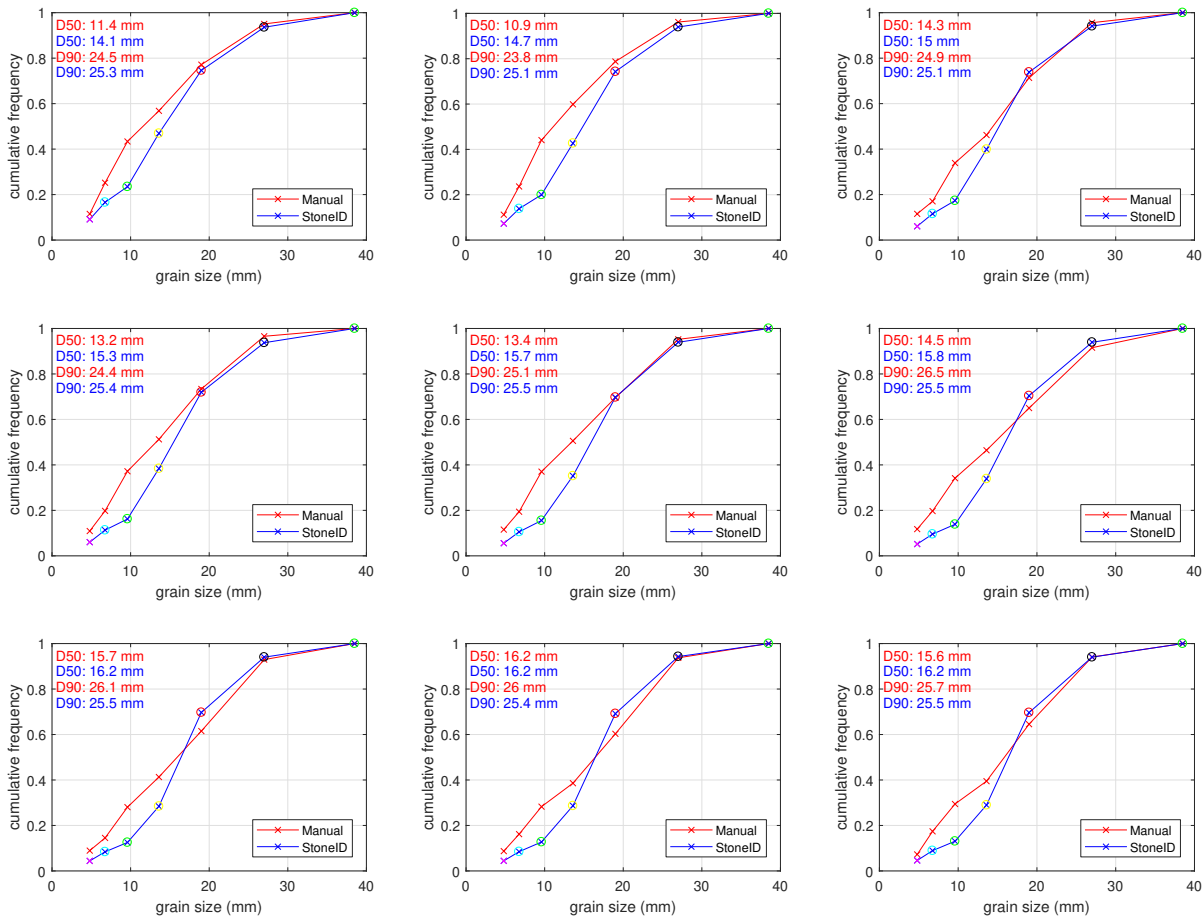

Figure 4.4: Comparison of StoneID derived GSDs to manual data. Coloured circles show the colouring of the stones.

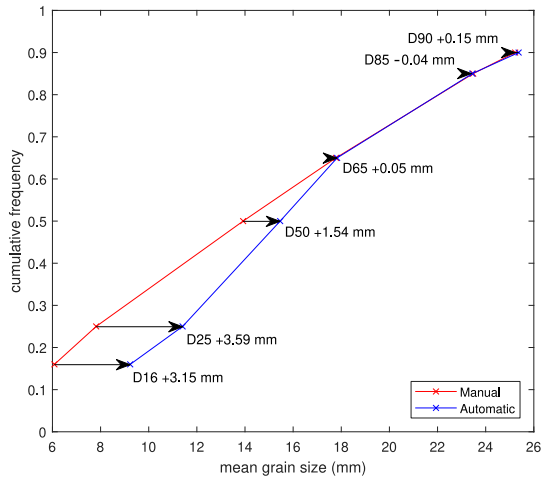

Figure 4.5: Comparison between mean sizes of D_{90}, D_{85}, D_{65}, D_{50}, D_{25}, and D_{16} from StoneID and manual data.

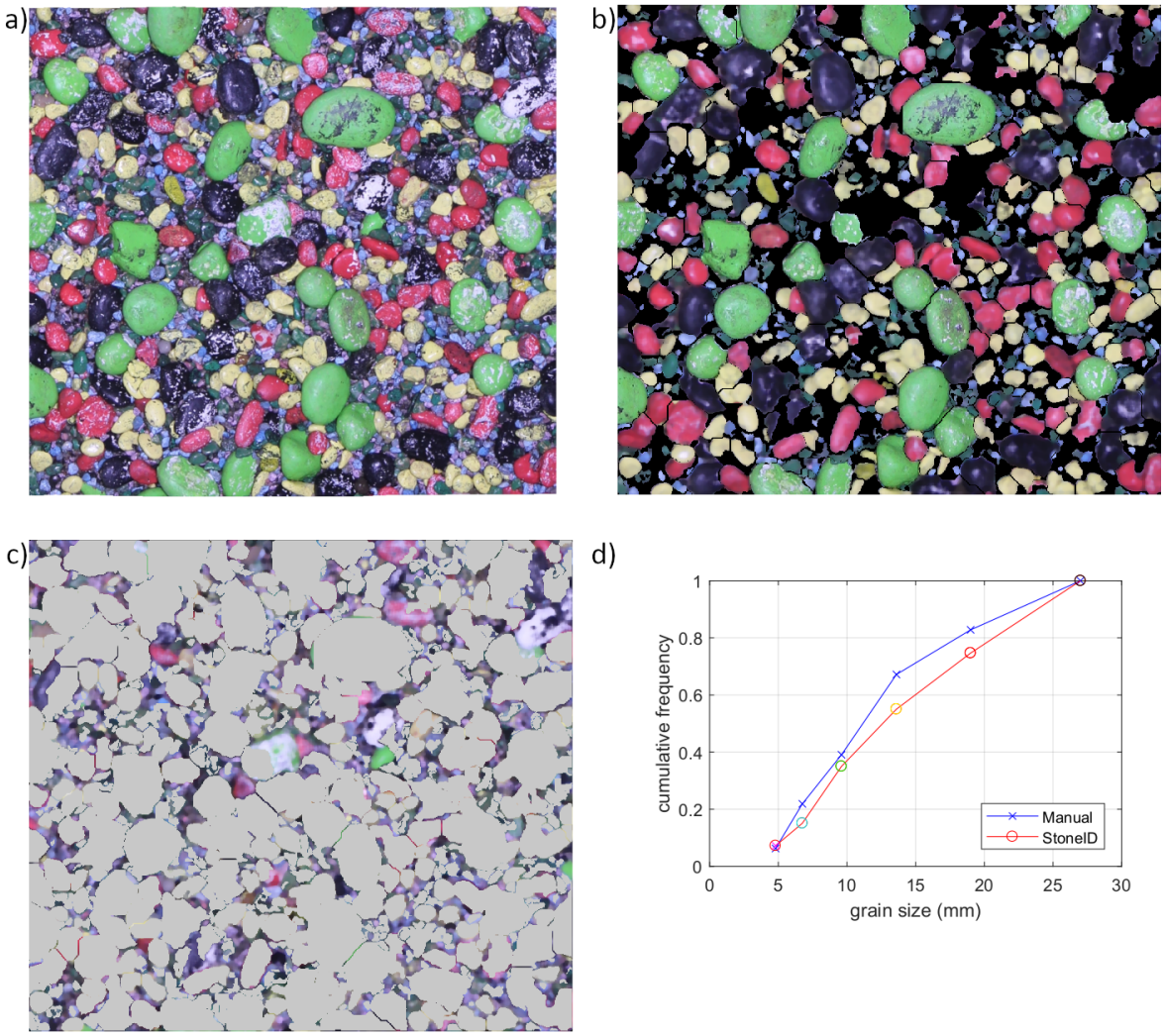

Figure 4.6: (a) Median-filtered input image for the stone recognition with StoneID. (b) Resulting image cropped by areas where stones were identified. (c) Residual area where no stones were identified shown in colour with grey background. (d) Derived GSD from stone area.

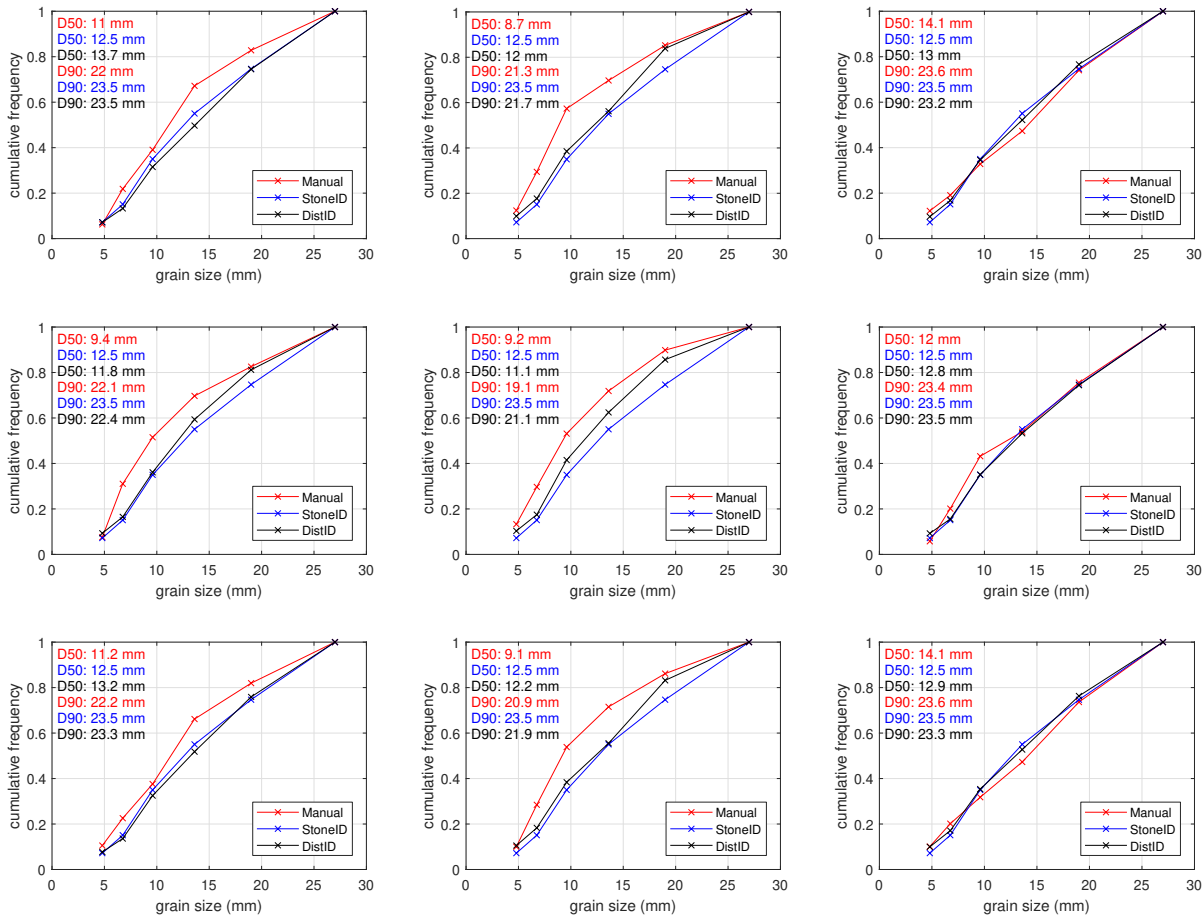

Figure 4.7: Comparison of StoneID and DistID (VGG19, HSV) derived GSDs to manual data.

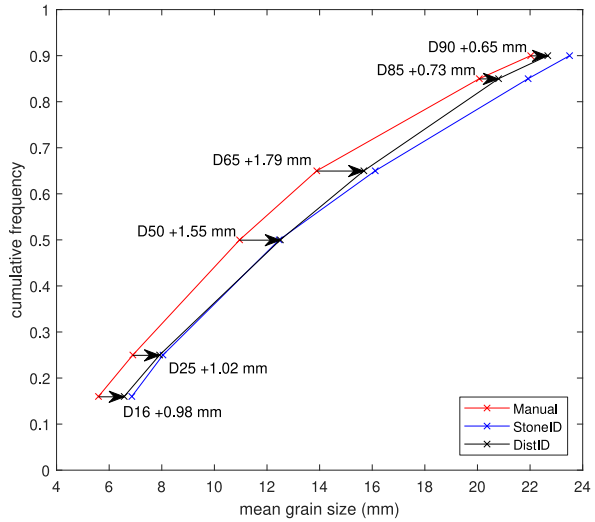

Figure 4.8: Comparison between mean sizes of D_{90}, D_{85}, D_{65}, D_{50}, D_{25}, and D_{16} from StoneID and DistID (VGG19,HSV) to data from manual grid-based counts.

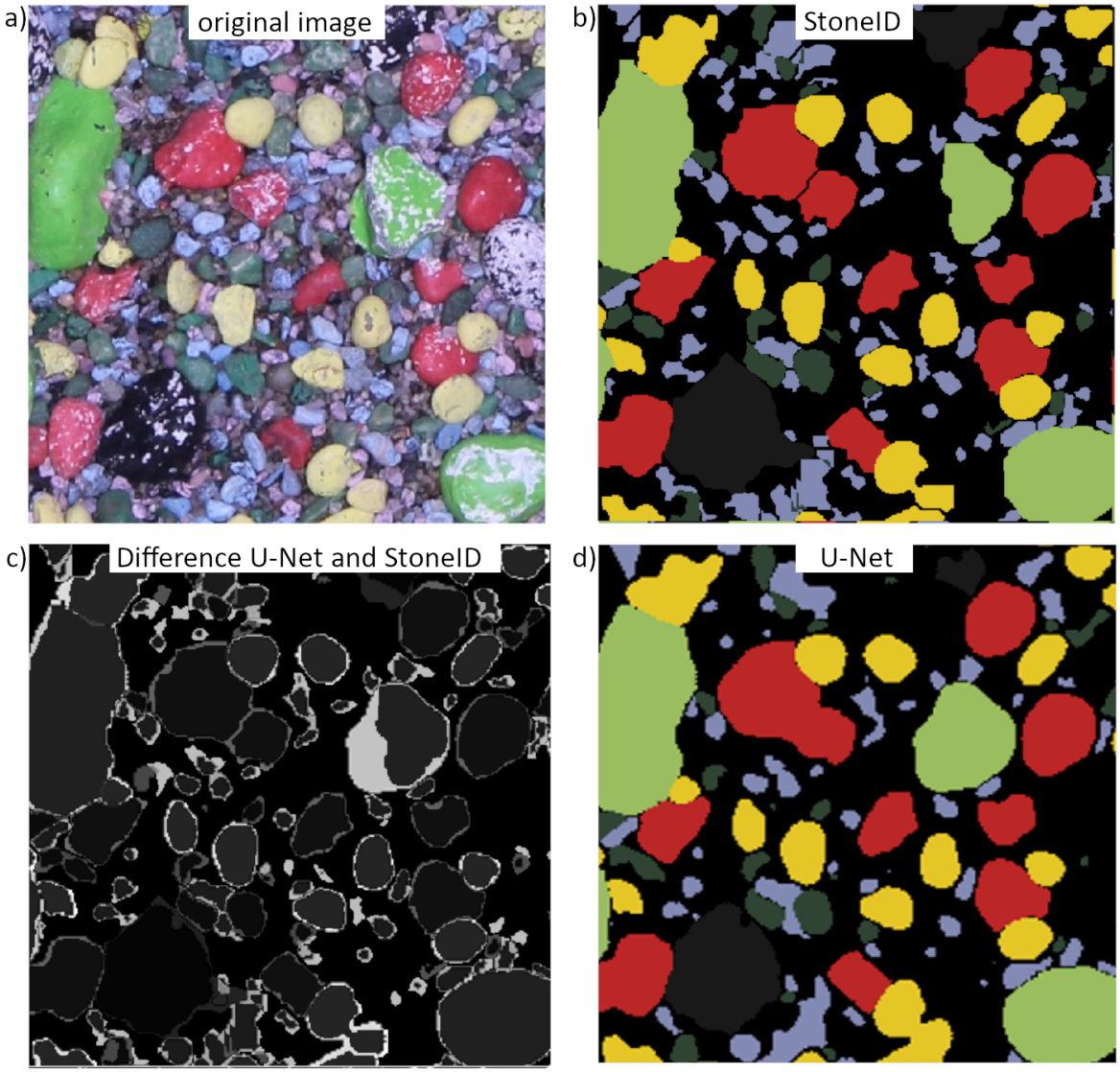

Figure 4.9: Comparison of StoneID and U-Net derived grain area predictions for a 13 by 13 cm large image sub-sample. (a) Original image. (b) StoneID grain classifications based on colour values and expected grain geometry. (c) Image of difference between U-Net and StoneID classifications. (d) U-Net classifications coloured by the respective grain size classes. The U-Net output resolution is reduced by about 40% in comparison to the StoneID method.

Chapter 5

Concluding remarks

The objective of this thesis is to build our understanding of how mountain rivers respond to episodic sediment supply. Field studies of channel response to these events are challenging to undertake, as a long data record is needed to reasonably assess a system's state of response in the context of episodic supply. A fluvial system might be undergoing transient adjustment to previous, potentially unknown, episodic events, or it might be approaching a steady state where no significant adjustment occurs. Greater confidence in the observed state of response of a system can be achieved with flume experiments where the fluvial response can be observed in detail after episodic events are introduced in a controlled fashion. Yet, the amount of work necessary to carry out these experiments is large, which limits the number of experimental conditions that can be studied, and thus their utility for addressing applied problems of channel adjustment. To overcome this limitation, the 1-D morphometric sediment transport model BESMo was developed, which allows large numbers of simulations to be run in batches, generating ensemble results. Chapter 2 presents the identification of thresholds in the fluvial response to episodic sediment supply, including the application to a field case. The general utility of BESMo for studying fluvial response to large sediment supply events is presented in Chapter 3 with the study of potential geomorphic effects following the removal of a dam in the Carmel River. Finally, to overcome data limitations on surface grain size distributions, machine-learning based methods were developed to detect grain size distributions from images, as described in Chapter 4.

A more detailed list of contributions made in this thesis is presented in the next section, followed by a discussion of potential avenues for future work.

5.1 Summary of contributions

The 1-D morphometric sediment transport model BESMo (Bedload Scenario Model) was developed and calibrated to recreate data from flume experiments.

As presented in Chapter 2, BESMo was developed to simulate the effect that different combinations of event frequencies, magnitudes, and grain size compositions have on a simplified fluvial channel. As described earlier, the study of episodic events is limited by the range of conditions that can be recreated and understood in flume and field based studies. Thus the calibration of BESMo with one set of flume experiments allowed for a broader range of simulated conditions to be assessed (320 instead of 4, an increase by a factor of 80) and for the observation time to be extended by a factor of 500 per simulation (20,000 hours instead of 40 hours each).

When a channel is impacted by multiple episodic supply events of different magnitudes, the sequencing of these events has only a short term effect on the slope and grain size response of the fluvial channel.

BESMo was used to recreate channel adjustments observed during flume experiments, showing that if a channel is impacted by multiple episodic supply events of different magnitudes, the sequencing of these events has only a short term effect on the slope and grain size response of the channel. If a large pulse occurs early in the time series, it causes an abrupt increase in channel slope and the effect of subsequent smaller pulses is subdued. If a series of small pulses occurs first, the slope responds more gradually and the effect of a subsequent large pulse is subdued. Both of these hypothetical time series lead to similar channel conditions in the long term, indicating that the total volume of sediment supply is the governing factor of channel equilibrium conditions. As the grain size response is quicker than the response in channel slope, the event sequencing has a small effect on the surface grain size distributions.

The fluvial response to episodic sediment supply regimes is either constant-feed-like or

pulse-dominated, which can be determined by ratios of the event return period (T_{pp}) to the fluvial evacuation time (T_{fe}) and the fluvial armouring time (T_{fa}).

In a second set of simulations, the range of simulated pulse frequencies, magnitudes, and grain size compositions were extended, representing different sediment supply regimes. During the simulations these conditions caused the fluvial channel to adjust its slope, with some combinations of input conditions resulting in similar slopes to the constant-feed simulations, while others led to significantly higher slopes. These two response types can be separated by a threshold ratio of the timescales of sediment supply to the timescale of the fluvial response. When the return period of sediment pulses (T_{pp}) is shorter than the fluvial evacuation time (T_{fe}), channel slopes are similar to constant-feed simulations. When $T_{pp} > T_{fe}$, channel slopes are significantly higher, indicating pulse-dominated conditions. A similar effect is observed for the armouring ratio of the channel, which shows a threshold in armouring response when T_{pp} is longer than the fluvial armouring time (T_{fa}). These thresholds allow for the categorization of fluvial response to episodic sediment supply regimes into one of (a) constant-feed-like, or (b) pulse-dominated. This distinction is useful for predicting the long-term behaviour of fluvial channels which experience irregular supply events.

Chapter 2 included a sample of such an application for the case of East Creek, showing that the threshold to a pulse-dominated regime lies at the fluvial evacuation time of roughly 2.2 years. This creek probably receives sediment at a lower interval, which indicates a pulse-dominated regime. The armouring timescale lies around 3.5 years, indicating that if the long-term sediment supply was introduced over event frequencies between 2.2 and 3.5 years, it would be removed most efficiently and result in a lower slope.

BESMo is an effective tool for applied problems of channel adjustment, and was used to predict channel response to the removal of the Los Padres Dam, on the Carmel River, California. In general, all scenarios show that the release of sediment from the dam will cause the river to aggrade. The bed will fine during phases of sediment release, but coarsen within several years after the reservoir is depleted of sediment.

As presented in Chapter 3, BESMo was used to study the geomorphic response of the Carmel

River to the removal of the Los Padres Dam for 60 years in the future. The simulations indicate that increased sediment supply from the reservoir can return the Carmel River sediment dynamics closer to pre-dam conditions, primarily due to the re-establishment of connectivity between the upper watershed and the main stem. Specifically, the predicted return to historical sediment connectivity will lead to channel bed aggradation and fining of the channel bed surface downstream of the dam. While these changes potentially increase fish habitat, widespread aggradation poses an increased flood risk.

Different sediment supply scenarios were developed to represent management options considered for the dam. Simulations in which sediment was released from the Los Padres reservoir in smaller, more frequent pulses proved to be more effective for establishing a finer surface texture which could last more than a decade. On the other hand, in simulations where the sediment release was less frequent and larger in magnitude, for example following an uncontrolled dam removal, the fine surface texture was only established intermittently. As small grain sizes were not replenished, their removal from the channel bed led to the development of channel armouring within a few years of low sediment supply.

Ensemble simulations of sediment transport are a useful approach for understanding how uncertainty in future conditions affects the system in the long term (>10 years).

Determining the response of the Carmel River to the Los Padres dam removal is a complex problem, as both current conditions and future changes on the river are not fully understood. As detailed prediction of such a system is nearly impossible, the application of a 1-D model like BESMo helps to explore the response of the river with simplified process interactions. Thus, the comparison between scenarios of sediment release from the Los Padres reservoir offers insight into large scale patterns of river response which are generally more meaningful for managers than highly localized predictions.

BESMo offers significant advantages over prior modelling work by allowing for the exploration and quantification of uncertainty in input parameters. The uncertainty in the occurrence of significant floods shortly after a potential dam removal necessitated an approach of creating synthetic hydrographs based on historical discharge records. This allowed for the generation

of flow series representing historically "wet" conditions, which have shown to be associated with situations where the sediment supply scenarios diverge most significantly. Including these uncertainties in the presentation of simulation data is of great practical importance for communicating complex modelling results. Despite the limitations of 1-D models, BESMo has shown to be an appropriate tool for understanding the future geomorphic response of the Carmel River to potential management options at Los Padres Dam.

The detection of grain size distributions from images can be greatly improved with machine learning-based models.

The lack of grain size distributions in field data for future studies of channel response to episodic events might be overcome by collecting drone based imagery. Currently employed semi-automatic methods to identify grain size distributions from images in the lab are unreliable due to paint chipping off stones and irregular lighting conditions. Furthermore, changing conditions between experiments (such as used camera type) make it necessary to recalibrate colour thresholds for grain size class identification.

Three different methods to identify grain size distributions from images of coloured grains were presented in Chapter 4. These methods were developed on two datasets of images showing grains coloured by size class, with the objective of reducing the manual work needed for the analysis of both the locations of coarse grains and grain size distributions. Machine learning methods can be less sensitive to variations in colouring of stones and lighting conditions when trained with datasets that reflect this range in conditions and that are manually validated. Even though the used datasets were not fully validated, the employed methods showed good results in matching the available data. Especially the larger grain size classes such as D_{90} were estimated within 2 mm by the DistID and the StoneID methods. The U-Net model was successfully used to classify stone areas within the accuracy of the training data, which promises great potential in automatically identifying individual stones if combined with the StoneID method. More manually validated training data is needed if these methods are to be applied to more datasets.

5.2 Future work

Network-scale model: BESMo has proven useful for recreating sediment transport conditions ranging from those at the small scale (flume experiment) to the large scale (Carmel River catchment). In the latter case, only the main-stem of the river was simulated while tributary sediment supply was derived from rating curves. In other settings, the explicit inclusion of tributaries in the simulation domain might be necessary to understand the network-scale impacts of episodic sediment supply in a catchment. BESMo could be used in such a study to investigate the geomorphic effects that changing episodic sediment supply frequency and magnitude has in a channel network.

Variation of hydrologic conditions in accordance to climate change scenarios: A wide range of synthetic hydrographs were generated for the Los Padres dam removal study. These discharge time series were based on static climatic conditions of flood frequency and magnitude captured by a single stream gauge. It is likely that climate change will impact flood frequency-magnitude relations, which could be represented in BESMo and used to understand the sensitivity of fluvial sediment transport to the impact of climate change.

Further applications of BESMo: Studies simulating sediment transport are never based on perfect input data, as field data characterising key processes is challenging, or in some cases, not possible to collect in adequate detail or over appropriate timescales (e.g. subsurface grain sizes or flow conditions). As stated before, BESMo offers a way to approach the uncertainty of real world systems by relying on ensembles of simulations.

While any modelling study of bedload sediment transport could benefit of this approach, a possible application related to episodic sediment supply is the study of appropriate gravel augmentation magnitudes and frequencies. For example, simulations of this type could help finding which sediment supply conditions are most effective, for improveing fish habitat while reducing problems with 'overloading' the channel with sediment and causing aggradation.

Application of developed time scales: The application of the fluvial evacuation time (T_{fe}) and the fluvial armouring time (T_{fa}) to more field cases is necessary to better understand the effect of episodic sediment supply on mountain streams. Such studies could investigate morphologic change at tributary junctions where sediment is supplied to the main channel from debris flows. An important aspect of a suitable field site would be the availability of records of episodic supply from which frequency-magnitude relations could be derived.

Improvement of machine learning based grain size identification More high quality validation data will help to improve the developed machine learning methods significantly, as these models are primarily limited by the quality of the input training data. This method should also be applicable for unpainted, or natural sediment: While the loss of colour information will reduce the accuracy of the models, incorporating other co-variables, such as elevation data, might offset this loss. Elevation data could not be utilized in this thesis, as the available laser-scanner DEMs are of low resolution (2 mm per pixel) in comparison to the image data and contains many artefacts. For all current and future experiments a newer method of generating DEMs is employed, which uses overlapping high resolution images. These new DEMs can improve the machine learning methods by switching the third channel in the HSV colour space to contain the DEM values. Preserving three channels is preferable, as this assures that pre-trained models can be used, which are shown to require less training data as some aspects of object detection are already established. Alternatively, a CNN (e.g. VGG19 or ResNet50) could be fully retrained on 4 channels (3 colour channel channels plus DEM values).

Automated grain size estimates from remotely sensed images: The stone identification from uncoloured sediment will open up the possibility to apply the machine learning methods on images captured remotely, such as with UAVs (Unmanned Aerial Vehicles), allowing for rapid grain size scanning of large areas. This can be achieved after collecting new validation data, as the method can not be directly translated from the flume setting due to differences in e.g. image resolution, DEM resolution, inconsistent lighting, and stone geometry. A reliable UAV-based method to identify grain size distribution can be tied back to the numerical modelling

work with BESMo, as this would help to generate larger input datasets in a fast and cost effective way.

Bibliography

AECOM (2017), Los Padres Dam and Reservoir Alternatives and Sediment Management Study Draft Preparation Technical Memorandum-Deliverable for Task 1. Consulting report prepared for Monterey Peninsula Water Management District in association with HDR Engineering and Stillwater Sciences.

Ahnert, F. (1994), Equilibrium, scale and inheritance in geomorphology, *Geomorphology*, *11*(2), 125–140, doi:10.1016/0169-555x(94)90077-9.

An, C., Y. Cui, X. Fu, and G. Parker (2017a), Gravel-bed river evolution in earthquake-prone regions subject to cycled hydrographs and repeated sediment pulses, *Earth Surface Processes and Landforms*, *42*(14), 2426–2438, doi:10.1002/esp.4195.

An, C., X. Fu, G. Wang, and G. Parker (2017b), Effect of grain sorting on gravel bed river evolution subject to cycled hydrographs: Bed load sheets and breakdown of the hydrograph boundary layer, *Journal of Geophysical Research: Earth Surface*, *122*(8), 1513–1533, doi:10.1002/2016jf003994.

Ayers, W. Y. (1995), Water Resources Data, California, Water Year 1994. Volume 2. Pacific Slope Basins from Arroyo Grande to Oregon State Line except Central Valley., *Tech. rep.*, doi:10.3133/wdrca942.

Balance Hydrologics, Inc. (2001), Unpublished Sediment Transport Measurements, Carmel River, Water Year 2001.

Bednarek, A. T. (2001), Undamming rivers: a review of the ecological impacts of dam removal, *Environmental management*, *27*(6), 803–814.

Benda, L. (1990), The influence of debris flows on channels and valley floors in the oregon coast range, usa, *Earth Surface Processes and Landforms*, *15*(5), 457–466, doi:10.1002/esp.3290150508.

Benda, L., and T. Dunne (1997a), Stochastic forcing of sediment supply to channel networks from landsliding and debris flow, *Water Resources Research*, *33*(12), 2849–2863, doi:10.1029/97WR02388.

Benda, L., M. A. Hassan, M. Church, and C. L. May (2005), Geomorphology of steepland headwaters: The transition from hillslopes to channels, *Journal of the American Water Resources Association*, *41*(4), 835–851.

Beven, K. (2002), Towards a coherent philosophy for modelling the environment, in *Proceedings of the Royal Society of London A: Mathematical, Physical and Engineering Sciences*, vol. 458, pp. 2465–2484, The Royal Society, The Royal Society, doi:10.1098/rspa.2002.0986.

Blom, A., L. Arkesteijn, V. Chavarrías, and E. Viparelli (2017), The equilibrium alluvial river under variable flow and its channel-forming discharge, *Journal of Geophysical Research: Earth Surface*, *122*(10), 1924–1948, doi:10.1002/2017jf004213.

Brardinoni, F., and M. A. Hassan (2006), Glacial erosion, evolution of river long profiles, and the organization of process domains in mountain drainage basins of coastal british columbia, *Journal of Geophysical Research*, *111*(F1), doi:10.1029/2005JF000358.

Brummer, C. J., and D. R. Montgomery (2006), Influence of coarse lag formation on the mechanics of sediment pulse dispersion in a mountain stream, Squire Creek, North Cascades, Washington, United States, *Water Resources Research*, *42*(7), doi:10.1029/2005wr004776.

Brunsden, D. (1980), Applicable model of long term landform evolution, *Zeitschr. Geomorph. NF, Suppl. Bd.*, *36*, 16–26.

Brunsden, D. (2001), A critical assessment of the sensitivity concept in geomorphology, *Catena*, *42*(2), 99–123, doi:10.1016/s0341-8162(00)00134-x.

Brunsden, D., and J. B. Thornes (1979), Landscape sensitivity and change, *Transactions of the Institute of British Geographers*, *4*(4), 463–484, doi:10.2307/622210.

Bull, W. B. (1991), *Geomorphic responses to climatic change*, 326 pp. pp., Oxford University Press, doi:10.2307/215397.

Bunte, K., and S. R. Abt (2001), Sampling surface and subsurface particle-size distributions in wadable gravel-and cobble-bed streams for analyses in sediment transport, hydraulics, and streambed monitoring, *Gen. Tech. Rep. RMRS-GTR-74. Fort Collins, CO: US Department of Agriculture, Forest Service, Rocky Mountain Research Station. 428 p.*, *74*.

Buscombe, D. (2013), Transferable wavelet method for grain-size distribution from images of sediment surfaces and thin sections, and other natural granular patterns, *Sedimentology*, *60*(7), 1709–1732, doi:10.1111/sed.12049.

Carrivick, J. L., and M. W. Smith (2018), Fluvial and aquatic applications of structure from motion photogrammetry and unmanned aerial vehicle/drone technology, *Wiley Interdisciplinary Reviews: Water*, *6*(1), e1328, doi:10.1002/wat2.1328.

Chartrand, S. M., M. A. Hassan, and V. Radić (2015), Pool-riffle sedimentation and surface texture trends in a gravel bed stream, *Water Resources Research*, *51*(11), 8704–8728, doi:10.1002/2015wr017840.

Chorley, R. J., and B. A. Kennedy (1971), *Physical geography: a systems approach*, Prentice-Hall London.

Chow, K., L. Luna, A. Delforge, and D. Smith (2016), 2015 Pre-San Clemente Dam Removal Morphological Monitoring of the Carmel River Channel in Monterey County, California.

Chung, C.-H., and F.-J. Chang (2013), A refined automated grain sizing method for estimating river-bed grain size distribution of digital images, *Journal of hydrology*, *486*, 224–233.

Church, M., and R. Ferguson (2015), Morphodynamics: Rivers beyond steady state, *Water Resources Research*, *51*(4), 1883–1897, doi:10.1002/2014wr016862.

Church, M., and R. Kellerhals (1978), On the statistics of grain size variation along a gravel river, *Canadian Journal of Earth Sciences*, *15*(7), 1151–1160, doi:10.1139/e78-121.

Church, M., M. A. Hassan, and J. F. Wolcott (1998), Stabilizing self-organized structures in gravel-bed stream channels: Field and experimental observations, *Water Resources Research*, *34*(11), 3169–3179, doi:10.1029/98wr00484.

Church, M. A., D. G. McLean, and J. F. Wolcott (1987), River bed gravels: sampling and analysis, in *Sediment transport in gravel-bed rivers*, edited by C. R. Thorne, J. C. Bathurst, and R. D. Hey, pp. 43–78, Wiley.

Cienciala, P., and M. A. Hassan (2013), Linking spatial patterns of bed surface texture, bed mobility, and channel hydraulics in a mountain stream to potential spawning substrate for small resident trout, *Geomorphology*, *197*, 96–107, doi:10.1016/j.geomorph.2013.04.041.

Coulthard, T., and M. Van De Wiel (2013), 9.34 Numerical Modeling in Fluvial Geomorphology, in *Treatise on Geomorphology*, pp. 694–710, Elsevier, doi:10.1016/b978-0-12-374739-6.00261-x.

Cui, Y., and G. Parker (2005), Numerical model of sediment pulses and sediment-supply disturbances in mountain rivers, *Journal of Hydraulic Engineering*, *131*(8), 646–656, doi:10.1061/(asce)0733-9429(2005)131:8(646).

Cui, Y., and A. Wilcox (2008), Development and application of numerical models of sediment transport associated with dam removal, *Chapter*, *23*, 995–1020.

Cui, Y., G. Parker, T. E. Lisle, J. Gott, M. E. Hansler-Ball, J. E. Pizzuto, N. E. Allmendinger, and J. M. Reed (2003), Sediment pulses in mountain rivers: 1. experiments, *Water Resources Research*, *39*(9), doi:10.1029/2002wr001803.

Cui, Y., G. Parker, C. Braudrick, W. E. Dietrich, and B. Cluer (2006), Dam removal express assessment models (dream). part 1: model development and validation, *Journal of Hydraulic Research*, *44*(3), 291–307, doi:10.1080/00221686.2006.9521683.

Curry, R., and G. Kondolf (1983), Sediment transport and channel stability, carmel river, california, *Unpublished report to MPWMD*.

De Rego, K. G. (2018), Decadal-scale evolution of elwha river downstream of glines canyon dam: perspectives from numerical modeling, Ph.D. thesis, University of British Columbia.

Detert, M., and V. Weitbrecht (2013), User guide to gravelometric image analysis by basegrain, *Advances in science and research*, pp. 1789–1795.

Detert, M., L. Kadinski, and V. Weitbrecht (2018), On the way to airborne gravelometry based on 3d spatial data derived from images, *International journal of sediment research*, *33*(1), 84–92, doi:10.1016/j.ijsrc.2018.02.001.

Dibblee, T., and J. Minch (2007), Geologic map of the bickmore canyon quadrangle, monterey and san benito counties.

Dietrich, W. E., and T. Dunne (1978), Sediment budget for a small catchment in mountainous terrain, *Z. Geomorphol*, *29*, 191–206.

Dietrich, W. E., J. W. Kirchner, H. Ikeda, and F. Iseya (1989), Sediment supply and the development of the coarse surface layer in gravel-bedded rivers, *Nature*, *340*(6230), 215–217, doi:10.1038/340215a0.

Dietrich, W. E., D. G. Bellugi, L. S. Sklar, J. D. Stock, A. M. Heimsath, and J. J. Roering (2003), Geomorphic transport laws for predicting landscape form and dynamics, *Prediction in geomorphology*, *135*, 103–132, doi:10.1029/135gm09.

East, A. E., G. R. Pess, J. A. Bountry, C. S. Magirl, A. C. Ritchie, J. B. Logan, T. J. Randle, M. C. Mastin, J. T. Minear, J. J. Duda, et al. (2015), Large-scale dam removal on the elwha river, washington, usa: River channel and floodplain geomorphic change, *Geomorphology*, *228*, 765–786, doi:10.1016/j.geomorph.2014.08.028.

Elgueta, M. A. (2014), Channel adjustment of a gravel-bed stream under episodic sediment supply regimes, Master's thesis, University of British Columbia, doi:10.14288/1.0165847.

Elgueta-Astaburuaga, M. A. (2018), Effects of episodic sediment supply on channel adjustment of an experimental gravel bed, PhD thesis, University of British Columbia, doi:10.14288/1.0364558.

Elgueta-Astaburuaga, M. A., and M. A. Hassan (2017), Experiment on temporal variation of bed load transport in response to changes in sediment supply in streams, *Water Resources Research*, *53*(1), 763–778, doi:10.1002/2016wr019460.

Escauriaza, C., C. Paola, and V. R. Voller (2017), Computational models of flow, sediment transport and morphodynamics in rivers, in *Gravel-Bed Rivers*, pp. 1–31, John Wiley & Sons, Ltd Chichester, UK, doi:10.1002/9781118971437.ch1.

Ferrer-Boix, C., and M. A. Hassan (2014), Influence of the sediment supply texture on morphological adjustments in gravel-bed rivers, *Water Resources Research*, *50*(11), 8868–8890, doi:10.1002/2013wr015117.

Ferrer-Boix, C., and M. A. Hassan (2015), Channel adjustments to a succession of water pulses in gravel bed rivers, *Water Resources Research*, *51*(11), 8773–8790, doi:10.1002/2015wr017664.

Ferrer-Boix, C., S. M. Chartrand, M. A. Hassan, J. P. Martín-Vide, and G. Parker (2016), On how spatial variations of channel width influence river profile curvature, *Geophysical Research Letters*, *43*(12), 6313–6323, doi:10.1002/2016gl069824.

Foley, M. M., J. Bellmore, J. E. O'Connor, J. Duda, A. E. East, G. Grant, C. Anderson, J. A. Bountry, M. J. Collins, P. J. Connolly, et al. (2017), Dam removal: Listening in, *Water Resources Research*, *53*(7), 5229–5246.

Freeman, L., M. Webster, and M. F. Friebel (1996), Pacific Slope Basins from Arroyo Grande to Oregon State Line except Central Valley. US Geological Survey Water-Data Report CA-96-2.

GMA (2008), 2007 Carmel River Surveys. Consulting report prepared for the Monterey Peninsula Water Management Agency by Graham Matthews and Associates.

Graf, W. L. (1999), Dam nation: A geographic census of american dams and their large-scale hydrologic impacts, *Water resources research*, *35*(4), 1305–1311.

Graham, D. J., I. Reid, and S. P. Rice (2005), Automated sizing of coarse-grained sediments: image-processing procedures, *Mathematical Geology*, *37*(1), 1–28, doi:10.1007/s11004-005-8745-x.

Graham, D. J., A.-J. Rollet, H. Piégay, and S. P. Rice (2010), Maximizing the accuracy of image-based surface sediment sampling techniques, *Water Resources Research*, *46*(2), doi:10.1029/2008wr006940.

Grant, G. (2001), Dam removal: Panacea or pandora for rivers?, *Hydrological Processes*, *15*(8), 1531–1532, doi:10.1002/hyp.473.

Grant, G. E., and S. L. Lewis (2015), The remains of the dam: What have we learned from 15 years of us dam removals?, in *Engineering Geology for Society and Territory-Volume 3*, pp. 31–35, Springer.

Gudde, E. G. (2010), *California place names: the origin and etymology of current geographical names*, Univ of California Press.

Guthrie, R., and S. Evans (2007), Work, persistence, and formative events: the geomorphic impact of landslides, *Geomorphology*, *88*(3), 266–275.

Hampson, L. (2018), Unpublished data of bank protection occurrence, extent and material type along the mainstem Carmel River. Microsoft Excel spreadsheet. .

Harrison, L. R., A. E. East, D. P. Smith, J. B. Logan, R. M. Bond, C. L. Nicol, T. H. Williams, D. A. Boughton, K. Chow, and L. Luna (2018), River response to large-dam removal in a mediterranean hydroclimatic setting: Carmel river, california, usa, *Earth Surface Processes and Landforms*.

Hassan, M. A., and M. Church (2000), Experiments on surface structure and partial sediment transport on a gravel bed, *Water Resources Research*, *36*(7), 1885–1895, doi:10.1029/2000wr900055.

Hassan, M. A., and A. E. Zimmermann (2012), Channel response and recovery to changes in sediment supply, in *Gravel-Bed Rivers*, pp. 464–473, John Wiley & Sons, Ltd, doi:10.1002/9781119952497.ch33.

Hassan, M. A., M. Church, T. E. Lisle, F. Brardinoni, L. Benda, and G. E. Grant (2005), Sediment transport and channel morphology of small, forested streams, *Journal of the American Water Resources Association*, *41*(4), 853–876, doi:10.1111/j.1752-1688.2005.tb03774.x.

Hassan, M. A., R. Egozi, and G. Parker (2006a), Experiments on the effect of hydrograph characteristics on vertical grain sorting in gravel bed rivers, *Water Resources Research*, *42*(9), doi:10.1029/2005wr004707.

Hassan, M. A., R. Egozi, and G. Parker (2006b), Experiments on the effect of hydrograph characteristics on vertical grain sorting in gravel bed rivers, *Water Resources Research*, *42*(9), doi:10.1029/2005wr004707.

Hassan, M. A., B. J. Smith, D. L. Hogan, D. S. Luzi, A. E. Zimmermann, and B. C. Eaton (2008a), 18 sediment storage and transport in coarse bed streams: scale considerations, in *Gravel-Bed Rivers VI: From Process Understanding to River Restoration*, edited by P.-H. Habersack, H. and M. Rinaldi, pp. 473–496, Elsevier, doi:10.1016/s0928-2025(07)11137-8.

Hassan, M. A., A. S. Gottesfeld, D. R. Montgomery, J. F. Tunnicliffe, G. K. C. Clarke, G. Wynn, H. Jones-Cox, R. Poirier, E. MacIsaac, H. Herunter, and S. J. Macdonald (2008b), Salmon-driven bed load transport and bed morphology in mountain streams, *Geophysical Research Letters*, *35*(4), doi:10.1029/2007gl032997.

Hassan, M. A., D. Brayshaw, Y. Alila, and E. Andrews (2014), Effective discharge in small formerly glaciated mountain streams of british columbia: Limitations and implications, *Water Resources Research*, *50*(5), 4440–4458, doi:10.1002/2013wr014529.

Hassan, M. A., S. Bird, D. Reid, C. Ferrer-Boix, D. Hogan, F. Brardinoni, and S. Chartrand (2018), Variable hillslope-channel coupling and channel characteristics of forested mountain streams in glaciated landscapes, *Earth Surface Processes and Landforms*, doi:10.1002/esp.4527.

He, K., X. Zhang, S. Ren, and J. Sun (2016), Deep residual learning for image recognition, in *Proceedings of the IEEE conference on computer vision and pattern recognition*, pp. 770–778, doi:10.1109/cvpr.2016.90.

Heritage, G. L., and D. J. Milan (2009), Terrestrial laser scanning of grain roughness in a gravel-bed river, *Geomorphology*, *113*(1-2), 4–11, doi:10.1016/j.geomorph.2009.03.021.

Hoey, T. B., and R. Ferguson (1994), Numerical simulation of downstream fining by selective transport in gravel bed rivers: Model development and illustration, *Water Resources Research*, *30*(7), 2251–2260, doi:10.1029/94wr00556.

Hoffman, D. F., and E. J. Gabet (2007), Effects of sediment pulses on channel morphology in a gravel-bed river, *Geological Society of America Bulletin*, *119*(1-2), 116–125, doi:10.1130/b25982.1.

Hoffmann, T., T. Mller, E. A. Johnson, and Y. E. Martin (2013), Postglacial adjustment of steep, low-order drainage basins, canadian rocky mountains, *Journal of Geophysical Research: Earth Surface*, *118*(4), 17p., doi:10.1002/2013jf002846.

Howard, A. D. (1982), Equilibrium and time scales in geomorphology: Application to sand-bed alluvial streams, *Earth Surface Processes and Landforms*, *7*(4), 303–325, doi:10.1002/esp.3290070403.

Istanbulluoglu, E. (2005), Vegetation-modulated landscape evolution: Effects of vegetation on landscape processes, drainage density, and topography, *Journal of Geophysical Research*, *110*(F2), doi:10.1029/2004jf000249.

Johnson, J. P. L., A. C. Aronovitz, and W. Kim (2015), Coarser and rougher: Effects of fine gravel pulses on experimental step-pool channel morphodynamics, *Geophysical Research Letters*, *42*(20), 8432–8440, doi:10.1002/2015gl066097.

Kondolf, G. (1982), Recent channel instability and historic channel changes of the carmel river, monterey county, california [masters thesis], *Santa Cruz: University of California Santa Cruz*.

Kondolf, G., and H. Piégay (2011), Geomorphology and society, in *Handbook of Geomorphology*, edited by K. Gregory, pp. 105–117, SAGE Publications, London.

Kondolf, G. M., and R. R. Curry (1986), Channel erosion along the carmel river, monterey county, california, *Earth Surface Processes and Landforms*, *11*(3), 307–319.

Kondolf, G. M., and M. G. Wolman (1993), The sizes of salmonid spawning gravels, *Water Resources Research*, *29*(7), 2275–2285, doi:10.1029/93wr00402.

Kondolf, G. M., Y. Gao, G. W. Annandale, G. L. Morris, E. Jiang, J. Zhang, Y. Cao, P. Carling, K. Fu, Q. Guo, R. Hotchkiss, C. Peteuil, T. Sumi, H.-W. Wang, Z. Wang, Z. Wei, B. Wu, C. Wu, and C. T. Yang (2014), Sustainable sediment management in reservoirs and regulated rivers: Experiences from five continents, *Earths Future*, *2*(5), 256–280, doi:10.1002/2013ef000184.

Korup, O. (2013), 9.15 Landslides in the Fluvial System, pp. 244–259, doi:10.1016/b978-0-12-374739-6.00240-2.

Lisle, T. E., and M. Church (2002), Sediment transport-storage relations for degrading, gravel bed channels, *Water Resources Research*, *38*(11), 1–1–1–14, doi:10.1029/2001wr001086.

Lisle, T. E., J. E. Pizzuto, H. Ikeda, F. Iseya, and Y. Kodama (1997), Evolution of a sediment wave in an experimental channel, *Water Resources Research*, *33*(8), 1971–1981, doi:10.1029/97wr01180.

Lisle, T. E., Y. Cui, G. Parker, J. E. Pizzuto, and A. M. Dodd (2001), The dominance of dispersion in the evolution of bed material waves in gravel-bed rivers, *Earth Surface Processes and Landforms*, *26*(13), 1409–1420, doi:10.1002/esp.300.

Luzi, D. S. (2014), Sediment transport and morphological response of a semi-alluvial channel: insights from a froude scaled laboratory model, PhD thesis, University of British Columbia, doi:10.14288/1.0165910.

MacKenzie, L. G., and B. C. Eaton (2017), Large grains matter: contrasting bed stability and morphodynamics during two nearly identical experiments, *Earth Surface Processes and Landforms*, *42*(8), 1287–1295, doi:10.1002/esp.4122.

Madej, M. A. (1999), Temporal and spatial variability in thalweg profiles of a gravel-bed river, *Earth Surface Processes and Landforms*, *24*(12), 1153–1169, doi:10.1002/(SICI)1096-9837(199911)24:12<1153::AID-ESP41>3.0.CO;2-8.

Madej, M. A. (2001), Development of channel organization and roughness following sediment pulses in single-thread, gravel bed rivers, *Water Resources Research*, *37*(8), 2259–2272, doi:10.1029/2001wr000229.

Madej, M. A., and V. Ozaki (1996), Channel response to sediment wave propagation and movement, Redwood Creek, California, USA, *Earth Surface Processes and Landforms*, *21*(10), 911–927, doi:10.1002/(sici)1096-9837(199610)21:10<911::aid-esp621>3.0.co;2-1.

Major, J. J., J. E. OConnor, C. J. Podolak, M. K. Keith, G. E. Grant, K. R. Spicer, S. Pittman, H. M. Bragg, J. R. Wallick, D. Q. Tanner, et al. (2012), *Geomorphic response of the Sandy River, Oregon, to removal of Marmot Dam*, US Department of the Interior, US Geological Survey.

Major, J. J., A. E. East, J. E. O'Connor, G. E. Grant, A. C. Wilcox, C. S. Magirl, M. J. Collins, and D. D. Tullos (2017), Geomorphic responses to dam removal in the united states–a two-decade perspective, *D. Tsutsumi, D. and JB Laronne (eds), Gravel-Bed Rivers: Processes and Disasters. New York, NY: John Wiley and Sons*, pp. 355–383, doi:10.1002/9781118971437.ch13.

Markham, K., J. Palmer, M. F. Friebel, and L. F. Trujillo (1992), Pacific Slope Basins from Arroyo Grande to Oregon State Line except Central Valley. US Geological Survey Water-Data Report CA-92-2.

Markstrom, S. L., R. S. Regan, L. E. Hay, R. J. Viger, R. M. Webb, R. A. Payn, and J. H. LaFontaine (2015), PRMS-IV, the precipitation-runoff modeling system, version 4, *US Geological Survey Techniques and Methods*, (6-B7).

May, C. L., and T. E. Lisle (2012), River profile controls on channel morphology, debris flow disturbance, and the spatial extent of salmonids in steep mountain streams, *Journal of Geophysical Research*, *117*, doi:10.1029/2011JF002324.

MEI (2002), Carmel River Sediment-Transport Study, Monterey County, California. Report prepared for California Department of Water Resources.

MEI (2003), San Clemente Reservoir and Carmel River Sediment-Transport Modeling to Evaluate Potential Impacts of Dam Retrofit Options. Submitted to American Water Works Service Company. .

Miller, D. J., and L. E. Benda (2000), Effects of punctuated sediment supply on valley-floor landforms and sediment transport, *Geological Society of America Bulletin*, *112*(12), 1814–1824, doi:10.1130/0016-7606(2000)112<1814:eopsso>2.0.co;2.

Montgomery, D. R. (1999), Process domains and the river continuum, *JAWRA Journal of the American Water Resources Association*, *35*(2), 397–410.

Montgomery, D. R., and J. M. Buffington (1997), Channel-reach morphology in mountain drainage basins, *Geological Society of America Bulletin*, *109*(5), 596–611.

Montgomery, D. R., and E. Foufoula-Georgiou (1993), Channel network source representation using digital elevation models, *Water Resources Research*, *29*(12), 3925–3934.

MPWD (1986), Unpublished sediment transport measurements, carmel river, water years 1984 - 1986.

MPWMD (2016), Request for Proposals Los Padres Dam and Reservoir Alternatives and Sediment Management Study.

Nelson, A. D., and M. Church (2012), Placer mining along the fraser river, british columbia: the geomorphic impact, *Bulletin*, *124*(7-8), 1212–1228.

Nelson, P. A., J. G. Venditti, W. E. Dietrich, J. W. Kirchner, H. Ikeda, F. Iseya, and L. S. Sklar (2009), Response of bed surface patchiness to reductions in sediment supply, *Journal of Geophysical Research: Earth Surface*, *114*(F2), doi:10.1029/2008jf001144.

Normandeau (2016), Carmel river cross-section surveys.

Oreskes, N., K. Shrader-Frechette, and K. Belitz (1994), Verification, validation, and confirmation of numerical models in the earth sciences, *Science*, *263*(5147), 641–646.

Paola, C., G. Parker, D. C. Mohrig, and K. X. Whipple (1999), The influence of transport fluctuations on spatially averaged topography on a sandy, braided fluvial fan, in *Numerical Experiments in Stratigraphy: Recent Advances in Stratigraphic and Sedimentologic Computer Simulations*, edited by J. Harbaugh, W. Watney, and E. Rankey, pp. 211–218, Special Publications of SEPM.

Papangelakis, E., and M. A. Hassan (2016), The role of channel morphology on the mobility and dispersion of bed sediment in a small gravel-bed stream, *Earth Surface Processes and Landforms*, *41*(15), 2191–2206, doi:10.1002/esp.3980.

Parker, G. (1991), Selective sorting and abrasion of river gravel. i: Theory, *Journal of Hydraulic Engineering*, *117*(2), 131–147, doi:10.1061/(asce)0733-9429(1991)117:2(131).

Parker, G. (2008), Transport of gravel and sediment mixtures, in *Sedimentation Engineering*, vol. 110, pp. 165–251, American Society of Civil Engineers, doi:10.1061/9780784408148.ch03.

Parker, G., M. Hassan, and P. Wilcock (2007), 10 adjustment of the bed surface size distribution of gravel-bed rivers in response to cycled hydrographs, in *Gravel-Bed Rivers VI: From Process Understanding to River Restoration*, pp. 241–285, Elsevier, doi:10.1016/s0928-2025(07)11127-5.

Pfeiffer, A. M., N. J. Finnegan, and J. K. Willenbring (2017), Sediment supply controls equilibrium channel geometry in gravel rivers, *Proceedings of the National Academy of Sciences*, *114*(13), 3346–3351, doi:10.1073/pnas.1612907114.

Phillips, J. D. (2003), Sources of nonlinearity and complexity in geomorphic systems, *Progress in Physical Geography*, *27*(1), 1–23.

Podolak, C. J. P., and P. R. Wilcock (2013), Experimental study of the response of a gravel streambed to increased sediment supply, *Earth Surface Processes and Landforms*, *38*(14), 1748–1764, doi:10.1002/esp.3468.

Pryor, B. S., T. Lisle, D. S. Montoya, and S. Hilton (2011), Transport and storage of bed material in a gravel-bed channel during episodes of aggradation and degradation: a field and flume study, *Earth Surface Processes and Landforms*, *36*(15), 2028–2041, doi:10.1002/esp.2224.

Recking, A. (2012), Influence of sediment supply on mountain streams bedload transport, *Geomorphology*, *175-176*, 139–150, doi:10.1016/j.geomorph.2012.07.005.

Rice, S., and M. Church (1996), Sampling surficial fluvial gravels; the precision of size distribution percentile sediments, *Journal of Sedimentary Research*, *66*(3), 654–665.

Rice, S., and M. Church (1998), Grain size along two gravel-bed rivers: statistical variation, spatial pattern and sedimentary links, *Earth Surface Processes and Landforms*, *23*(4), 345–363, doi:10.1002/(sici)1096-9837(199804)23:4<345::aid-esp850>3.0.co;2-b.

Roberts, R. G., and M. Church (1986), The sediment budget in severely disturbed watersheds, queen charlotte ranges, british columbia, *Canadian Journal of Forest Research*, *16*(5), 1092–1106, doi:10.1139/x86-189.

Ronneberger, O., P. Fischer, and T. Brox (2015), U-net: Convolutional networks for biomedical image segmentation, in *International Conference on Medical image computing and computer-assisted intervention*, pp. 234–241, Springer, Springer International Publishing, doi:10.1007/978-3-319-24574-4_28.

Schrott, L., G. Hufschmidt, M. Hankammer, T. Hoffmann, and R. Dikau (2003), Spatial distribution of sediment storage types and quantification of valley fill deposits in an alpine basin, reintal, bavarian alps, germany, *Geomorphology*, *55*(1), 45–63.

Simonyan, K., and A. Zisserman (2014), Very deep convolutional networks for large-scale image recognition, *arXiv preprint arXiv:1409.1556*.

Sklar, L. S., J. Fadde, J. G. Venditti, P. Nelson, M. A. Wydzga, Y. Cui, and W. E. Dietrich (2009), Translation and dispersion of sediment pulses in flume experiments simulating gravel augmentation below dams, *Water Resources Research*, *45*(8), doi:10.1029/2008wr007346.

Slaymaker, O. (2003), The sediment budget as conceptual framework and management tool, in *The Interactions between Sediments and Water*, *Developments in Hydrobiology*, vol. 169, edited by B. Kronvang, pp. 71–82, Springer Netherlands, doi:10.1007/978-94-017-3366-3_12.

Sthly, S., H. Friedrich, and M. Detert (2017), Size ratio of fluvial grains' intermediate axes assessed by image processing and square-hole sieving, *Journal of Hydraulic Engineering*, *143*(6), 06017,005, doi:10.1061/(asce)hy.1943-7900.0001286.

Tetra Tech (2015), Final Design Report for Channel Restoration Design for the Carmel River Reroute and San Clemente Dam Removal (CRRDR) project.

Thomas, M. F. (2001), Landscape sensitivity in time and spacean introduction, *Catena*, *42*(2-4), 83–98, doi:10.1016/s0341-8162(00)00133-8.

Tucker, G. E., and R. L. Bras (1998), Hillslope processes, drainage density, and landscape morphology, *Water Resources Research*, *34*(10), 2751–2764, doi:10.1029/98wr01474.

URS (2013), Carmel River Reroute & San Clemente Dam Removal Project: Draft Subtask 4.2.2 River Flood & Sediment Transport Modeling Technical Memorandum. Consulting report prepared for the State Coastal Conservancy and California American Water.

Van De Wiel, M. J., T. J. Coulthard, M. G. Macklin, and J. Lewin (2011), Modelling the response of river systems to environmental change: progress, problems and prospects for palaeo-environmental reconstructions, *Earth-Science Reviews*, *104*(1-3), 167–185, doi:10.1016/j.earscirev.2010.10.004.

Venditti, J. G., W. E. Dietrich, P. A. Nelson, M. A. Wydzga, J. Fadde, and L. Sklar (2010), Effect of sediment pulse grain size on sediment transport rates and bed mobility in gravel bed rivers, *Journal of Geophysical Research: Earth Surface*, *115*(F3), doi:10.1029/2009jf001418.

Viparelli, E., O. E. Sequeiros, A. Cantelli, P. R. Wilcock, and G. Parker (2010), River morphodynamics with creation/consumption of grain size stratigraphy 2: numerical model, *Journal of Hydraulic Research*, *48*(6), 727–741, doi:10.1080/00221686.2010.526759.

Viparelli, E., D. Gaeuman, P. Wilcock, and G. Parker (2011), A model to predict the evolution of a gravel bed river under an imposed cyclic hydrograph and its application to the trinity river, *Water Resources Research*, *47*(2).

von Flotow, C. (2013), Temporal adjustments of a streambed following an episodic sediment supply regime, Master's thesis, University of British Columbia, doi:10.14288/1.007421.

Warrick, J. A., D. M. Rubin, P. Ruggiero, J. N. Harney, A. E. Draut, and D. Buscombe (2009), Cobble cam: grain-size measurements of sand to boulder from digital photographs and autocorrelation analyses, *Earth Surface Processes and Landforms*, *34*(13), 1811–1821, doi:10.1002/esp.1877.

Whitson Engineers (2017), Carmel River Thalweg Survey.

Wilcock, P. R. (2001), Toward a practical method for estimating sediment-transport rates in gravel-bed rivers, *Earth Surface Processes and Landforms*, *26*(13), 1395–1408, doi:10.1002/esp.301.

Wilcock, P. R., and J. C. Crowe (2003), Surface-based transport model for mixed-size sediment, *Journal of Hydraulic Engineering*, *129*(2), 120–128, doi:10.1061/(asce)0733-9429(2003)129:2(120).

Wilcock, P. R., and R. M. Iverson (2003), *Prediction in geomorphology*, 3–11 pp., Wiley Online Library, doi:10.1029/135gm01.

Wilcock, P. R., and B. W. McArdell (1993), Surface-based fractional transport rates: Mobilization thresholds and partial transport of a sand-gravel sediment, *Water Resources Research*, *29*(4), 1297–1312.

Wilcox, A. C., J. E. O'Connor, and J. J. Major (2014), Rapid reservoir erosion, hyperconcentrated flow, and downstream deposition triggered by breaching of 38 m tall condit dam, white salmon river, washington, *Journal of Geophysical Research: Earth Surface*, *119*(6), 1376–1394, doi:10.1002/2013jf003073.

Willgoose, G. R., G. R. Hancock, and G. Kuczera (2003), A framework for the quantitative testing of landform evolution models, *Prediction in geomorphology*, *135*, 195–216, doi:10.1029/135gm14.

Witten, I. H., E. Frank, M. A. Hall, and C. J. Pal (2016), *Data Mining: Practical machine learning tools and techniques*, Morgan Kaufmann.

Wohl, E. (2013), *Mountain rivers revisited*, vol. 19, John Wiley & Sons.

Wolman, M. G. (1954), A method of sampling coarse river-bed material, *EOS, Transactions American Geophysical Union*, *35*(6), 951–956.

Wolman, M. G., and J. P. Miller (1960), Magnitude and frequency of forces in geomorphic processes, *The Journal of Geology*, *68*(1), 54–74, doi:10.1086/626637.

Wong, M., and G. Parker (2006), One-dimensional modeling of bed evolution in a gravel bed river subject to a cycled flood hydrograph, *Journal of Geophysical Research: Earth Surface*, *111*(F3), n/a–n/a, doi:10.1029/2006jf000478.

Woodget, A., C. Fyffe, and P. Carbonneau (2018), From manned to unmanned aircraft: Adapting airborne particle size mapping methodologies to the characteristics of suas and sfm, *Earth Surface Processes and Landforms*, *43*(4), 857–870, doi:10.1002/esp.4285.

Zimmermann, A., M. Church, and M. A. Hassan (2010), Step-pool stability: Testing the jammed state hypothesis, *Journal of Geophysical Research: Earth Surface (2003–2012)*, *115*(F2).

Zimmermann, A. E., M. Church, and M. A. Hassan (2008), Video-based gravel transport measurements with a flume mounted light table, *Earth Surface Processes and Landforms*, *33*(14), 2285–2296.

Appendix A

Sensitivity analysis plots for BESMo in episodic supply experiments

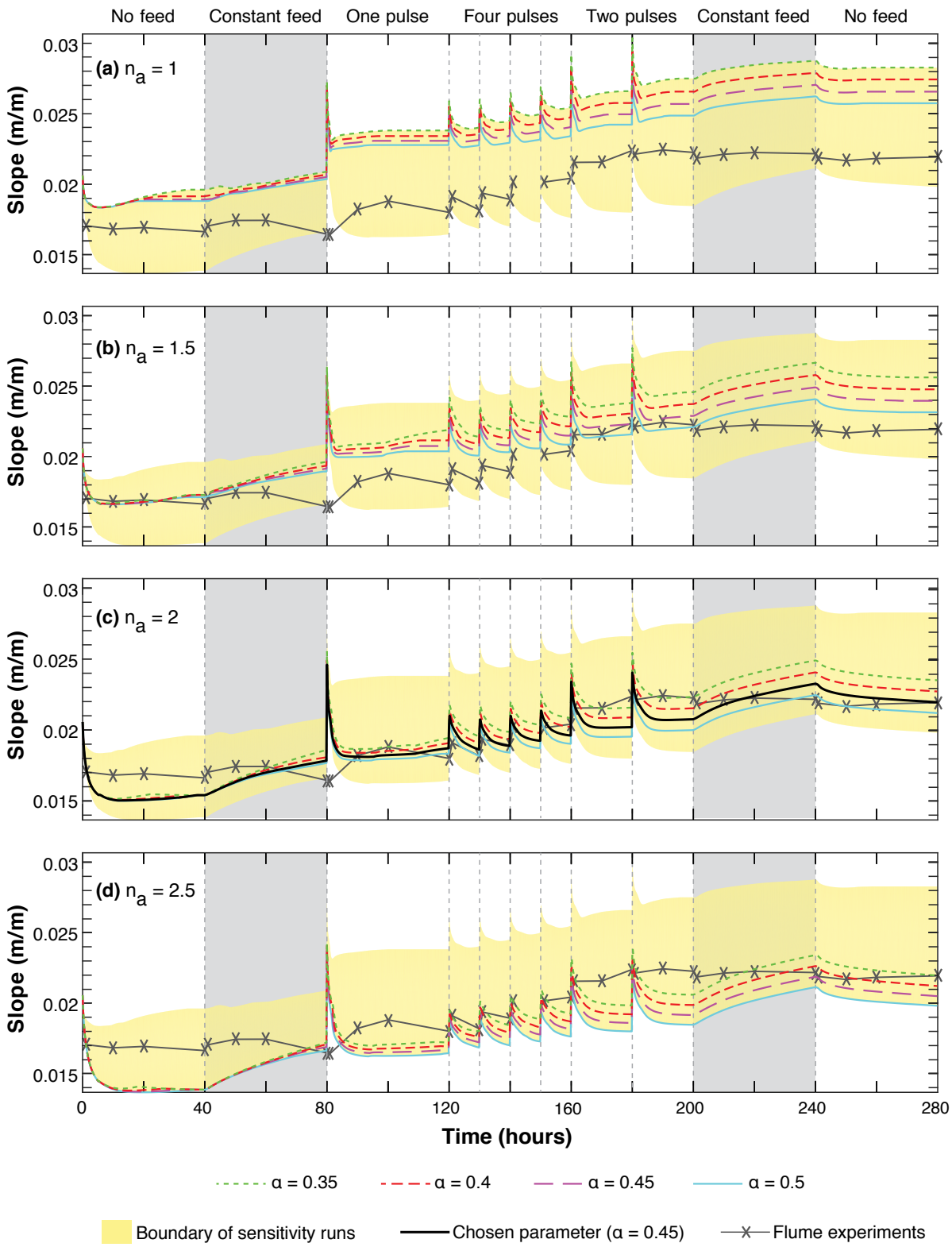

Figure A.1: Sensitivity of modelled slope to active layer thickness factor n_a and active layer exchange ratio α in the 'Original flume' (OF) event sequence.

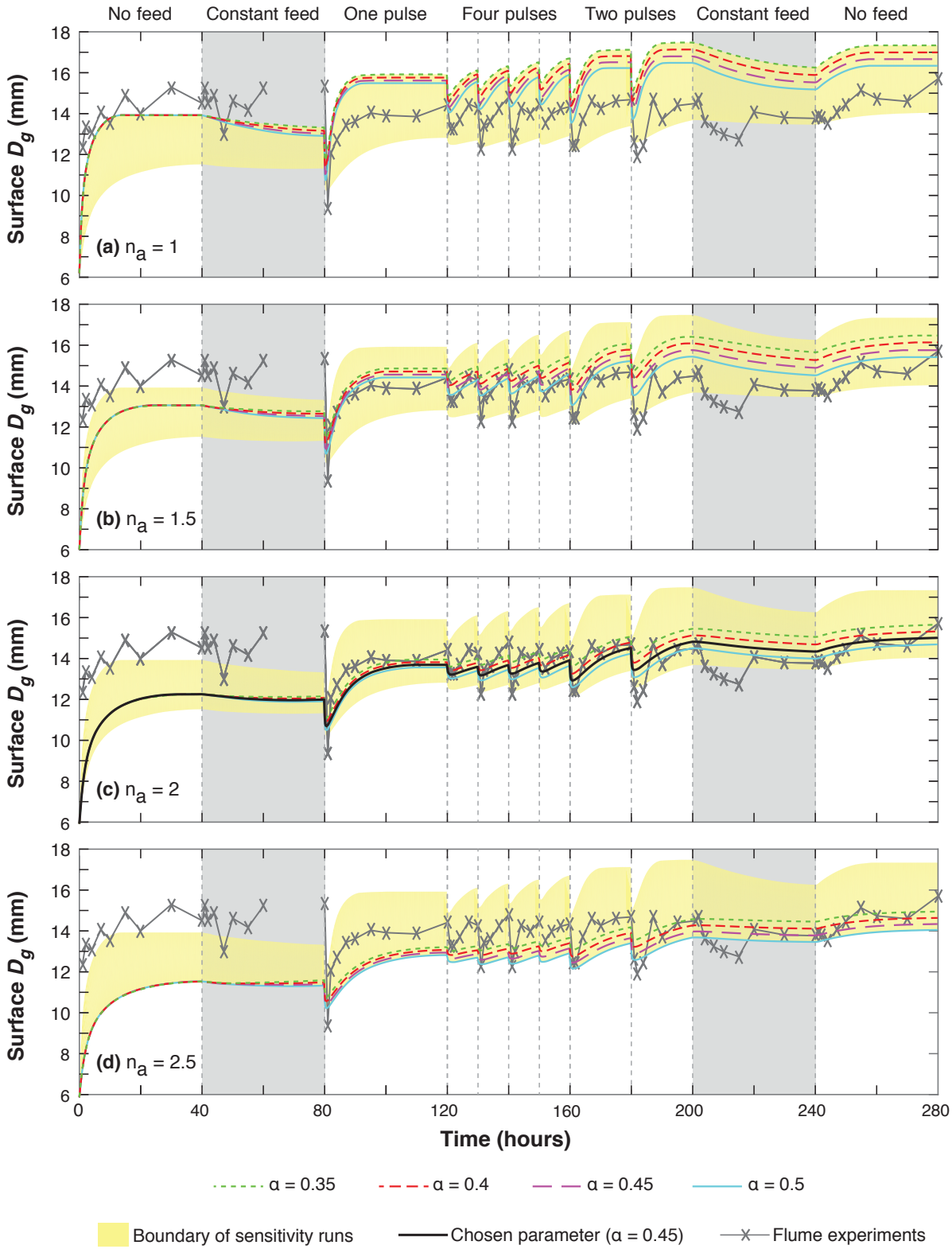

Figure A.2: Sensitivity of modelled Surface D_g to active layer thickness factor n_a and active layer exchange ratio α in the 'Original flume' (OF) event sequence.

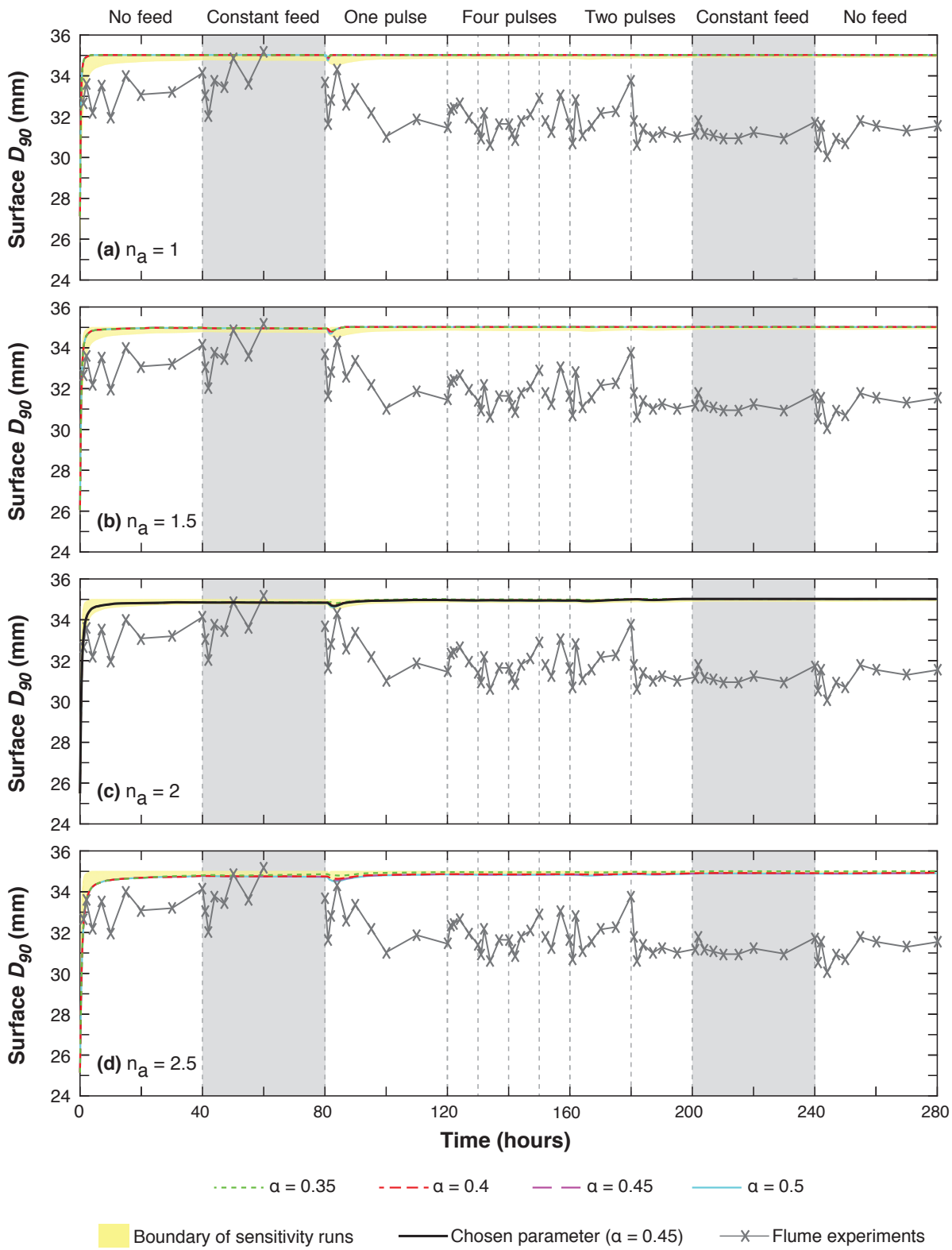

Figure A.3: Sensitivity of modelled Surface D_{90} to active layer thickness factor n_a and active layer exchange ratio α in the 'Original flume' (OF) event sequence.

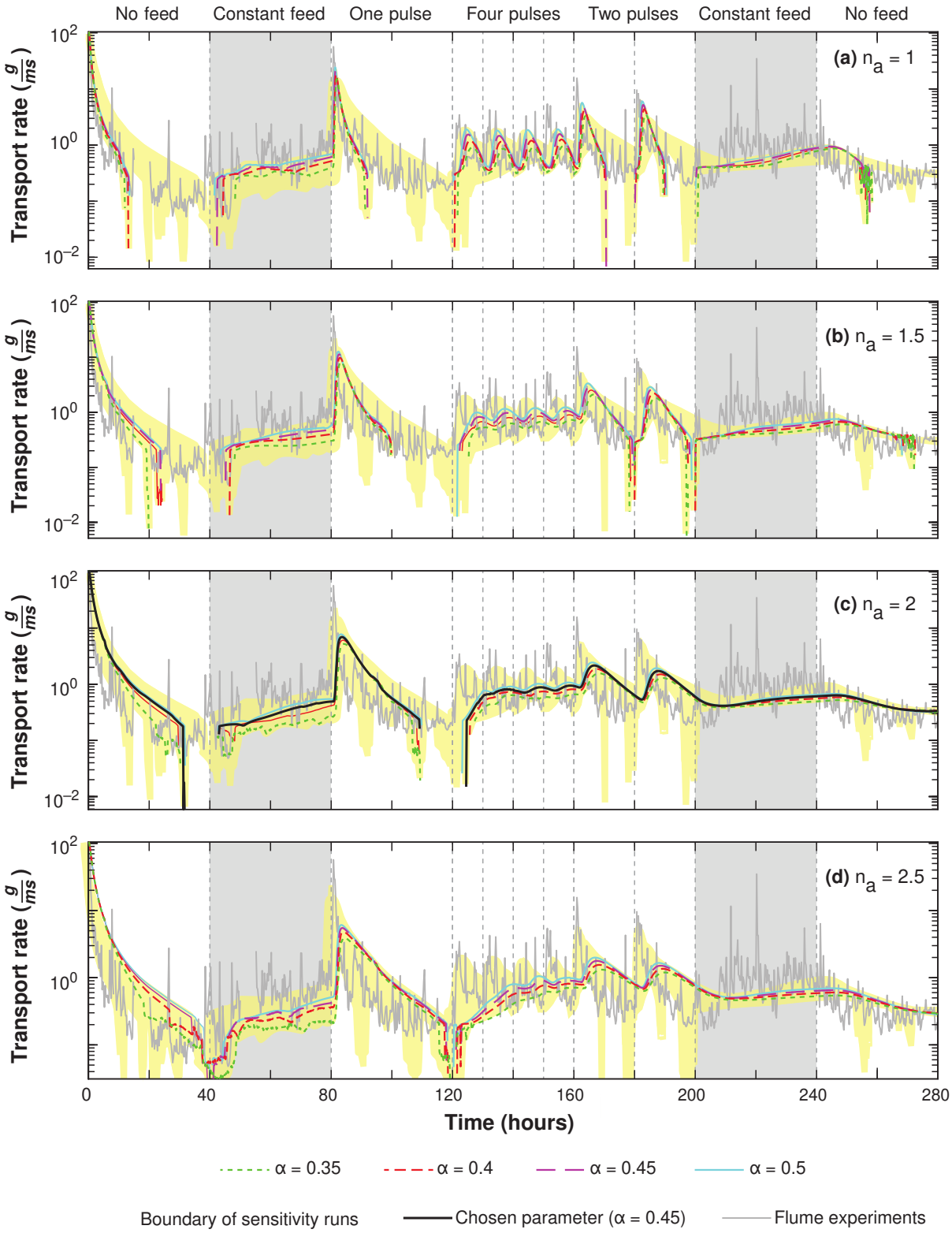

Figure A.4: Sensitivity of modelled transport rate to active layer thickness factor n_a and active layer exchange ratio α in the 'Original flume' (OF) event sequence.

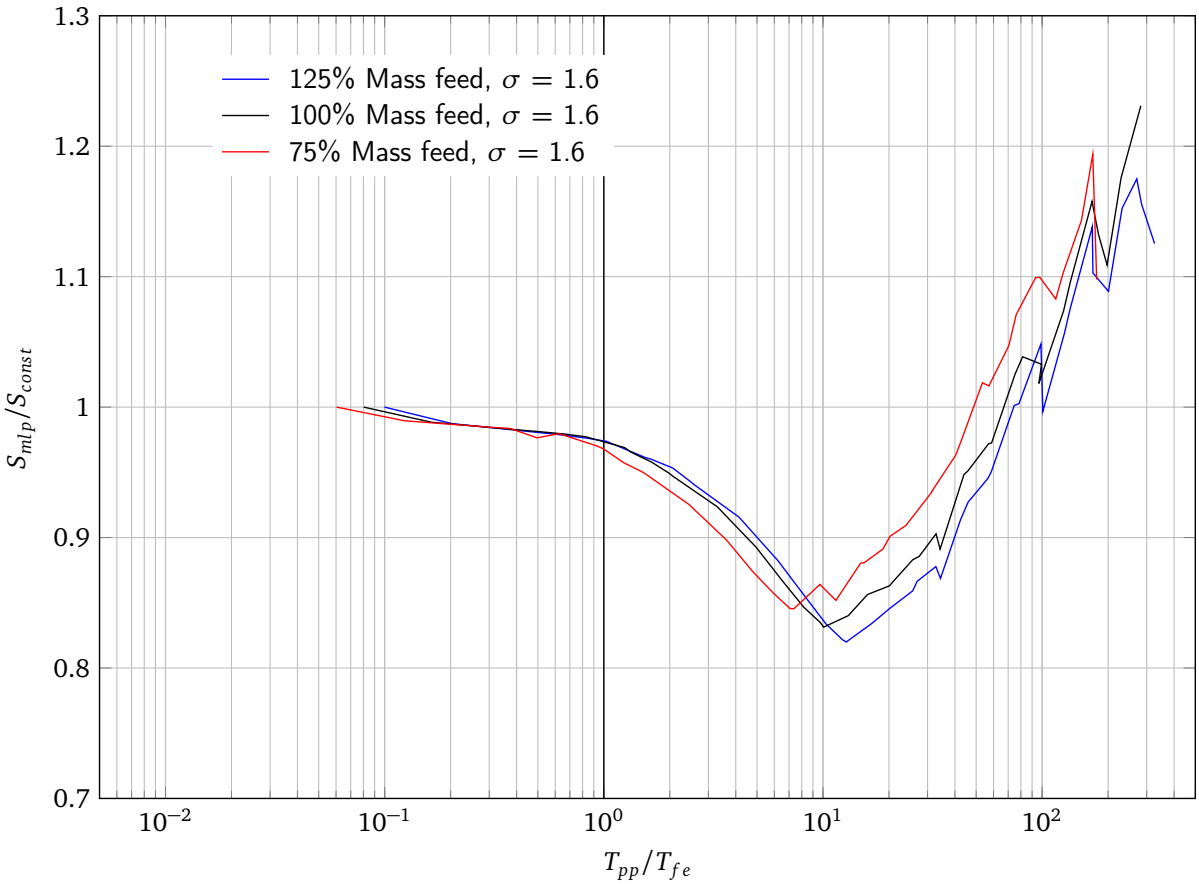

Figure A.5: Effect of a 25% increased and 25% decreased total sediment feed on the equilibrium slope in the non-dimensionalized time scale. All simulations were executed with $\sigma = 1.6$.

Appendix B

Los Padres Dam removal supplementary material

B.1 Model testing

The following demonstrates the key model evaluation steps and tests directed by the technical review committee (TRC) and evaluated by the project team. Model iterations were pursued to produce results that are more suitable for informing the project alternative assessment process and so the results of those iterative tests are included in this report.

Prior to executing the No Action Simulation, the TRC requested a comparison of longitudinal profile adjustment within the San Clemente project reach (model station 99,015 to 105,000 feet upstream of the Pacific Ocean), for the period water years 2015- 2017 (WY2015-17). Comparison was made between BESMo and observations of channel elevation change at select channel locations within the San Clemente project reach. The comparison period was simulated within BESMo for the hydrograph shown in Figure B.1, subject to the peaking factor adjustments. The measured longitudinal profiles for the project reach were collected in early 2014 and in 2017 and were generously provided to us by Doug Smith of CSUMB.

We modified the Carmel River build of BESMo for this comparison in three ways. First, we implemented a local model build with more closely spaced nodes within the project reach in order to provide for a better comparison between model and observation. The inset plot

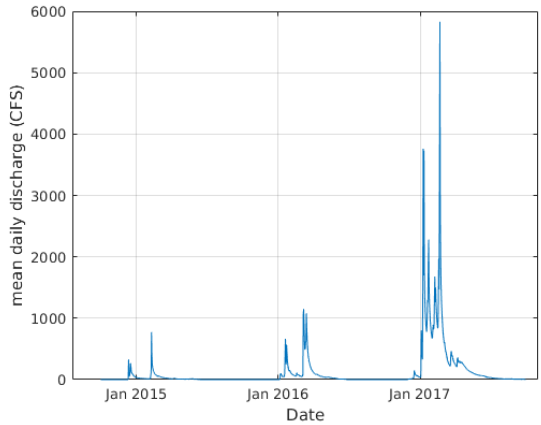

Figure B.1: Hydrograph used in the San Clemente comparison. Hydrograph represents mean daily flow reported for the RR gage by the USGS.

of Figure B.2 illustrates the nodes used for the San Clemente comparative simulation, and the initial model longitudinal profile for the project reach was taken from the final San Clemente project design (Tetra Tech, 2015). Second and after a few trial runs to evaluate model fidelity within the relatively steep and coarse combined flow steppool segments of the San Clemente project reach, we lowered the volumetric content of fine channel substrate to 33% (from 50%) and accordingly increased the coarse mixture content to 66% (from 50%). Figure B.3 illustrates the GSD used in the BESMo simulation for the former reservoir deposits upstream of the reroute reach, and for the steeper constructed step-pool channel segments. Last, due to the short distance between nodes, we reduced the model time step to 1 second during periods of bedload transport, otherwise we used a time step of 5 minutes. This change in the model was tested and confirmed to not affect the simulated results. No other changes were made to the Carmel River build of BESMo.

The San Clemente project reach comparative results are shown in Figure B.4 and Figure B.5. Figure B.4 shows the longitudinal profiles for BESMo and observation (labeled as post within the legend) in WY2014 and WY2017, separately. The WY2017 profiles represent the adjustment through the project reach due primarily to the floods of WY2017 (Figure B.5). A few relevant observations can be made. First, differences between BESMo and the WY2017 observations generally range from less than 0.5 to 1.0 meters, for most of the project reach, except at the San Clemente Creek tributary node and the very downstream end of the project reach. Second,

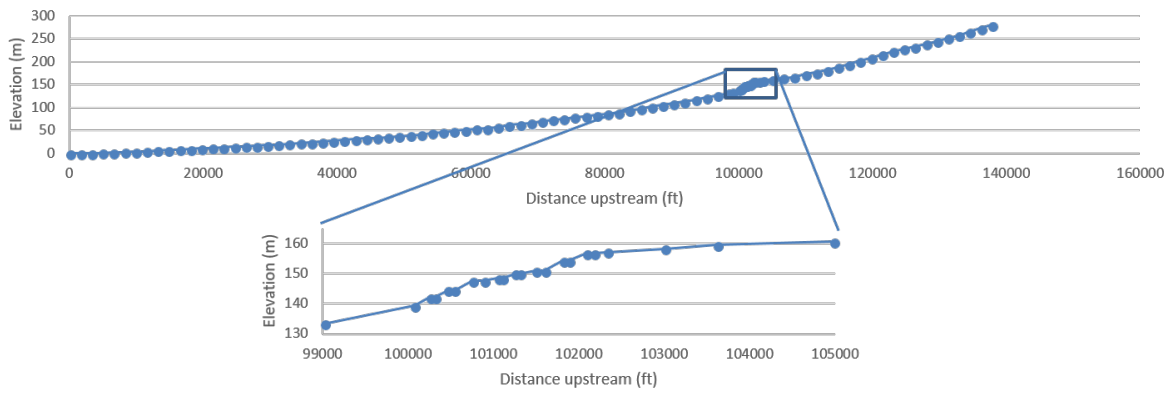

Figure B.2: BESMo simulation nodes for the reroute corridor at the former San Clemente Reservoir. The detailed view shows the higher-resolution of nodes within the reroute channel.

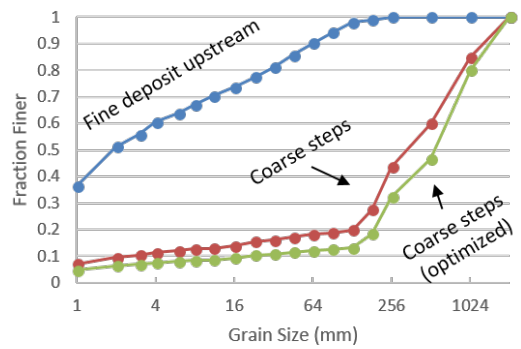

Figure B.3: Grain size distributions of both the fine upstream deposits (MEI, 2002) and the coarse steps (Tetra Tech, 2015).

the general spatial pattern of erosion and deposition between BESMo and the WY2017 observations is similar. There is notable agreement within the upper former reservoir deposits and through the middle part of the steeper step-pool channel segments. This is a bit surprising given the simplicity of how BESMo represents actual physical conditions and processes that give rise to river profiles.

Third, differences between BESMo and WY2017 observations flip in trend around the San Clemente Creek tributary node. Last, BESMo simulates up to 1.5 feet of deposition by WY2017 within the downstream end of the combined flow reach, upstream of the former San Clemente Dam. Simulated deposition is largely a result of bed erosion simulated upstream from the downstream most channel segment. Despite these differences, BESMo does a reasonably good

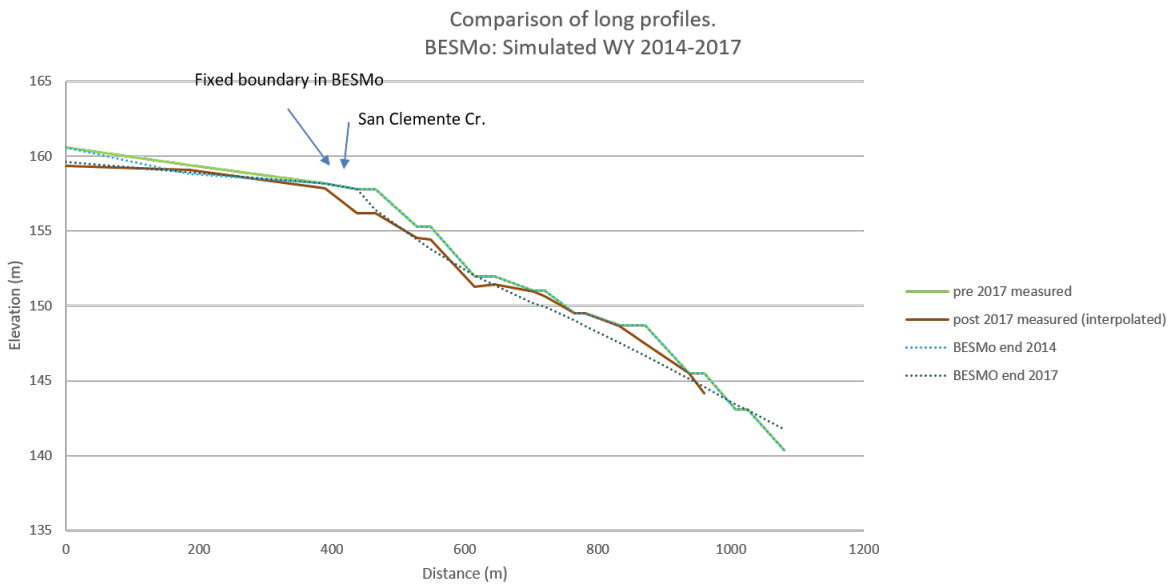

Figure B.4: 4 Comparison between the measured and simulated reroute channel long profiles over the comparative period of WY2014-17.

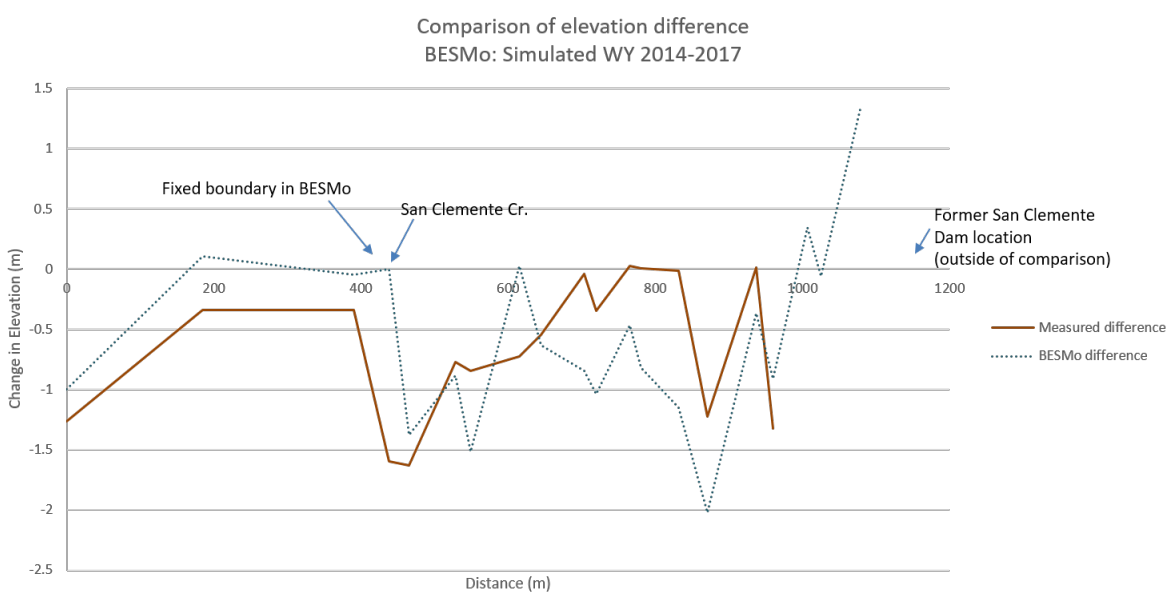

Figure B.5: Elevation difference between the measured and simulated reroute channel long profiles over three years.

job of capturing net erosion within the former reservoir deposit, as well as the reach average bed slope downstream of San Clemente Creek to just upstream of the former San Clemente Dam. As discussed above, results are sensitive to the initial GSDs for the surface and sub-

surface sediments. Given this sensitivity, it is encouraging that BESMo compares with observations as well as it does because a 3-year simulation period with very little net adjustment during the first two years is a difficult basis for comparison between a simplified numerical model, and real-world conditions within a steep, and spatially complex channel segment within which sediment transport processes depart substantially from the empirical Wilcock-Crowe transport function.

B.2 Elevation data availability

We use three different sources of channel elevation data to construct the initial simulation longitudinal profile for the BESMo simulations (Figure B.6)

- Whitson Engineers survey of the main stem from the Lagoon to river station approximately 24 km upstream of the Lagoon (*Whitson Engineers*, 2017);
- URS HEC-RAS model build from the river station at 24 km to approximately 32 km for the San Clemente Dam removal scenario (*URS*, 2013);
- USGS National Elevation Dataset, spatial resolution 1/9th arc-second (NED19) from head of former San Clemente Dam reservoir to Los Padres Dam at river station approximately 42 km. This NED19 dataset was compiled by the authors of this report, as detailed channel geometry surveys are not available for the channel between the former reservoir deposit of San Clemente Dam and the Los Padres Dam. To convert the digital elevation model data to a channel long profile, we averaged elevation values recorded along the channel within a circular 100m area around the model nodes (Figure B.7).

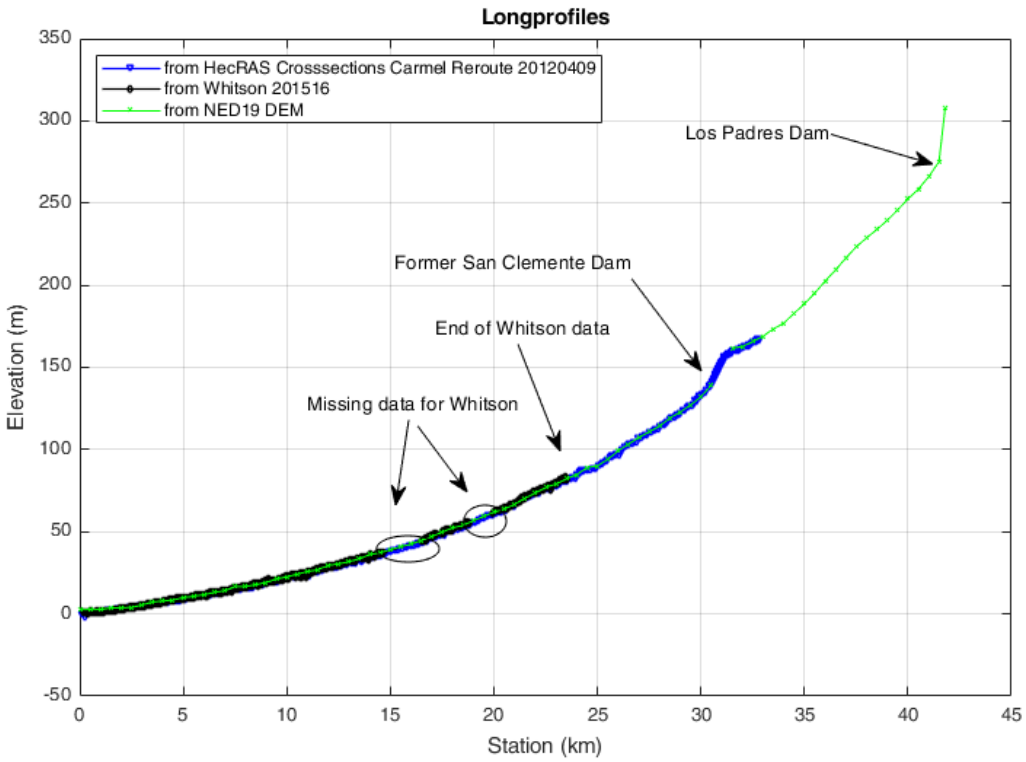

Figure B.6: Channel profile from the three data sources. Both *Whitson Engineers* (2017) and *URS* (2013) lack coverage of the upper section of the river. We used the NED19 dataset to fill the holes of the other data and generate a full profile of the study reach.

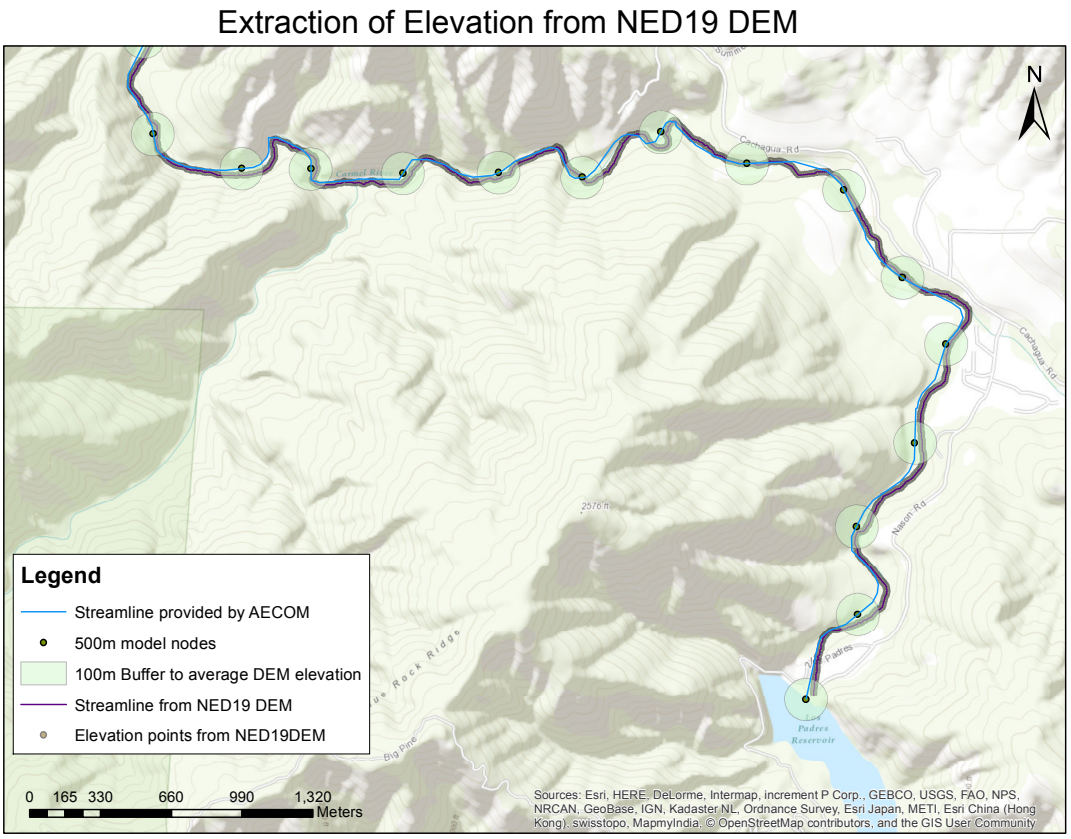

Figure B.7: Extraction of model node elevation from the NED19 (1/9th arc second digital elevation model) below the Los Padres Reservoir. For each 500m model node along the streamline, we averaged the elevation from NED19 within a 100m buffer along the streamline.

B.3 Sediment transport data availability

Sediment transport data has been collected in the Carmel River watershed sporadically from 1981 to 2001 in the mainstem and tributary channels. Sediment availability and transport rates can vary considerably both temporally and spatially in the watershed. Due to extreme episodic events such as fires and landslides, large pulses of sediment can significantly increase the sediment transport rates. We have collated the available bedload transport data, for both bedload and suspended sediment, and updated previous rating curves for each tributary and mainstem location.Each rating curve was estimated from available sediment transport data sourced from the USGS Water-Data Reports (*Markham et al.*, 1992; *Ayers*, 1995; *Freeman et al.*, 1996), Monterey Peninsula Water District field office data archives (*MPWD*, 1986), (*Curry and Kondolf*, 1983), and unpublished data collected by Balance Hydrologics for the San Clemente Dam Removal efforts (*Balance Hydrologics, Inc.*, 2001). Each rating curve was estimated using the best-fit power law when possible. When applicable, more representative rating curves were developed manually or with outliers not included.

Carmel River Mainstem Sediment Supply

The Carmel River at Via Mallorca has the most abundant sediment transport dataset. The site has been a USGS stream gage since 1962 making this site an ideal location to collect paired sediment-flow measurements. Data has also been collected at Schulte Bridge, Robinson Canyon Road, and Robles del Rio. Appendix B.4 presents the sediment rating curves for each mainstem location with available data.

Carmel River Watershed Tributary Sediment Supply

A considerable portion of the total sediment load in the Carmel River watershed comes from the tributaries. There are seven major tributaries in the Carmel River watershed that have been historically monitored: Tularcitos Creek, Cachagua Creek, San Clemente Creek, Las Garzas Creek, Robinson Canyon Creek, Potrero Creek, and Hitchcock Creek. The hydrologic and sediment contribution from each tributary to the mainstem Carmel River varies, dependent upon the mean annual rainfall in the contributing watershed and the underlying geology and as-

sociated sediment production processes. For example, the underlying geology in the Tularcitos Creek watershed is largely sourced from the easily erodible Santa Margarita sandstone, which introduces an abundance of sand. Despite a low mean annual precipitation, the Tularcitos Creek watershed supplies a lot of sand, considerably changing the sediment character downstream of the Tularcitos Creek confluence. Table B.1 summarizes the differences in mean annual precipitation and geology in each of the main tributaries.

Table B.1: Summary of Carmel River watershed major tributaries; Mean annual precipitation, watershed size, and geology.

Tributary	Watershed Size (km^2)	Mean Annual Percipitation (mm)[1]	Geology[2]
Tularcitos Creek	90.6	546	San Margarita Sandstone, Miocene Marine clastic shale, sandstone, and conglomerate
Cachagua Creek	74.5	805	Mixed Miocene marine sandstone and Mesozoic granitic rocks
San Clemente Creek	25.1	950	Mesozoic granitic rocks, with some Mesozoic metasedimentary rocks
Las Garcas Creek	21.2	724	Mesozoic granitic rocks, with some Miocene unnamed sedimentary redbeds
Robinson Canyon Creek	8.7	564	Miocene unnamed sedimentary redbeds and marine sandstone
Potrero Creek	9.3	582	Miocene Monterey Formation shale, and Quaternary landslide and alluvial gravel, sand, and silt/clay
Hitchcock Creek	7.4	635	Mesozoic granitic rocks, primarily granodiorite, some Miocene marine rocks

[1] Estimated using Monterey County Isohyetal lines of average annual Rainfall in inches, published May 14,2014, accessed April 30, 2018

[2] Geologic information sourced from Geologic maps of various quadrangles scale 1:24,000, *Dibblee and Minch* (2007)

Pine Creek, located to the south of San Clemente Creek, is another major tributary in the Carmel River watershed. Because access to Pine Creek is difficult, there is limited sediment transport and hydrologic data available and so rating curves were not developed. Ap-

pendix B.5 presents the sediment rating curves for each tributary with available data.Bedload data for Tularcitos Creek suggests a two-phase rating curve with one rating curve for flows less than 0.4 m^3s^{-1} and another for flows 0.4 m^3s^{-1} and greater. Although the precise reason for this two-phase rating curve cannot be conclusively determined without further study, we hypothesize sediment availability is a function of bank geometry and erodibility changes with height. The data used to develop the San Clemente Creek rating curves were collected at two different locations on San Clemente Creek; *Curry and Kondolf* (1983) collected samples at the inlet to the former San Clemente Reservoir and Balance Hydrologics staff collected samples approximately 3.2 km upstream. For the bedload rating curve, 4 of the 5 available points were collected by Balance Hydrologics at the upper site. The one measurement presented in *Curry and Kondolf* (1983) is consistent with the Balance Hydrologics rating curve. No sediment transport data was collected in Hitchcock Canyon Creek, but *Curry and Kondolf* (1983) report sediment rating curves, which are presented here.

B.4 Rating Curves Mainstem

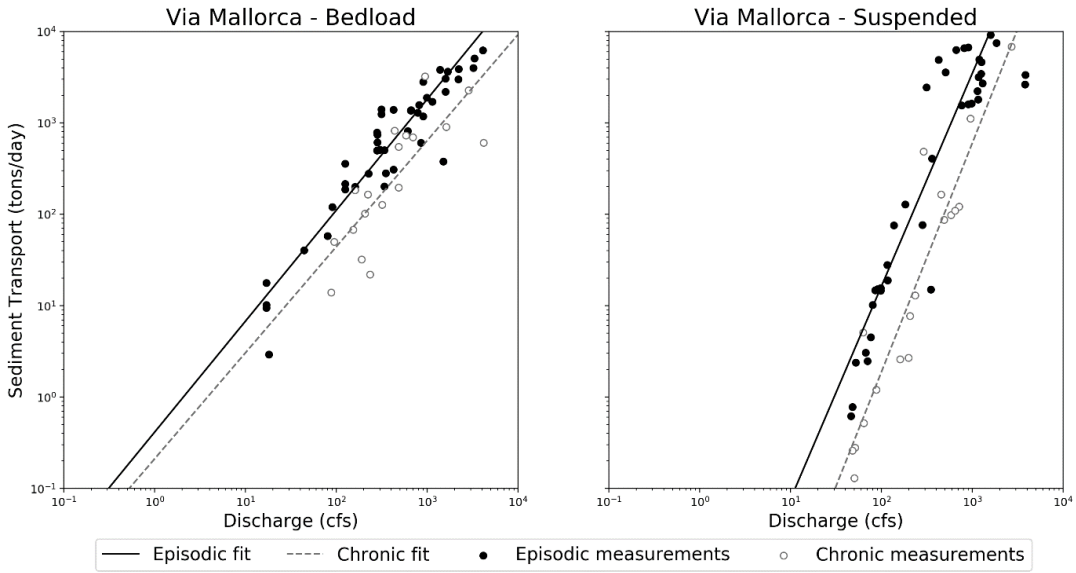

Figure B.8: Rating curves for Carmel River at Via Mallorca. The site is co-located with USGS gage 11143250.

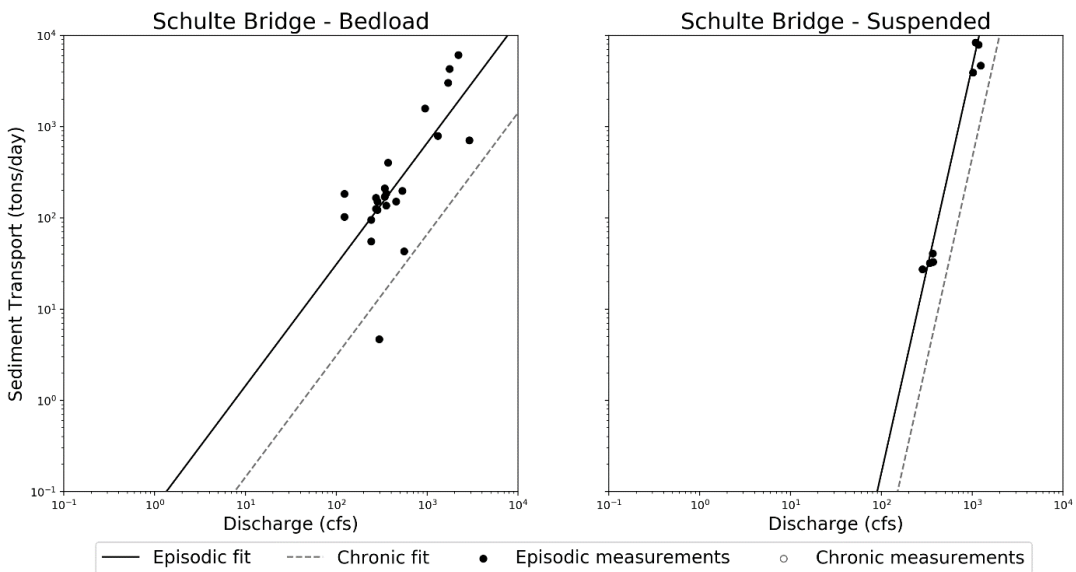

Figure B.9: Rating curves for Carmel River at Schulte Bridge.

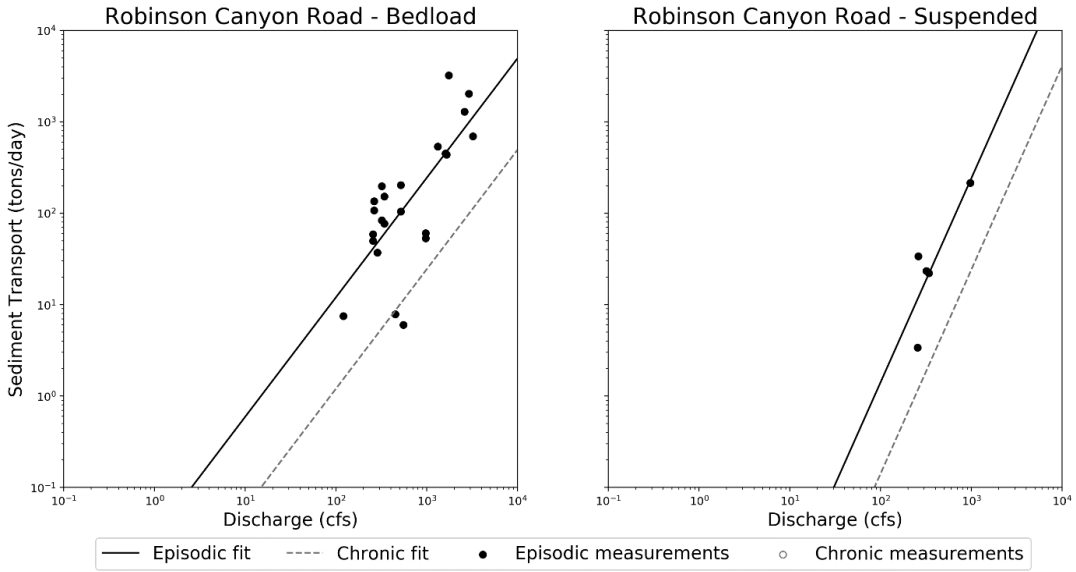

Figure B.10: Rating curves for Carmel River at Robinson Canyon Road.

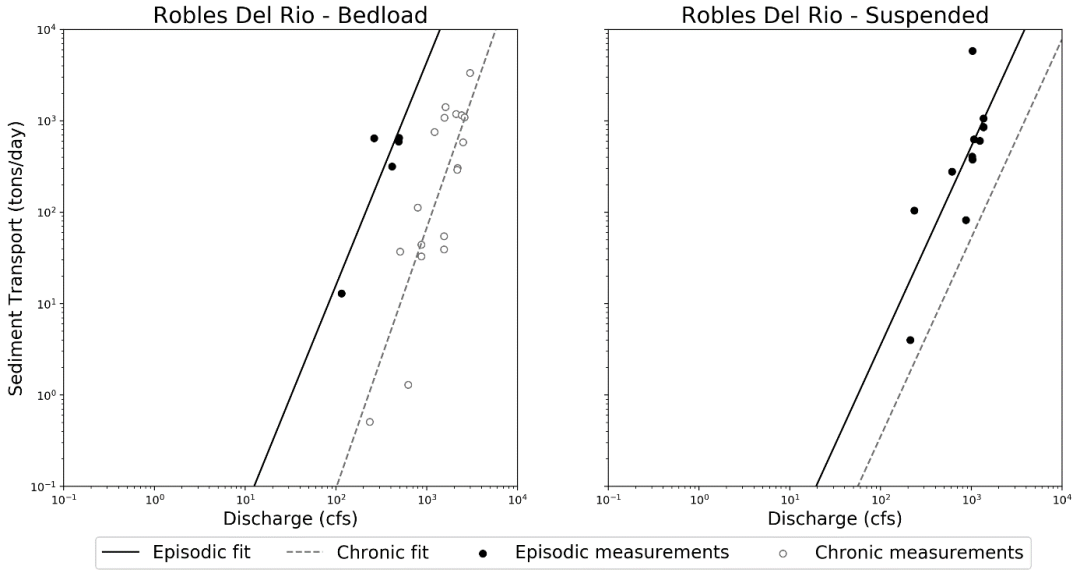

Figure B.11: Rating curves for Carmel River at Robles del Rio.

B.5 Rating Curves Tributaries

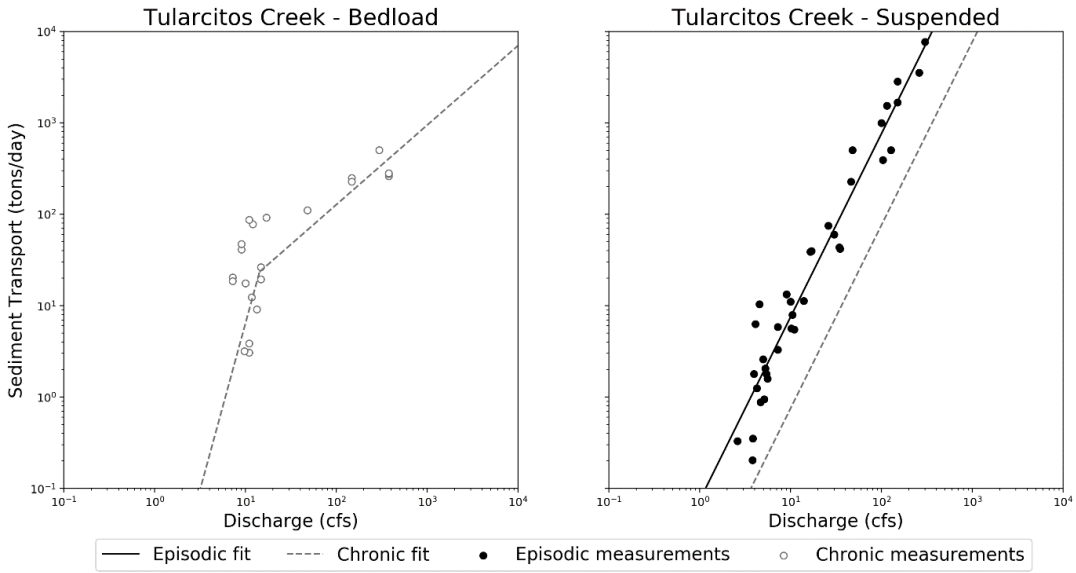

Figure B.12: Rating curves for Tularcitos Creek at Sleepy Hollow.

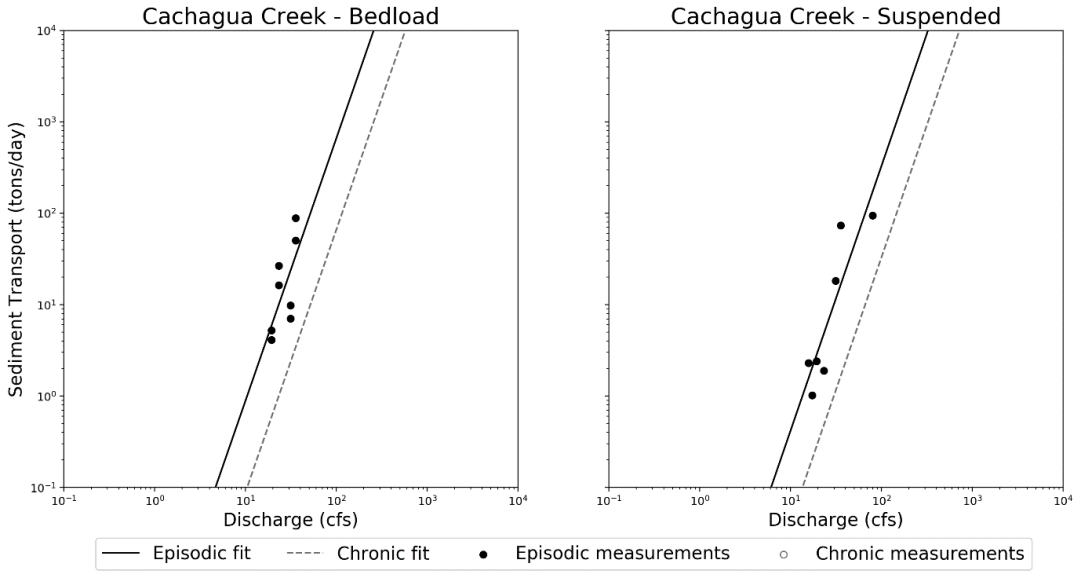

Figure B.13: Rating curves for Cachagua Creek at Princess Camp.

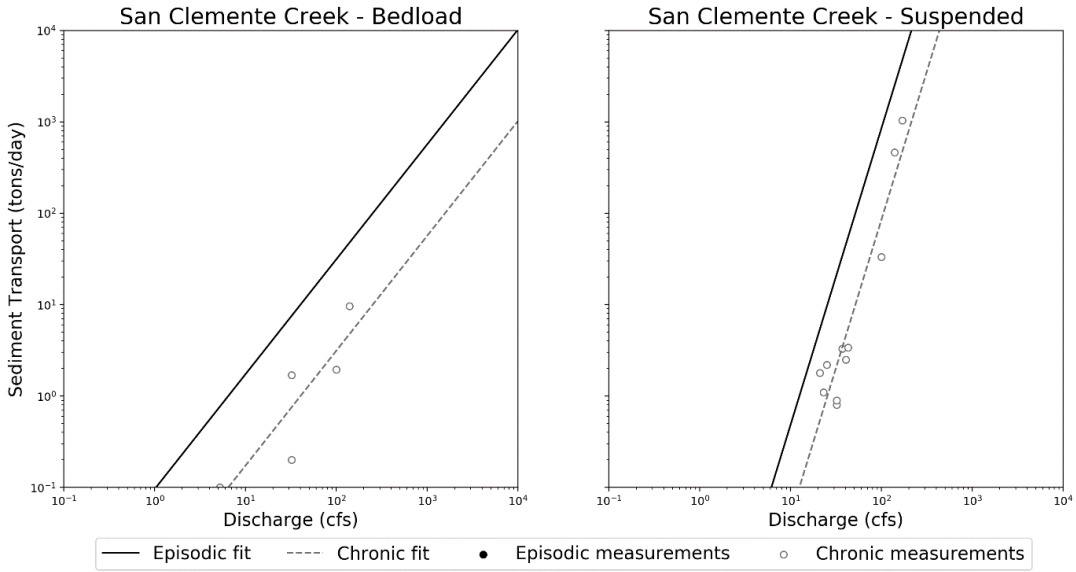

Figure B.14: Rating curves for San Clemente Creek.

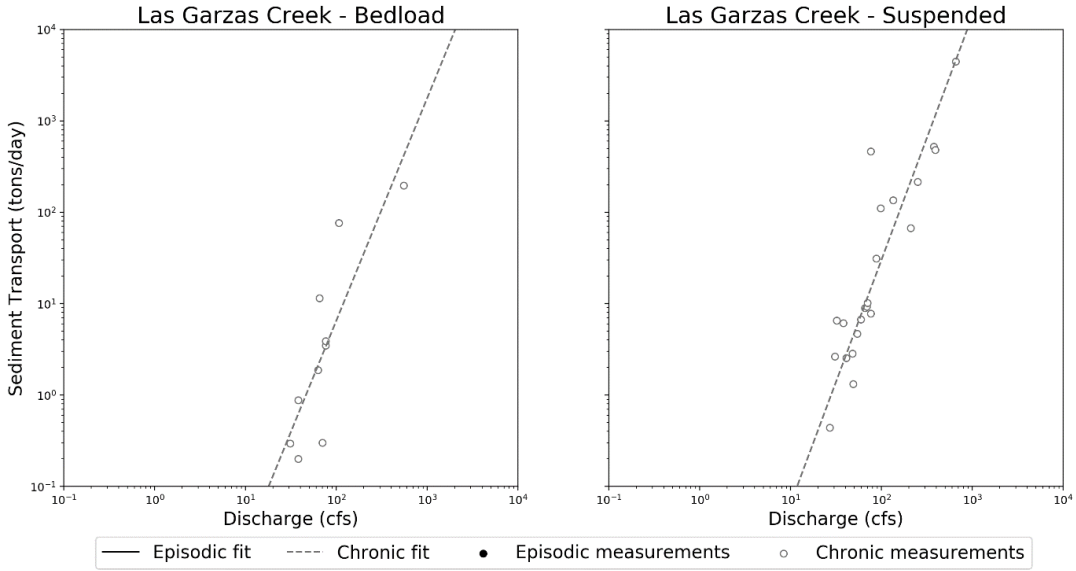

Figure B.15: Rating curves for Las Garzas Creek.

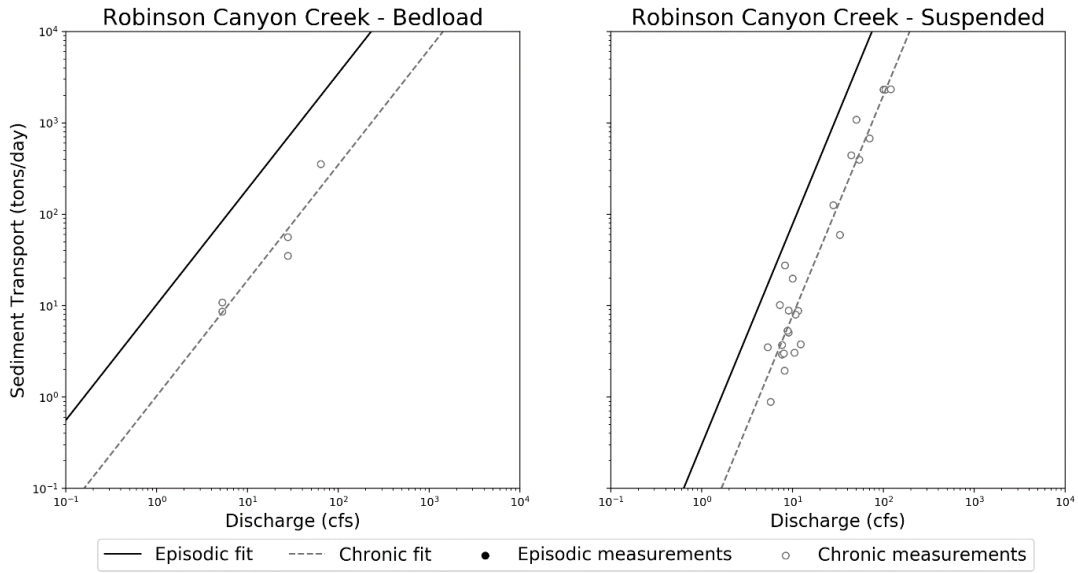

Figure B.16: Rating curves for Robinson Canyon Creek at Robinson Canyon Road.

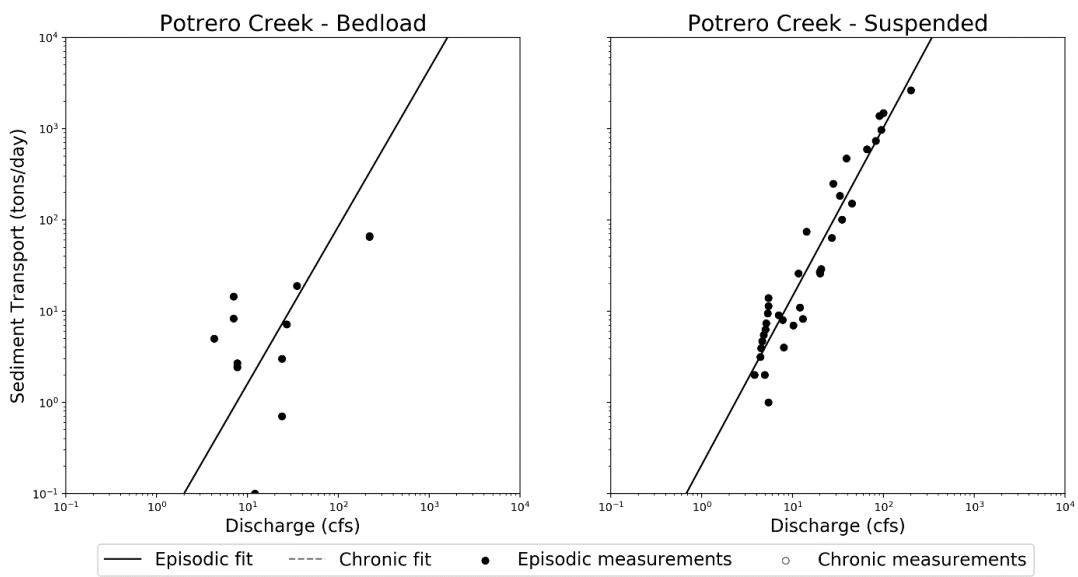

Figure B.17: Rating curves for Potrero Creek.

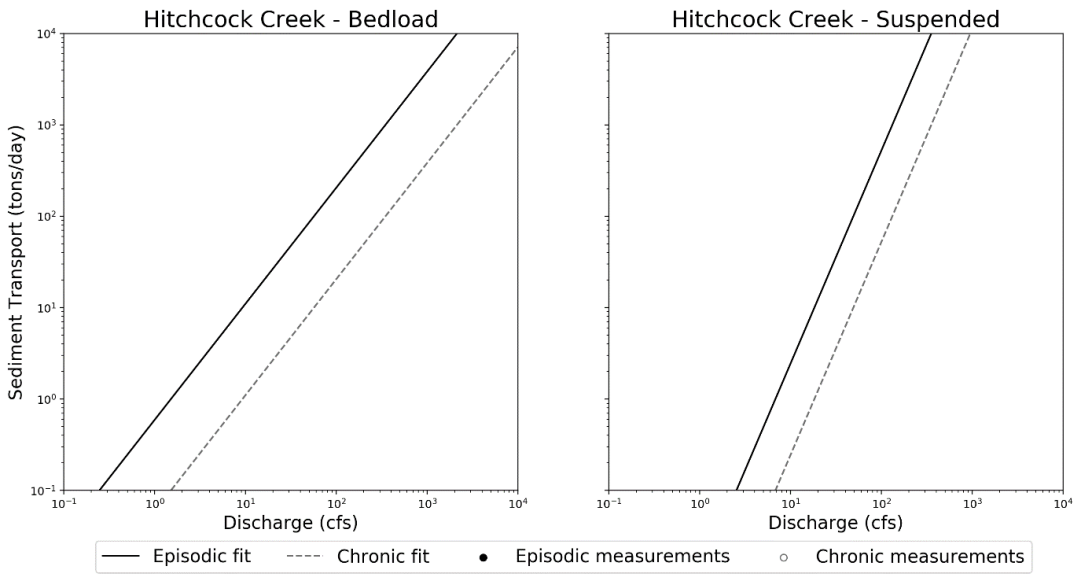

Figure B.18: Rating curves for Hitchcock Canyon Creek.

B.6 Node Initialization

Table B.2: Input parameters for the full runs by simulation node. The first two nodes (ID 1 and 2) were added to provide a smoother boundary condition from high-magnitude sediment input events from the former Los Padres reservoir. Reaches change where the hydrology changes, as different backwater curves are applied for each reach. The depth of maximum subsurface grain size is different between spinup runs (indicated by *) and the full length runs (trial runs and alternatives).

Node ID	Elevation (ft)	Distance from mouth (ft)	Reach ID	Hydrology Station ID	Initial Surface Grain Size Distribution ID	External Sediment Feed ID	Initial Subsurface Grain Size Distribution ID	Depth of maximum subsurface grain size (ft)	Maximum subsurface grain size (mm)	Northing in m	Easting in m
1	965.8		D1A	BL	URS_Active_99577	DAM	MEI80k	2	512	4027565.6	619425.2
2	942.4		D1A	BL	URS_Active_99577	DAM	MEI80k	2	512	4027565.6	619425.2
Analysis domain begins here / End of extended boundary											
3	918.2	137795	D1A	BL	URS_Active_99577		MEI80k	2	512	4027565.6	619425.2
4	893.8	136155	D1A	BL	URS_Active_99577		MEI80k	2	512	4027565.6	619425.2
5	869.7	134514	D1A	BL	URS_Active_99577		MEI80k	2	512	4027960.2	619666.0
6	845.7	132874	D1A	BL	URS_Active_99577		MEI80k	2	512	4028370.0	619661.4
7	824.9	131234	D1A	BL	URS_Active_99577		MEI80k	2	512	4028759.9	619932.9
8	803.2	129593	D1A	BL	URS_Active_99577		MEI80k	2	512	4029219.6	620077.5
9	782.8	127953	D1B	BL+CA	URS_Active_99577	CA_trib	MEI80k	2	512	4029530.6	619874.6
10	764.2	126312	D1B	BL+CA	URS_Active_99577		MEI80k	2	512	4029937.5	619602.6
11	746.8	124672	D1B	BL+CA	URS_Active_99577		MEI80k	2	512	4030061.2	619150.9
12	728.2	123031	D1B	BL+CA	URS_Active_99577		MEI80k	2	512	4030208.8	618749.9
13	706.6	121391	D1B	BL+CA	URS_Active_99577		MEI80k	3.3	512	4029996.8	618384.1
14	683.4	119751	D1B	BL+CA	URS_Active_99577		MEI80k	3.3	512	4030020.0	617994.8
15	661.0	118110	D1B	BL+CA	URS_Active_99577		MEI80k	6.6	512	4030016.6	617549.9
16	637.8	116470	D1B	BL+CA	URS_Active_99577		MEI80k	6.6	512	4030036.9	617120.4
17	616.1	114829	D1B	BL+CA	URS_Active_99577		MEI80k	6.6	512	4030038.3	616799.4
18	596.9	113189	D1B	BL+CA	URS_Active_99577		MEI80k	6.6	512	4030199.7	616385.9
19	577.3	111549	D1B	BL+CA	URS_Active_99577		MEI80k	6.6	512	4030648.3	616343.6
20	563.4	109908	D1B	BL+CA	URS_Active_99577		MEI80k	6.6	512	4030822.7	615908.0
21	544.2	108268	D1B	BL+CA	URS_Active_99577		MEI80k	6.6	512	4031028.3	615498.2
22	535.4	106627	D1B	BL+CA	URS_Active_99577		MEI80k	6.6	512	4031493.4	615454.3
23	527.5	104987	D1B	BL+CA	URS_Active_99577		MEI80k	6.6	512	4031958.7	615578.6
24	518.8	103346	D1B	BL+CA	URS_Active_99577		MEI80k	6.6	512	4032127.8	615309.2
25	495.4	101706	D1B	SHW	URS_Active_99577	CL_trib	MEI80k	0	512	4032509.4	615416.1
26	461.7	100066	D1B	SHW	URS_Active_99577		MEI80k	2	512	4032914.0	615645.3
Spinup run begins here											
27	441.1	98425	D2	SHW	URS_Active_99577		MEI80k	2 / 1.6*	512	4033245.0	615791.5
28	431.7	96785	D2	SHW	URS_Active_99577		MEI80k	2 / 1.6*	512	4033476.2	616148.8
29	414.7	95144	D2	SHW	URS_Active_99577		MEI80k	16 / 3.3*	512	4033861.6	615860.3
30	400.1	93504	D2	SHW	URS_Active_99577		MEI80k	16 / 3.3*	512	4034068.1	615509.6
31	386.1	91864	D2	SHW	URS_Active_86400		MEI80k	16 / 3.3*	512	4034088.1	615093.6
32	372.3	90223	D2	SHW	URS_Active_86400		MEI80k	16 / 3.3*	512	4034499.7	615008.2
33	359.2	88583	D2	SHW	URS_Active_86400		MEI80k	16 / 3.3*	512	4034973.5	614973.5
34	346.3	86942	D2	SHW	URS_Active_86400		MEI80k	16 / 3.3*	512	4035415.8	615145.1
35	333.7	85302	D2	SHW	URS_Active_86400		MEI80k	16 / 3.3*	512	4035843.5	615212.8

36	320.3	83661	D2	SHW	URS_Active_81900		MEI80k	16 / 3.3*	512	4036292.7	615198.3
37	306.9	82021	D3A	RR	URS_Active_81900	TU_trib	MEI80k	16 / 3.3*	512	4036724.7	615244.5
38	296.0	80381	D3A	RR	URS_Active_81900		MEI80k	16 / 3.3*	512	4036986.4	614882.9
39	285.4	78740	D3A	RR	URS_Active_81900		MEI80k	16 / 3.3*	512	4037387.0	614597.1
40	275.6	77100	D3A	RR	URS_Active_81900		MEI80k	16 / 3.3*	512	4037322.1	614196.0
41	266.3	75459	D3A	RR	URS_Active_71400		MEI80k	16 / 3.3*	512	4037335.6	613709.4
42	257.3	73819	D3A	RR	URS_Active_71400	HI_trib	MEI60k	16 / 3.3*	512	4037513.1	613262.6
43	248.2	72178	D3A	RR	URS_Active_71400		MEI60k	16 / 3.3*	512	4037602.1	612785.9
44	239.0	70538	D3A	RR	URS_Active_71400		MEI60k	16 / 3.3*	512	4038088.3	612720.3
45	229.4	68898	D3A	RR	URS_Active_71400		MEI60k	16 / 3.3*	512	4038397.6	612388.6
46	219.6	67257	D3A	RR	URS_Active_71400		MEI60k	16 / 3.3*	512	4038838.0	612173.0
47	209.9	65617	D3B	RR	URS_Active_62100		MEI60k	16 / 3.3*	512	4039263.2	611918.7
48	201.1	63976	D3B	DJ	URS_Active_62100	GA_trib	MEI60k	16 / 3.3*	512	4039648.7	611620.3
49	191.5	62336	D3B	DJ	URS_Active_62100		MEI60k	16 / 3.3*	512	4039862.7	611191.0
50	182.2	60696	D3B	DJ	URS_Active_62100		MEI60k	16 / 3.3*	512	4040236.7	610871.2
51	174.7	59055	D3B	DJ	URS_Active_62100		MEI60k	16 / 3.3*	512	4040716.9	610760.4
52	167.3	57415	D3B	DJ	URS_Active_62100		MEI60k	16 / 3.3*	512	4041132.5	610516.8
53	160.4	55774	D3B	DJ	URS_Active_62100		MEI60k	16 / 3.3*	512	4041325.0	610056.3
54	152.3	54134	D3B	DJ	URS_Active_62100		MEI60k	16 / 3.3*	512	4041488.4	609606.3
55	144.3	52493	D3B	DJ	URS_Active_42400		MEI60k	16 / 3.3*	512	4041704.0	609182.5
56	135.4	50853	D3B	DJ	URS_Active_42400		MEI60k	16 / 3.3*	512	4041888.8	608735.3
57	127.9	49213	D3B	DJ	URS_Active_42400		MEI40k	16 / 3.3*	512	4041868.4	608249.0
58	121.2	47572	D4A	DJ	URS_Active_42400		MEI40k	16 / 3.3*	512	4042226.1	607903.6
59	116.0	45932	D4A	NC	URS_Active_42400		MEI40k	16 / 3.3*	512	4042518.6	607510.6
60	111.3	44291	D4A	NC	URS_Active_42400		MEI40k	16 / 3.3*	512	4042482.2	607063.5
61	106.2	42651	D4A	NC	URS_Active_42400		MEI40k	16 / 3.3*	512	4042275.7	606614.2
62	101.2	41010	D4A	NC	URS_Active_42400	RC_trib	MEI40k	16 / 3.3*	512	4042241.9	606178.4
63	95.8	39370	D4A	NC	URS_Active_42400		MEI40k	16 / 3.3*	512	4042645.5	605892.4
64	90.3	37730	D4A	NC	URS_Active_35900		MEI40k	16 / 3.3*	512	4042857.4	605458.8
65	85.4	36089	D4A	NC	URS_Active_35900		MEI40k	16 / 3.3*	512	4042717.4	604998.9
66	79.7	34449	D4A	NC	URS_Active_35900		MEI40k	16 / 3.3*	512	4042805.1	604643.2
67	74.1	32808	D4A	NC	URS_Active_35900		MEI40k	16 / 3.3*	512	4043196.8	604349.3
68	69.9	31168	D4A	NC	URS_Active_29200		MEI40k	16 / 3.3*	512	4043122.1	603964.0
69	64.3	29528	D4A	NC	URS_Active_29200		MEI40k	16 / 3.3*	512	4042844.6	603586.7
70	60.1	27887	D4A	NC	URS_Active_29200		MEI40k	16 / 3.3*	512	4043033.6	603136.2
71	55.2	26247	D4A	NC	URS_Active_29200		MEI40k	16 / 3.3*	512	4043023.9	602667.5
72	50.6	24606	D4A	NC	URS_Active_29200		MEI40k	16 / 3.3*	512	4043321.2	602282.6
73	47.1	22966	D4A	NC	URS_Active_29200		MEI40k	16 / 3.3*	512	4043728.2	602073.1
74	42.6	21325	D4A	NC	SC		MEI40k	2	512	4043944.1	601631.6
75	38.2	19685	D4A	NC	SC	PO_trib	MEI40k	2	512	4044089.8	601214.9
76	35.5	18045	D4A	NC	SC		MEI40k	2	512	4044248.6	600782.7
77	32.5	16404	D4A	NC	SC		MEI40k	2	512	4044302.9	600296.2
78	27.5	14764	D4B	NC	CRO		MEI40k	2	512	4044024.2	599955.0
79	25.8	13123	D4B	HWY1	CRO		MEI40k	2	512	4044148.5	599604.5
80	22.0	11483	D4B	HWY1	CRO		MEI40k	2	512	4044210.6	599137.1
81	17.8	9843	D4B	HWY1	CRO		MEI40k	2	512	4043944.3	598734.0
82	14.0	8202	D4B	HWY1	CRO		MEI40k	2	512	4043978.5	598244.6
83	10.6	6562	D4B	HWY1	CRO		MEI40k	2	512	4043874.1	597757.5
84	8.3	4921	D4B	HWY1	CRO		MEI40k	2	512	4043999.9	597316.4
85	4.9	3281	D4B	HWY1	CRO		MEI40k	2	512	4044321.8	596935.8
86	2.1	1640	D4B	HWY1	CRO		MEI40k	2	512	4044370.3	596514.6
87	0.0	0	D4B	HWY1	CRO		MEI40k	2	512	4044017.2	596177.6

B.7 Grain Size Distributions

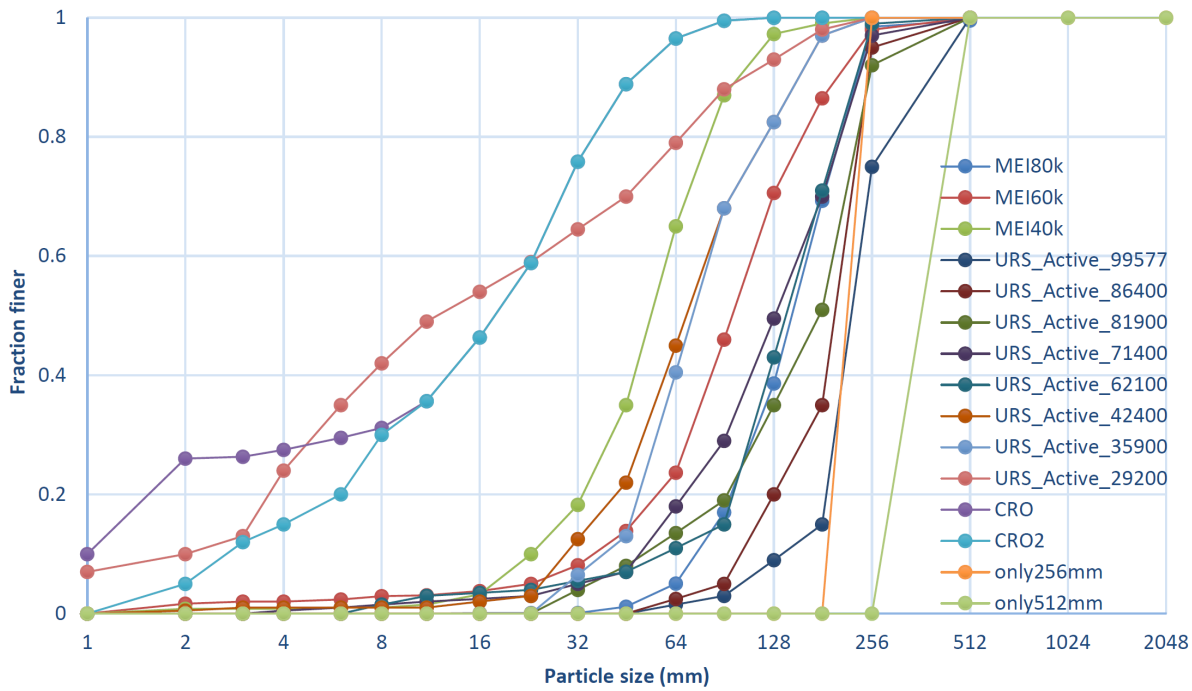

Figure B.19: Grain size distributions used for the node initialization. SC and CRO were provided by Douglas Smith, who reported them in the report '2015 Pre-San Clemente Dam Removal Morphological Monitoring of the Carmel River Channel in Monterey County, California'. The three MEI40k, 60k and 80k grain size distributions were compiled from plots the MEI 2002 San Clemente dam modelling report. The URS_Active grain size distributions were compiled from the URS modelling report. The 'only256mm' and 'only512mm' grain size distributions were used to artificially prevent erosion of deeper subsurface layers.

B.8 Reach Averaged Crosssections

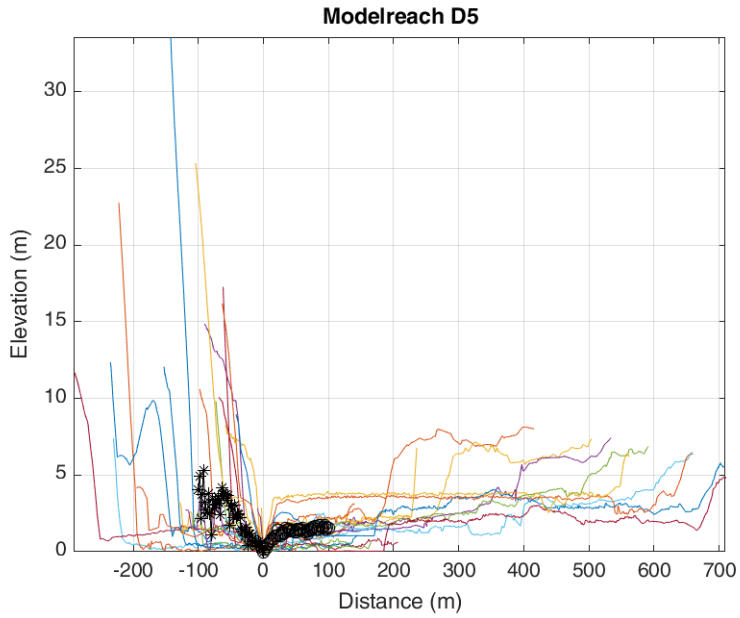

Figure B.20: Averaged crosssection for reach D5

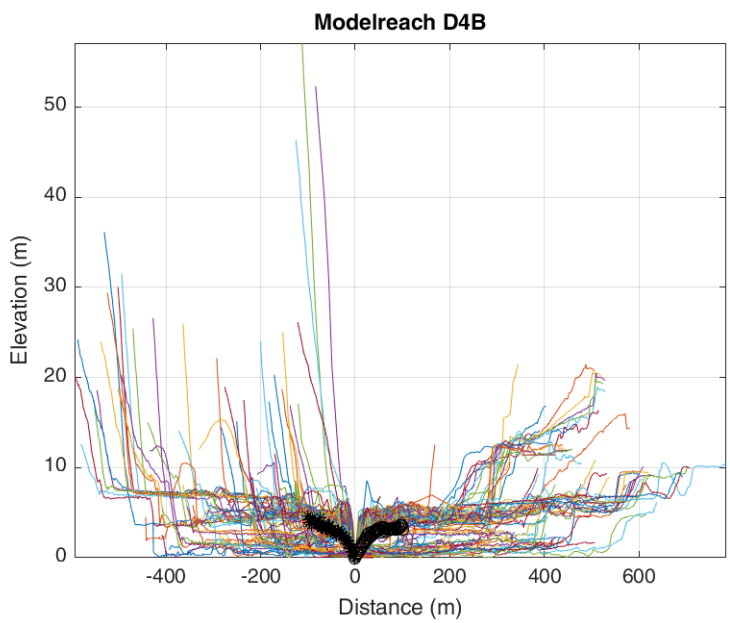

Figure B.21: Averaged crosssection for reach D4B

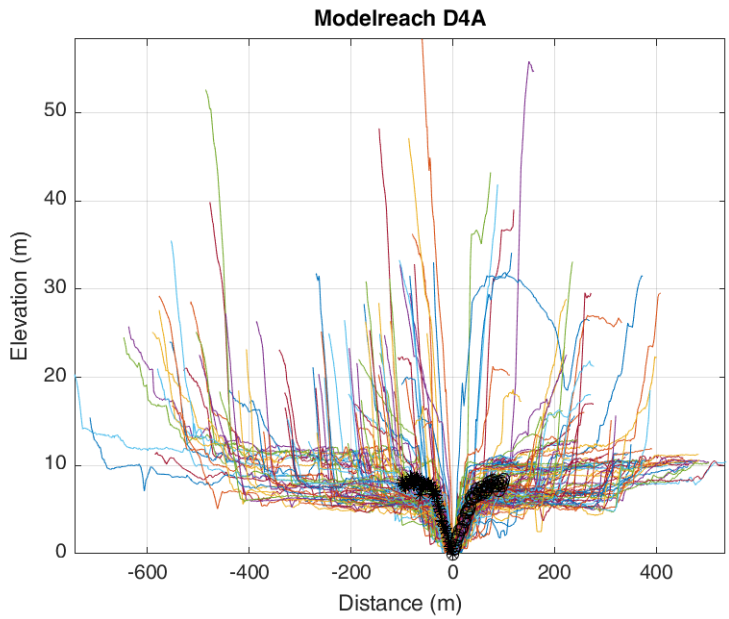

Figure B.22: Averaged crosssection for reach D4A

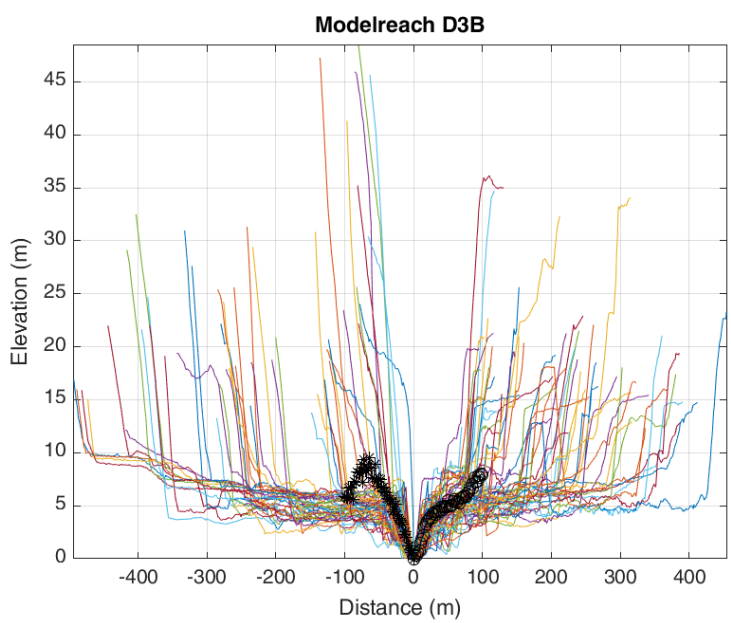

Figure B.23: Averaged crosssection for reach D3B

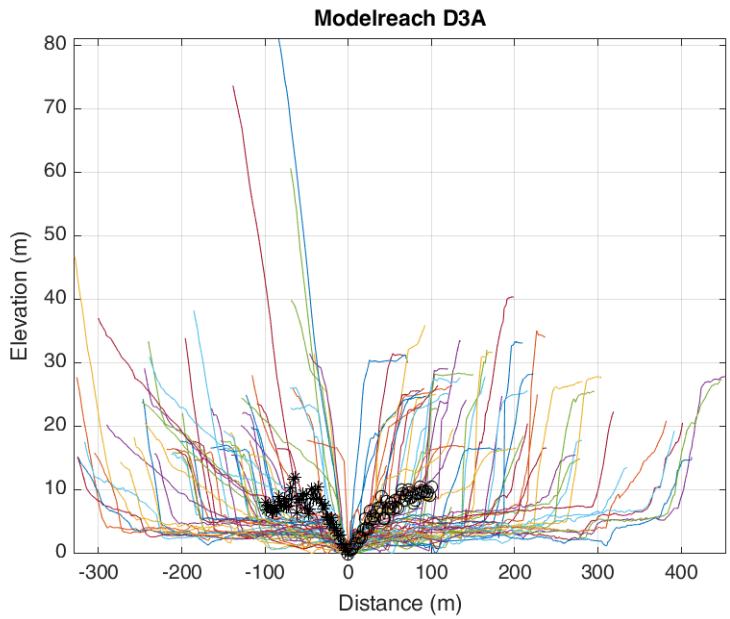

Figure B.24: Averaged crosssection for reach D3A

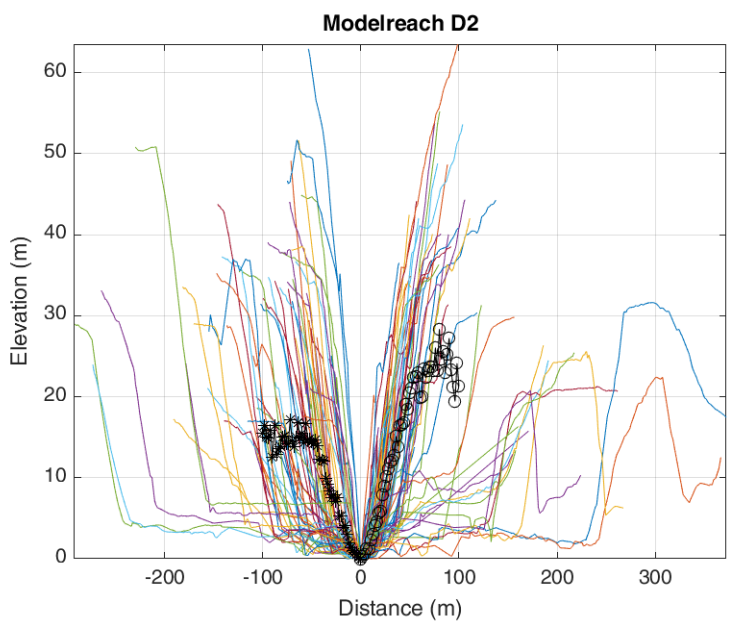

Figure B.25: Averaged crosssection for reach D2

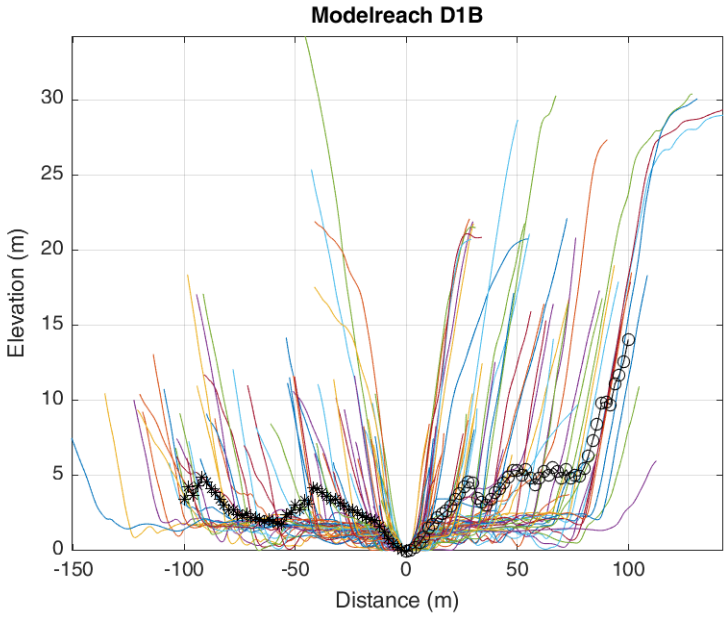

Figure B.26: Averaged crosssection for reach D1B

B.9 Reach Flow Calculations

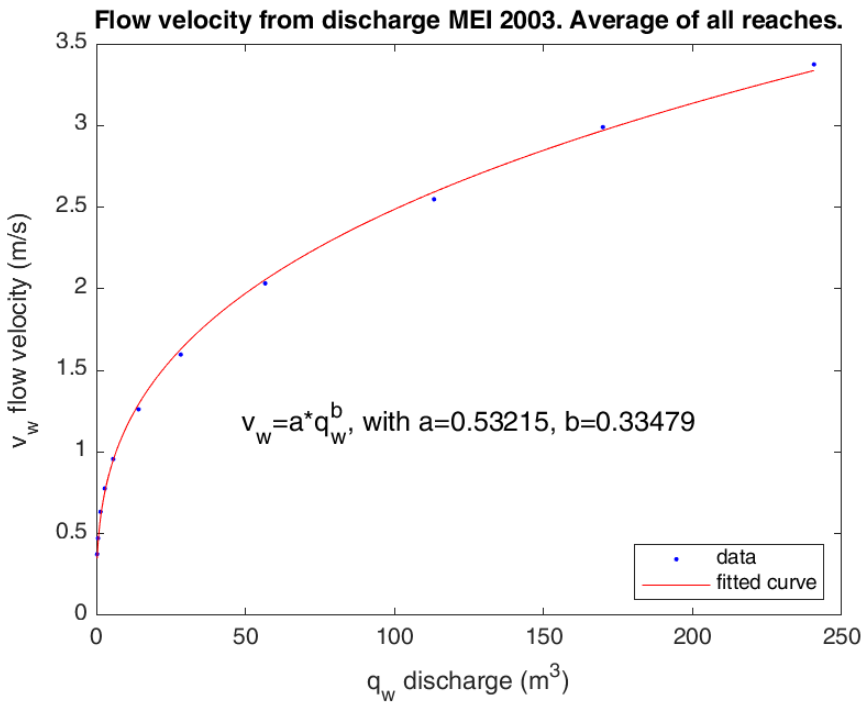

Figure B.27: Flow velocity from discharge, based on data from MEI (2003)

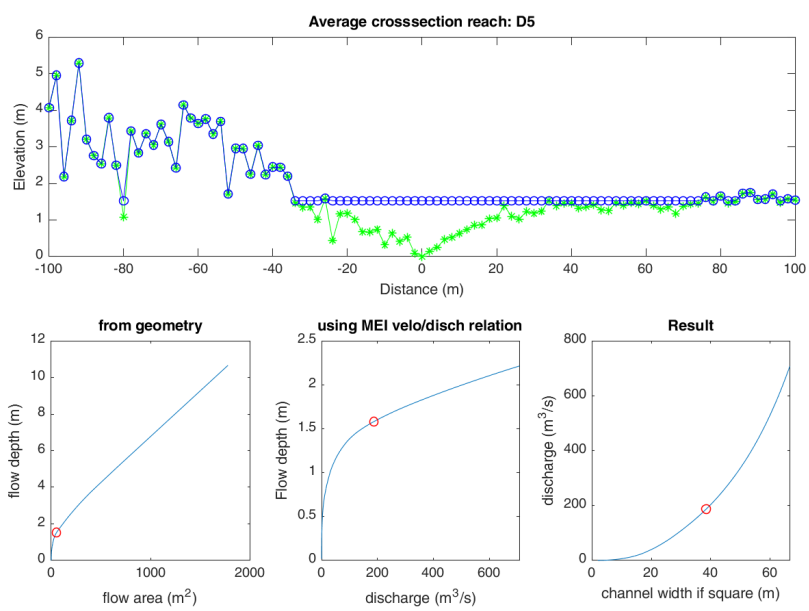

Figure B.28: Averaged crosssection for reach D5

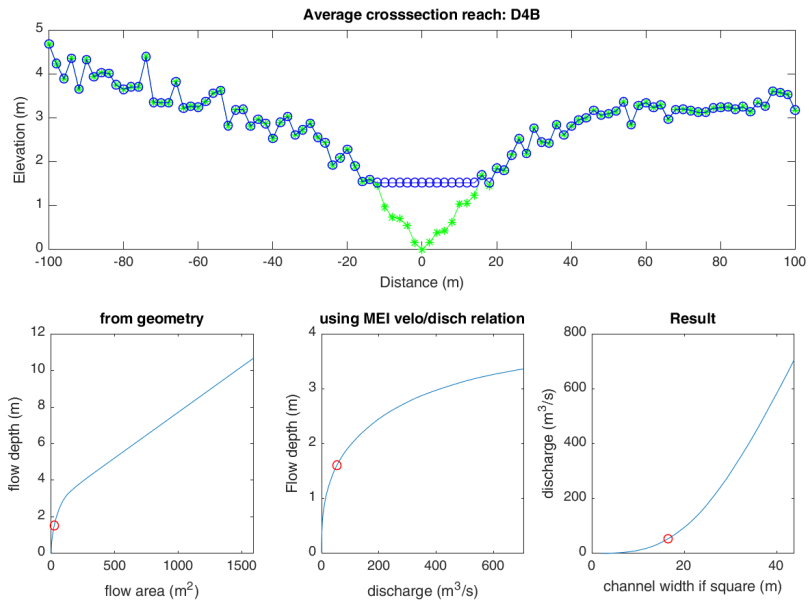

Figure B.29: Averaged crosssection for reach D4B

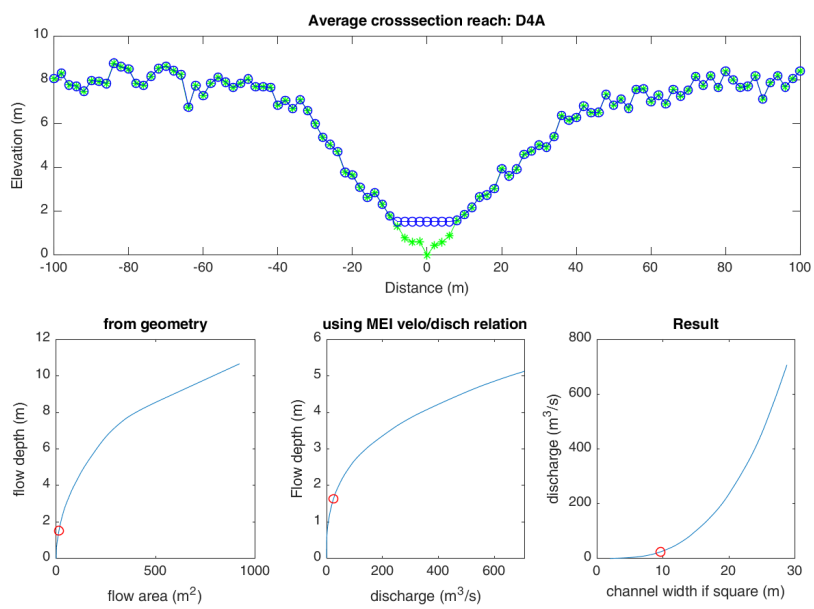

Figure B.30: Averaged crosssection for reach D4A

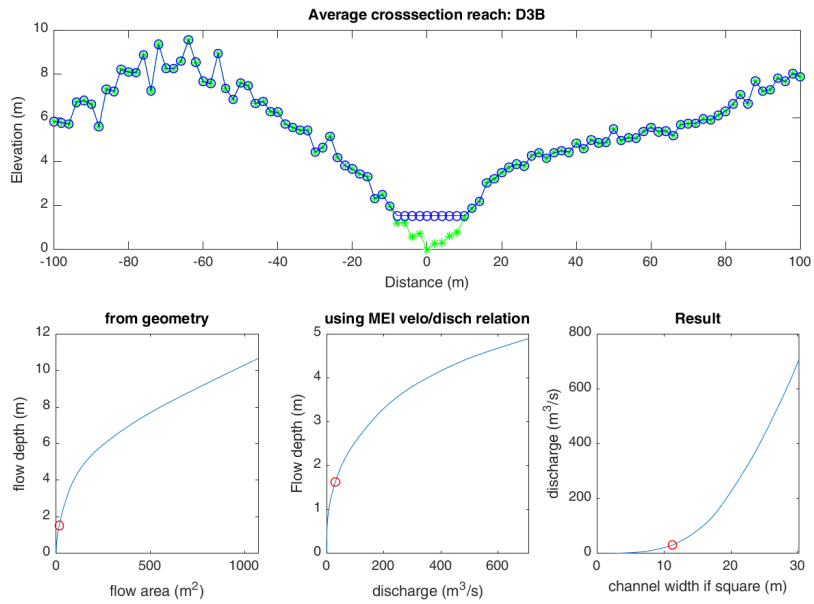

Figure B.31: Averaged crosssection for reach D3B

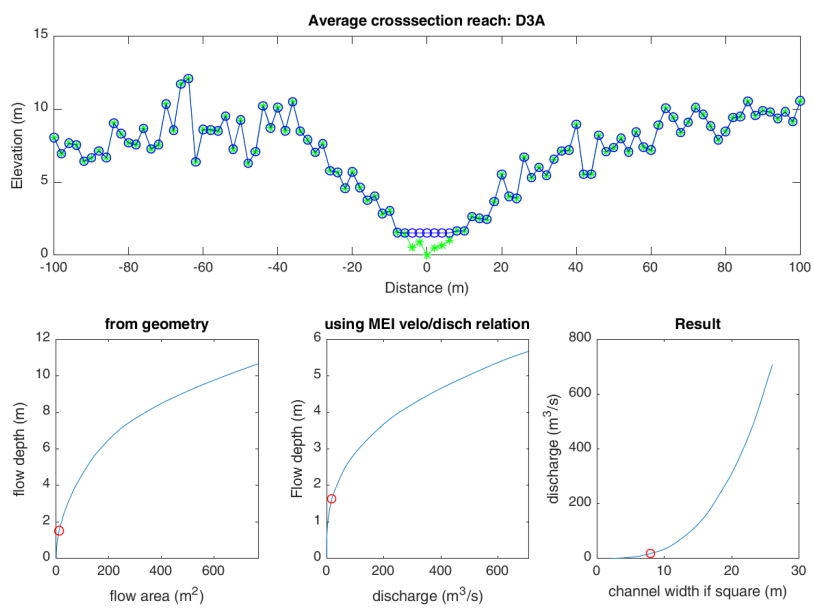

Figure B.32: Averaged crosssection for reach D3A

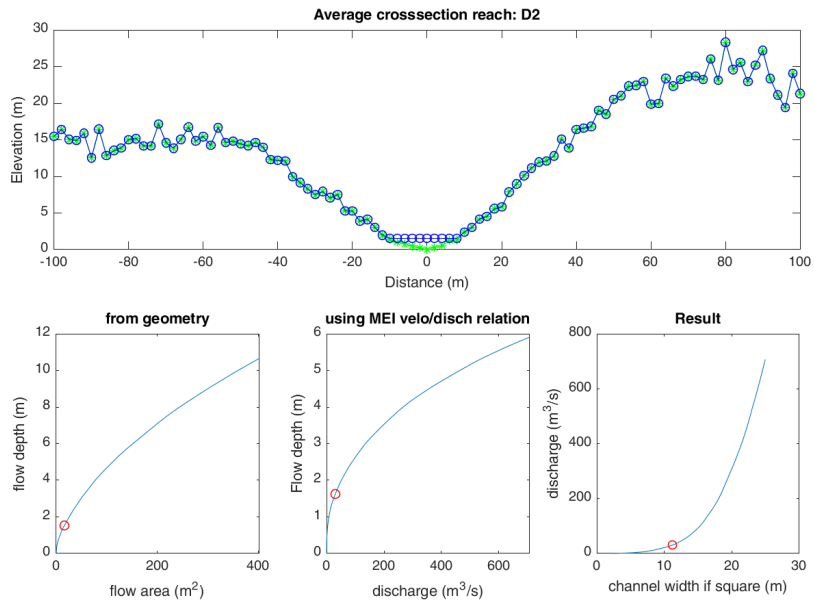

Figure B.33: Averaged crosssection for reach D2

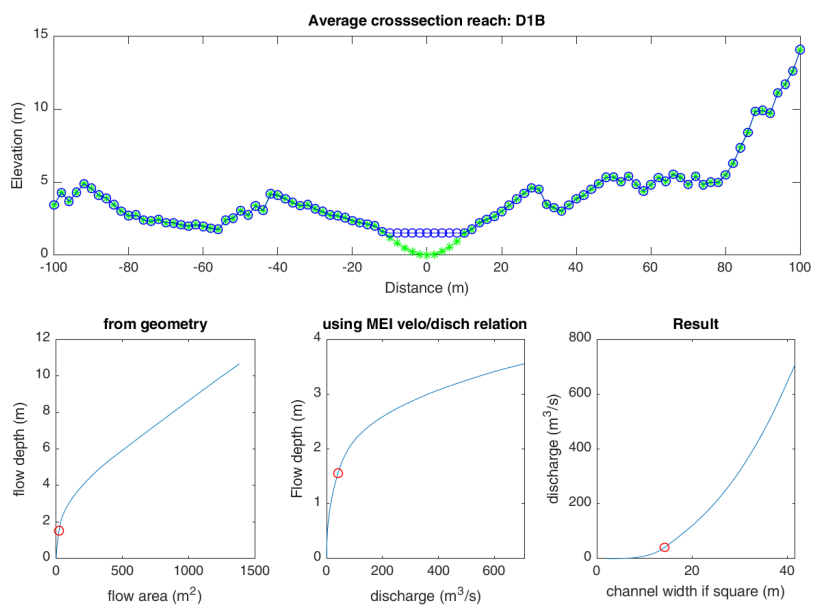

Figure B.34: Averaged crosssection for reach D1B

B.10 Median Sediment Supply and Reservoir Depletion Curves

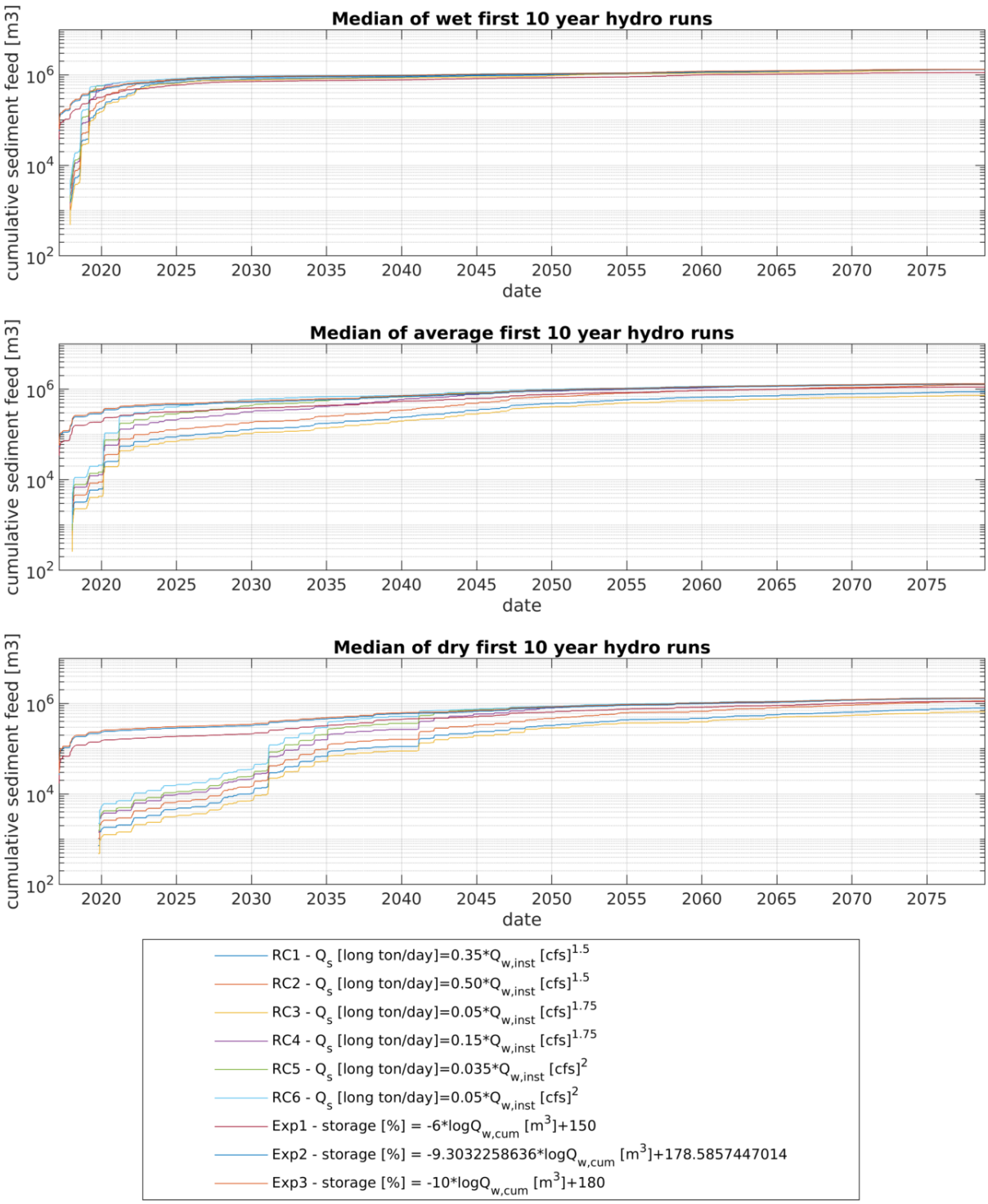

Figure B.35: Uncontrolled Supply (Exp1-3) scenarios. Each line represents the median of 100 simulations.

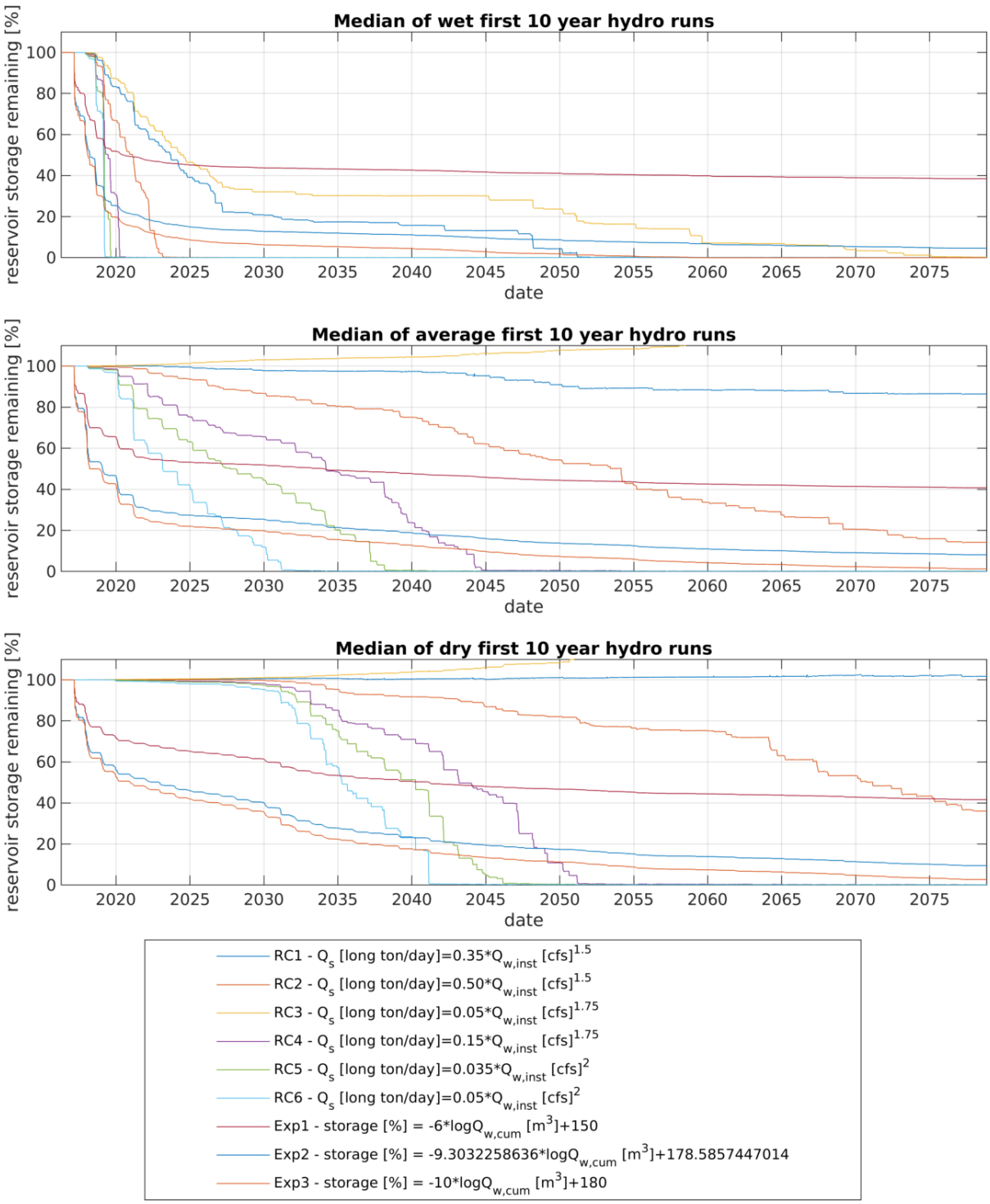

Figure B.36: Median reservoir depletion in the Pulse Supply (RC1-6) and Uncontrolled Supply (Exp1-3) scenarios. Each line represents the median of 100 simulations.

B.11 Detailed Results of the focus scenarios

B.11.1 No Action Simulation Results

We review the No Action project alternative results for the five model reaches running from Los Padres Dam to the Pacific Ocean. Results are summarized in Figure B.37 through Figure B.41 for the average hydrologic condition. Within each Figure the top plot illustrates results for the wet hydrologic condition, the middle plot for the average condition and the bottom plot for the dry condition. Each profile-type line plot illustrates results for 100 simulations at three different simulation times: 10-, 30- and 60-years. To highlight the most probable response trajectory for the simulations, we also plot the median response for the 100 simulations at each simulation time; the median responses are shown as the thicker lines in the plots. We focus on the following figures:

- Figure B.37 shows the simulated change in channel bed elevation;
- Figure B.38 shows the simulated change of the bed surface median grain size (D_g);
- Figure B.39 shows the simulated change of the bed surface 90th-percentile grain size (D_{90});
- Figure B.40 shows the simulated change of the longitudinal channel bed slope; and
- Figure B.41 shows the simulated unit bedload sediment transport rate.

Downstream of Los Padres (42-32 km): As expected, reaches downstream of Los Padres Dam up to channel station 35 km are projected to degrade for the wet, average and dry hydrologic conditions. The median simulation projection of channel bed degradation at year 60 ranges from 0 to roughly -1.5 m relative to initial channel bed elevations (circa 2017) across all three hydrologic conditions. The location of the most severe degradation along this segment appears to follow an existing spatial trend of downstream increasing bed slope (see Figure B.40). Some of the eroded bed material is transported downstream and deposited between stations 32 km and 35 km, where the downstream trend of bed slopes is presently decreasing.

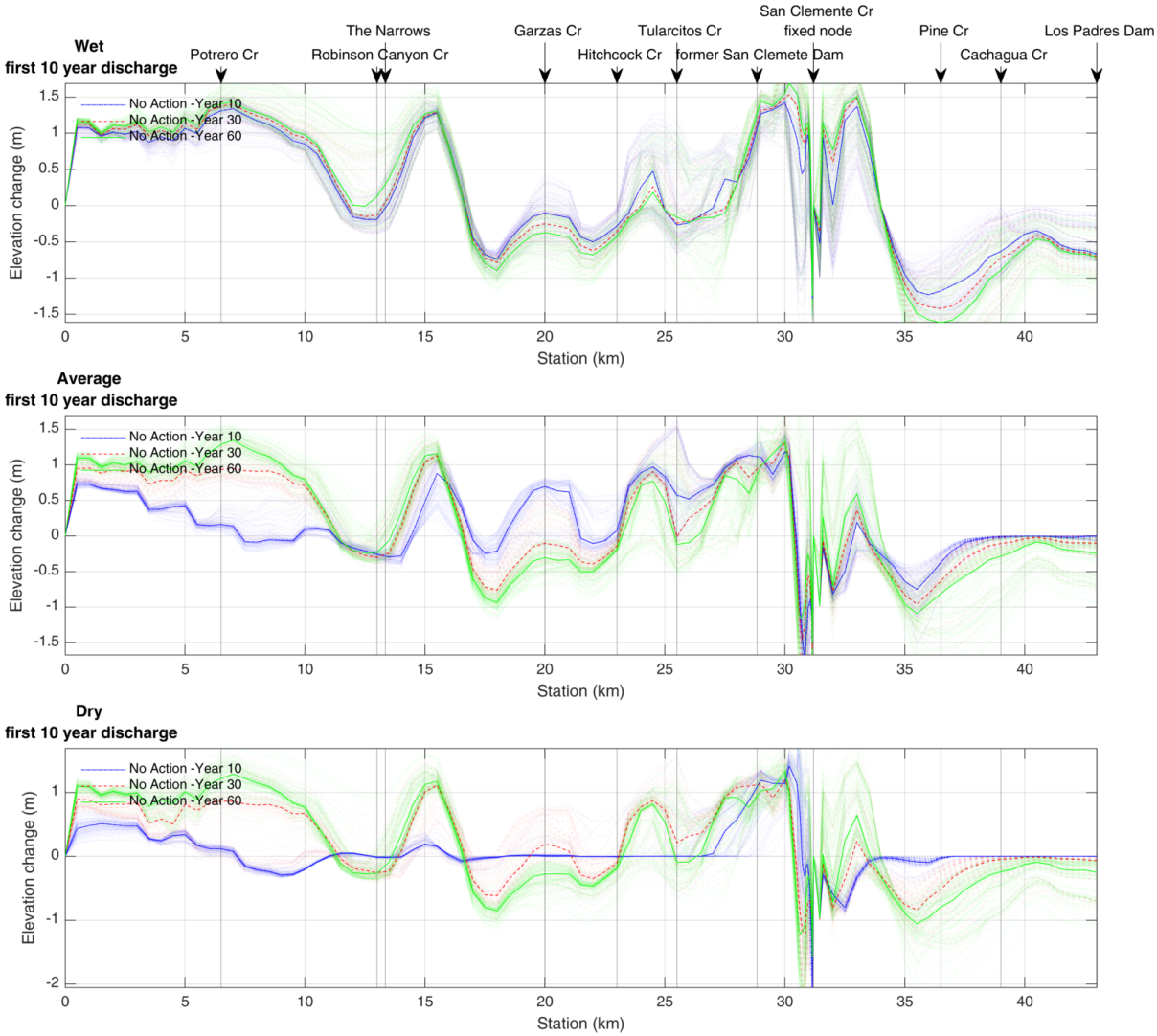

Figure B.37: Change in elevation compared to the initial elevation profile from 2017. While BESMo reports only change in sediment volume, we translated the volume change to an elevation change by using the averaged crosssection profiles shown in Appendix B.8 and converting the sediment storage from cross sectional area to depth using the same ratios shown in Appendix B.9 for flow area to flow depth. In the case of erosion, we assumed a rectangular cross section with constant channel width. Top: high, Middle: average, bottom: low cumulative discharge in the first 10 years. Per subplot the profiles of 100 simulations is shown in 10, 30, and 60-year time slices. The three solid lines in each subplot signify the median condition at each node for each of the three time slices; all other lines represent data from individual model runs.

In all cases, timing of the largest projected changes to bed elevation occur during the simulation period of the largest floods. Both the D_g and the D_{90} are projected to increase from 15-

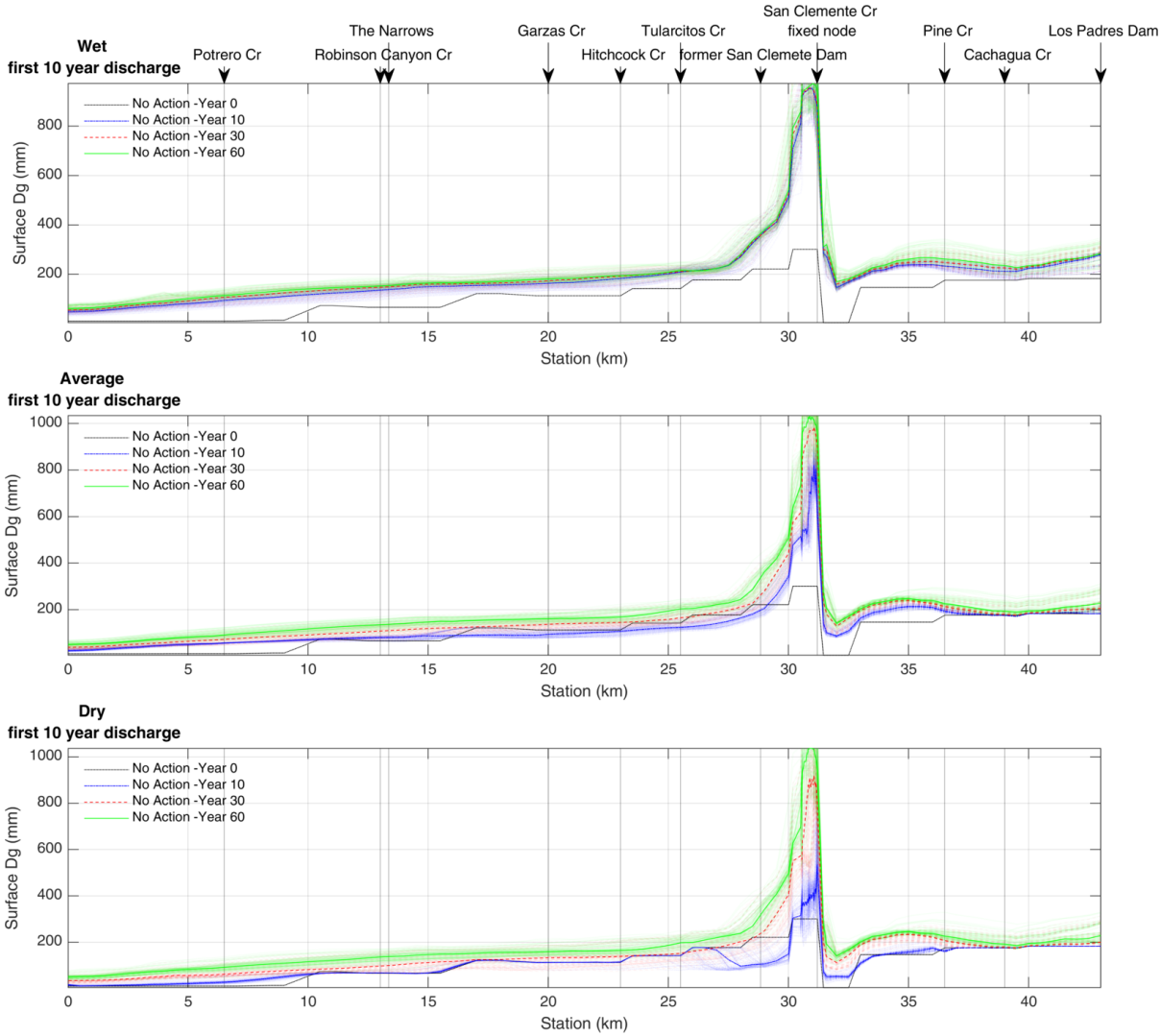

Figure B.38: Mean surface grain size (D_g) for top: high, Middle: average, bottom: low cumulative discharge in the first 10 years. Per subplot the profiles of 100 simulations is shown in 10, 30, and 60-year time slices. The three solid lines in each subplot signify the median condition at each node for each of the three time slices; all other lines represent data from individual model runs.

to 40% within this section of the channel. Transport rates here are comparably low due to the relatively low discharge and low bedload sediment supply.

Former San Clemente Dam project reach (32.5-30.5 km): The simulations project two dominant responses within the former San Clemente project reach: channel bed degradation within the former reservoir deposits, and extending about 1000 m upstream, and downstream progressive channel bed aggradation from approximately the San Clemente Creek confluence

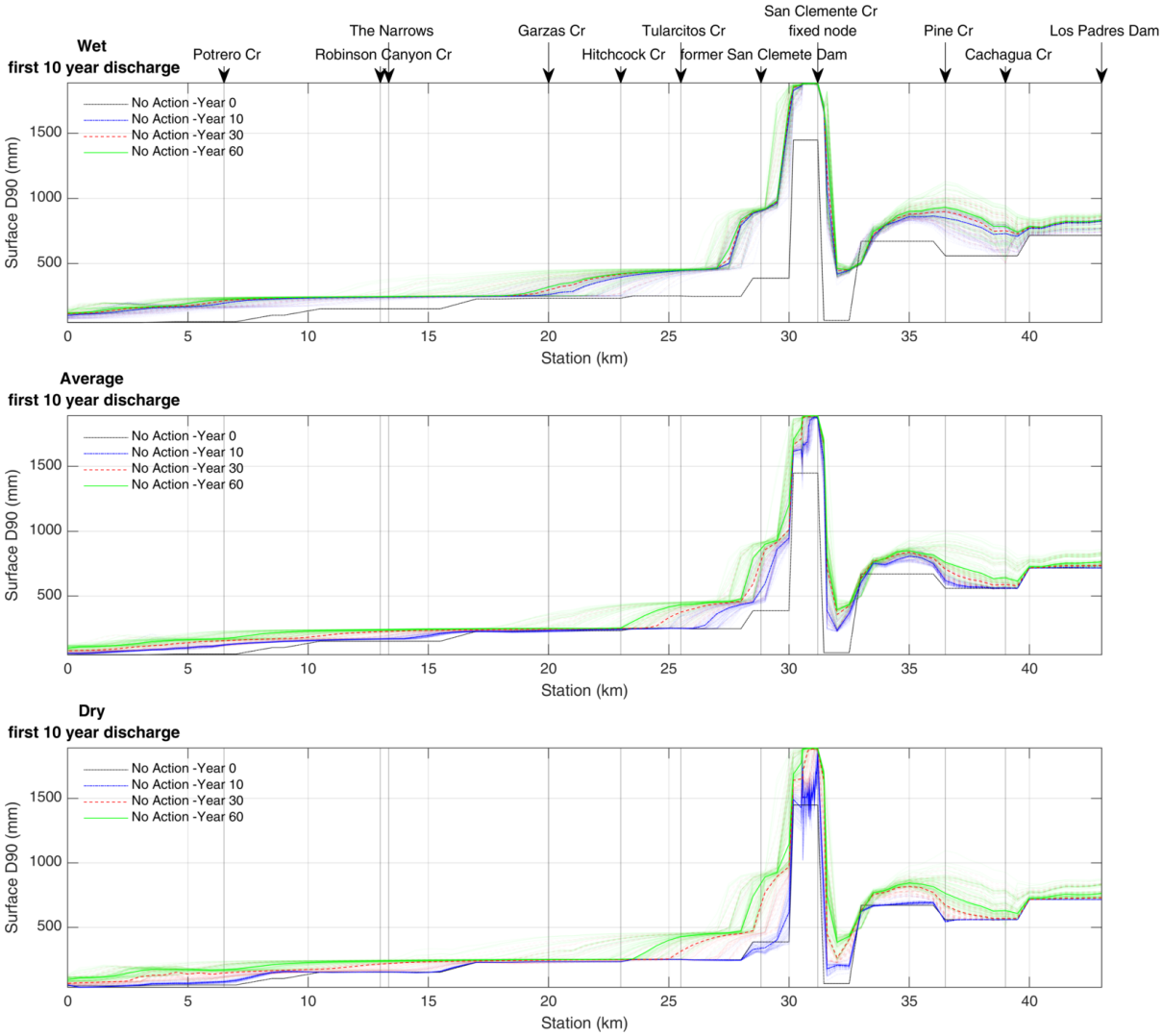

Figure B.39: Coarse fractions of the surface grain size expressed as 90th percentile size (D_{90}) for top: high, Middle: average, bottom: low cumulative discharge in the first 10 years. Per subplot the profiles of 100 simulations is shown in 10, 30, and 60-year time slices. The three solid lines in each subplot signify the median condition at each node for each of the three time slices; all other lines represent data from individual model runs.

to the former dam site. The median simulation projection of channel bed degradation at year 60 ranges from 0 to about -1.5 m relative to initial channel bed elevations (circa 2017) across all three hydrologic conditions. The location of the most severe degradation response occurs just upstream of the reroute reach. Notably, the dry scenario produces the largest magnitude degradation response because a majority of the bedload transporting flows occur later in the simulation. The median simulation projection of channel bed aggradation at year 60 ranges is

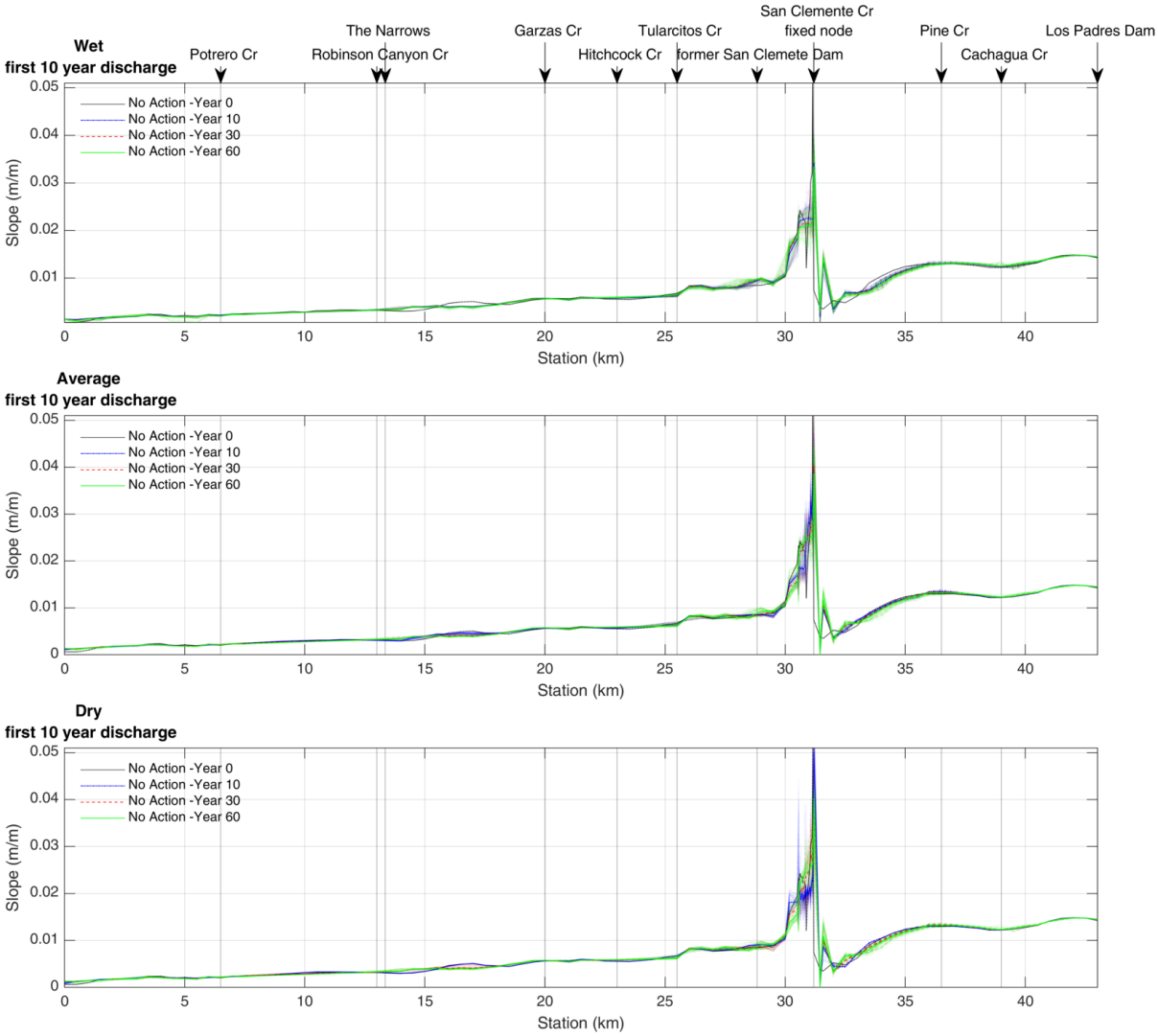

Figure B.40: Slope profile for top: high, Middle: average, bottom: low cumulative discharge in the first 10 years. Per subplot the profiles of 100 simulations is shown in 10, 30, and 60-year time slices. The three solid lines in each subplot signify the median condition at each node for each of the three time slices; all other lines represent data from individual model runs.

comparatively similar to the degradation case, ranging from 0 to about +1.5 m relative to initial channel bed elevations (circa 2017) across all three hydrologic conditions. The location of the most severe aggradation response is coincident with the former dam location node, or within a few nodes downstream. Also, the largest magnitude aggradation is produced under the dry scenario. Erosion within the former reservoir deposit is a function of the relatively fine bed surface GSD there, and projected deposition downstream suggests that the model is evolv-

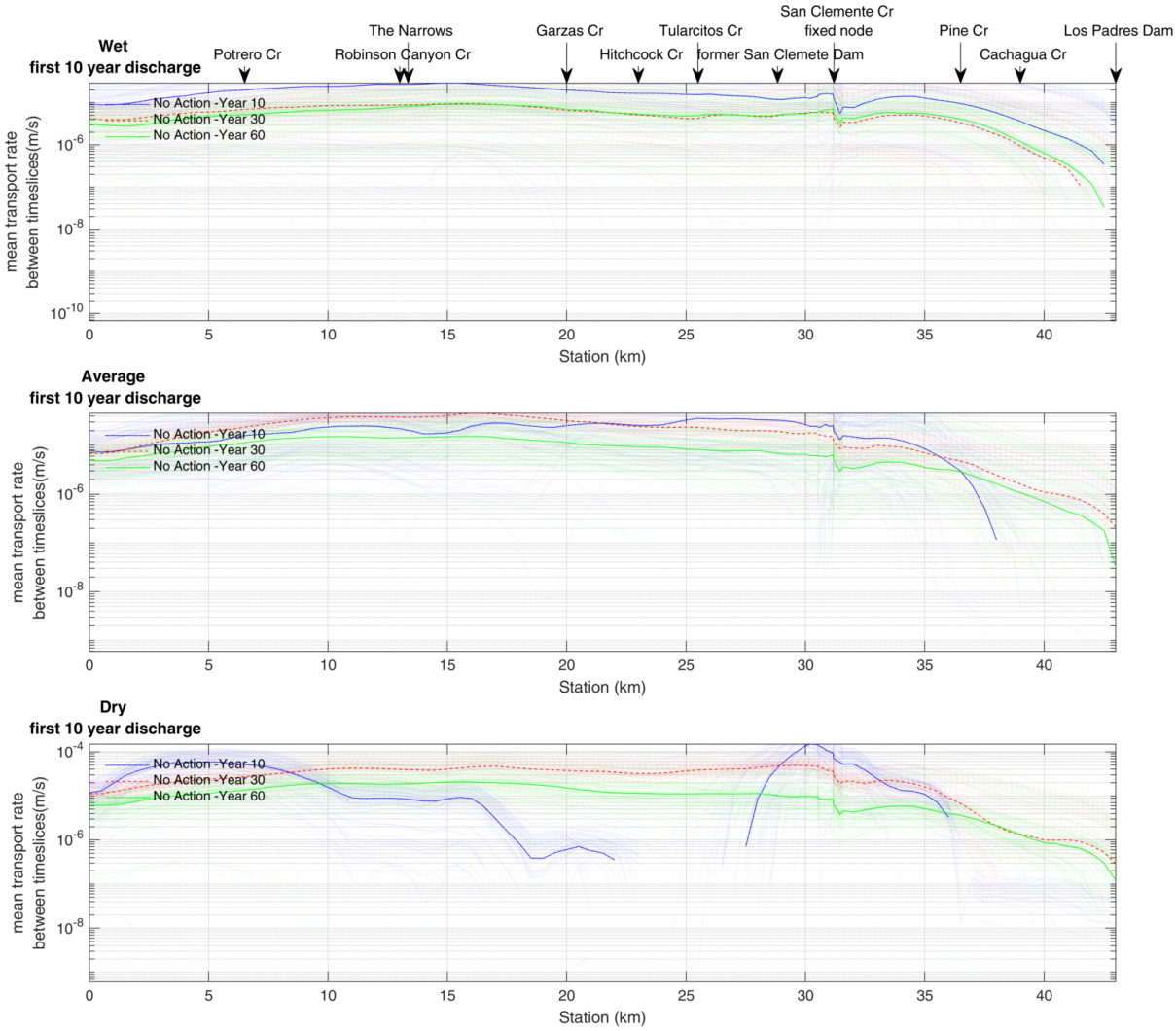

Figure B.41: Averaged transport rate between time slices (Year 10: data from 0-10 years, Year 30: data from 10-30 years, Year 60: data from 30-60 years). For top: high, Middle: average, bottom: low cumulative discharge in the first 10 years. Per subplot the profiles of 100 simulations is shown in 10, 30, and 60-year time slices. The three solid lines in each subplot signify the median condition at each node for each of the three time slices; all other lines represent data from individual model runs.

ing to an overall flatter profile through the San Clemente project reach. This is a reasonable projected model result because the San Clemente project reach is a significant downstream perturbation to the longitudinal slope trend. Erosion within the upstream segment and deposition downstream produces an overall significant coarsening of the D_g and D_{90} bed surface grain sizes. Coarsening of the D_g ranges from 10s to many 100s of mm coarser than initial

conditions, and coarsening of the D_{90} ranges from 10s of mm up to roughly 1500 mm more coarse than initial. This suggests that the projected spatial pattern of changes to bed elevation and bed slope may be limited beyond the 60-year model simulation period.

Between former San Clemente Dam and Tularcitos creek (30.5-25.5 km): The simulations indicate that aggradational responses simulated within the downstream part of the San Clemente project reach progressively diminish moving downstream through this reach. As a result, this reach is a buffer for upstream changes and therefore shows a large range of temporal and spatial variation across the three hydrologic conditions and the 300 simulations. Elevation responses range from upwards of +3.7 m relative to initial channel bed elevations (circa 2017) just downstream of the former dam to approximately +1.5 m by year 60. As with the two upstream reaches, the timing of bed elevation response is governed by the sequencing of flood events. However, unlike the two upstream reaches, the simulated range and magnitude of elevation responses is similar across the hydrologic conditions. All simulations indicate that the D_g and D_{90} bed surface grain sizes will coarsen over time, and that the downstream propagation of the D_{90} response is stronger relative to the D_g.

Tularcitos to Robinson Canyon Creek (25.5-13 km): The simulations indicate a general tendency for channel bed aggradation downstream of station 20.5 km, with little net change suggested for locations upstream of this station. Aggradation through the lower 8 km of this reach may be associated with downstream occurrence of the Narrows, where the depositional signal begins to steadily diminish moving downstream. The Narrows could trigger local deposition with resumption of bedload supply from the watershed in between Los Padres and San Clemente, and this response could then propagate upstream. Across the three hydrologic conditions, net deposition ranges from 0 to upwards of 2 m by year 60 relative to initial channel bed elevations (circa 2017). The D_g and D_{90} bed surface grain sizes show general coarsening trends across the three hydrologic conditions, but the magnitude of coarsening diminishes in the downstream direction for the 60-year simulation. The D_{90} shows variation in the downstream extent of coarsening relative to the D_g, suggesting that spatial propagation of the coarsening response is dependent on the sequencing of flood events. Coarsening of the D_g ranges from roughly 20 to 100 mm coarser than initial conditions over the 60-year simu-

lation, whereas coarsening of the D_{90} ranges upwards to about 200 mm coarser than initial conditions.

Robinson Canyon Creek to Outlet (13-0 km): The lower most reach of the simulation domain shows two general spatial and temporal trends with respect to bed elevation: little net change of bed topography immediately downstream of the Narrows and aggradation along the lower most 9 km of the river. Across the three hydrologic conditions, aggradation by year 60 ranges from +0.6 to +1.5 m relative to initial channel bed elevations (circa 2017), diminishing to 0 at the downstream most model node at the Pacific Ocean. Coarsening of the D_g and D_{90} bed surface grain sizes continue through this reach, and steadily diminishes moving downstream toward the ocean.

Synthesis For the No Action project simulation at Los Padres Dam, persistence of low relative sediment supply downstream of Los Padres Dam is simulated to drive further channel bed degradation to roughly channel station 35 km. Downstream of this station, BESMo projects the most significant spatial gradients in channel response likely due to constructed channel conditions at the San Clemente project reach. Strong profile adjustment here suggests that constructed conditions are not in steady-state with upstream projected supplies of water and bedload sediment for the No Action project simulation. In general, the former reservoir deposit area is a location of channel bed erosion, with deposition downstream of San Clemente Creek up and to the former San Clemente Dam site.

The reach from the former dam site to Tularcitos Creek is a response transition reach, having a somewhat wide range in the magnitude and spatial extent of aggradation. As a result, the evolution of future conditions from the former San Clemente Dam site to Tularcitos Creek are particularly sensitive to the sequencing and magnitude of future floods. A general aggradation response of +1.5 m relative to initial channel bed elevations is simulated from Garzas Creek to the Narrows, followed by little to no net bed elevation change downstream of the Narrows to station 9 km. The lower most 9 km have a consistent aggradation response ranging from +0.6 to +1.5 m relative to initial channel bed elevations.

The channel bed surface is projected to coarsen throughout the simulation reach, from Los

Padres Dam to the Pacific Ocean, despite the reintroduction of bedload supply from in between Los Padres and the former San Clemente Dam to downstream reaches. This simulation response highlights that the magnitude and gradation of the reintroduced bedload supply is insufficient to limit general bed coarsening, which is substantial over much of the model domain (i.e. factor 2 increase of the D_g at a minimum). This result for the No Action project simulation is not encouraging for steelhead or resident trout. The sequencing of floods governs the timing of profile adjustment from Los Padres to the Pacific Ocean, particularly from the former San Clemente Dam site to Tularcitos Creek, with earlier floods driving early change, and later floods driving later change. However, the general magnitude of profile response is independent of large flood timing of the 60- year simulation. These set of results raise the expectation that resumption of bedload supply from the area upstream of Los Padres Dam will have spatial patterns of response similar to those for the No Action project simulation, downstream of the former San Clemente Dam site, however the magnitudes may be more pronounced.

B.11.2 Historical Supply Simulation Results

The results of the Historical Supply simulations are shown in the following figures:

- Figure B.42 shows the simulated change in channel bed elevation;
- Figure B.43 shows the simulated change of the bed surface median grain size (D_g);
- Figure B.44 shows the simulated change of the bed surface 90th-percentile grain size (D_{90});
- Figure B.45 shows the simulated change of the longitudinal channel bed slope; and
- Figure B.46 shows the simulated unit bedload sediment transport rate.

Resumption of the estimated long-term average natural sediment supply of 13,400 m^3/yr to reaches downstream of Los Padres Dam result in the projection of nearly 4.6 m of aggradation just downstream of the Dam. Using historical topographic data, we estimate that approximately 6 m of net bed erosion has occurred downstream of the dam since construction in

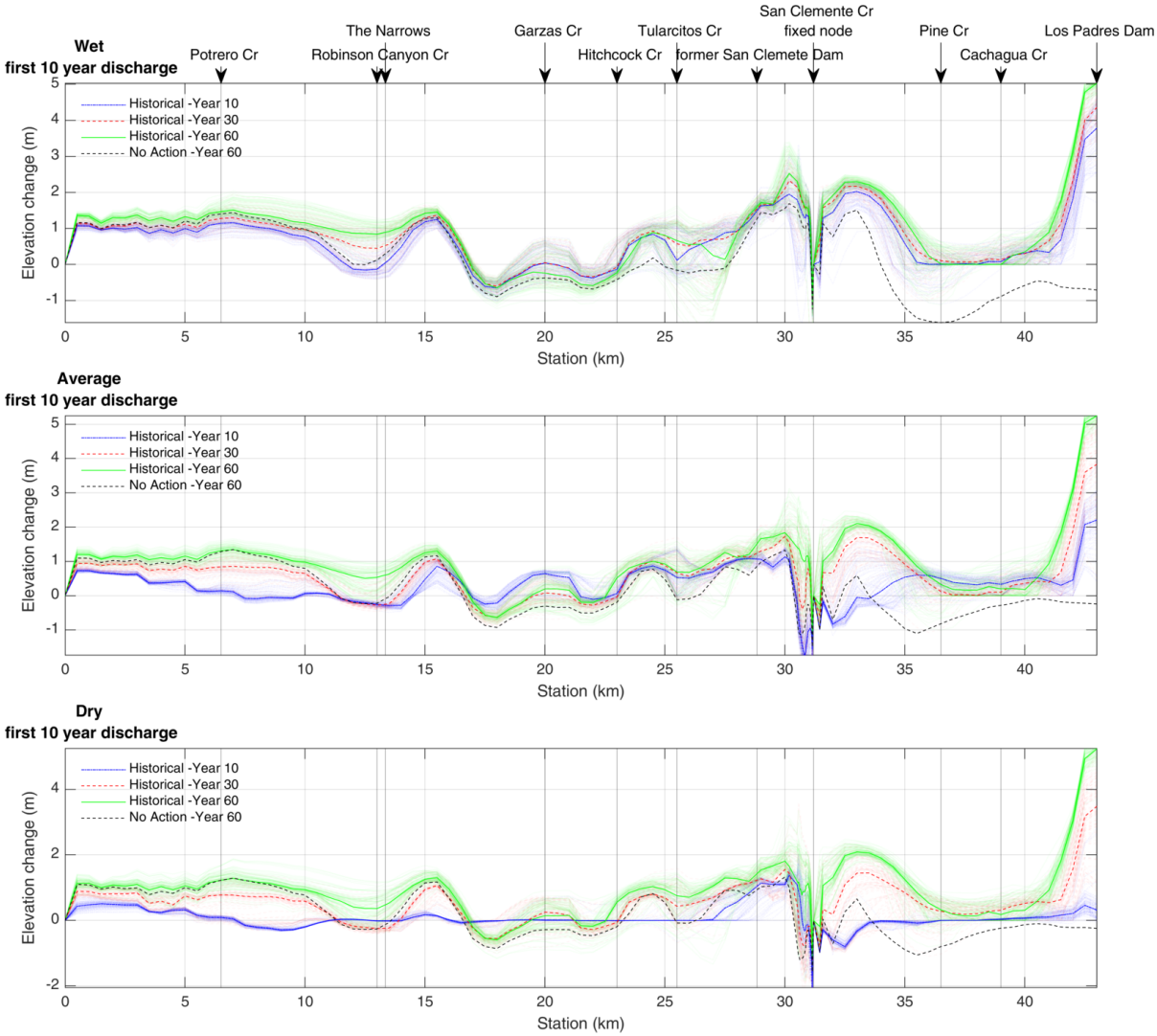

Figure B.42: Change in elevation compared to the initial elevation profile from 2017. While BESMo reports only change in sediment volume, we translated the volume change to an elevation change by using the averaged crosssection profiles shown in Appendix B.8 and converting the sediment storage from cross sectional area to depth using the same ratios shown in Appendix B.9 for flow area to flow depth. In the case of erosion, we assumed a rectangular cross section with constant channel width. Top: high, Middle: average, bottom: low cumulative discharge in the first 10 years. Per subplot the profiles of 100 simulations is shown in 10, 30, and 60-year time slices. The three solid lines in each subplot signify the median condition at each node for each of the three time slices; all other lines represent data from individual model runs.

1949. As a result, simulated bedload deposition downstream of the dam of up to 4.6 m over the 60-year simulation time period is plausible. The aggradation response at the dam lessens

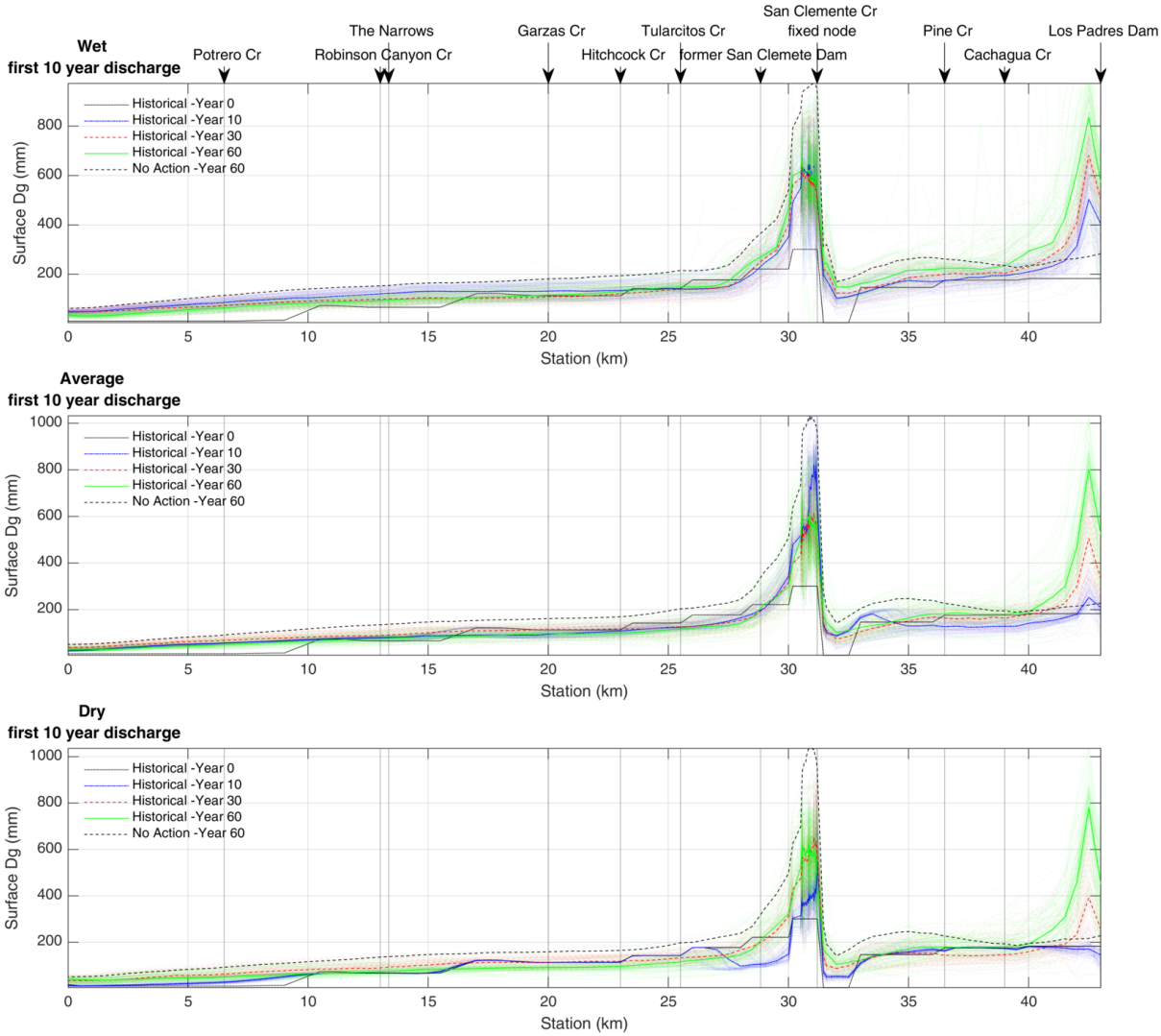

Figure B.43: Mean surface grain size (D_g) for top: high, Middle: average, bottom: low cumulative discharge in the first 10 years. Per subplot the profiles of 100 simulations is shown in 10, 30, and 60-year time slices. The three solid lines in each subplot signify the median condition at each node for each of the three time slices; all other lines represent data from individual model runs.

downstream as expected, but increases up to an estimated 1.5 m as the former San Clemente reservoir backwater zone and deposit is approached. This response also makes sense because the average bed slope through this formerly reservoir affected region is flatter than the pre-dam condition.

Careful inspection of Figure B.42 also reveals that episodes of bed erosion are simulated within the first 10 years of the simulation within the former reservoir affected region and

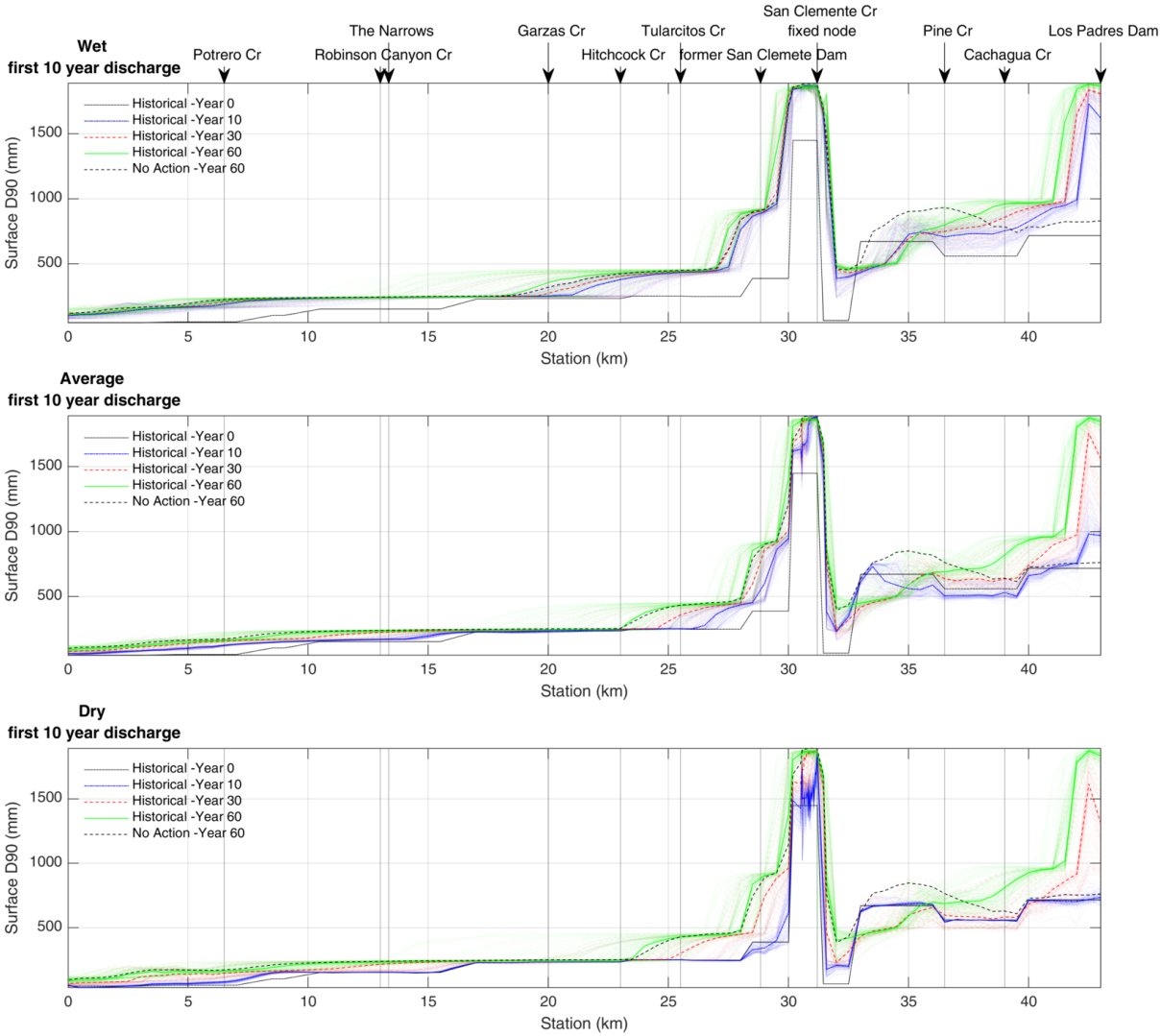

Figure B.44: Coarse fractions of the surface grain size expressed as 90th percentile size (D_{90}) for top: high, Middle: average, bottom: low cumulative discharge in the first 10 years. Per subplot the profiles of 100 simulations is shown in 10, 30, and 60-year time slices. The three solid lines in each subplot signify the median condition at each node for each of the three time slices; all other lines represent data from individual model runs.

upstream for primarily average and dry hydrologic conditions. We assume this is due to relatively low local sediment supply as a result of deposition downstream of Los Padres Dam (Figure B.46). As the deposition downstream of the dam continues in time, bedload supply increases and all hydrologic conditions tend toward a similar spatial pattern of bed profile response in between Los Padres Dam and the upstream end of the San Clemente project reach.

Downstream of the former San Clemente Dam all three hydrologic conditions project up

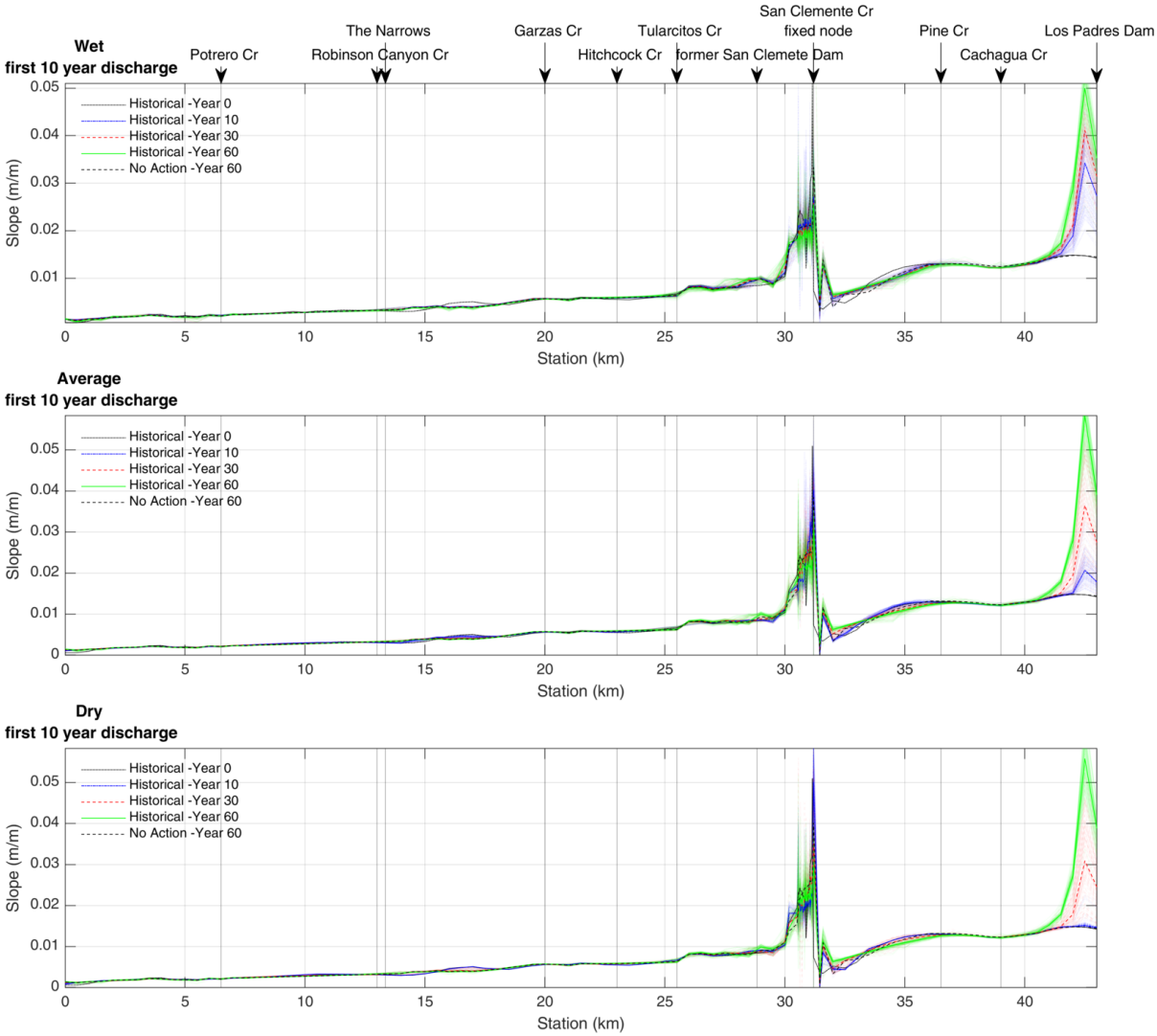

Figure B.45: Slope profile for top: high, Middle: average, bottom: low cumulative discharge in the first 10 years. Per subplot the profiles of 100 simulations is shown in 10, 30, and 60-year time slices. The three solid lines in each subplot signify the median condition at each node for each of the three time slices; all other lines represent data from individual model runs.

to 2.1 m of bed deposition, with relaxation of net bed aggradation toward Hitchcock Creek. This result is similar to the result discussed and presented above for the No Action updated simulation. The increased local sediment budget is driven by redistribution of material from the reroute reach at San Clemente Creek.

Downstream of Hitchcock Creek the Historical Supply simulations project a varied response of a net elevation change between -0.6 and +0.3 m by the end of the 60-year simulation

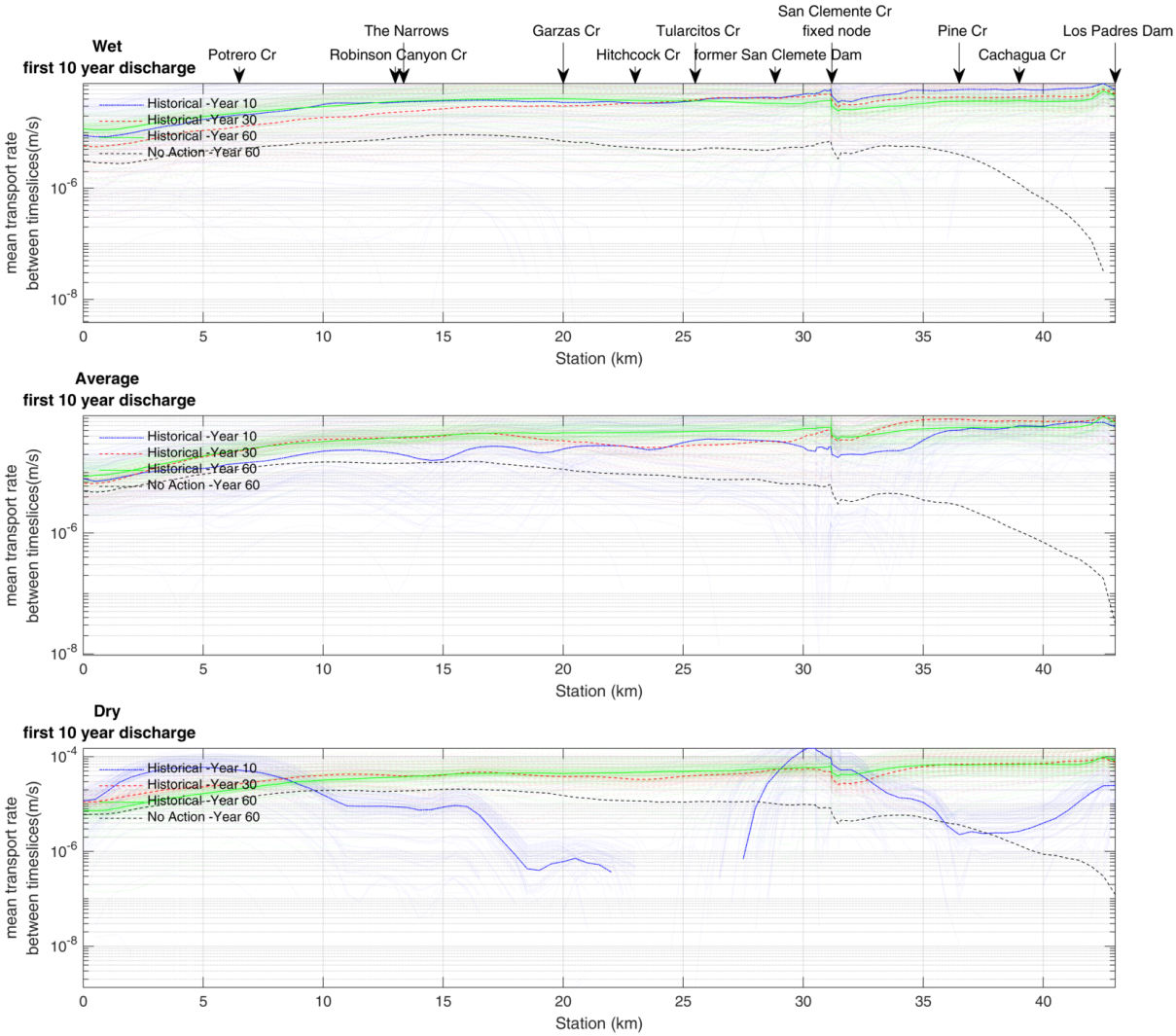

Figure B.46: Averaged transport rate between time slices (Year 10: data from 0-10 years, Year 30: data from 10-30 years, Year 60: data from 30-60 years). For top: high, Middle: average, bottom: low cumulative discharge in the first 10 years. Per subplot the profiles of 100 simulations is shown in 10, 30, and 60-year time slices. The three solid lines in each subplot signify the median condition at each node for each of the three time slices; all other lines represent data from individual model runs.

time period. This response is consistent across all three hydrologic conditions, and the profile is about 0.3 to 0.6 m higher than in the No Action simulation for the whole lower part of the river. Comparability of the aggradational response and magnitude along the lower 23 km of the Carmel River across the three hydrologic conditions for the Historical Supply conditions suggests deposition is likely to occur and independently of hydrology, given sufficient time

for the channel to respond. A similar conclusion was drawn for the No Action simulation.

Downstream of Los Padres Dam, the channel bed is projected to coarsen. With additional sediment supplied from upstream, we would expect increased sediment mobility and bed mixing, eventually winnowing the finer grain sizes from both the surface and shallow subsurface. The trajectory of the surface D_{90} is dependent upon the hydrologic conditions of the first 10 years of the simulation, with wet years producing a coarser bed, likely as a result of high mobility and bed mixing. Results from the end of the 60-year simulation run times are similar between the hydrologic scenarios, with the coarsest bed just downstream of the Los Padres Dam and near the former San Clemente Dam site. In each of the hydrologic conditions, a coarser D_{90} has prograded downstream to Las Garzas Creek in wet conditions, and just upstream of Las Garzas Creek in average and dry conditions.

Compared to the No Action simulation, the geometric mean grain size (D_g), has more variability in the lower reaches across the 60-year simulation time frame, suggesting an overall higher sediment mobility throughout the simulation period in the lower reaches. The Historical Supply simulation also produces a mean surface grain size similar to the model input grain size distribution (indicated on the plots by the dashed cyan line, hidden behind the simulation results), and is finer than the final D_g for the No Action simulation (dashed black line). This result suggests that resumption of the Historical Supply to the river downstream of Los Padres may have tangible benefits for steelhead habitat conditions within the simulation time period of 60 years. It further implies that the Historical Supply is sufficient to prevent further bed surface coarsening along the lower river downstream of the former San Clemente Dam, relative to initial conditions. This was not the case for the No Action simulation results where we concluded that the additional bedload sediment supply sourced in between Los Padres Dam and the former San Clemente Dam, as represented in the model, was insufficient to prevent net bed surface coarsening along the lower Carmel River over the simulation time period.

B.11.3 Pulsed Supply Simulation Results

To simplify the discussion, we will only describe the results for the pulse scenario using rating curve RC4. The results of the other curves are presented as median values in Appendix B.13.

Following the structure from the previous results, we review the Pulsed Supply simulation in the following figures:

- Figure B.47 shows the simulated change in channel bed elevation;
- Figure B.48 shows the simulated change of the bed surface median grain size (D_g);
- Figure B.49 shows the simulated change of the bed surface 90th-percentile grain size (D_{90});
- Figure B.50 shows the simulated change of the longitudinal channel bed slope; and
- Figure B.51 shows the simulated unit bedload sediment transport rate.

The sediment supply from rating curve RC4 to reaches downstream of Los Padres Dam causes up to 5.8 m of aggradation just downstream of the Dam (see Figure B.47). This is about 1.2 m more than in the Historical scenario and within the range of measured historical elevation profiles below the dam. The aggradation response at the dam lessens downstream but increases up to an estimated 2.4 m (Historical supply 1.5 m) as the former San Clemente reservoir backwater zone and deposit is reached.

The channel between Los Padres Dam and the upstream end of the San Clemente project reach shows a 0.3-0.9 m higher deposition compared with the Historical Supply simulation, with an exception between Pine creek and Cachagua creek where both simulations show no elevation change.

Downstream of the former San Clemente Dam all three hydrologic conditions result in up to 2.7 m of sediment deposition, which steadily decreases until Tularcitos Creek, where the Pulsed Supply scenario shows about 0.5 m less deposition than the Historical Supply scenario. At the request of the TRC, we apply a 50% increase in boundary shear stress resistance to prevent perhaps unrealistic erosion because of incomplete bed surface and subsurface grain size distribution data. After 60 years, the Pulsed Supply scenario RC4 does not show significant erosion or deposition within 3 km upstream and downstream of Garzas Creek, which agrees with the Historical Supply scenario. Further downstream of this reach and up to the mouth of

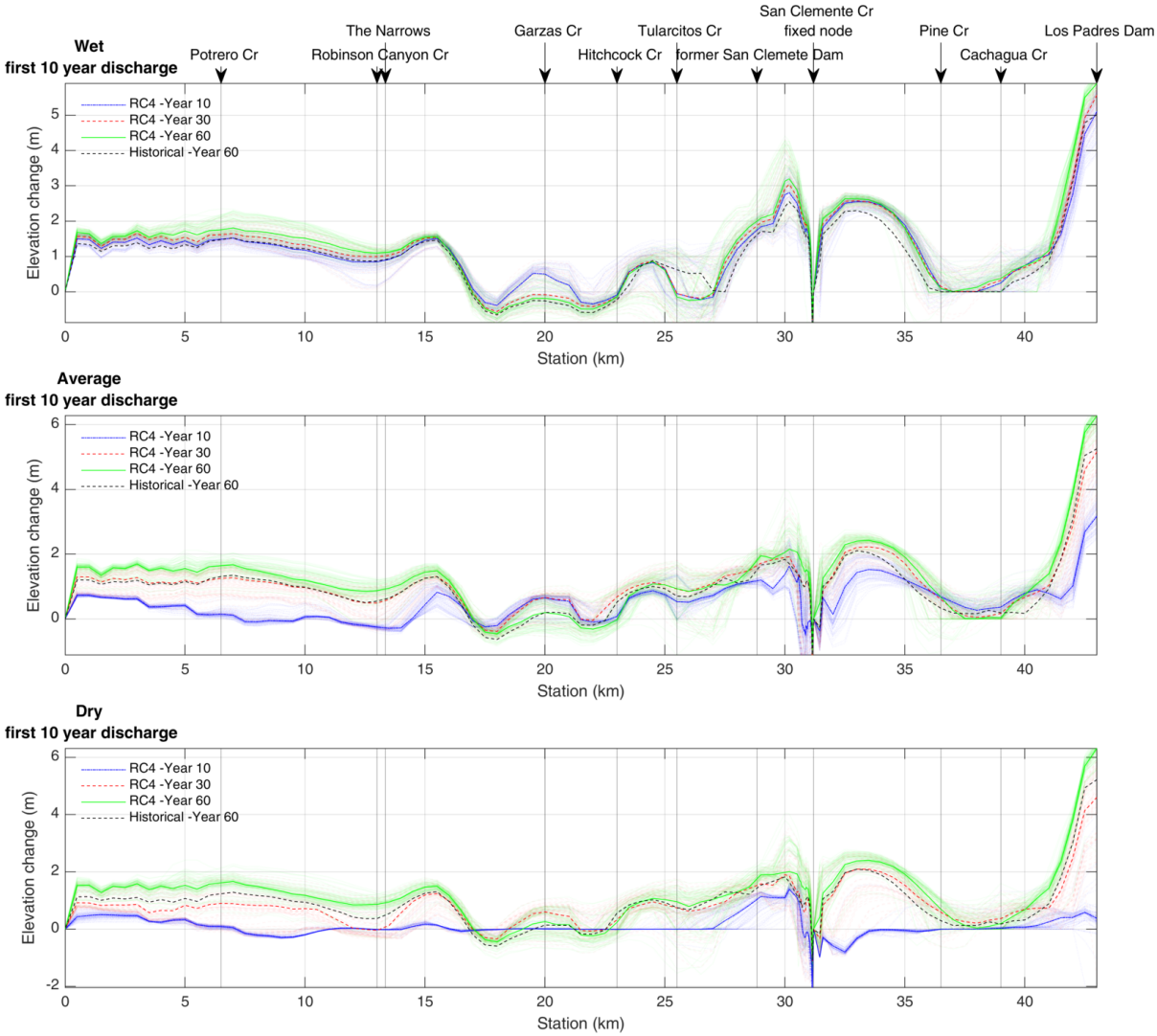

Figure B.47: Change in elevation compared to the initial elevation profile from 2017. While BESMo reports only change in sediment volume, we translated the volume change to an elevation change by using the averaged crosssection profiles shown in Appendix B.8 and converting the sediment storage from cross sectional area to depth using the same ratios shown in Appendix B.9 for flow area to flow depth. In the case of erosion, we assumed a rectangular cross section with constant channel width. Top: high, Middle: average, bottom: low cumulative discharge in the first 10 years. Per subplot the profiles of 100 simulations is shown in 10, 30, and 60-year time slices. The three solid lines in each subplot signify the median condition at each node for each of the three time slices; all other lines represent data from individual model runs.

the river we observe relatively consistent deposition of 1.5 m of sediment after 60 simulation years, which is about 0.3 m more deposition than in the Historical Supply scenario.

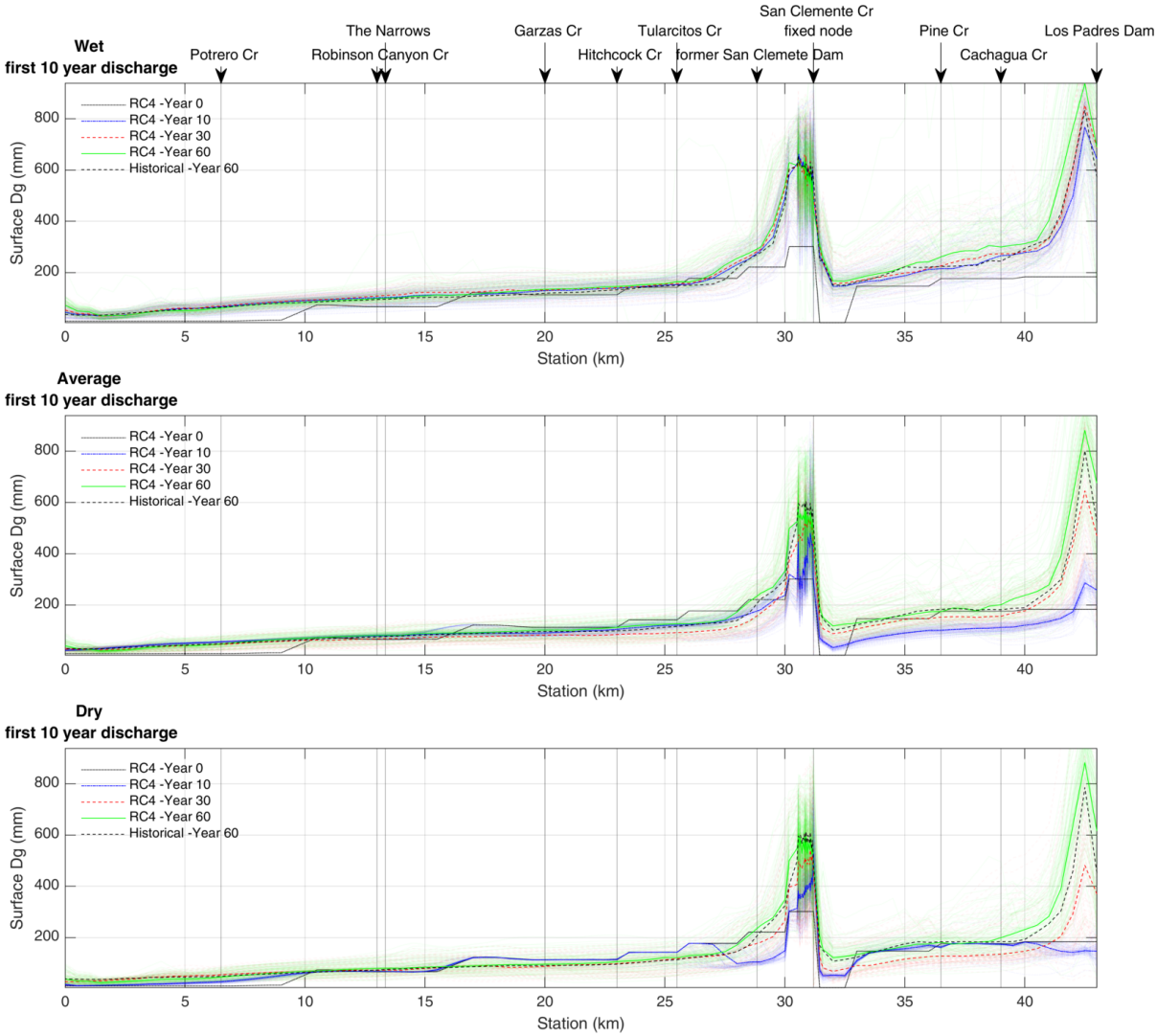

Figure B.48: Mean surface grain size (D_g) for top: high, Middle: average, bottom: low cumulative discharge in the first 10 years. Per subplot the profiles of 100 simulations is shown in 10, 30, and 60-year time slices. The three solid lines in each subplot signify the median condition at each node for each of the three time slices; all other lines represent data from individual model runs.

Comparability of the aggradational response and magnitude along the lower 23 km of the Carmel River across the three hydrologic conditions for the Pulsed Supply conditions suggests deposition is likely to occur and independently of hydrology, given enough time for the channel to respond. A similar conclusion was drawn for the No Action and Historical Supply simulations.

The median grain size adjustments (D_g, Figure B.48), the Pulsed Supply scenario shows

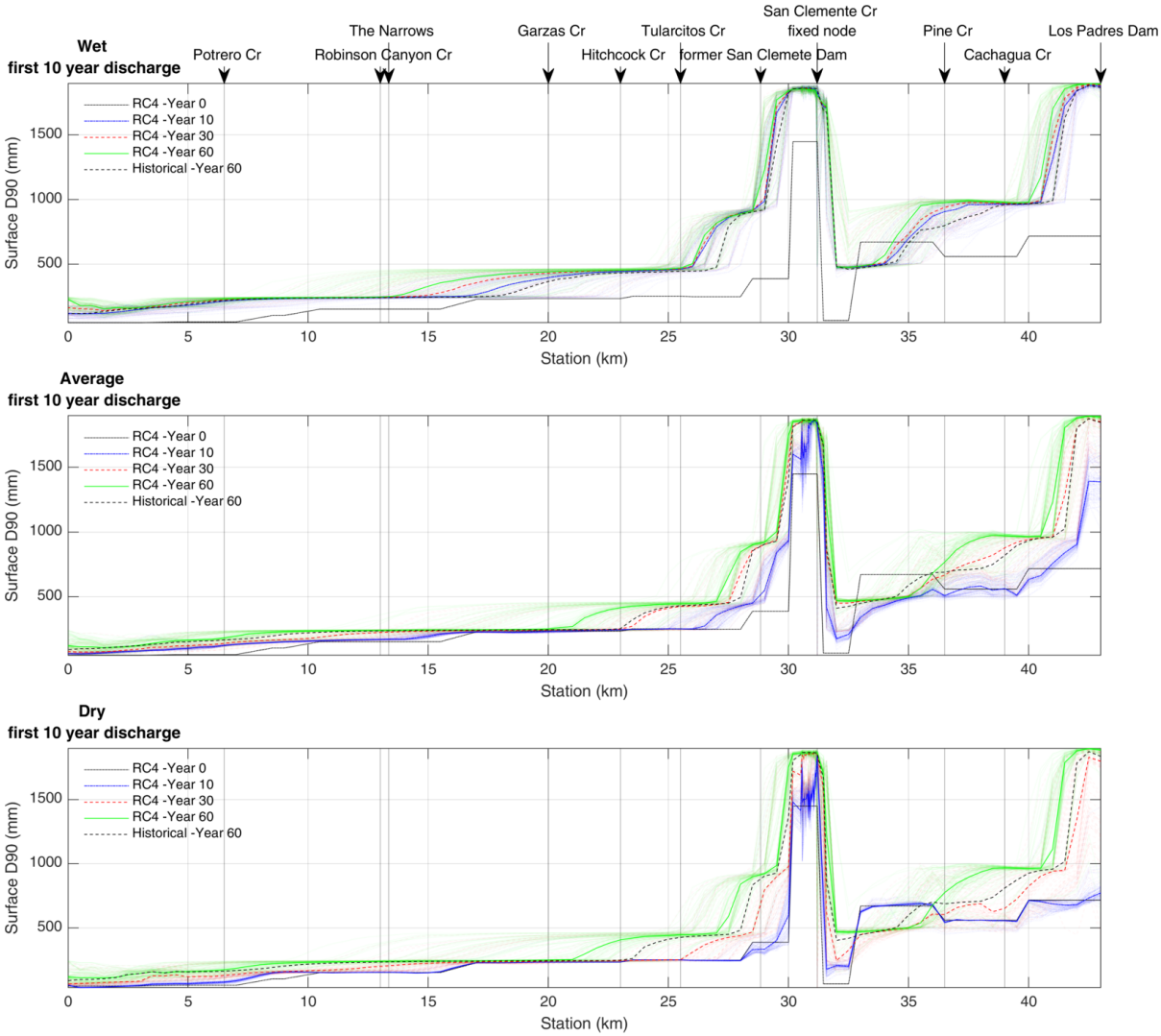

Figure B.49: Coarse fractions of the surface grain size expressed as 90th percentile size (D_{90}) for top: high, Middle: average, bottom: low cumulative discharge in the first 10 years. Per subplot the profiles of 100 simulations is shown in 10, 30, and 60-year time slices. The three solid lines in each subplot signify the median condition at each node for each of the three time slices; all other lines represent data from individual model runs.

similar conditions as the Historical scenario. The biggest difference occurs below the Los Padres reservoir, where the sediment feed introduces more fine material. The coarse fractions signified by the 90th-percentile grain sizes (D_{90}, Figure B.49) show a distinct coarsening in response to the increased sediment supply. This might be caused by the increased mobility of the finer material, as the transport function used in BESMo will cause higher transport rates for higher contents of sand in the bed.

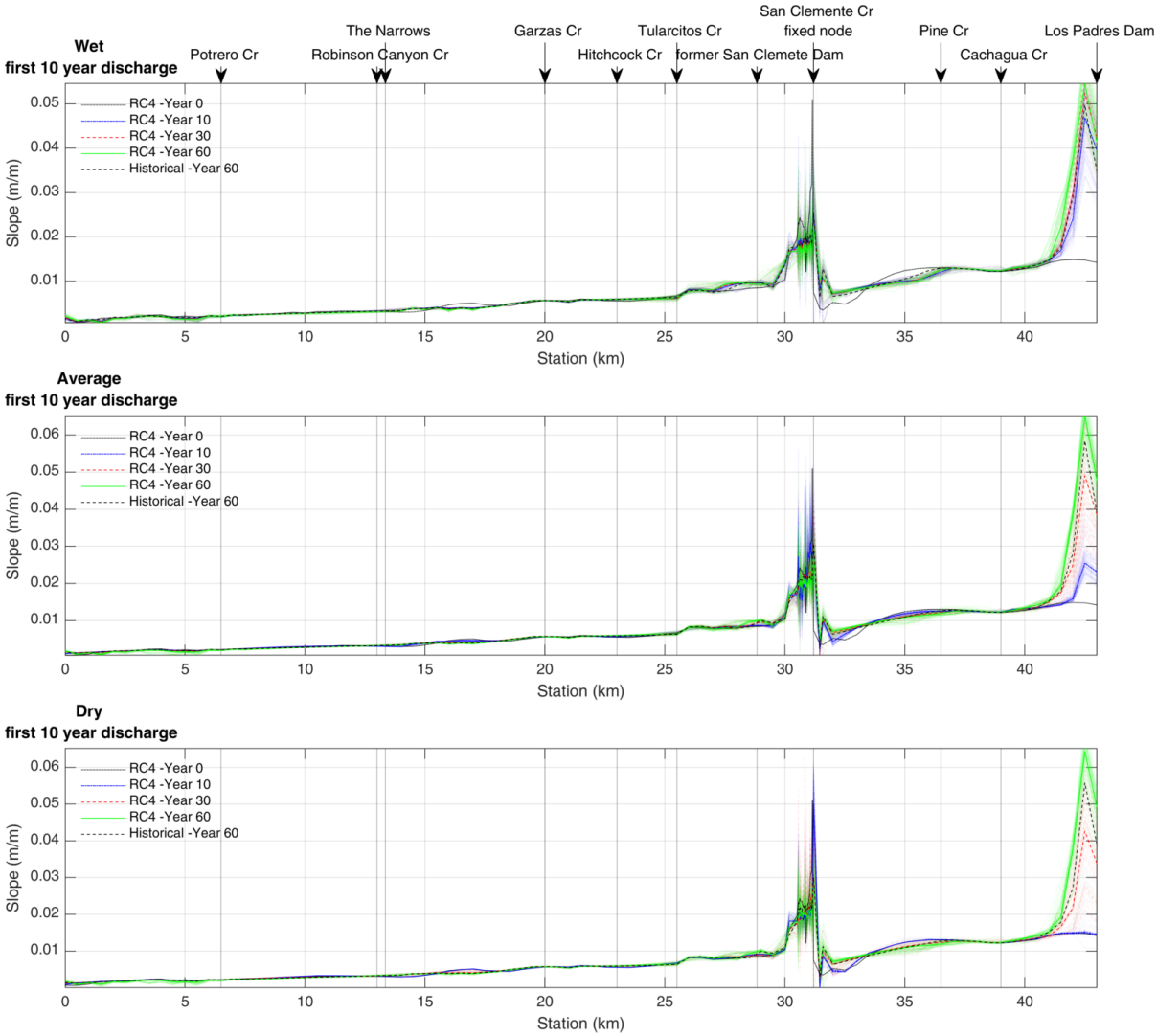

Figure B.50: Slope profile for top: high, Middle: average, bottom: low cumulative discharge in the first 10 years. Per subplot the profiles of 100 simulations is shown in 10, 30, and 60-year time slices. The three solid lines in each subplot signify the median condition at each node for each of the three time slices; all other lines represent data from individual model runs.

In conclusion, the elevation profile modestly aggrades in the Pulsed Supply scenario RC4 compared to the Historical Supply scenario, which follows the large increase in sediment supply due to the inclusion of the reservoir deposits (over 60 years Historical Supply: 1,087,900 m^3, Pulsed Supply: 1,667,700 m^3). Fining of the bed close to Los Padres reservoir is caused by the increased supply of relatively fine fractions. It is notable that the surface grain size does not seem to be significantly changed between the two scenarios, even though the aver-

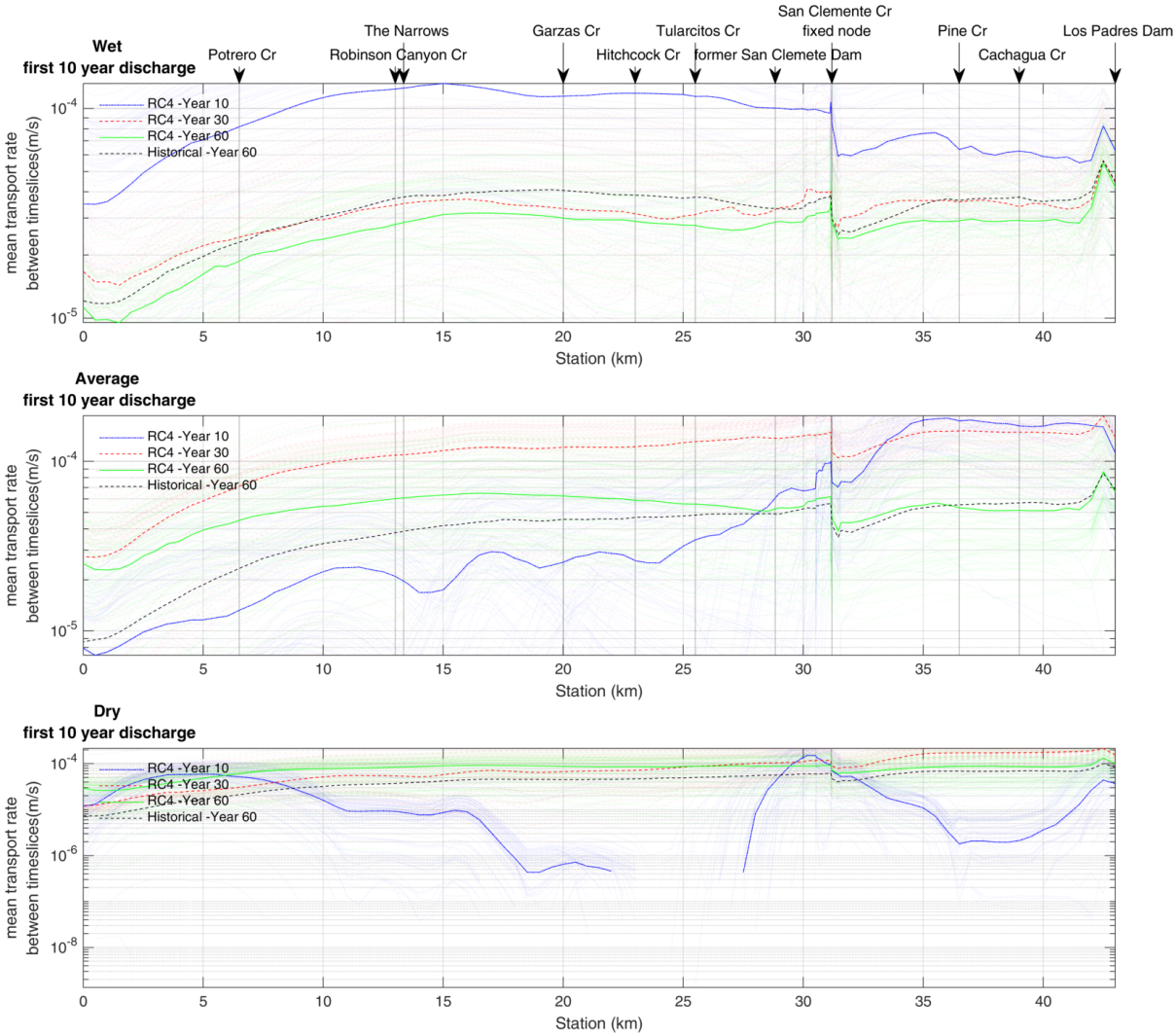

Figure B.51: Averaged transport rate between time slices (Year 10: data from 0-10 years, Year 30: data from 10-30 years, Year 60: data from 30-60 years). For top: high, Middle: average, bottom: low cumulative discharge in the first 10 years. Per subplot the profiles of 100 simulations is shown in 10, 30, and 60-year time slices. The three solid lines in each subplot signify the median condition at each node for each of the three time slices; all other lines represent data from individual model runs.

age transport rates throughout the river (Figure B.51) increases by often a factor of two. We want to note that the Pulse scenario RC3, which evacuates reservoir sediment more slowly, projects a finer bed grain size distribution (D_g 10-40% lower). This implies that a more constant sediment feed from the Los Padres reservoir is more effective in fining the bed than a steeper, pulse-like rating curve.

Our findings suggest that the Pulsed sediment supply may have tangible benefits for steelhead habitat conditions within the simulation time period of 60 years. These simulations further show that the rate of supply of sediment from the reservoir has a strong impact on the bed surface composition along the whole river.

B.11.4 Uncontrolled Release Simulation Results

To simplify the discussion, we will only describe the results for the pulse scenario using the exponential decay curve Exp2. The results of the other curves are presented as median values in Appendix B.13. Following the structure from the previous results, we review the Uncontrolled Release simulation in the following figures:

- Figure B.52 shows the simulated change in channel bed elevation;
- Figure B.53 shows the simulated change of the bed surface median grain size (D_g);
- Figure B.54 shows the simulated change of the bed surface 90th-percentile grain size (D_{90});
- Figure B.55 shows the simulated change of the longitudinal channel bed slope; and
- Figure B.56 shows the simulated unit bedload sediment transport rate.

The sediment supply from the Uncontrolled Release scenario Exp 2 to reaches downstream of Los Padres Dam causes up to 6.7 m of aggradation just downstream of the Dam (see Figure B.52). This is about 2 m more than in the Historical scenario. The aggradation response at the dam lessens downstream but increases up to an estimated 2.7 m (Hist. 2 m) as the former San Clemente reservoir backwater zone and deposit is approached. The channel between Los Padres Dam and the upstream end of the San Clemente project reach shows a 0.6-1.8 m higher deposition than in the Historical scenario, which is about double than in the Pulsed supply scenario RC4.

Downstream of the former San Clemente Dam all three hydrologic conditions project up to 4 m of sediment deposition, which steadily decreases until Hitchcock Creek, with the uncontrolled release scenario showing about 0.6 m more deposition than the Historical scenario.

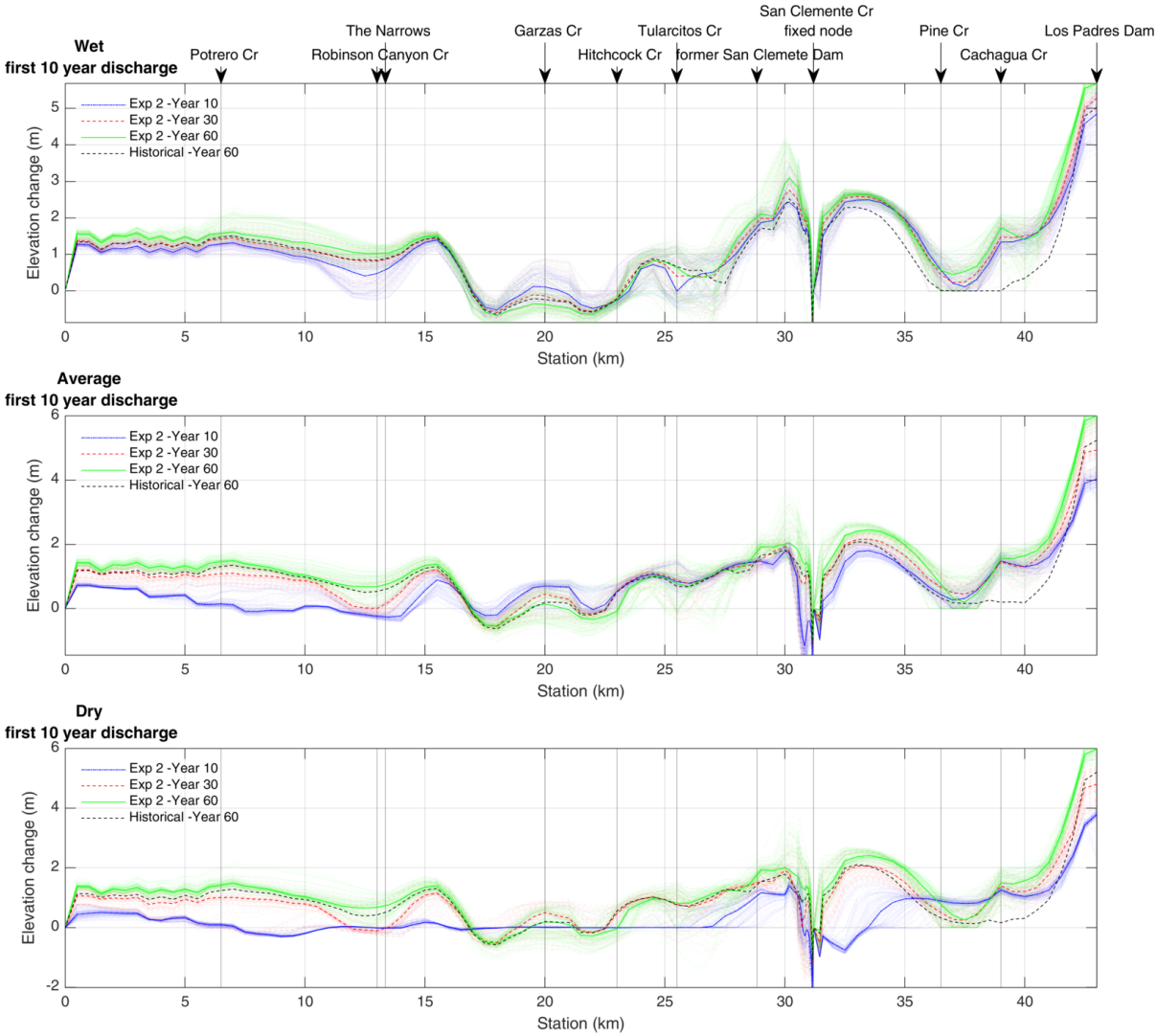

Figure B.52: Change in elevation compared to the initial elevation profile from 2017. While BESMo reports only change in sediment volume, we translated the volume change to an elevation change by using the averaged crosssection profiles shown in Appendix B.8 and converting the sediment storage from cross sectional area to depth using the same ratios shown in Appendix B.9 for flow area to flow depth. In the case of erosion, we assumed a rectangular cross section with constant channel width. Top: high, Middle: average, bottom: low cumulative discharge in the first 10 years. Per subplot the profiles of 100 simulations is shown in 10, 30, and 60-year time slices. The three solid lines in each subplot signify the median condition at each node for each of the three time slices; all other lines represent data from individual model runs.

Per request of the TRC, in this section of the river we apply a 50increase in boundary shear stress resistance to prevent an erosional signal which occurred in early runs of the Historical

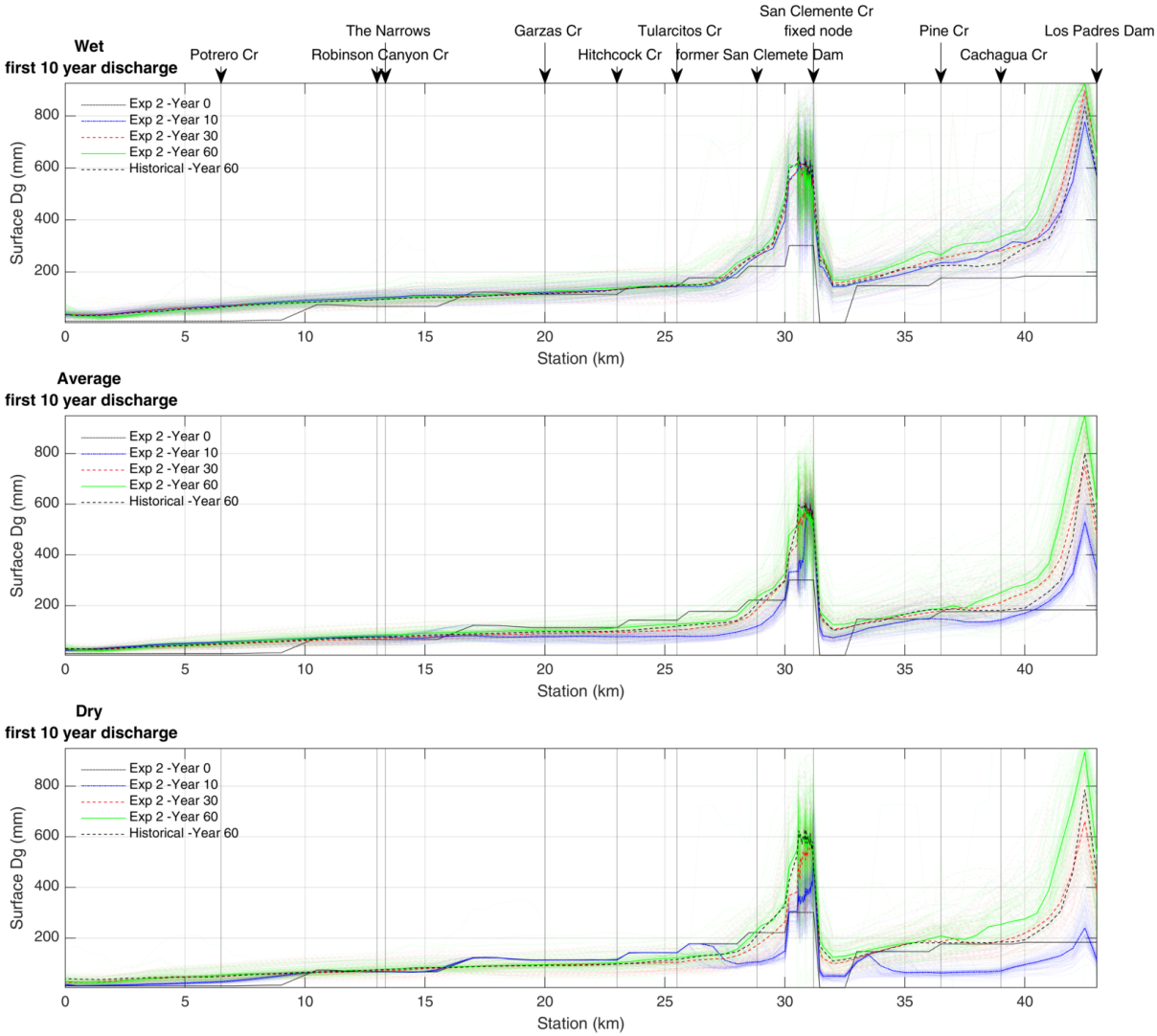

Figure B.53: Mean surface grain size (D_g) for top: high, Middle: average, bottom: low cumulative discharge in the first 10 years. Per subplot the profiles of 100 simulations is shown in 10, 30, and 60-year time slices. The three solid lines in each subplot signify the median condition at each node for each of the three time slices; all other lines represent data from individual model runs.

scenario.

Within 3 km upstream and downstream of Garzas Creek the Uncontrolled Release after 60 years shows between 0.6 m of erosion under wet hydrographs, or between 0.6 m erosion and 0.6 m deposition under average and dry hydrographs, which agrees with the Historical scenario. Further downstream of this reach and up to the mouth of the river we observe relatively consistent deposition of 1.5 m of sediment after 60 simulation years. The trend is

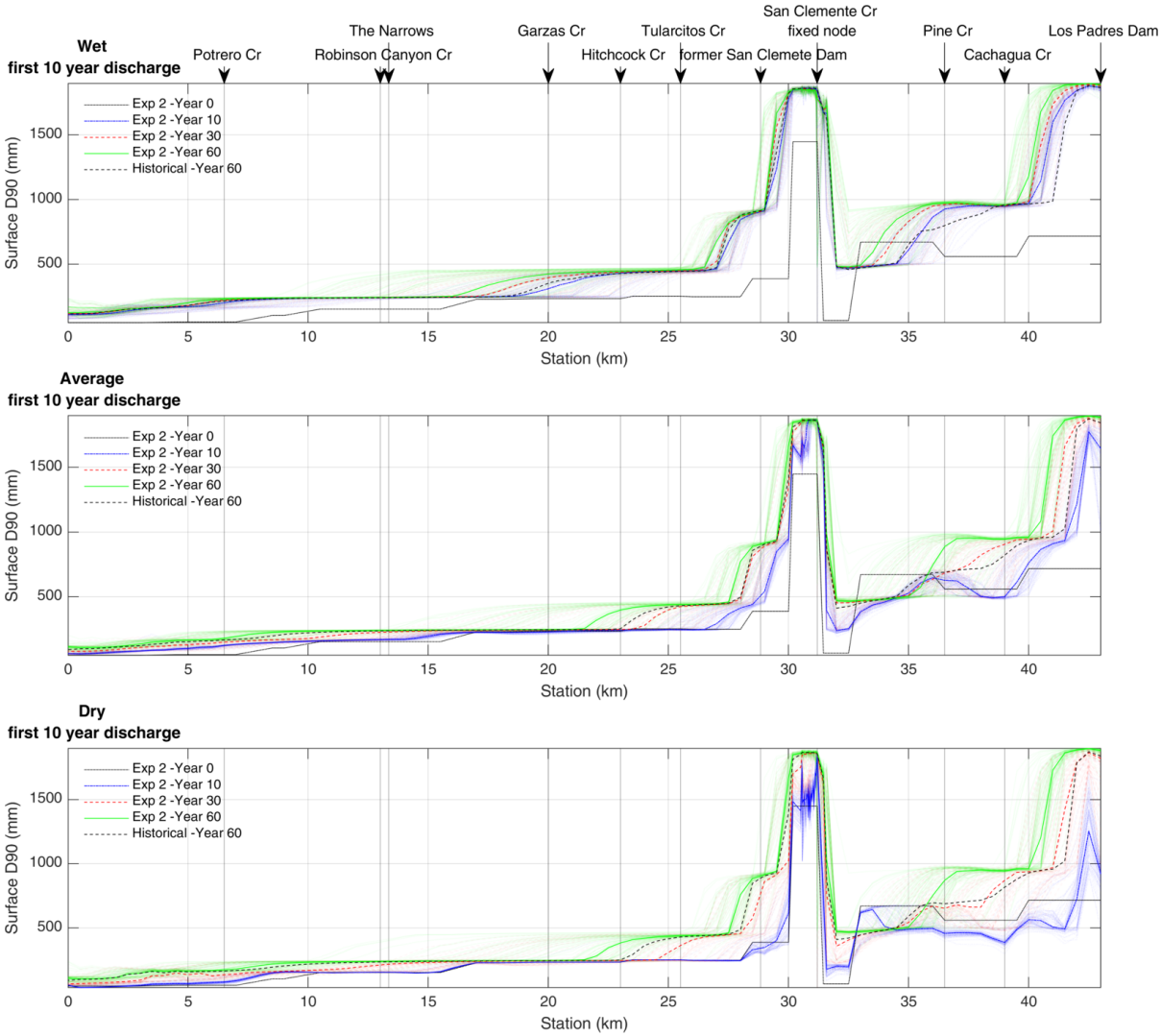

Figure B.54: Coarse fractions of the surface grain size expressed as 90th percentile size (D_{90}) for top: high, Middle: average, bottom: low cumulative discharge in the first 10 years. Per subplot the profiles of 100 simulations is shown in 10, 30, and 60-year time slices. The three solid lines in each subplot signify the median condition at each node for each of the three time slices; all other lines represent data from individual model runs.

about 0.3 m more elevation change than in the Historical scenario and matches data from the Pulsed Supply scenarios.

The comparable aggradational response along the lower 23 km of the Carmel River across the three hydrologic conditions for both the Uncontrolled Release and the Pulsed Supply simulations suggests that the deposition is likely to occur independently of hydrology if given enough time for the channel to respond. A similar conclusion was drawn for the No Action

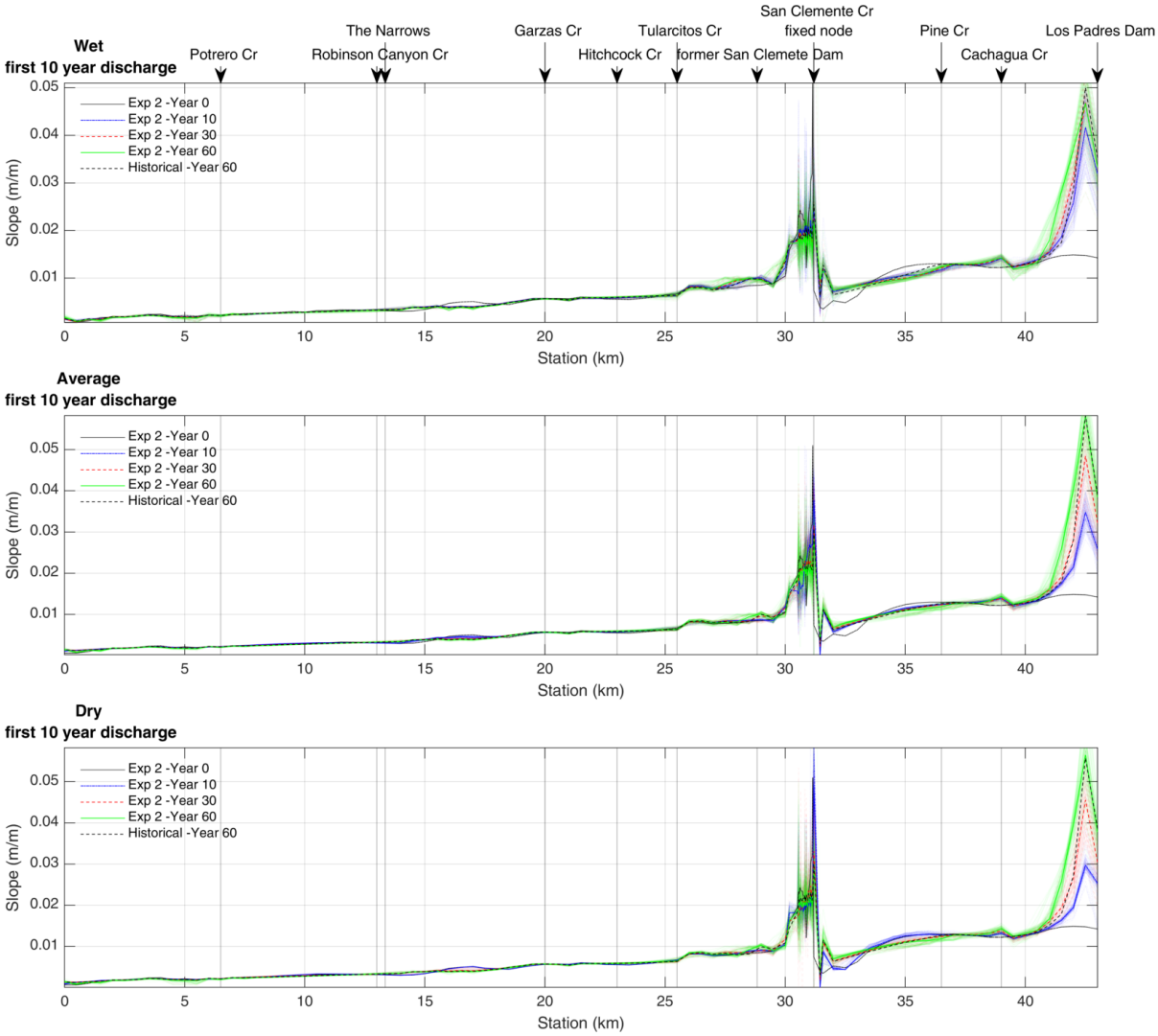

Figure B.55: Slope profile for top: high, Middle: average, bottom: low cumulative discharge in the first 10 years. Per subplot the profiles of 100 simulations is shown in 10, 30, and 60-year time slices. The three solid lines in each subplot signify the median condition at each node for each of the three time slices; all other lines represent data from individual model runs.

and Historical Supply simulations.

In regards of median grain size adjustments (D_g, Figure B.53), the Uncontrolled Release scenario shows similar conditions as both the Pulsed Supply and the Historical scenarios, except that under the dry hydrograph more fine material leaves the reservoir and reduces the average grain size below the Los Padres dam in the early phase of the simulations (10 year lines). The coarse fractions signified by the 90th-percentile grain sizes (D_{90}, Figure B.54) show

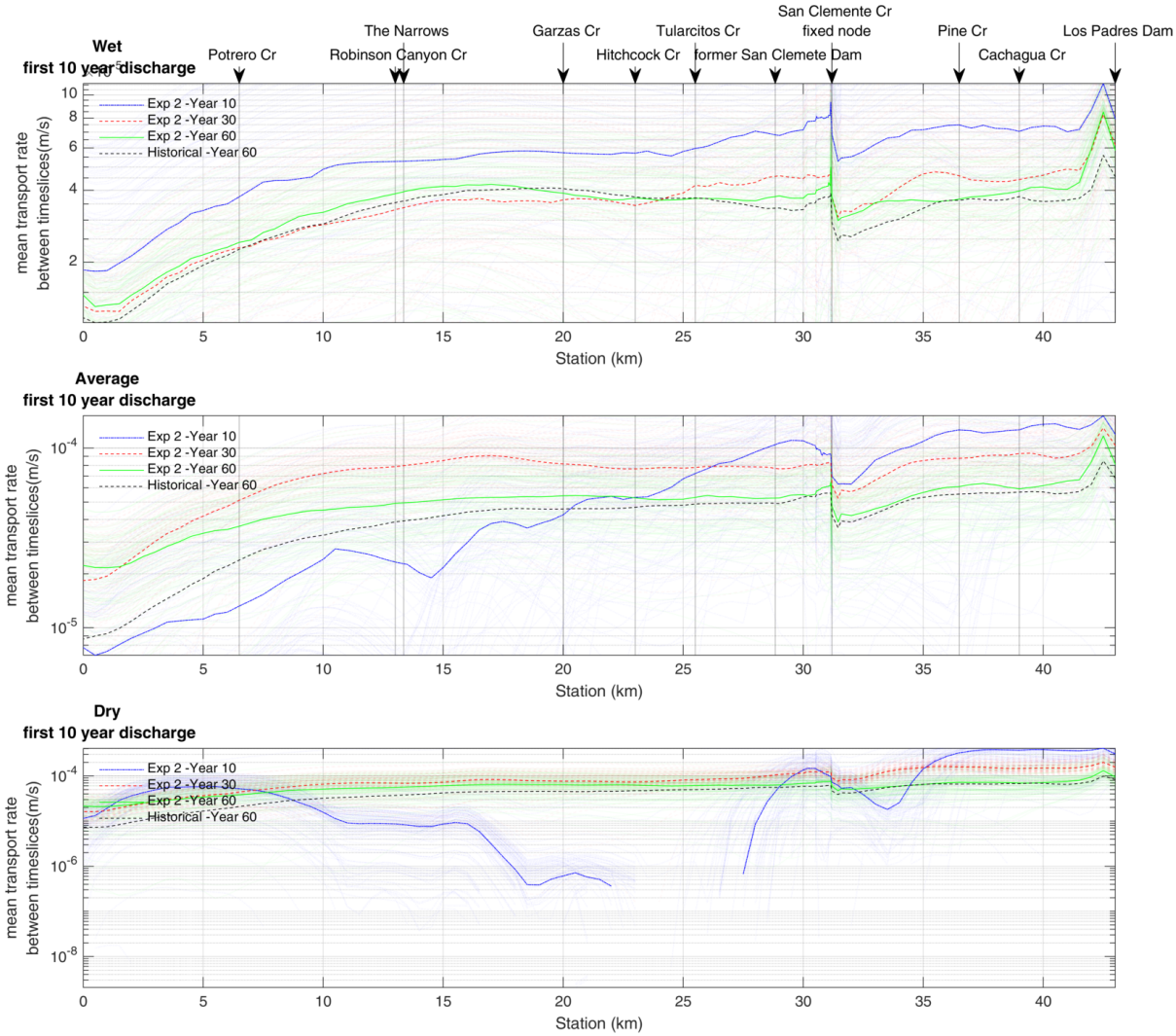

Figure B.56: Averaged transport rate between time slices (Year 10: data from 0-10 years, Year 30: data from 10-30 years, Year 60: data from 30-60 years). For top: high, Middle: average, bottom: low cumulative discharge in the first 10 years. Per subplot the profiles of 100 simulations is shown in 10, 30, and 60-year time slices. The three solid lines in each subplot signify the median condition at each node for each of the three time slices; all other lines represent data from individual model runs.

a similar response, also mainly in the first 10 years of the simulations. At the 30 and 60 year marks the bed surface is generally coarser than in the Historical scenario, which is due to the increased mobility of the bed due to the finer material supplied by the reservoir, as the transport function used in BESMo will cause higher transport rates for higher contents of sand in the bed.

In conclusion, the elevation profile increases moderately in the Uncontrolled Release scenario Exp 2 in comparison to the Historical scenario, which stands in contrast to the large increase in sediment supply due to the inclusion of the reservoir deposits (over 60 years Historical: 1,087,900 m^3, Exp 2: 1,541,800 m^3). Fining of the bed close to Los Padres reservoir is caused by the increased supply of relatively fine fractions. In comparison to the Pulsed Supply scenarios, this fine sediment is introduced mainly within the first 10-20 years of the simulations. It is notable that the surface grain size does not seem to be significantly changed between the scenarios, even though the average transport rates throughout the river (Figure B.56) increases by often a factor of two.

In comparison to the Pulsed Supply scenarios, the Uncontrolled Release scenarios show more change in grain size and bed surface elevation within the first years of the simulations. Generally, in the Pulsed Supply scenarios the sediment feed from the reservoir is spread over a longer time frame, which leads to a more continuous supply of fine material into the upper Carmel River. Due to the quick decrease in supply rates in the Uncontrolled Release scenarios, the bed surface coarsens stronger.

B.12 Median Results of focus Scenarios

B.12.1 Average Hydrographs

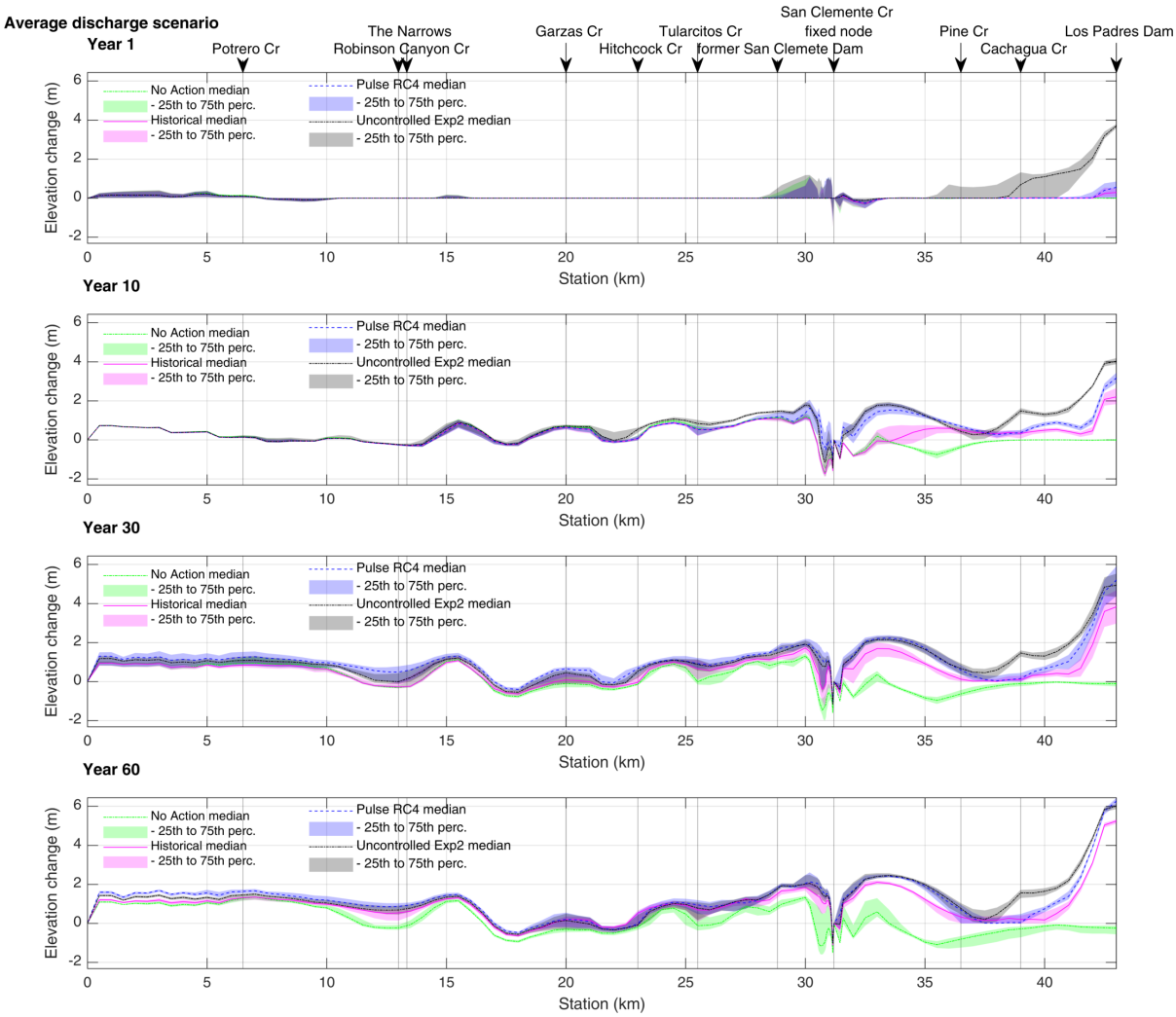

Figure B.57: Comparison of projected bed elevation change from the 2017 initial profile for the average hydrologic condition and the Historical, Pulse and Uncontrolled sediment supply simulations. Shaded regions capture the 25th-75th percentile responses across the 100 simulations for the average condition. Results shown for simulation year 1, 10, 30 and 60.

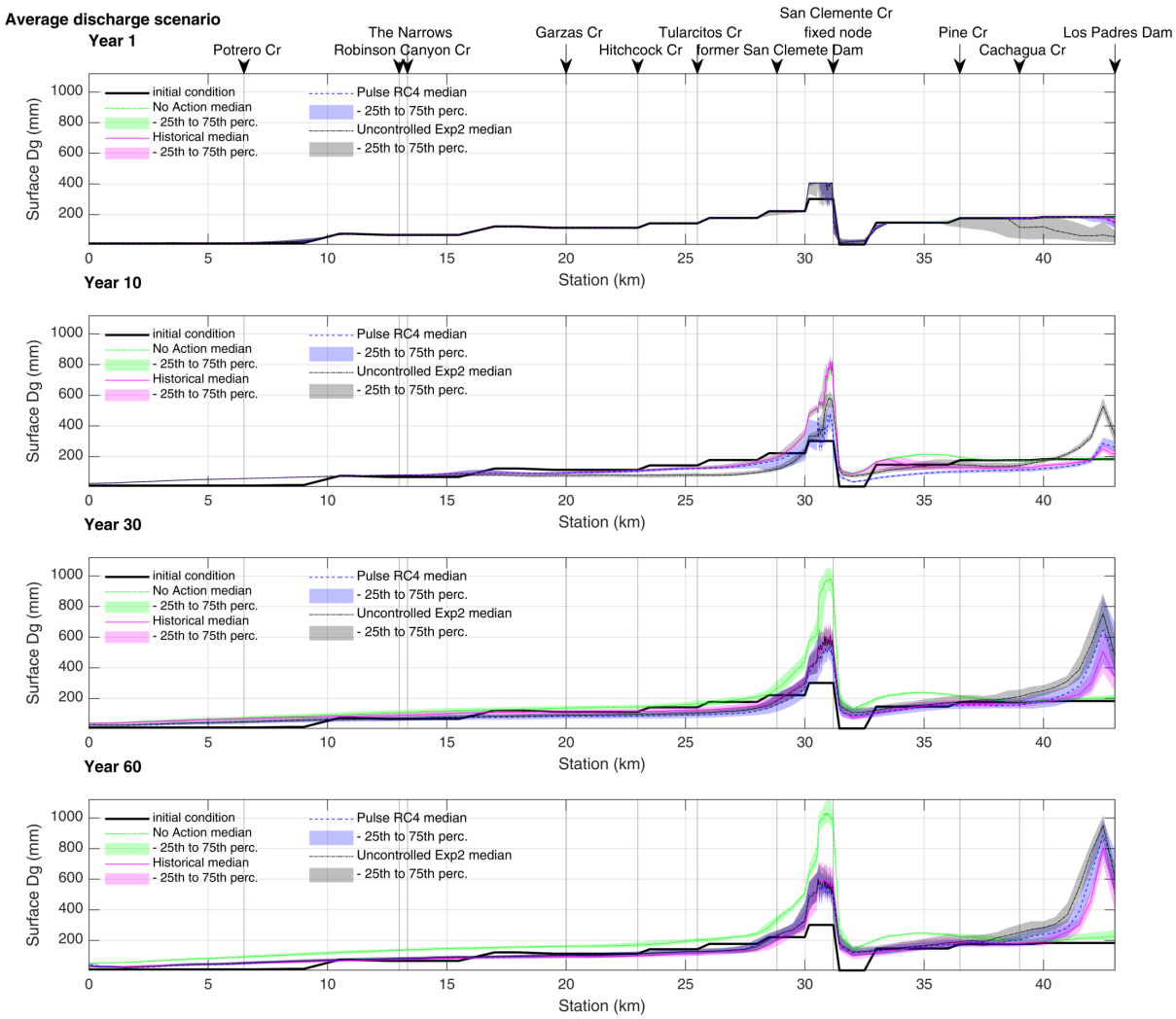

Figure B.58: Comparison of projected change of the geometric mean grain size of the bed surface D_g for the average hydrologic condition and the Historical, Pulse and Uncontrolled sediment supply simulations. Shaded regions capture the 25th-75th percentile responses across the 100 simulations for the average condition. Results shown for simulation year 1, 10, 30 and 60.

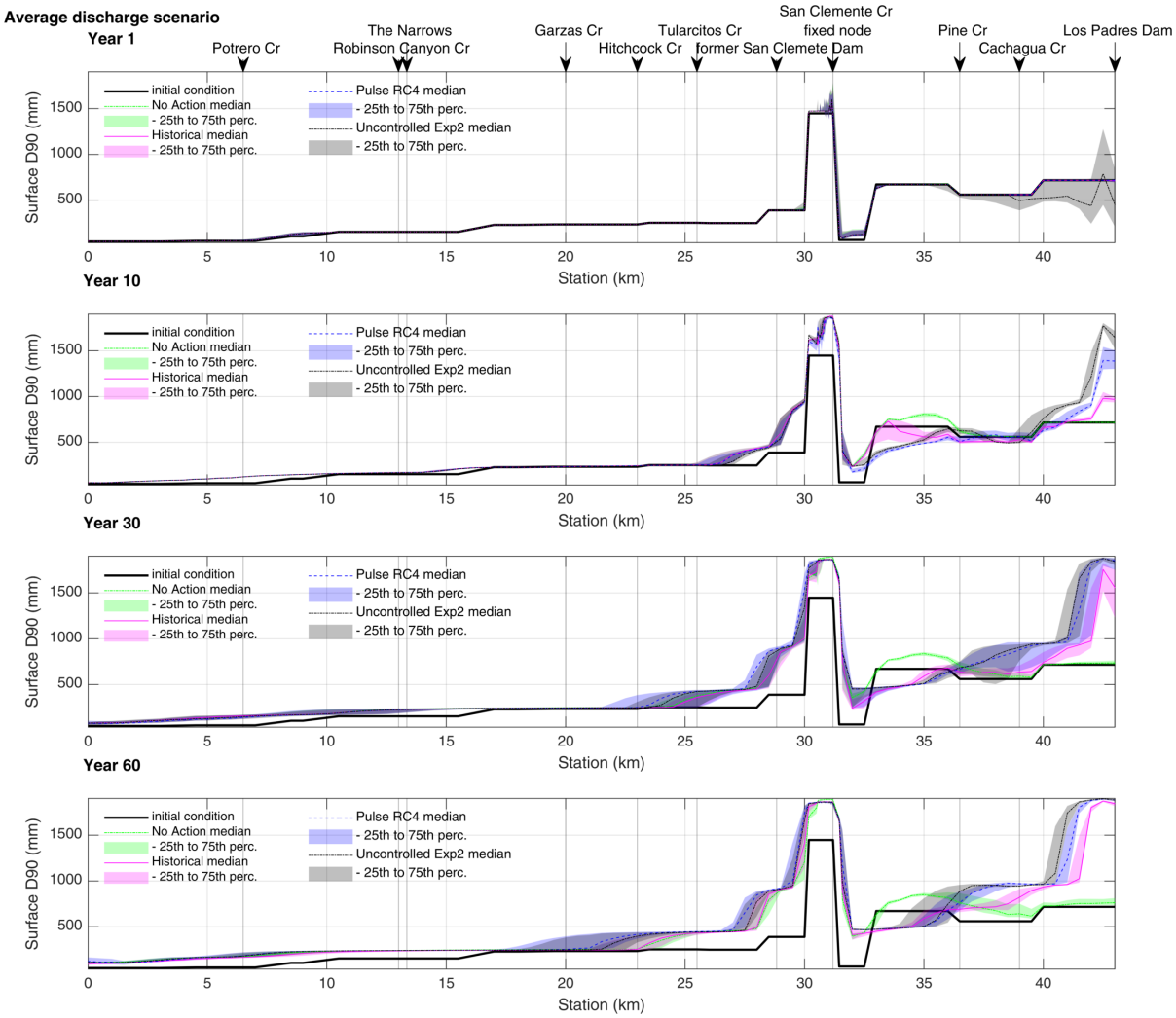

Figure B.59: Comparison of projected change of the geometric mean grain size of the bed surface D_{90} for the average hydrologic condition and the Historical, Pulse and Uncontrolled sediment supply simulations. Shaded regions capture the 25th-75th percentile responses across the 100 simulations for the average condition. Results shown for simulation year 1, 10, 30 and 60.

B.12.2 Dry Hydrographs

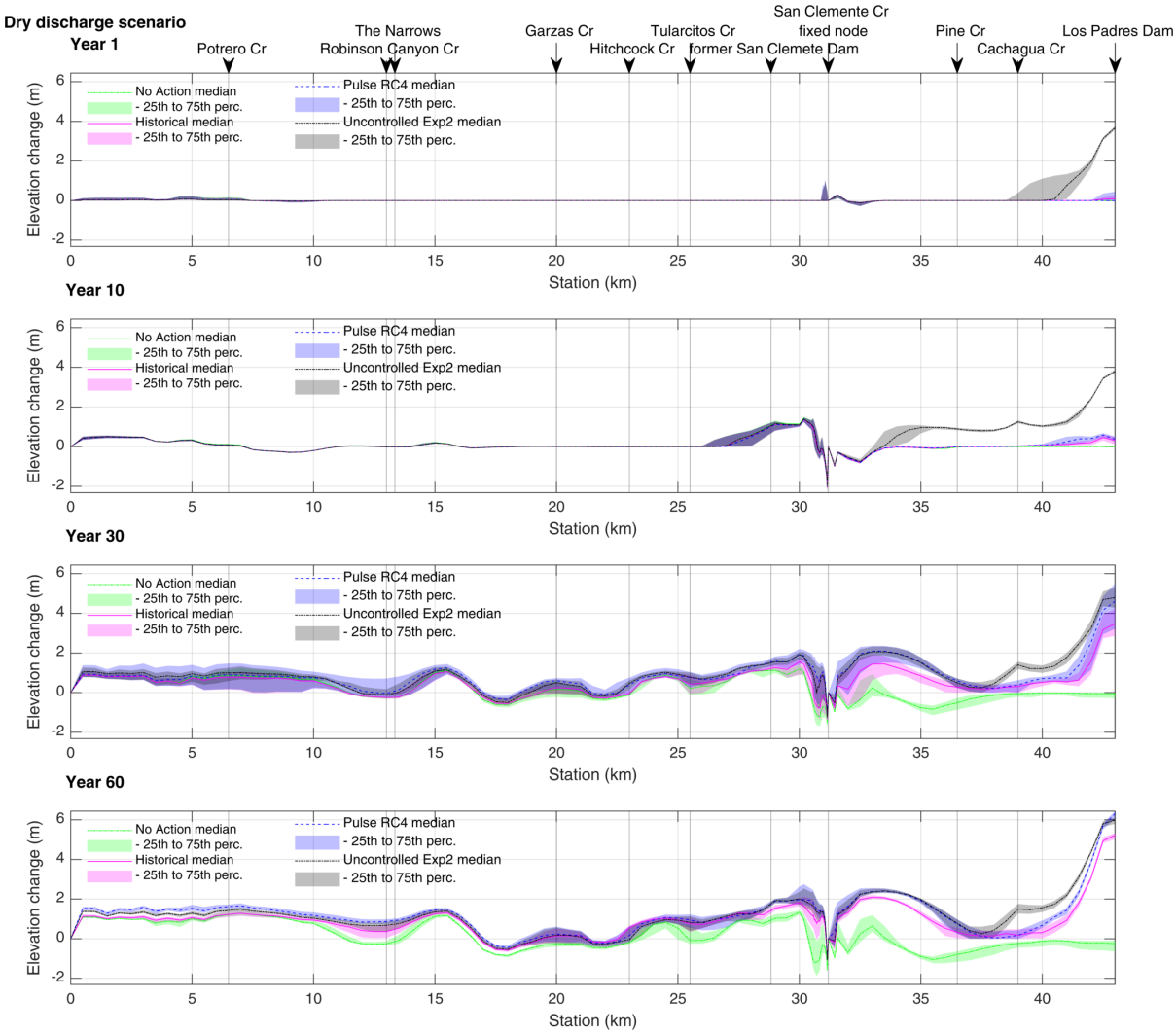

Figure B.60: Comparison of projected bed elevation change from the 2017 initial profile for the dry hydrologic condition and the Historical, Pulse and Uncontrolled sediment supply simulations. Shaded regions capture the 25th-75th percentile responses across the 100 simulations for the dry condition. Results shown for simulation year 1, 10, 30 and 60.

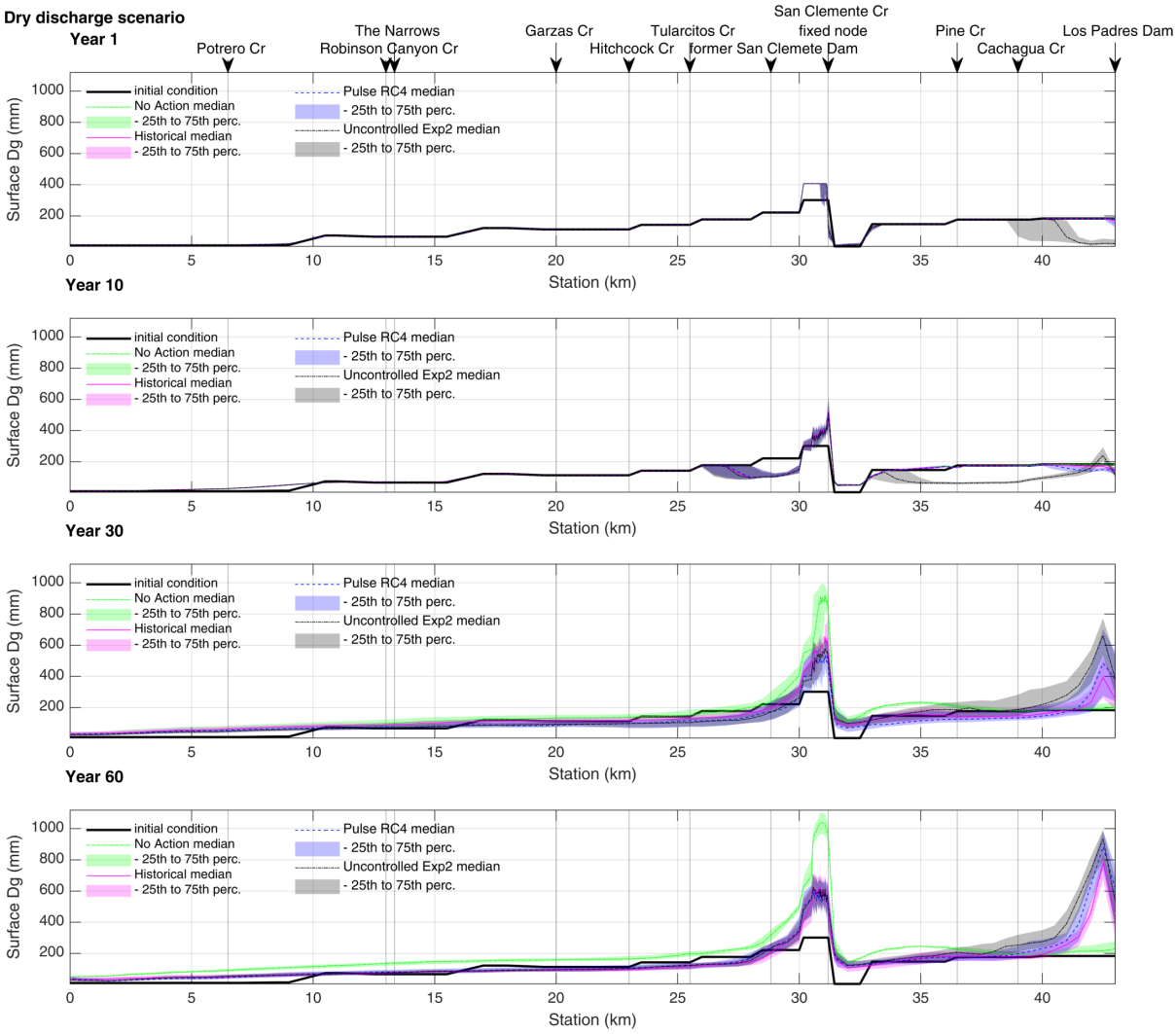

Figure B.61: Comparison of projected change of the geometric mean grain size of the bed surface D_g for the dry hydrologic condition and the Historical, Pulse and Uncontrolled sediment supply simulations. Shaded regions capture the 25th-75th percentile responses across the 100 simulations for the dry condition. Results shown for simulation year 1, 10, 30 and 60.

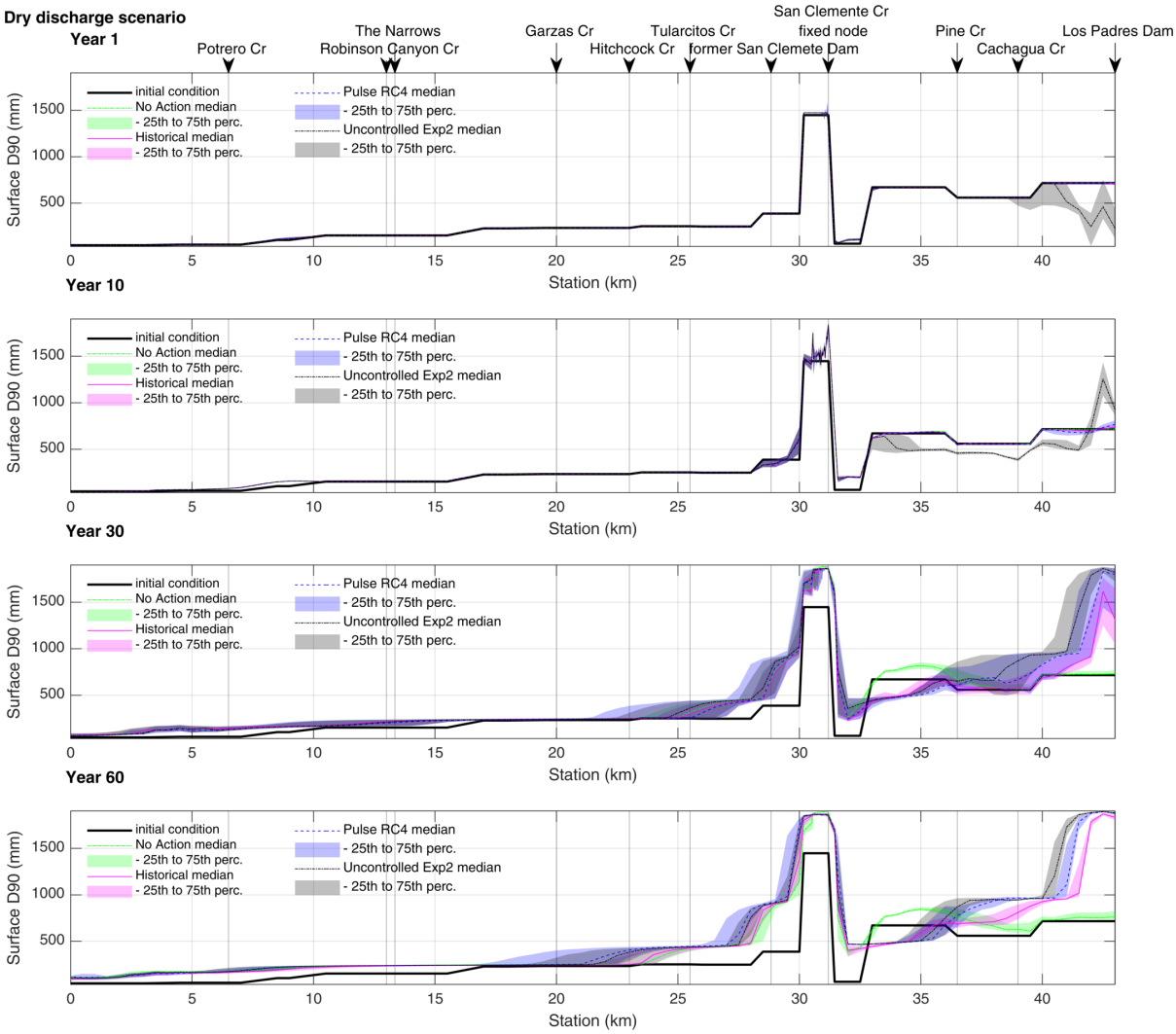

Figure B.62: Comparison of projected change of the geometric mean grain size of the bed surface D_{90} for the dry hydrologic condition and the Historical, Pulse and Uncontrolled sediment supply simulations. Shaded regions capture the 25th-75th percentile responses across the 100 simulations for the dry condition. Results shown for simulation year 1, 10, 30 and 60.

B.13 Median Results of all Scenarios

Elevation change

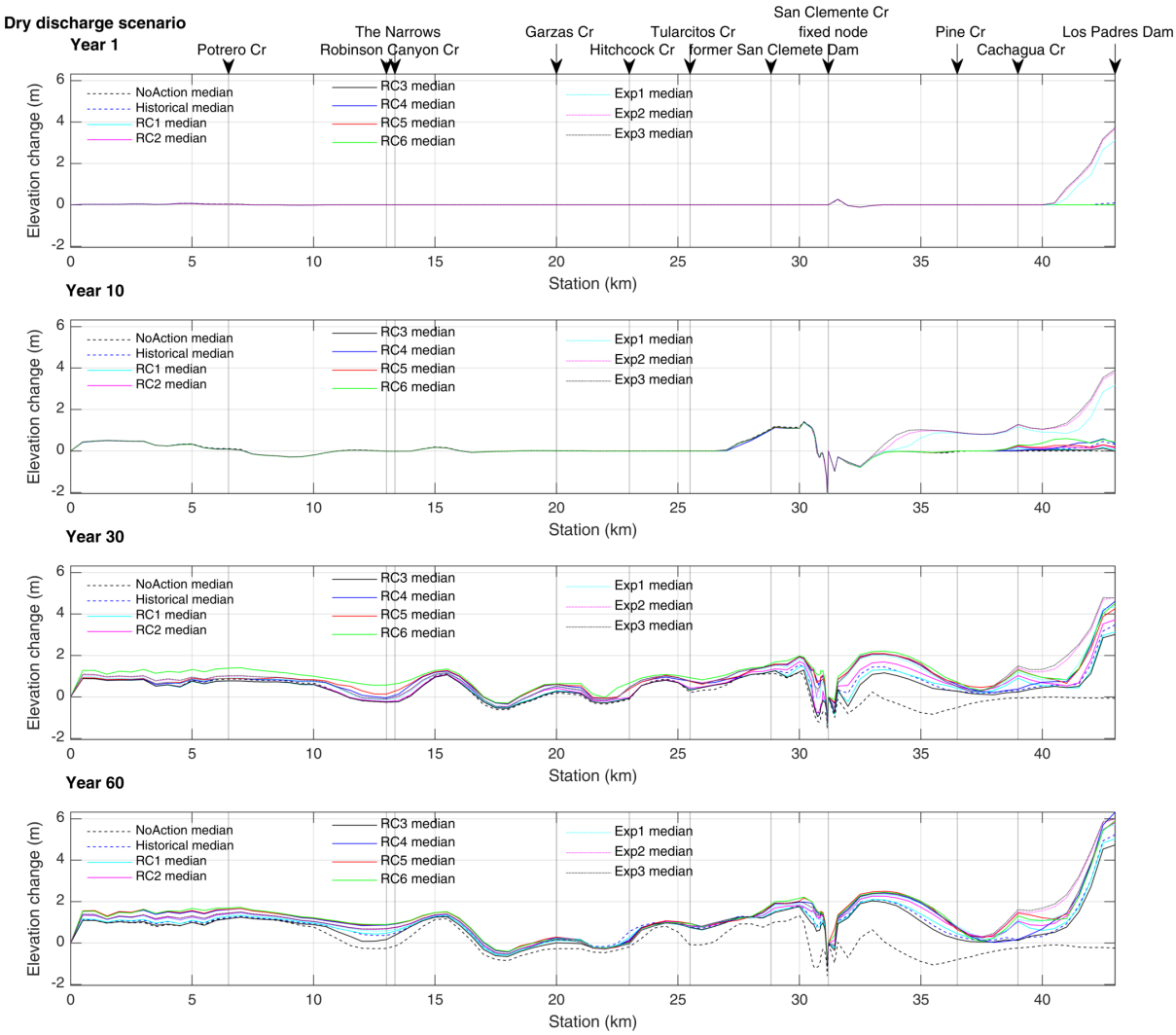

Figure B.63: Median elevation change in the Pulse Supply (RC1-6) and Uncontrolled Supply (Exp1-3) scenarios under the 'Dry' hydrologic regime. Each line represents the median of 100 simulations.

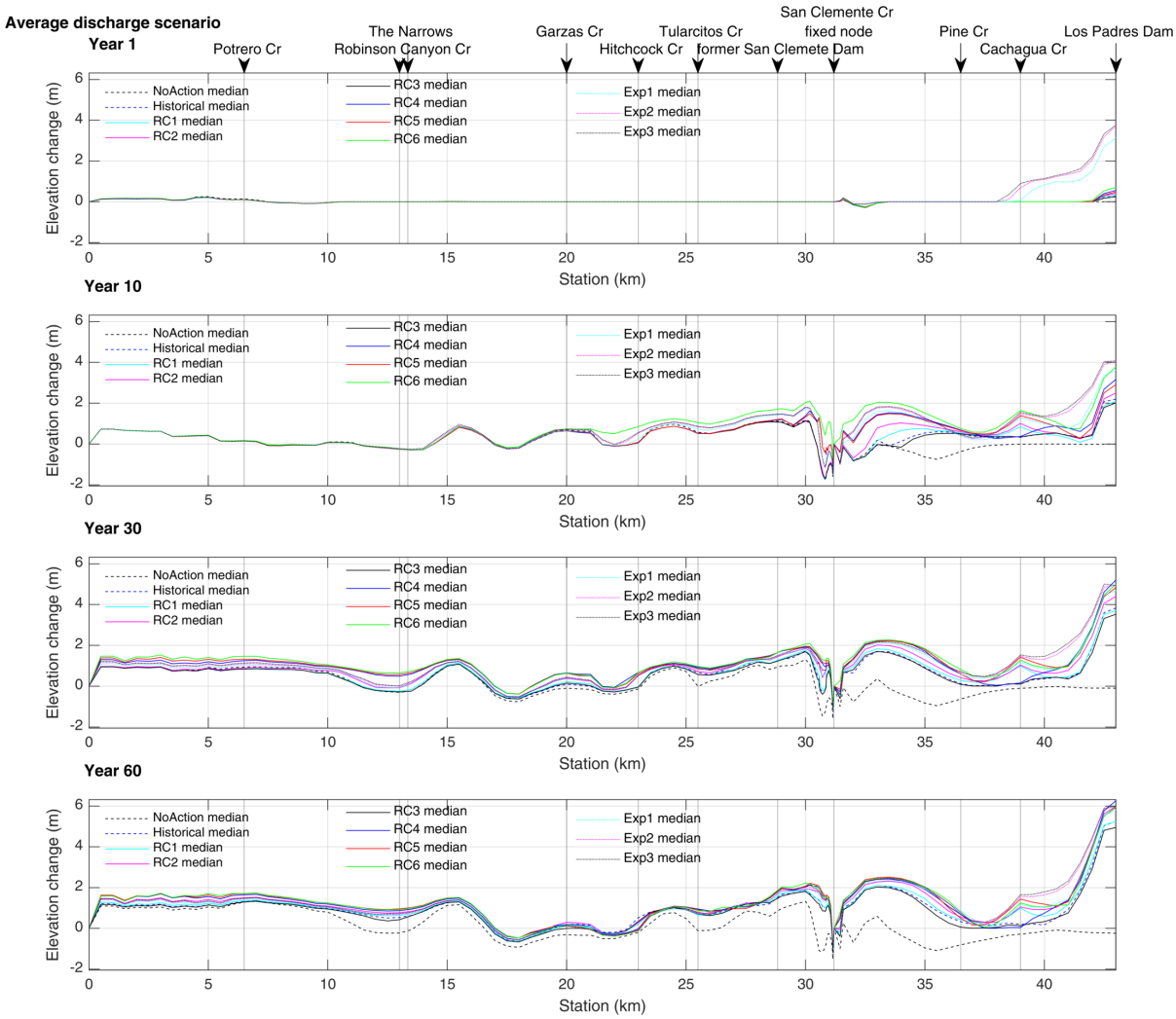

Figure B.64: Median elevation change in the Pulse Supply (RC1-6) and Uncontrolled Supply (Exp1-3) scenarios under the 'Average' hydrologic regime. Each line represents the median of 100 simulations.

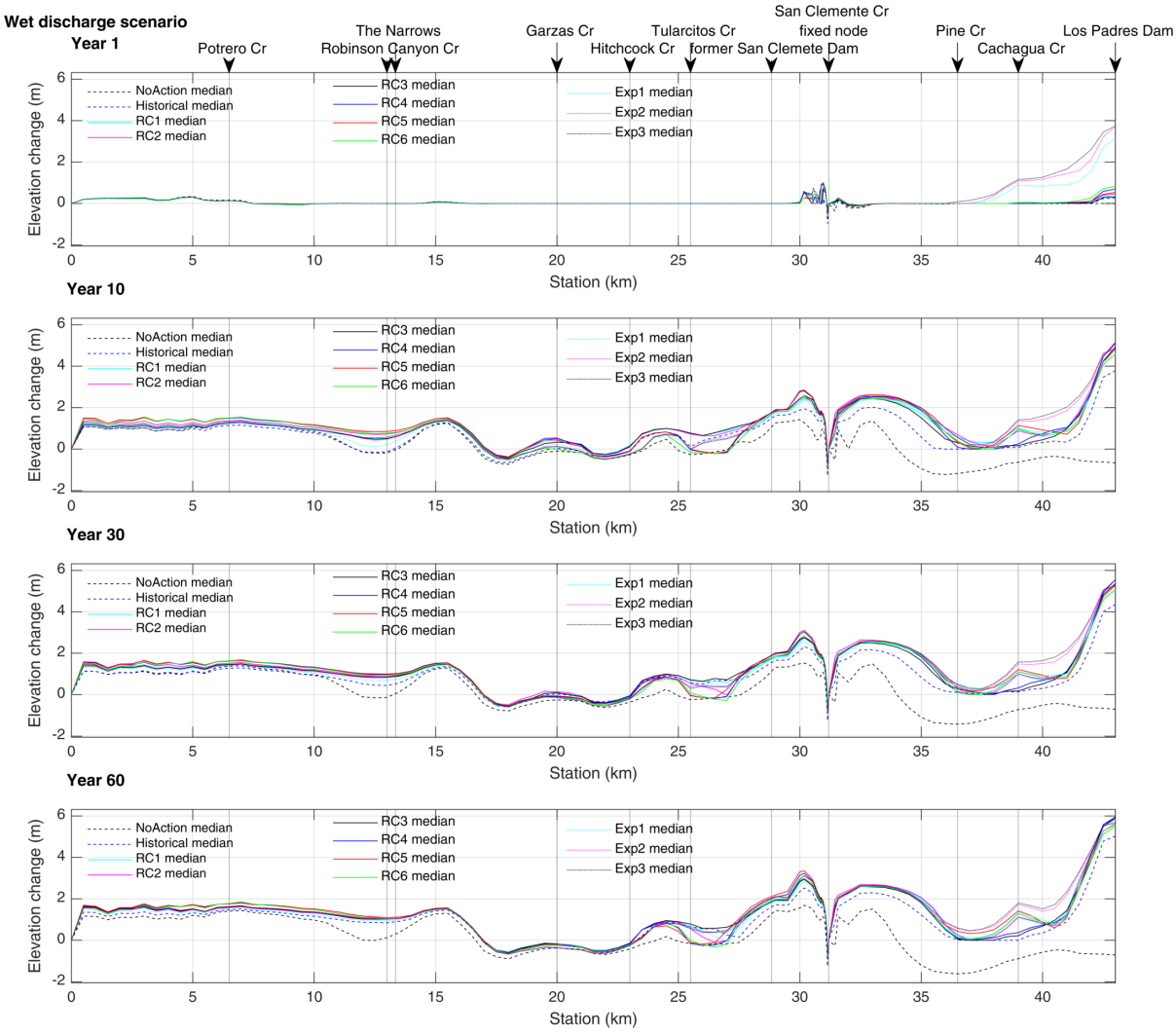

Figure B.65: Median elevation change in the Pulse Supply (RC1-6) and Uncontrolled Supply (Exp1-3) scenarios under the 'Wet' hydrologic regime. Each line represents the median of 100 simulations.

Surface D_{90}

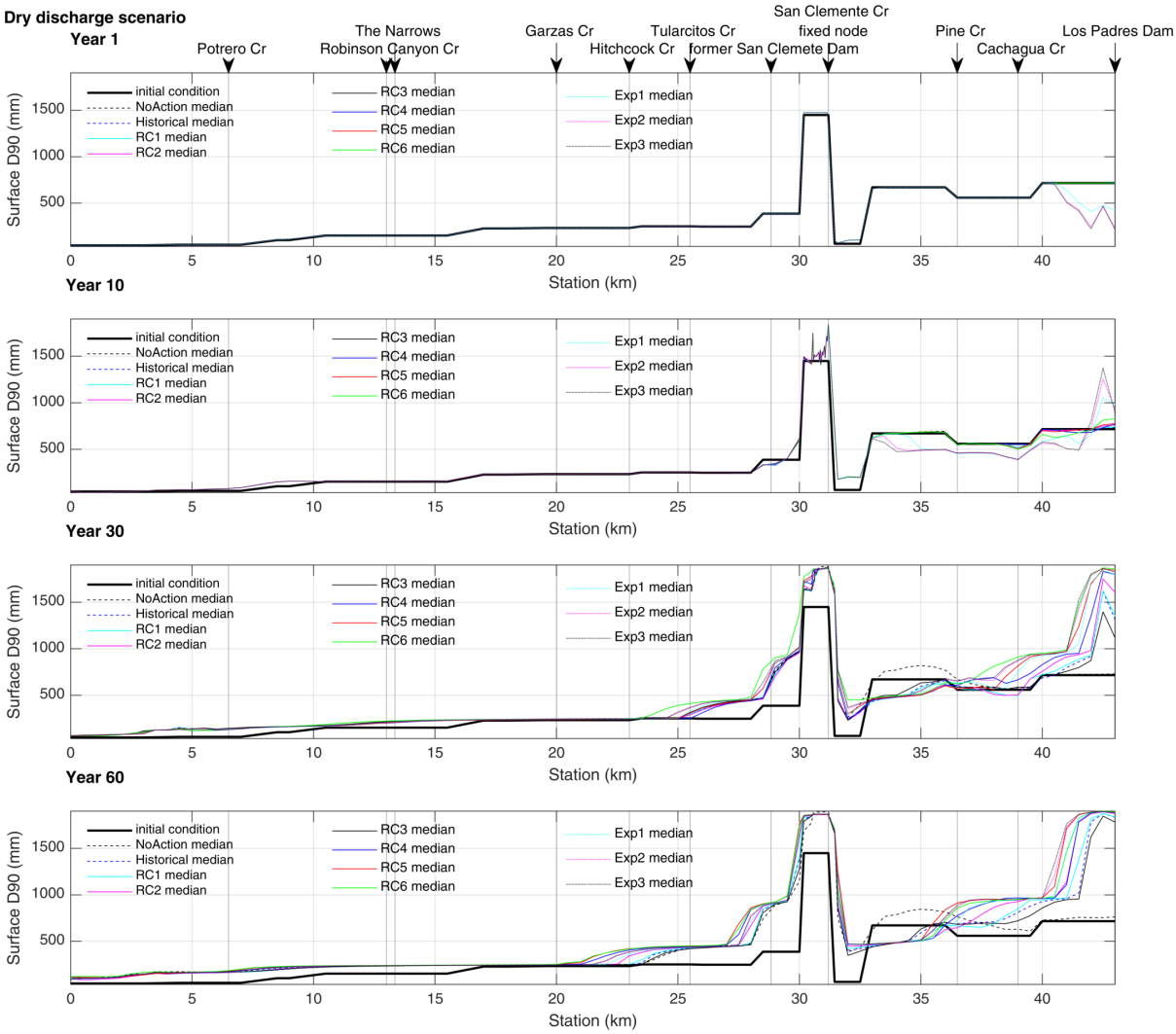

Figure B.66: Median surface D90 in the Pulse Supply (RC1-6) and Uncontrolled Supply (Exp1-3) scenarios under the 'Dry' hydrologic regime. Each line represents the median of 100 simulations.

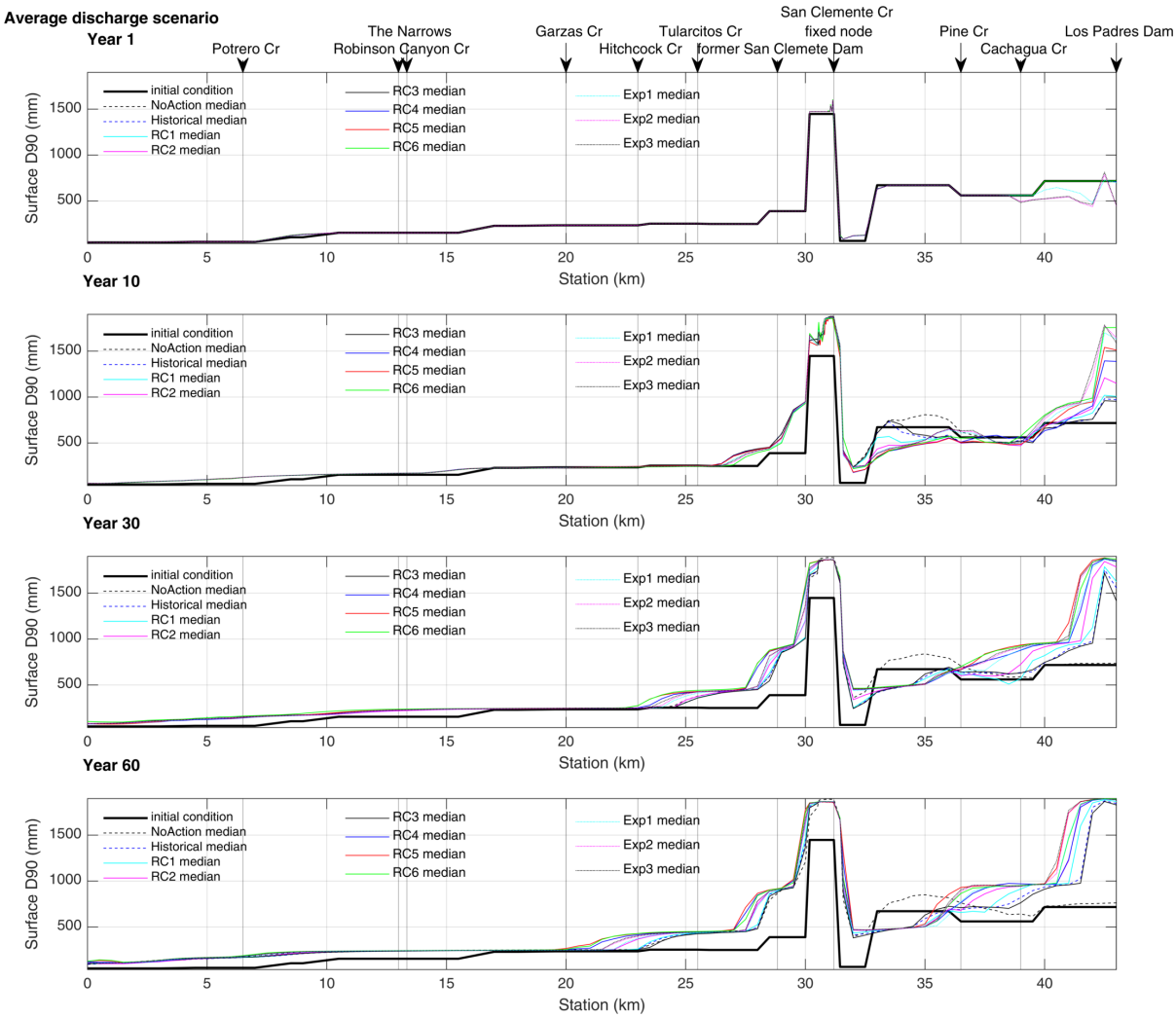

Figure B.67: Median surface D90 in the Pulse Supply (RC1-6) and Uncontrolled Supply (Exp1-3) scenarios under the 'Average' hydrologic regime. Each line represents the median of 100 simulations.

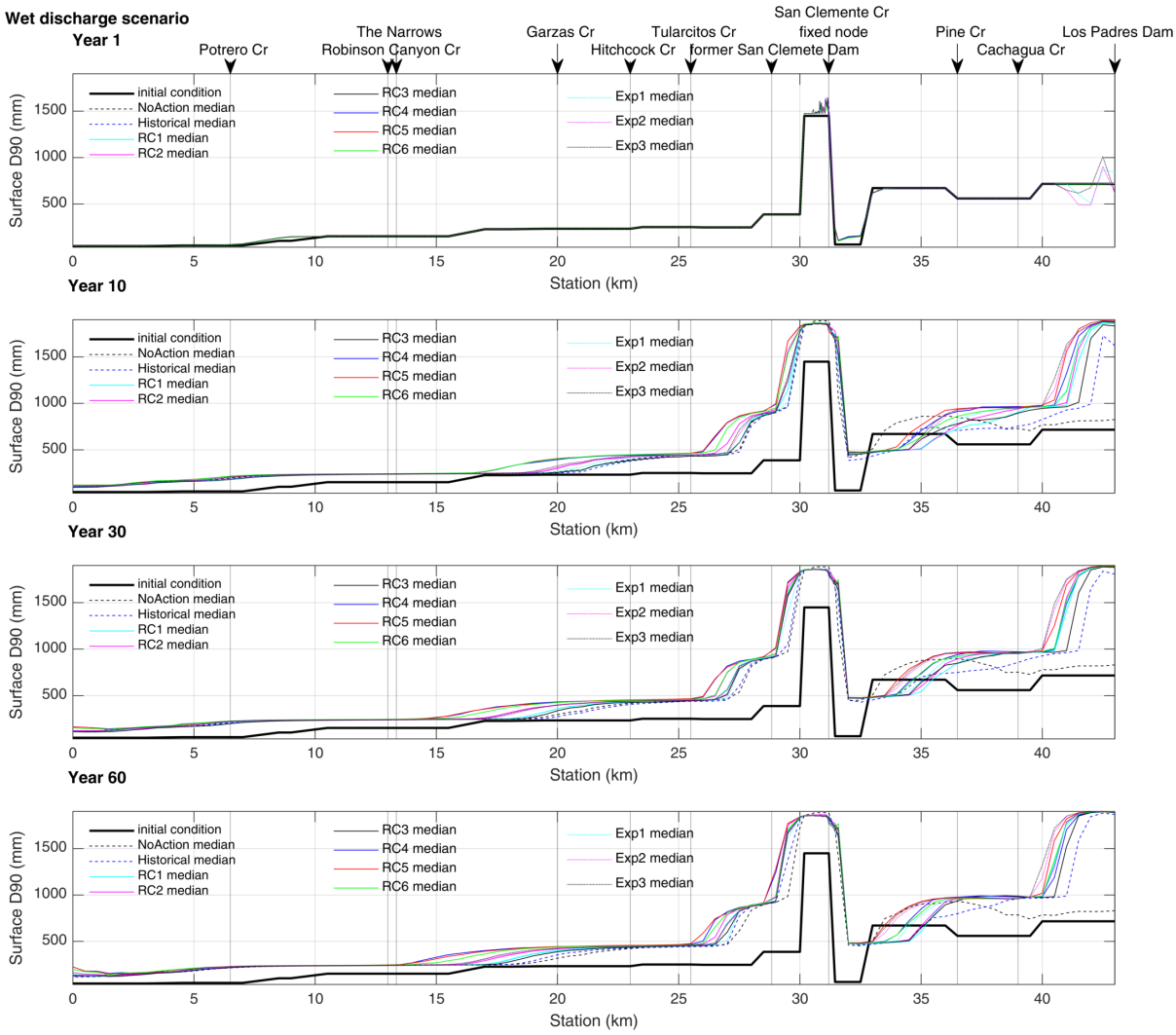

Figure B.68: Median surface D90 in the Pulse Supply (RC1-6) and Uncontrolled Supply (Exp1-3) scenarios under the 'Wet' hydrologic regime. Each line represents the median of 100 simulations.

Surface D_g

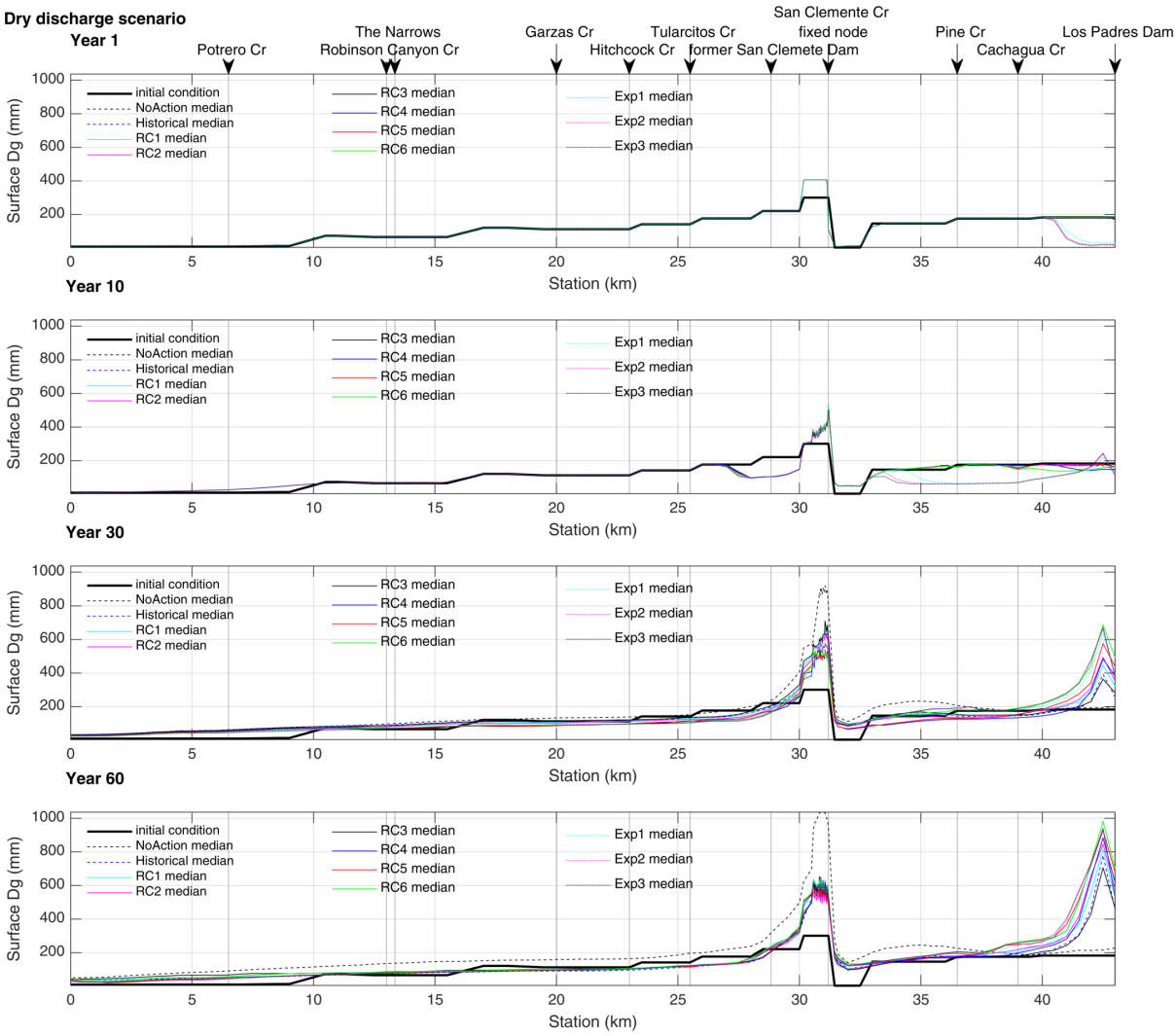

Figure B.69: Median surface Dg in the Pulse Supply (RC1-6) and Uncontrolled Supply (Exp1-3) scenarios under the 'Dry' hydrologic regime. Each line represents the median of 100 simulations.

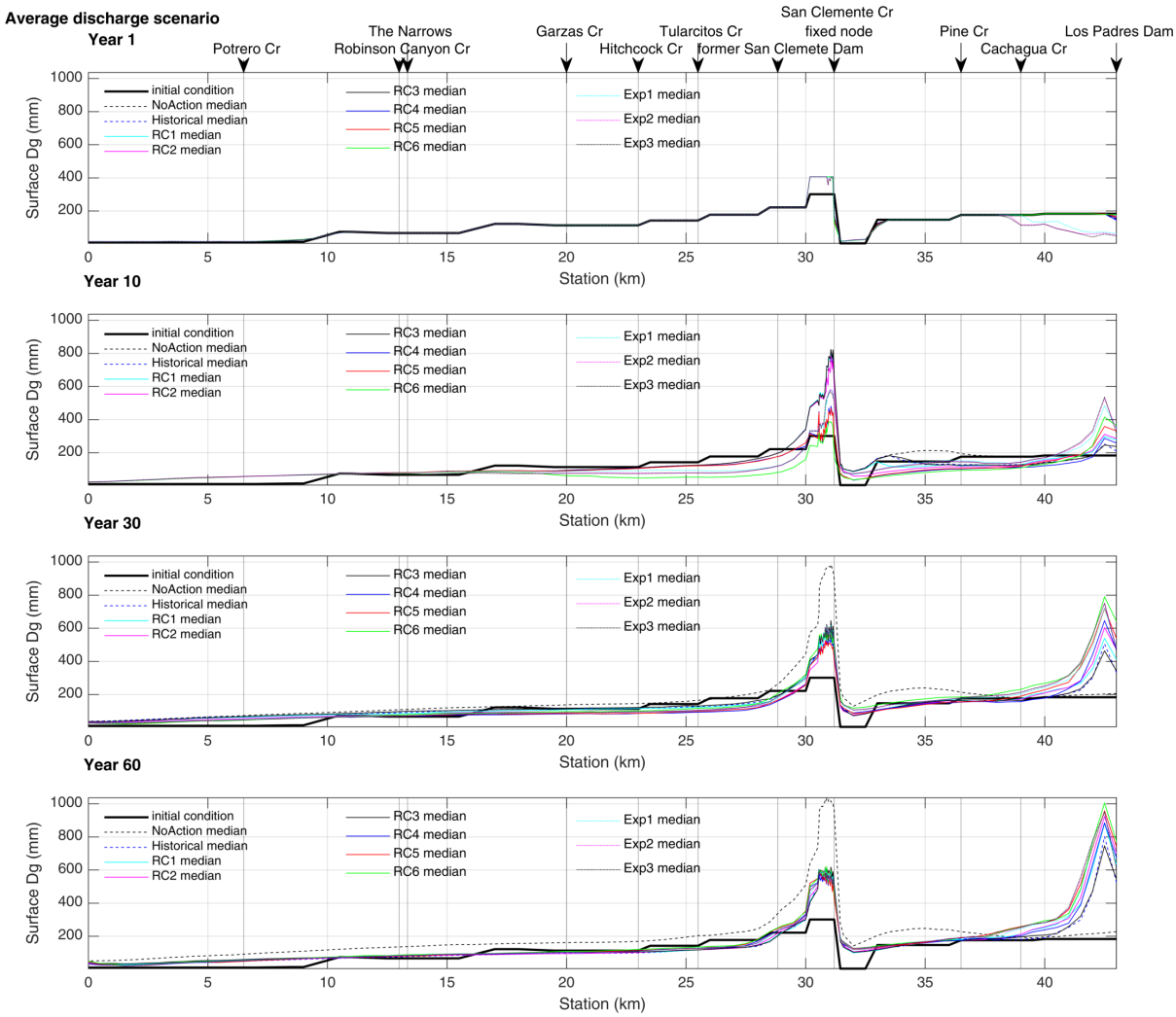

Figure B.70: Median surface Dg in the Pulse Supply (RC1-6) and Uncontrolled Supply (Exp1-3) scenarios under the 'Average' hydrologic regime. Each line represents the median of 100 simulations.

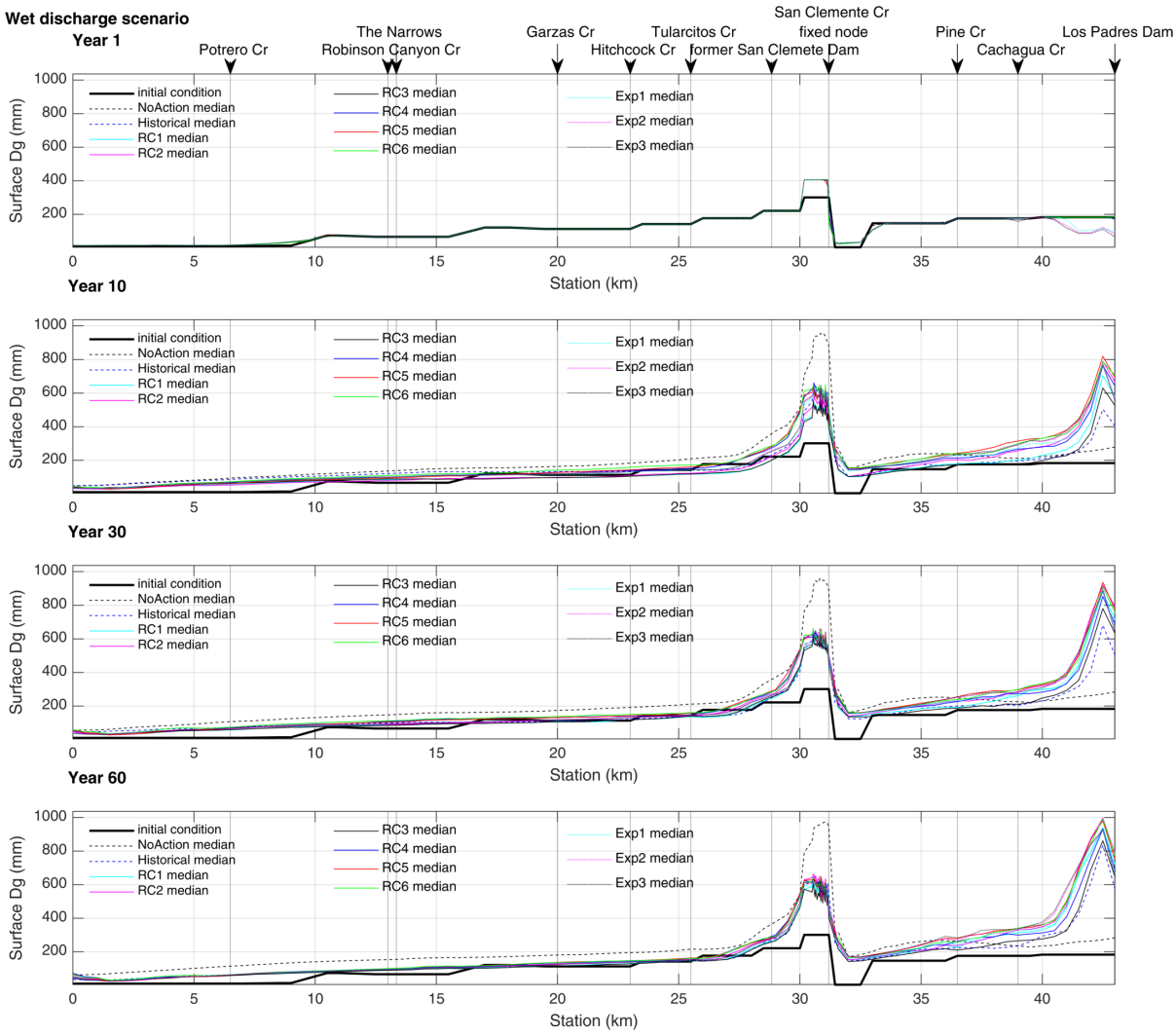

Figure B.71: Median surface Dg in the Pulse Supply (RC1-6) and Uncontrolled Supply (Exp1-3) scenarios under the 'Wet' hydrologic regime. Each line represents the median of 100 simulations.

Slope

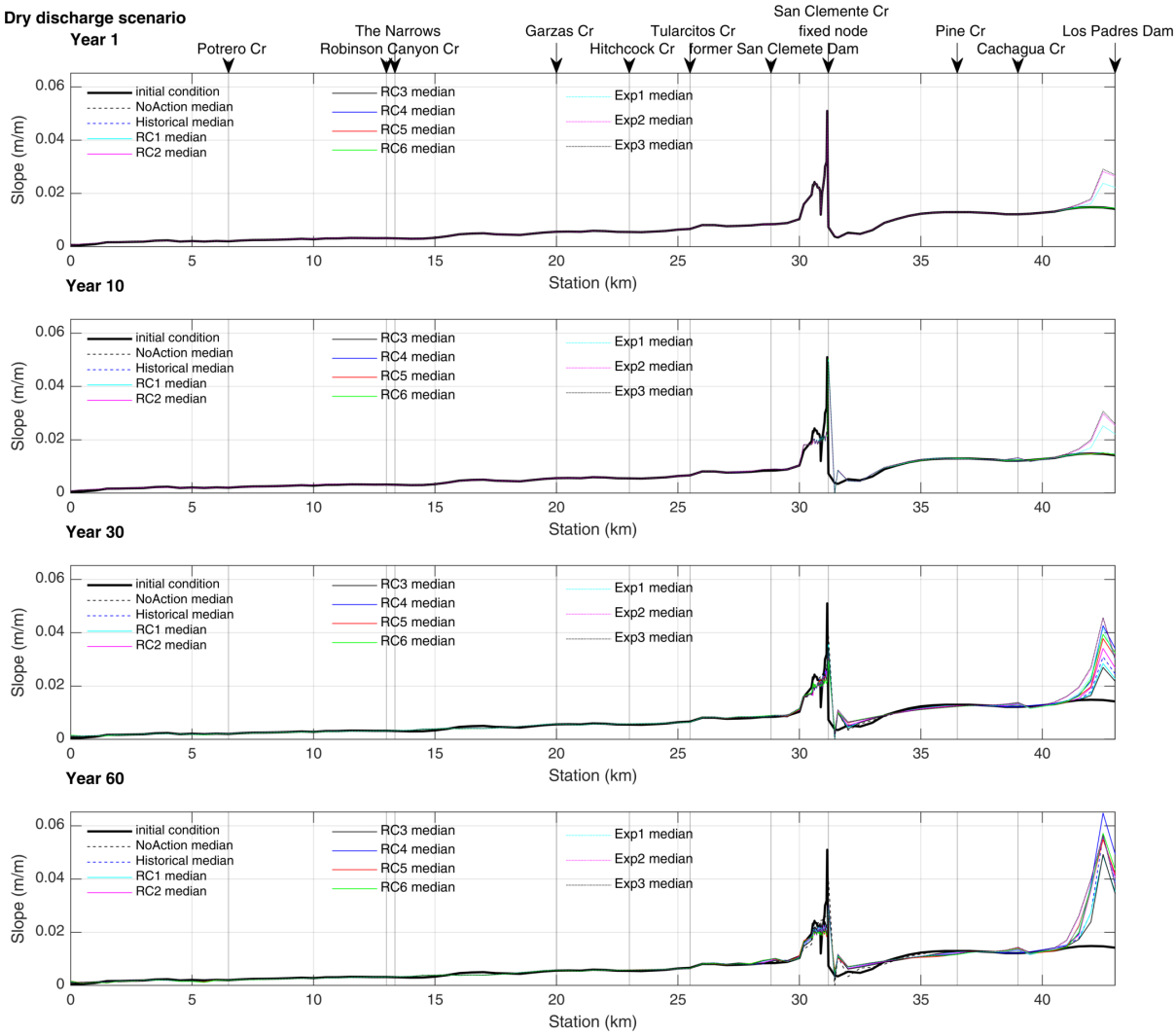

Figure B.72: Median slope in the Pulse Supply (RC1-6) and Uncontrolled Supply (Exp1-3) scenarios under the 'Dry' hydrologic regime. Each line represents the median of 100 simulations.

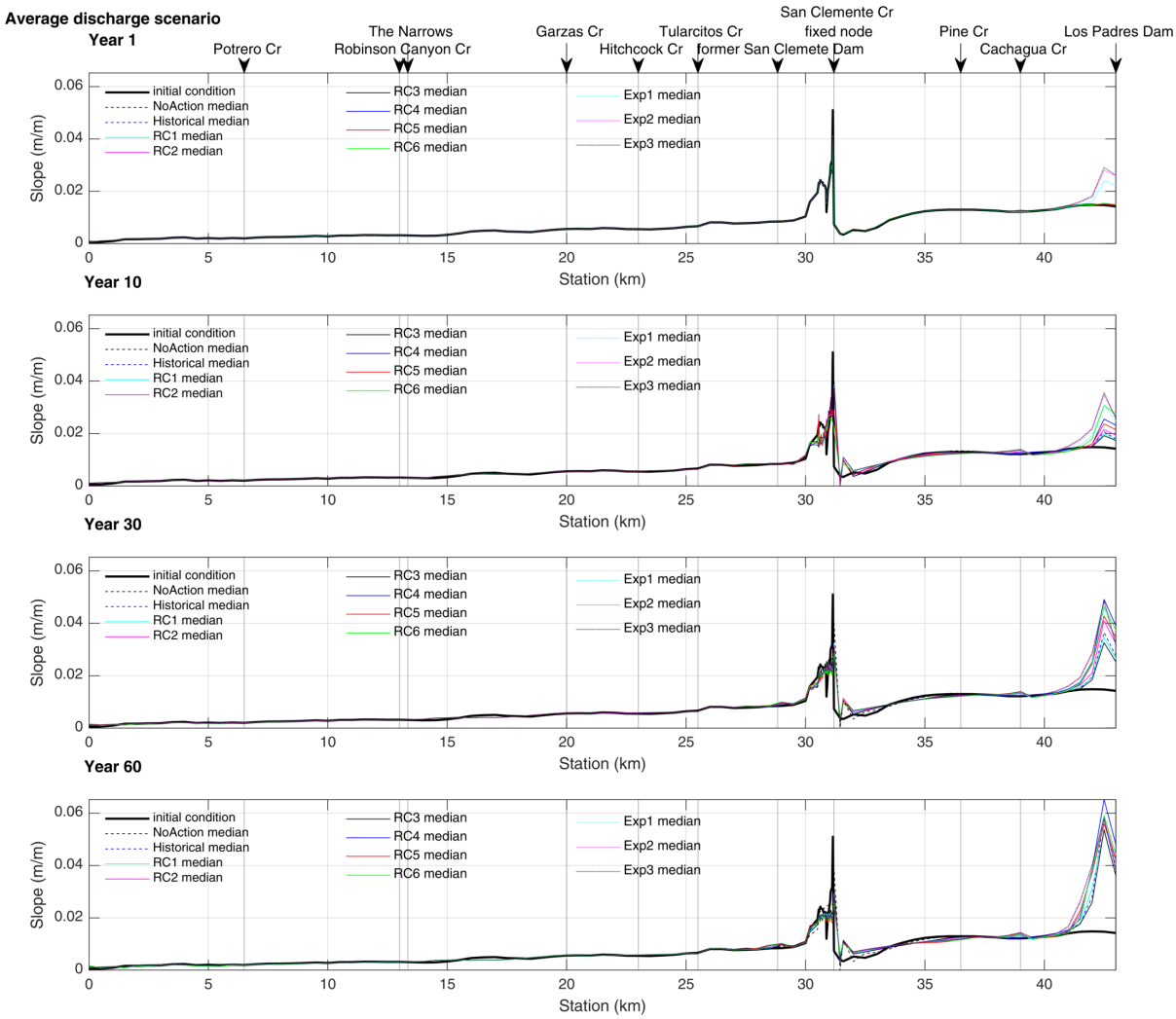

Figure B.73: Median slope in the Pulse Supply (RC1-6) and Uncontrolled Supply (Exp1-3) scenarios under the 'Average' hydrologic regime. Each line represents the median of 100 simulations.

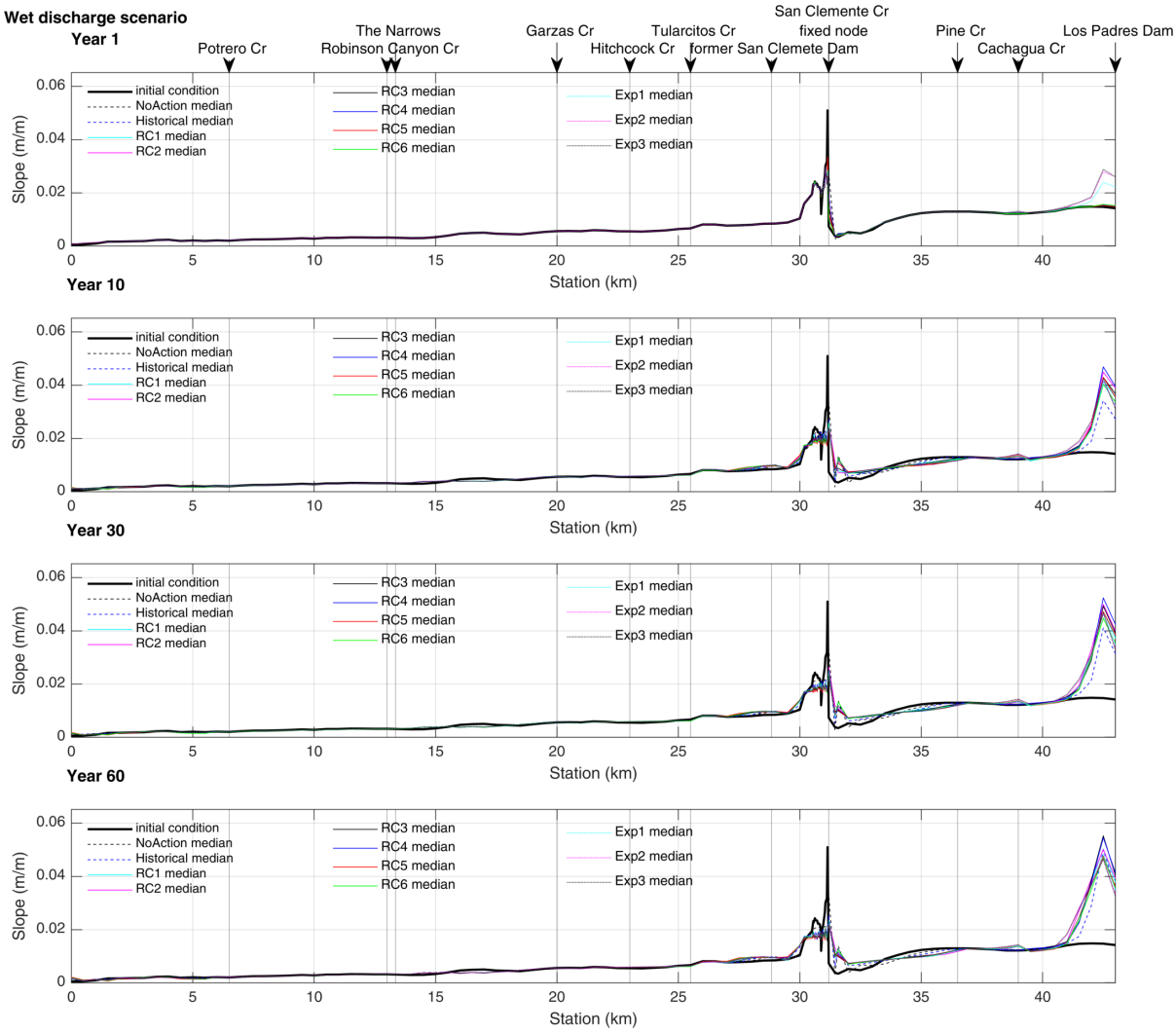

Figure B.74: Median slope in the Pulse Supply (RC1-6) and Uncontrolled Supply (Exp1-3) scenarios under the 'Wet' hydrologic regime. Each line represents the median of 100 simulations.

Appendix C

DistID and U-Net model parameters

C.1 Employed ResNet50 architecture

```
----------------------------------------------------------------------------------------
Layer (type)                    Output Shape         Param #     Connected to
========================================================================================
         ### 48 layers omitted from the Keras implementation for ResNet50 ####
----------------------------------------------------------------------------------------
activation_49 (Activation)      (None, 10, 10, 2048) 0           add_16[0][0]
----------------------------------------------------------------------------------------
flatten_1 (Flatten)             (None, 204800)       0           activation_49[0][0]
----------------------------------------------------------------------------------------
dense_1 (Dense)                 (None, 512)          104858112   flatten_1[0][0]
----------------------------------------------------------------------------------------
dropout_1 (Dropout)             (None, 512)          0           dense_1[0][0]
----------------------------------------------------------------------------------------
dense_2 (Dense)                 (None, 256)          131328      dropout_1[0][0]
----------------------------------------------------------------------------------------
dropout_2 (Dropout)             (None, 256)          0           dense_2[0][0]
```

```
----------------------------------------------------------------------------------------
dense_3 (Dense)                  (None, 128)          32896       dropout_2[0][0]
----------------------------------------------------------------------------------------
dense_4 (Dense)                  (None, 10)           1290        dense_3[0][0]
========================================================================================
Total params: 128,611,338
Trainable params: 128,558,218
Non-trainable params: 53,120
----------------------------------------------------------------------------------------
```

```
optimizer: stochastic gradient descent
optimizers.SGD(lr=0.0003, momentum=0.9, nesterov=True, decay=1e-7)
loss: mean absolute error
```

C.2 Employed VGG19 architecture

```
------------------------------------------------------------------
Layer (type)                 Output Shape              Param #
==================================================================
input_1 (InputLayer)         (None, 300, 300, 3)       0
------------------------------------------------------------------
block1_conv1 (Conv2D)        (None, 300, 300, 64)      1792
------------------------------------------------------------------
block1_conv2 (Conv2D)        (None, 300, 300, 64)      36928
------------------------------------------------------------------
block1_pool (MaxPooling2D)   (None, 150, 150, 64)      0
------------------------------------------------------------------
block2_conv1 (Conv2D)        (None, 150, 150, 128)     73856
------------------------------------------------------------------
```

```
block2_conv2 (Conv2D)        (None, 150, 150, 128)     147584
_________________________________________________________________
block2_pool (MaxPooling2D)   (None, 75, 75, 128)       0
_________________________________________________________________
block3_conv1 (Conv2D)        (None, 75, 75, 256)       295168
_________________________________________________________________
block3_conv2 (Conv2D)        (None, 75, 75, 256)       590080
_________________________________________________________________
block3_conv3 (Conv2D)        (None, 75, 75, 256)       590080
_________________________________________________________________
block3_conv4 (Conv2D)        (None, 75, 75, 256)       590080
_________________________________________________________________
block3_pool (MaxPooling2D)   (None, 37, 37, 256)       0
_________________________________________________________________
block4_conv1 (Conv2D)        (None, 37, 37, 512)       1180160
_________________________________________________________________
block4_conv2 (Conv2D)        (None, 37, 37, 512)       2359808
_________________________________________________________________
block4_conv3 (Conv2D)        (None, 37, 37, 512)       2359808
_________________________________________________________________
block4_conv4 (Conv2D)        (None, 37, 37, 512)       2359808
_________________________________________________________________
block4_pool (MaxPooling2D)   (None, 18, 18, 512)       0
_________________________________________________________________
block5_conv1 (Conv2D)        (None, 18, 18, 512)       2359808
_________________________________________________________________
block5_conv2 (Conv2D)        (None, 18, 18, 512)       2359808
_________________________________________________________________
block5_conv3 (Conv2D)        (None, 18, 18, 512)       2359808
```

```
_________________________________________________________________
block5_conv4 (Conv2D)        (None, 18, 18, 512)       2359808
_________________________________________________________________
block5_pool (MaxPooling2D)   (None, 9, 9, 512)         0
_________________________________________________________________
flatten_1 (Flatten)          (None, 41472)             0
_________________________________________________________________
dense_1 (Dense)              (None, 512)               21234176
_________________________________________________________________
dropout_1 (Dropout)          (None, 512)               0
_________________________________________________________________
dense_2 (Dense)              (None, 256)               131328
_________________________________________________________________
dropout_2 (Dropout)          (None, 256)               0
_________________________________________________________________
dense_3 (Dense)              (None, 128)               32896
_________________________________________________________________
dense_4 (Dense)              (None, 10)                1290
=================================================================
Total params: 41,424,074
Trainable params: 41,424,074
Non-trainable params: 0
_________________________________________________________________
```

```
optimizer: stochastic gradient descent
optimizers.SGD(lr=0.0003, momentum=0.9, nesterov=True, decay=1e-7)
loss: mean absolute error
```

C.3 Employed UNet architecture

```
____________________________________________________________________________________________
Layer (type)                     Output Shape         Param #     Connected to
============================================================================================
input_2 (InputLayer)             (None, 512, 512, 3)  0
____________________________________________________________________________________________
lambda_2 (Lambda)                (None, 512, 512, 3)  0           input_2[0][0]
____________________________________________________________________________________________
conv2d_20 (Conv2D)               (None, 512, 512, 16) 448         lambda_2[0][0]
____________________________________________________________________________________________
dropout_10 (Dropout)             (None, 512, 512, 16) 0           conv2d_20[0][0]
____________________________________________________________________________________________
conv2d_21 (Conv2D)               (None, 512, 512, 16) 2320        dropout_10[0][0]
____________________________________________________________________________________________
max_pooling2d_5 (MaxPooling2D)   (None, 256, 256, 16) 0           conv2d_21[0][0]
____________________________________________________________________________________________
conv2d_22 (Conv2D)               (None, 256, 256, 32) 4640        max_pooling2d_5[0][0]
____________________________________________________________________________________________
dropout_11 (Dropout)             (None, 256, 256, 32) 0           conv2d_22[0][0]
____________________________________________________________________________________________
conv2d_23 (Conv2D)               (None, 256, 256, 32) 9248        dropout_11[0][0]
____________________________________________________________________________________________
max_pooling2d_6 (MaxPooling2D)   (None, 128, 128, 32) 0           conv2d_23[0][0]
____________________________________________________________________________________________
conv2d_24 (Conv2D)               (None, 128, 128, 64) 18496       max_pooling2d_6[0][0]
____________________________________________________________________________________________
dropout_12 (Dropout)             (None, 128, 128, 64) 0           conv2d_24[0][0]
____________________________________________________________________________________________
```

```
conv2d_25 (Conv2D)              (None, 128, 128, 64) 36928       dropout_12[0][0]
__________________________________________________________________________________________________
max_pooling2d_7 (MaxPooling2D)  (None, 64, 64, 64)   0           conv2d_25[0][0]
__________________________________________________________________________________________________
conv2d_26 (Conv2D)              (None, 64, 64, 128)  73856       max_pooling2d_7[0][0]
__________________________________________________________________________________________________
dropout_13 (Dropout)            (None, 64, 64, 128)  0           conv2d_26[0][0]
__________________________________________________________________________________________________
conv2d_27 (Conv2D)              (None, 64, 64, 128)  147584      dropout_13[0][0]
__________________________________________________________________________________________________
max_pooling2d_8 (MaxPooling2D)  (None, 32, 32, 128)  0           conv2d_27[0][0]
__________________________________________________________________________________________________
conv2d_28 (Conv2D)              (None, 32, 32, 256)  295168      max_pooling2d_8[0][0]
__________________________________________________________________________________________________
dropout_14 (Dropout)            (None, 32, 32, 256)  0           conv2d_28[0][0]
__________________________________________________________________________________________________
conv2d_29 (Conv2D)              (None, 32, 32, 256)  590080      dropout_14[0][0]
__________________________________________________________________________________________________
conv2d_transpose_5 (Conv2DTrans (None, 64, 64, 128)  131200      conv2d_29[0][0]
__________________________________________________________________________________________________
concatenate_5 (Concatenate)     (None, 64, 64, 256)  0           conv2d_transpose_5[0][0]
                                                                 conv2d_27[0][0]
__________________________________________________________________________________________________
conv2d_30 (Conv2D)              (None, 64, 64, 128)  295040      concatenate_5[0][0]
__________________________________________________________________________________________________
dropout_15 (Dropout)            (None, 64, 64, 128)  0           conv2d_30[0][0]
__________________________________________________________________________________________________
conv2d_31 (Conv2D)              (None, 64, 64, 128)  147584      dropout_15[0][0]
__________________________________________________________________________________________________
```

```
conv2d_transpose_6 (Conv2DTrans (None, 128, 128, 64) 32832       conv2d_31[0][0]
__________________________________________________________________________________________
concatenate_6 (Concatenate)     (None, 128, 128, 128 0           conv2d_transpose_6[0][0]
                                                                 conv2d_25[0][0]
__________________________________________________________________________________________
conv2d_32 (Conv2D)              (None, 128, 128, 64) 73792       concatenate_6[0][0]
__________________________________________________________________________________________
dropout_16 (Dropout)            (None, 128, 128, 64) 0           conv2d_32[0][0]
__________________________________________________________________________________________
conv2d_33 (Conv2D)              (None, 128, 128, 64) 36928       dropout_16[0][0]
__________________________________________________________________________________________
conv2d_transpose_7 (Conv2DTrans (None, 256, 256, 32) 8224        conv2d_33[0][0]
__________________________________________________________________________________________
concatenate_7 (Concatenate)     (None, 256, 256, 64) 0           conv2d_transpose_7[0][0]
                                                                 conv2d_23[0][0]
__________________________________________________________________________________________
conv2d_34 (Conv2D)              (None, 256, 256, 32) 18464       concatenate_7[0][0]
__________________________________________________________________________________________
dropout_17 (Dropout)            (None, 256, 256, 32) 0           conv2d_34[0][0]
__________________________________________________________________________________________
conv2d_35 (Conv2D)              (None, 256, 256, 32) 9248        dropout_17[0][0]
__________________________________________________________________________________________
conv2d_transpose_8 (Conv2DTrans (None, 512, 512, 16) 2064        conv2d_35[0][0]
__________________________________________________________________________________________
concatenate_8 (Concatenate)     (None, 512, 512, 32) 0           conv2d_transpose_8[0][0]
                                                                 conv2d_21[0][0]
__________________________________________________________________________________________
conv2d_36 (Conv2D)              (None, 512, 512, 16) 4624        concatenate_8[0][0]
__________________________________________________________________________________________
```

```
dropout_18 (Dropout)            (None, 512, 512, 16) 0           conv2d_36[0][0]
__________________________________________________________________________________________________
conv2d_37 (Conv2D)              (None, 512, 512, 16) 2320        dropout_18[0][0]
__________________________________________________________________________________________________
conv2d_38 (Conv2D)              (None, 512, 512, 6)  102         conv2d_37[0][0]
==================================================================================================
Total params: 1,941,190
Trainable params: 1,941,190
Non-trainable params: 0
__________________________________________________________________________________________________
```

```
batch_size=5,
epochs=50,
optimizer='adam',
loss='binary_crossentropy'
```